THE UNIVERSITY *of* EDINBURGH

BEHAVIOUR OF REINFORCED CONCRETE FRAME STRUCTURE AGAINST PROGRESSIVE COLLAPSE

by

Ofonime Akpan Harry

A thesis submitted in partial fulfilment of the requirements for the degree of Doctor of Philosophy

Institute for Infrastructure and the Environment

School of Engineering

The University *of* Edinburgh

March, 2018

Declaration

This thesis entitled, ‘‘Behaviour of reinforced concrete frame structure against progressive collapse’’ is submitted to the University of Edinburgh for the degree of Doctor of Philosophy. The research work described and reported in this thesis has been completed solely by Ofonime Akpan Harry under the supervision of Professor Yong Lu and Dr Tim Stratford. I can confirm:

- that the thesis has been composed by the author, and
- either that the work is the author’s own or if the author has been a member of a research group, that the author has made a substantial contribution to the work, such contributions are clearly indicated, and
- that the work in this thesis has not been submitted for any other degree or professional qualifications.

Publications based on this thesis:

Harry, O. **A.** and Lu, Y., 2016. “Effect of reinforcement detailing on progressive collapse resistance” 16th International Conference & Exhibition on Structural Faults & Repair. May 2016, Edinburgh, Scotland, United Kingdom.

Harry, O. **A.** and Lu, Y., 2017. “Progressive collapse-arching effect in reinforced concrete beams” CONFAB 2017: 2nd International Conference on Structural Safety under Fire & Blast Loading. September 2017, London, United Kingdom.

Cheng, X., **Harry, O.**, Irvine, M., Jacobs, P. and Lu, Y., 2017. “Progressive collapse - a laboratory perspective of beam assemblies in a column loss scenario” CONFAB 2017: 2nd International Conference on Structural Safety under Fire & Blast Loading. September 2017, London, United Kingdom.

Harry, O. **A.** and Lu, Y. “A theoretical model for prediction of catenary effect in beam assemblies considering strength degradations” (Journal paper in preparation)

Harry, O. **A.** and Lu, Y. "A semi-empirical analysis approach to predicting arching action in RC beam assemblies under a column removal scenario" (Journal paper in preparation)

Signed:

Dated:

Abstract

A structure subjected to extreme load due to explosion or human error may lead to progressive collapse. One of the direct methods specified by design guidelines for assessing progressive collapse is the Alternate Load Path method which involves removal of a structural member and analysing the structure to assess its potential of bridging over the removed member without collapse. The use of this method in assessing progressive collapse therefore requires that the vertical load resistance function of the bridging beam assembly, which for a typical laterally restrained reinforced concrete (RC) beams include flexural, compressive arching action and catenary action, be accurately predicted.

In this thesis, a comprehensive study on a reliable prediction of the resistance function for the bridging RC beam assemblies is conducted, with a particular focus on a) the arching effect, and b) the catenary effect considering strength degradations. A critical analysis of the effect of axial restraint, flexural reinforcement ratio and span-depth ratio on compressive arching action are evaluated in quantitative terms. A more detailed theoretical model for the prediction of load-displacement behaviour of RC beam assemblies within the compressive arching response regime is presented. The proposed model takes into account the compounding effect of bending and arching from both the deformation and force points of view. Comparisons with experimental results show good agreement.

Following the compressive arching action, catenary action can develop at a much larger displacement regime, and this action could help address collapse. A complete resistance function should adequately account for the catenary action as well as the arching effect. To this end, a generic catenary model which takes into consideration the strength degradation due to local failure events (e.g. rupture of bottom rebar or fracture of a steel weld) and the eventual failure limit is proposed. The application of the model in predicting the resistance function in beam assemblies with strength degradations is discussed. The validity of the proposed model is checked against

predictions from finite element model and experimental tests. The result indicate that strength degradation can be accurately captured by the model.

Finally, the above developed model framework is employed in investigative studies to demonstrate the application of the resistance functions in a dynamic analysis procedure, as well as the significance of the compressive arching effect and the catenary action in the progressive collapse resistance in different designs. The importance of an accurate prediction of the arching effect and the limiting displacement for the catenary action is highlighted.

Acknowledgement

I would like to sincerely appreciate my supervisor Professor Yong Lu for his immense support throughout the duration of my PhD study. His thorough guidance and advice made the successful completion of this study possible.

I am deeply grateful to the Nigerian Government for the financial support without which this study would not have been accomplished.

Life in Edinburgh would have been boring without amazing friends. For this I thank my friends: Dr JP Morrissey, Dr Chuanchuan Hou, Dr Jiaming Xu, Dr Ronzin, Dr Xizhong Chen, Mr Fahad Gulib, Mr Xiaobo Cheng, Mr Tim, Mr. Yu Gu and Mr Joel Keishing for making my stay in Edinburgh worth the while. I would not fail to thank Dr Lige Wang, Dr Utibe Umoh and Dr Ranga Radhakrishnan for their invaluable time in discussing topical issues beyond research.

I will like to specially appreciate my parent Deacon and Deaconness A. H. Etukudoh for their prayers and support. To my siblings Rose, Jane, Enobong and Christiana thank you for always having my back and for the words of encouragement. Not forgetting my in-laws Chijioke Anyawu and Nsisong Charles, I say thank you for all your support.

Finally, I appreciate my mentors Professor Charles Uko and Dr Edet Amana for their unwavering supports towards my academic pursuit.

Table of Content

Declaration.… i

Abstract..... iii

Acknowledgement..... v

Table of Content..... vi

List of Figures.… xii

Listof Tables.…..... xxi

Symbols..... …xxiv

Chapter 1: Introduction 1

1.1 Background..... 1

1.2 Objectives of study 3

1.3 Scope of work 4

1.4 Organisation of the thesis 4

Chapter 2: Literature review 7

2.1 Introduction 7

2.2 Definition of key terminologies..... 7

2.2.1 Progressive collapse 7

2.2.2 Robustness..... 8

2.3 Defining cases of progressive collapse..... 8

2.3.1 Ronan point apartment building in London 8

2.3.2 Murrah building located in Oklahoma City, USA 9

2.3.3 Pentagon building located in Virginia, USA..... 10

2.4 Code and design guidelines against progressive collapse 12

2.5 Experimental studies on progressive collapse..... 16

2.5.1 Studies on RC subassemblies..... 19

2.6 Parameters affecting compressive arching action in axially restrained reinforced concrete beams..... 33

2.6.1 Effect of axial restraint on compressive arching action capacity..... 33

2.6.2 Effect of reinforcement ratio on compressive arching action capacity 35

2.6.3 Effect of span depth ratio on compressive arching action capacity 37

2.6.4 Effect of concrete compressive strength on compressive arching capacity 38

2.7 Analytical studies 39

2.7.1 Analytical studies on compressive arching action 39

2.7.2 Analytical studies on catenary action..... 46

2.8 Concluding remarks 49

Chapter 3: Critical evaluation of compressive arching action - a semi empirical study 51

3.1 Introduction 51

3.2 Existing experimental studies..... 51

3.2.1 Test by Su et al. (2009) 53

3.2.2 Test by Yu & Tan (2013a) and Yu & Tan (2013b) 59

3.2.3 Test by Vesali et al. (2013) and Vali et al. (2015) 64

3.2.4 Test by Sadek et al. (2011) 69

3.3 Critical analysis of all the experimental results 72

3.4 A simplified formulation for arching action 76

3.5 Effect of parameters affecting relative increase in load due to compressive arching action 85

3.5.1 Effect of axial restraint on compressive arching action capacity 85

3.5.2 Effect of reinforcement ratio on compressive arching action capacity 90

3.5.3 Effect of span depth ratio on compressive arching action capacity 93

3.5.4 Effect of concrete compressive strength 95

3.6 Empirical method for the prediction of the arching effect 96

3.6.1 Consideration of effect of the parameters 96

3.6.2 Validation of the proposed semi empirical formulae 98

3.7 Conclusions 100

Chapter 4: Numerical modelling of reinforced concrete beam assembly under a progressive collapse scenario 101

4.1 Introduction 101

4.2 Background of KCC model 102

4.2.1 Performance of KCC model 105

4.3 Modelling of reinforcement 115

4.4 Model checks 116

4.4.1 Reinforcement strain localization 116

4.4.2 Mesh sensitivity 120

4.4.3 Hour glass effect 126

4.5 Validation of numerical models with experimental study by (Yu & Tan 2013b) 128

4.5.1 Detail of the experiment 128

4.5.2 Overview of the finite element model for the test beam assemblies 130

4.6 Concluding remarks 136

Chapter 5: Theoretical model on compressive arching action and associated deformation limit state in axially restrained reinforced concrete beam 139

5.1 Introduction 139

5.2 Development of the Analytical Model: Basic Considerations 140

5.2.1 General Concept 140

5.2.2 Different stages of response 143

5.2.3 Stresses and force equilibrium in the arching effective stage 152

5.2.4 Kinematics for flexible axial support 155

5.2.5 Additional moment of resistance due to arching 156

5.3 Determination of plastic length due to bending and arching 158

5.3.1 Introduction 158

5.3.2 Plastic hinge length for bending 158

5.3.3 Determination of effective “plastic” arching depth to length ratio (x/L_N) 159

5.4 Validation of the proposed model 166

5.5 Conclusions 168

Chapter 6: Simplified theoretical model for prediction of catenary action incorporating strength degradation in axially restrained beams 169

6.1 Introduction 169

6.2 Scope of the model 170

6.3 Analysis procedure for a simplified beam model without consideration of strength degradation 171

6.3.1 Elastic stage 174

6.3.2 Transient stage/catenary action stage 175

6.4 Illustrative example of finite element simulation and theoretical prediction of load-displacement response of beam without considering strength degradation . 182

6.4.1 Finite element model description 182

6.4.2 Result and discussion for FE and theoretical models with no strength degradation 184

6.5 Degradation of yield surface 187

6.5.1 Concept of strength degradation and implications on catenary effect 187

6.5.2 Implementation of degradation of yield surfaces in the beam analysis procedure 189

6.6 Verification of the theoretical model for prediction of load-displacement resistance function with strength degradation 194

6.6.1 Validation with a conceptual FE simulation 194

6.6.2 Validation with existing experiment 197

6.7 Application of the proposed model to reinforced concrete beam-column assemblies 201

6.7.1 General assumptions 201

6.7.2 Formulation for fixed end RC beams with plastic hinges at support and middle sections 202

6.7.3 Equilibrium of forces 204

6.7.4 Failure criteria during catenary action 205

6.8 Conclusions 208

Chapter 7: Assessment of progressive collapse of RC frame using the developed model framework 209

7.1 Introduction 209

7.2 Design of the building frame 211

7.3 Simplified column loss representation 213

7.4 Numerical modelling 217

7.4.1 Detail of the model 217

7.4.2 Nonlinear dynamic analysis modelling approach 218

7.4.3 Analysis of quasi static behaviour of the two subassemblies 220

7.5 Comparison of the predicted and FE modelling results 224

7.5.1 Determination of the yield function for the end and middle section of the plastic hinge 224

7.5.2 Determination of equivalent axial stiffness of the end support 227

7.5.3 Comparison and discussion of results 229

7.6 Progressive collapse-resisting capacity curve 229

7.7 Concluding remarks 233

Chapter 8: Conclusions and recommendation for future work 235

8.1 Main conclusions 236

8.2 Recommendations for future work 237

References 239

Table of Figures

Figure 2.1: Ronan point apartment building after collapse 9

Figure 2.2: North side of Murray building after collapse (Hinman & Hammond 1997) 10

Figure 2.3: Collapse area of the Pentagon building (Mlakar et al. 2003a) 12

Figure 2.4: Locations of column removal for assessing collapse (GSA, 2013)..... 15

Figure 2.5: Test RC frame detail (Yi et al. 2008) 16

Figure 2.6: Load versus unloading displacement of the middle column (Yi et al. 2008) 17

Figure 2.7: Reinforcement arrangement of tested specimen (Stinger & Orton 2013)18

Figure 2.8: Vertical load-displacement relationship for the specimen (Stinger & Orton 2013) 19

Figure 2.9: Effect of reinforcement ratio on compressive arching action in RC subassemblies (Su et al. 2009) 21

Figure 2.10: Effect of span-to-depth ratio on compressive arching action in RC subassemblies (Su et al. 2009) 22

Figure 2.11: Reinforcement detailing of tested beam (Sasani and Kropelnicki, 2008) 23

Figure 2.12: Load-middle column displacement relationship (Sasani and Kropelnicki, 2008) 24

Figure 2.13: Vertical and axial load against middle column displacement for RC specimens (Orton 2007) 25

Figure 2.14: Relationship of load- displacement and horizontal force-displacement of the middle column (Yu & Tan 2013a) 27

Figure 2.15: Effect of bottom reinforcement ratio on structural behaviour of subassemblies (Yu and Tan, 2013b) 29

Figure 2.16: Effect of top reinforcement ratio on structural behaviour of subassemblies (Yu and Tan, 2013b) 30

Figure 2.17: Effect of span-depth ratio on structural behaviour of subassemblies (Yu and Tan, 2013b)..... 31

Figure 2.18: Geometric and reinforcement details for IMF specimen (Lew et al. 2014) 32

Figure 2.19: Vertical load against centre column displacement of tested specimens (Sadek et al. 2011)..... 33

Figure 2.20: Effect of axial restraint stiffness on normalized CAA capacity (Yu & Tan 2014)..... 35

Figure 2.21: Effect of reinforcement ratio on enhancement factor for different L/d ratio (Yu & Tan 2014) 37

Figure 2.22: Effect of L/d ratio on enhancement factor from experimental test..... 38

Figure 2.23: Effect of concrete strength on enhancement factor (Vali et al. 2015) ... 39

Figure 2.24: Horizontal forces at support and mid-span (Christiansen 1963) 40

Figure 2.25: Plan and elevation view of RC assemblages with idealised geometry for half span laterally restrained slab after McDowell et al (1956) (Rankin & Long 1997b) 41

Figure 2.26: Equivalent three hinge arches (a) with flexible restraint (b) rigid restraint (Rankin & Long 1997b) 43

Figure 2.27: Compatibility condition of one-half of RC beam (Yu and Tan, 2014) . 45

Figure 2.28: Four response stages (Izzuddin 2005) 46

Figure 3.1: Cross section showing the assumed stress distribution at the middle and end section in specimen A1..... 52

Figure 3.2: Plan and elevation view of RC assemblages (after Su et al., 2009) 54

Figure 3.3: Schematic representation of the test set up and tested specimen (after Su et al., 2009)..... 56

Figure 3.4: Test set up (after Su et al., 2009)..... 56

Figure 3.5: Reinforcement detail of sub-assemblage (Yu & Tan 2013b)..... 59

Figure 3.6: Reinforcement detail of sub-assemblage (Yu & Tan 2013a) 61

Figure 3.7: Damage pattern of specimen S5 at compressive arching capacity with middle joint displacement of 75mm (Yu & Tan 2013b)..... 62

Figure 3.8: Damage pattern of specimen S8 at compressive arching capacity with middle joint displacement of 75mm (Yu & Tan 2013b)..... 63

Figure 3.9: Geometric and reinforcement arrangement of the test specimens (Vesali et al. 2013)..... 65

Figure 3.10: Anchoring of subassembly to test set up (Vali et al. 2015)..... 66

Figure 3.11: Damage pattern of the tested specimen (Vali et al. 2015)..... 68

Figure 3.12: Geometric and reinforcement details of the test assemblies..... 70

Figure 3.13: Test set up (Sadek et al. 2011)..... 71

Figure 3.14: Variation of normalized increase in load due to arching with span depth ratio for all specimens 75

Figure 3.15: Trend line through the data points 75

Figure 3.16: “Rigid” body rotation analogy for arching deformations 77

Figure 3.17: “Rigid” body movement of beam with consideration of flexible restraint 80

Figure 3.18: Flow chart for the incremental procedure..... 84

Figure 3.19: Effect of axial restraint stiffness on normalized CAA capacity 89

Figure 3.20: Illustration of the arching effect vs. L/d with all data “corrected” to rigid end supports..... 90

Figure 3.21: Effect of reinforcement ratio on relative increase/decrease in normalized increase in load capacity (normalized with bending capacity) 92

Figure 3.22: Effect of reinforcement ratio on relative increase/decrease in $\Delta\omega_N$ 93

Figure 3.23: Effect of L/d ratio on $\Delta\omega_N$ from simplified model..... 94

Figure 3.24: Effect of L/d ratio relative factor with L/d=4 as a base reference 95

Figure 3.25: Correlation of predictions with test results for different L/d ratios 100

Figure 4.1: Three strength surfaces represented in K&C model (Mat_072R3) (Malvar et al. 1997)..... 103

Figure 4.2: Default η-λ curve in KCC model..... 105

Figure 4.3: Tension softening for modified Maekawa model (adopted from DIANA manual)..... 107

Figure 4.4: Stress strain relationship of concrete in tension (Maekawa et al. 2003) 108

Figure 4.5: Modified η-λ curve with and without residual capacity 109

Figure 4.6: Uniaxial stress-strain curve of single element simulation test (element size=25mm)..... 110

Figure 4.7: Uniaxial compressive stress-strain curve of single element simulation test (element size=25mm)..... 111

Figure 4.8: Axial stress-strain curves of concrete under different confining pressure (Ansari & Li 1998)..... 112

Figure 4.9: Stress-strain curves under confined compression with and without residual capacity (mesh size=25mm)..... 112

Figure 4.10: Stress-strain curves under confined compression with and without residual capacity (mesh size=25mm)..... 113

Figure 4.11: Uniaxial tension and damage index..... 115

Figure 4.12: FE model of RC beam (mesh size=20mm) 117

Figure 4.13: Different stress-strain curve used for the study..... 118

Figure 4.14: Axial load-axial displacement response for model with elastic perfectly plastic stress-strain behaviour of reinforcement 119

Figure 4.15: Axial load-axial displacement response for model with trilinear stress-strain behaviour (with hardening) of reinforcement 119

Figure 4.16: Axial load-axial displacement response for model with curvilinear stress-strain (with hardening) behaviour of reinforcement 120

Figure 4.17: Finite element mesh of model C..... 121

Figure 4.18: Stress-strain curves for reinforcement..... 122

Figure 4.19: Load and axial force-displacement responses for RC beam with trilinear stress-strain behaviour..... 123

Figure 4.20: Load and axial force-displacement responses for RC beam with trilinear stress-strain behaviour 124

Figure 4.21: Strain contour distribution in FE model A at displacement of 500mm 125

Figure 4.22: Bottom rebar strain distribution along the beam 126

Figure 4.23: Illustration of hour glassing arising from bending deformation with no straining 127

Figure 4.24: Ratio of Hour glass and internal energies during the quasi static loading for model A. 128

Figure 4.25: Elevation and plan view of the tested specimen (Yu & Tan 2013b) ... 129

Figure 4.26: Details of boundary condition in the experimental test and FE assemblies 131

Figure 4.27: Comparison of responses from FE and experiment for specimen S4 .. 132

Figure 4.28: Comparison of responses from FE and experiment for specimen S6 .. 133

Figure 4.29: Comparison of damage pattern from FE and experiment for Specimen S4 (SDF=1.98-2.0) 135

Figure 4.30: Comparison of damage pattern from FE and experiment for Specimen S6 (SDF=1.98-2.0) 136

Figure 5.1: A beam-column subassembly under concentrated load at middle column (Yu and Tan, 2014) 141

Figure 5.2: Free body diagram showing all forces acting on the beam, and the co-existing bending and arching modes of resistance 142

Figure 5.3: Free body diagram showing the two sets of forces corresponding to bending and arching action modes 142

Figure 5.4: Load-displacement response showing the elastic and plastic stages in the proposed model 143

Figure 5.5: Section stress and strain distribution at elastic bending mode 144

Figure 5.6: Rigid block movement of the beam 147

Figure 5.7: Simple illustration of geometrically compatible combinations of compression zone scenarios 149

Figure 5.8: Schematic of concrete strain distribution in the compression zone..... 151

Figure 5.9: Superposition of strain due to bending and arching 152

Figure 5.10: Stress distribution considering the concurrent bending and arching deformation modes 153

Figure 5.11: Rigid block movement of beam with flexible restraint 155

Figure 5.12: Horizontal forces at support and mid-span sections considering only forces attributed to arching..... 157

Figure 5.13: An infinitive RC element 160

Figure 5.14: Strain variation along top fibre of beam for x=0.1d 161

Figure 5.15: Stress distribution and strain distribution across depth for x=0.1d 162

Figure 5.16: strain contour of (a) RC element (b) compression zone area only at a compressed displacement of 0.3mm 163

Figure 5.17: strain distribution along top fibre of beam for x=0.3d 164

Figure 5.18: Stress distribution and strain distribution across depth for x=0.3d 165

Figure 6.1: Simply supported beam with flexible axial restraint 171

Figure 6.2: Schematics of load-displacement curves 172

Figure 6.3: Moment-curvature behaviour at section and plastic hinge 174

Figure 6.4: Moment-curvature behaviour at section and plastic hinge 176

Figure 6.5: Free body diagram showing forces acting on the beam 179

Figure 6.6: Flow chart for calculating internal forces and vertical resistance without considering strength degradation 181

Figure 6.7: Geometric and boundary Details of the FE model 184

Figure 6.8: Load-displacement curve for FE and theoretical model without consideration of strength degradation 185

Figure 6.9: Moment-axial force relationship comparison for FE and theoretical model 186

Figure 6.10: Plastic strain distribution along the bottom fibre of the beam 186

Figure 6.11: A representative joint connection and process of strength degradation 188

Figure 6.12: Ultimate and residual yield surfaces 189

Figure 6.13: Illustration of migration between ultimate and residual surfaces 190

Figure 6.14: Flow chart for calculating internal forces and vertical resistance with consideration of strength degradation 193

Figure 6.15: Section near middle column with the degraded section shown in the highlighted area 194

Figure 6.16: Schematic showing the sections before and after degradation 195

Figure 6.17: Moment-axial force interaction curves for full and degraded sections 196

Figure 6.18: Comparison of load-displacement response from FE and proposed model with strength degradation 197

Figure 6.19: Middle beam-column joint and section details of tested specimen (Li et al. 2015)..... 198

Figure 6.20: Determination of M-N curves for the critical region of the tested beam (dimensions in mm) 199

Figure 6.21: Moment-axial force curves before and after fracture of bottom weld. 199

Figure 6.22: Comparison of load-displacement response from experimental result and proposed model 201

Figure 6.23: Idealised load-displacement resistance function for RC assemblies in the proposed model 202

Figure 6.24: Free body diagram showing force acting on a fixed end beam 204

Figure 6.25: Flow chart for calculating internal forces and vertical resistance without considering strength degradation 207

Figure 7.1: Plan view of the building (dimension in metres)..... 212

Figure 7.2: Bending moment distribution of the periphery frame 212

Figure 7.3: Bending moment distribution of Periphery frame without the missing column..... 214

Figure 7.4: Deformation shape of the frame under a unit horizontal at points A and B 215

Figure 7.5: Simplified representation of left part of the RC frame..... 215

Figure 7.6: Directly affected subassembly of the building 217

Figure 7.7: Stress strain curve for longitudinal reinforcement 218

Figure 7.8: Loading history for simulating sudden column loss..... 219

Figure 7.9: Applied load-middle column displacement and axial force-middle column displacement relationship of the subassemblies 221

Figure 7.10: Strain damage contour during the catenary action stage (middle column displacement of 1000mm) 222

Figure 7.11: Reinforcement strain distribution in model A and B at selected displacement 224

Figure 7.12: Complete axial force-moment interaction curves for model A and B 225

Figure 7.13: Normalised axial force-bending moment interaction curves for the models 226

Figure 7.14: Effect of beam axial stiffness on the RC assembly behaviour during catenary action stage 228

Figure 7.15: Load-middle column displacement response 229

Figure 7.16: Illustration of the conversion of nonlinear static curve to pseudo static curve 230

Figure 7.17: Pseudo static curves for the different RC subassemblies 231

Figure 7.18: Pseudo static curves for the different RC subassemblies 233

List of Tables

Table 3.1: Geometric and reinforcement details of tested specimens by Su et al. (2009) 55

Table 3.2: Compressive arching and recalculated flexural capacities of specimens tested by Su et al. (2009) 58

Table 3.3: Geometric and reinforcement detail of test specimens (Yu & Tan 2013a; Yu & Tan 2013b) 60

Table 3.4: Compressive arching and recalculated flexural capacities of specimens tested by (Yu & Tan 2013c) 64

Table 3.5: Compressive arching and recalculated flexural capacities of specimens tested by Vesali et al. (2013) and Vali et al. (2015) 69

Table 3.6: Compressive arching and recalculated flexural capacities of specimens tested by Sadek et al. (2011) 72

Table 3.7: Comparison of axial restraint stiffness from experimental data set 87

Table 3.8: Effect of axial stiffness coefficient on the normalized increase in load due to arching 88

Table 3.9: Effect of mechanical reinforcement ratio on normalized increased in load 92

Table 3.10: Comparison of experimental and predicted result 99

Table 4.1: Details of mesh size and number of element in the different models 121

Table 4.2: Reinforcement detail of beam-column sub-assemblage (Yu & Tan 2013b) 129

Table 5.1: Expressions for plastic hinge length from different researchers 159

Table 5.2: Determination of x/L_N for FE model with x=0.1d 163

Table 5.3: Determination of x/L_N for FE model with x=0.3d 166

Table 5.4: Comparison of experimental and predicted result 167

Table 7.1: Summary of design data..... 213

Symbols

$A_{s1'}$, A_{s2}' Area of compression reinforcements at the end and middle section respectively

a_t Distance from the centroid of utmost top reinforcement to the extreme top fibre of concrete at end and middle sections

a_b Distance from the centroid of utmost bottom reinforcement to the extreme bottom fibre of concrete at end and middle sections.

b Width of beam

C_s, C_s' Steel compressive forces acting at beams end and mid-span section respectively

d Depth of beam section

E_c Elastic modulus of concrete

f_c' Compressive strength of concrete

F_{cN1} Compression force in concrete at the end section attributed to arching

F_{cN2} Compression force in concrete at the middle section attributed to arching

F_{sN1} Compressive steel at the end section attributed to arching

F_{sN2} Compressive steel at the middle section attributed to arching

H_R Horizontal reaction

I_{cr} Moment of inertia of a cracked section

I_g Cross moment of inertia of a section

K_a Axial restraint stiffness

K_s Axial stiffness of beam

L Length of double bay beam

L_p Plastic zone length for catenary action

L_{pc} Plastic zone length for compressive arching action

M_{cr} Cracking moment of a section

M_e Bending moment of end section

M_m	Bending moment of middle section
N	Axial force
P_a	Compressive arching capacity of the beam
P_b	Flexural capacity of RC beam
P_t	Total vertical resistance of the RC beam
T_y, T_y'	Steel tensile forces acting at beam end and mid-span section respectively
U_i	Axial elongation/shortening of beam
x_{bp1}	Effective compression depth in concrete at the end section attributed to bending
x_{bp2}	Effective compression depth in concrete at the middle section attributed to bending
x_1	Effective compression depth of the rigid block at the end section
x_2	Effective compression depth of the rigid block at the middle section
ε_{max}	Maximum strain in the plastic zone
β	Ratio of equivalent rectangular stress block depth to neutral axis depth
δ	Displacement of the middle joint
Δ_N	Compression depth available for arching
θ_p	Plastic rotation angle
$\Delta_{\omega N}$	Distance between the compression force at mid-span and support

Chapter 1: Introduction

1.1 Background

Conventionally, building structures are designed to resist loads based on ultimate capacities evaluated from the intact structural system. When a structure is subjected to abnormal loading due to terrorist attack or human error, one or more vertical structural members such as columns or structural walls may be severely compromised. In such a circumstance, the original load transfer path of the building may be altered. If the directly affected part such as a column is not strong enough to resist the attack and the associated dynamic effect, failure may initiate there and eventually lead to collapse of a large portion or even the entire building. This is called progressive collapse. It is generally recognised (see e.g. definition by the American Society of Civil Engineers, ASCE 7), progressive collapse is the failure of entire structure or disproportionate part of it, caused by a local member failure which spread from member to member.

Interest in the study of progressive collapse began after the collapse of 22-storey Ronan Point apartment building following a gas explosion in 1968. The 1995 terrorist attack on Murrah Federal Building in USA and the terrorist attack on the twin tower building of World Trade Centre in New York in 2001 further brought to fore the need for public buildings to be adequately protected against progressive collapse in the event of an attack. Consequent upon this, a number of measures aimed at preventing or reducing the possibility of collapse in existing and new public buildings have been incorporated into design guidelines (GSA 2013; DoD 2010). Typical design analysis against progressive collapse is based on two methods: Indirect and direct method. The indirect method requires that effective ties be provided within the building without any explicit means of assessing or quantifying the potential of collapse. The direct method consists of the specific local resistance method and the alternate load path method. In the specific local resistance method, key structural members are intentionally hardened to resist a clearly defined threat. On the other hand, alternate load path method allows

for local damage but seeks to provide alternate load path to ensure that the major damage is averted. Due to the inability to determine the exact nature and magnitude of the attack and the need to put to use the reserve capacity of the structure, the alternate load path which is a treat independent approach is mostly preferred to the specific local resistance method. Accordingly, a number of studies on progressive collapse of RC assemblies based on alternate load path method exist in the literature. Lew et al. (2014) investigated the behaviour of laterally restraint beam-column RC assemblies using a full-scale testing. The effect of parameters affecting the compressive arching action and catenary action was investigated in these studies (Yu & Tan 2013b; Yu & Tan 2013c; Yu & Tan 2013a; Vali et al. 2015; Vesali et al. 2013). In another study, Albrifkani & Wang (2016) developed a 3D finite element model of RC assemblies which can be used to assess progressive collapse.

From the review of studies on progressive collapse of laterally restraint RC assemblies, the load path that exists includes flexural, compressive arching action and catenary action. Accurate assessment of the progressive collapse potential of a structure therefore requires that all load paths be taken into consideration. GSA (2013) recommend linear static, nonlinear static and nonlinear dynamic analysis procedure for assessing progressive collapse potential of structures based on alternate load path method.

Of the three methods of analysis, nonlinear dynamic analysis approach is considered as the most accurate; but nonlinear dynamic analysis method may be too cumbersome for a routine use. For a simplified analysis of progressive collapse, the nonlinear static method may be used. However, the accuracy of this method depends on the accurate determination of the load-displacement behaviour (resistance function) of the critical assembly, and this includes capturing the key damage events that may occur during the course of response, such as strength degradation due to failure of weld in steel structures and rupture of rebar in RC assemblies.

This thesis therefore aims to develop a sufficiently accurate and sound mechanics-based theoretical model framework to determine the resistance function of beams assemblies under a column loss scenario. The resistance functions so determined can

be used for quick assessment of progressive collapse potential in existing and new buildings.

1.2 Objectives of study

The main objective of this research are as follows:

- ✓ To collate and analyse different experimental studies on arching compression action in RC beams available in the literature. Based on the collated data, investigate the different effect of parameters such as reinforcement ratio, concrete strength, axial restraint and span-depth ratio on the arching capacity of RC beams. With an informed understanding of the aforementioned parameters, formulate an empirical expression that can quantify the arching effect and compare the predictions with experimental results.

- ✓ To develop analytical model for predicting the complete load-displacement behaviour (resistance function) in axially restrained RC beam assemblies, with a particular focus on the resistance within the arching effective regime. The theoretical model is formulated by considering the compounding effect of bending and arching deformation modes and an equivalent plastic zone length.

- ✓ To develop an analytical model for the prediction of load-displacement behaviour (resistance function) within the catenary stage, with a particular focus on the representation of strength degradation due to partial failure in critical regions. Application of the proposed model in steel and RC assemblies and the conditions for the activation of the strength degradation are covered.

- ✓ To apply the developed framework in the analysis of progressive collapse behaviour of RC frame assemblies. This is achieved by predicting the complete load-displacement behaviour (resistance function) of the RC assemblies using the analytical models for compressive arching and catenary actions developed in this study.

- ✓ To investigate the behaviour of different RC beam assemblies under progressive collapse by converting the resistance function into pseudo dynamic curves based on the energy principle.

1.3 Scope of work

The research in this study only considers beams located at the middle of periphery frame structures without the consideration of slab contribution. More so the contribution from transverse beams are not considered. In developing the model for the compressive arching and catenary action, no loading rate effect is considered; however, such effect may be easily incorporated into the analysis method developed in this study using rate-sensitive material properties.

1.4 Organisation of the thesis

There are total of eight chapters in this thesis.

Chapter 2 presents a general review of studies in the area of progressive collapse. Code provisions for assessing progressive collapse are also explained with particular focus on the alternate load path method. Experimental tests on RC assemblies and frames are reviewed including their behaviour and deformation patterns up to collapse. Finally, a review of existing analytical models on compressive arching action is presented and gaps in the existing studies are highlighted.

Chapter 3 presents the evaluation of arching action and the effect of span-depth ratio, reinforcement ratio, concrete compressive strength and axial restraint stiffness on the normalised arching capacity. Critical scrutiny of each of the parameters mentioned above is presented. A semi-empirical model is formulated to predict the effect of the parameters on arching compression, and predictions from the model are compared with relevant experimental tests.

Chapter 4 presents a numerical modelling framework for the progressive collapse of RC frame assemblies. Issues commonly encountered in the finite element modelling of RC beams in large deformations are discussed and possible ways of avoiding these issues are presented. The modelling framework is validated with experimental test results.

Chapter 5 presents a theoretical model for compressive arching action by considering the compounding effect of arching and bending deformation modes. The contribution from bending and arching from the deformation and force point of view are discussed.

Chapter 6 shows the development of a theoretical model for catenary action in axially restraint beam considering strength degradation. The application of the model to beam assemblies involving partial local failure is also discussed.

In Chapter 7, the progressive collapse behaviour of a typical RC frame based on two representative designs is investigated using the developed framework in previous chapters. Comparison of the results with a nonlinear dynamic analysis of the RC frame assemblies is also presented.

In Chapter 8, a summary of the main conclusions from the research is presented and scope for further research is recommended.

Chapter 2: Literature review

2.1 Introduction

Research in the field of progressive collapse dates back to the 1960's after the Ronan Point apartment collapse due to gas explosion. Since that unfortunate incident, effort has been geared towards preventing progressive collapse or reducing the extent of damage in the event of extreme attack on the buildings structures. As a result of extensive research, a large body of knowledge on progressive collapse of reinforced and steel structures exist in the literature.

The review herein is focused on studies relevant to the progressive collapse of RC structures. In particular, code provisions and design guidelines aimed at reducing collapse are reviewed with a further focus on the Alternate Load Path Method (ALP), to which the theme of this study is closely related. Following that, a review of experimental studies on RC structures and subassemblies are presented to provide an in-depth understanding of the factors affecting the compressive arching action in a laterally restrained RC structure and subsequent process through the catenary stage leading up to the final failure modes. Lastly, the current state of analytical models on compressive arching action and catenary action is reviewed and discussed.

2.2 Definition of key terminologies

2.2.1 Progressive collapse

Progressive collapse occurs when a local failure of a structural member caused the adjoining members to collapse leading to additional collapse (GSA 2003). In most cases, the damage level is disproportionate to the original cause hence it is sometimes referred to as disproportionate collapse. For instance, if the failure of one column leads to the collapse of the entire building, then the initial cause is disproportionate to the final failure.

2.2.2 Robustness

According to General Service Administration (2003) Robustness is the defined as:

''*Ability of a structure or structural component to resists damage without premature and/or brittle failure due to events like explosions, impacts, fire or consequences of human error, due to its vigorous strength and toughness*''

From the above definition, it can be said that robustness is an inherent property of the structure and it depends on the structural design and detailing considerations. Thus, in an unforeseen extreme action, a robust structure is more likely to resist progressive collapse compared to a less robust structure.

2.3 Defining cases of progressive collapse

There has been a number of collapse cases in the world. According to Taylor (1975), about 110 collapse events was recorded in USA between 1968 and 1971. Of these number, 22 were termed to be progressive in nature. In Canada, the number of collapse cases between 1962 and 1971 was 495 out of which 72 was considered as progressive collapse. This section only seeks to review a notable number of collapse event in history.

2.3.1 Ronan point apartment building in London

In May 1968, a match was lit on the 18th floor of a 22-story Ronan Point apartment building. This led to gas explosion which damaged the walls of the apartment. The floor and walls of the building were made of precast concrete panels. The partial collapse of the building was triggered by the damage of the precast panel wall of the directly affected part and the failure of the load bearing walls at the corner of the building.

The failure of the load bearing wall at the 18th floor caused the collapse of floors above and beneath the affected floor as shown in Figure 2.1. It could be said that the collapse was progressive in nature or disproportionate to the original cause as it initiated on the

18th floor and subsequently spread to other floors. Prior to the Ronan point building collapse, there was no code provisions against progressive collapse and existing design code at a time only accounted for gravity loading. The Ronan point building collapse was a wakeup call on the need for buildings to be adequately protected against collapse in the event of unforeseen extreme event and this led to the modification of national codes in the UK and other part of the world.

Figure 2.1: Ronan point apartment building after collapse

2.3.2 Murrah building located in Oklahoma City, USA

In the early hours of April 19, 1995 a truck loaded with bomb parked near the Murray building exploded resulting in many casualties and causing severe damage to the

Murray building and other nearby buildings. The truck was parked about 5m metres away from one of the ground floor columns. The explosion caused the failure of the column and due to the absent of alternate load path to transfer the additional load caused by the sudden loss column, the transfer girder collapse causing the failure of the entire bay supported by the damaged column. Extensive investigation into the cause of collapse showed that the building could have still collapsed because of the magnitude of the bomb and the close proximity of the explosion; however, the presence of alternate load path could have reduced the magnitude of damage (Mlakar, Sr. et al. 1998; Corley et al. 1998). Following the review on the cause of Murray Building collapse, Osteraas (2006) noted that a robust structure should (1) possess a three dimensional space frame which is able to connect all load path and also have a redundant load path. (2) possess mechanical fuse such that failure of slabs and wall will not result in the failure of the frame (3) have adequate ductility to bear overload and (4) the perimeter columns should be purposefully designed against blast.

Figure 2.2: North side of Murray building after collapse (Hinman & Hammond 1997)

2.3.3 Pentagon building located in Virginia, USA

The most catastrophic collapse in history occurred on September 11, 2001. At about 9:38am, a Boeing 757 aircraft flew into the first storey of the Pentagon building.

Following the impact, fire engulf the part of the buildings which directly came in contact with the plane (Figure 2.3). The initial impact damaged about 30 first floor columns and significantly affected 20 other columns. In addition to the damage on the ground floor, about six columns at the second-floor were also destroyed and 30 more columns were affected (Mlakar et al. 2003b). It was reported that despite the damage caused by the initial impact, the building was able to resist collapse and subsequent collapse was due to the fire that engulf the building (Mlakar et al. 2003b; Mlakar et al. 2005b; Mlakar et al. 2003a; Mlakar et al. 2005a). The reason for the good performance of the structure against the initial impact was attributed to (Mlakar et al. 2003b):

- Availability of redundant and additional load path for the beams and girder
- Exterior wall of the building acted as a transfer girder.
- The warehouse was design for a live load well in excess of its service load.
- The use of spiral reinforcement in column increase the residual capacity of the column after initial damage.
- Short spacing of columns.
- Continuity of bottom reinforcement through the support.
- Exterior wall acted as a transfer girder

Figure 2.3: Collapse area of the Pentagon building (Mlakar et al. 2003a)

2.4 Code and design guidelines against progressive collapse

Following the Ronan point collapse in 1968, different approaches to prevent progressive collapse have gradually been incorporated in design codes and guidelines. Most of the design codes adopt the implicit approach by specifying tying requirements without any explicit assessment.

In ACI 318-05 and commentary (ACI 318M-05), it is recommended that a structure be designed to possess structural integrity through provision of vertical, horizontal and transverse ties around the perimeter of the structure without any explicit procedure to assess the potential of collapse. The code further recommends using continuous reinforcement through the support within the critical section. In cases where reinforcement are lapped, the use of adequate splice length and provision of adequate hooks at the splice termination points are advised.

Eurocode 1 (CEN 2006) also adopt the descriptive tied force method. For public buildings such as hotels, offices not exceeding four (4) storeys, the code recommends provision of effective horizontal ties only. For buildings such as hotel greater than (4) storeys or hospitals greater than 3 storeys but less than 15 storeys, Eurocode requires horizontal internal ties to be provided in orthogonal directions at each floor level and the periphery of the buildings. In the vertical direction, each column or wall should be tied from the roof level to the foundation. For frame buildings, the columns and walls should be designed to resist accidental load which is the greater of design permanent load and variable load reaction applied to the column from a single storey. In addition, a notional column removal by one column at a time is also recommended by the code, however the column removal procedure is not explicitly stated.

Unlike in Eurocode and ACI 318 code, the ASCE code (ASCE 7-10) does not provide any prescriptive design requirement for progressive collapse, rather it requires removal of selected load bearing members one at a time and assessing the capacity of the remaining structure. The recommended load combination for the assessment is:

$$(0.9 \text{ or } 1.2)D + 0.5L + 0.2S \tag{2.1}$$

where D is the dead load, L is the live load and S is the snow load.

The General Service Administration and Department of Defence provide detailed procedure for assessing progressive collapse in new and existing buildings. While UFC 4-023-03 (DoD 2010) recommends both indirect and direct approach depending on the occupancy category, GSA (2013) only recommends the direct method based on the alternate load path method.

In UFC 4-023-03 (DoD 2010) building structures are classified into four occupancy categories. For occupancy I, no specific requirement is needed. For category 2 and above, assessment of progressive collapse of the structure after removal of specified columns are to be performed using alternate load path method. Similar classification is used in GSA (2013), where buildings to be assessed are grouped based on their Facility Security Levels (FSL). For low occupancy and low risk level buildings (FSL

I and II), no checks are required and buildings in this group are exempted from further checks for progressive collapse. For buildings with four storeys or more (FSL III, IV, and V), assessment using alternate load path method is recommended. The alternate load path method requires that a vertical load bearing member be notionally removed and the structure analysed to ascertain if it can bridge over the removed member. The location of the vertical members (columns) to be removed for internal and external columns are shown in Figure 2.4.

Linear elastic, nonlinear static and nonlinear analysis procedures are recommended for use with the alternate load path method in both GSA (2013) and UFC 4-023-03 (DoD 2010) and the load combination for the different types of analysis is shown in Equation 2.2.

$$\begin{aligned} G_{LD} &= \Omega_L[1.2D + (0.5L \ or \ 0.5S)] && \text{for linear static} \\ G_N &= \Omega_N[1.2D + (0.5L \ or \ 0.2S)] && \text{for nonlinear static} \\ G_{ND} &= 1.2D + (0.5L \ or \ 0.2S) && \text{for nonlinear dynamic} \end{aligned} \tag{2.2}$$

where G_{LD}, G_N and G_{ND} are the increased gravity loading for deformation-controlled actions for linear static, nonlinear static and nonlinear dynamic analysis respectively. D, L and S are the dead, live and snow load respectively. Ω_L and Ω_N are the load increase factors for linear static and dynamic increase factor for nonlinear static analysis respectively.

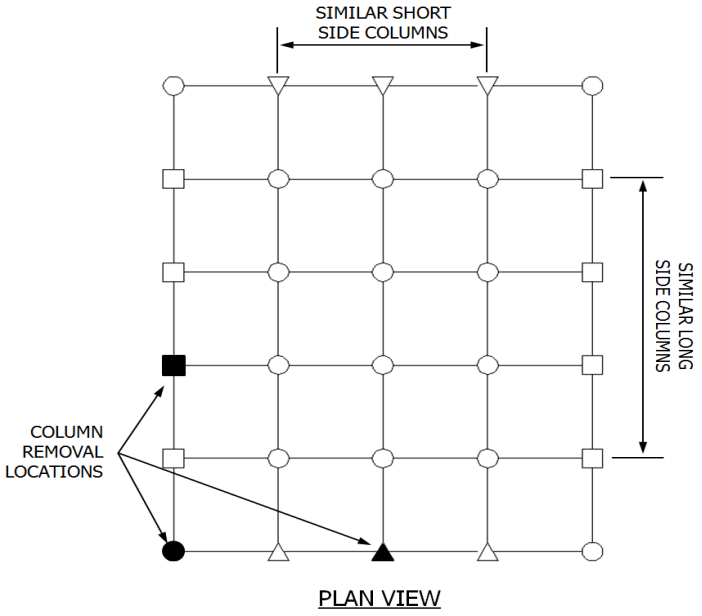

(a) External column removal

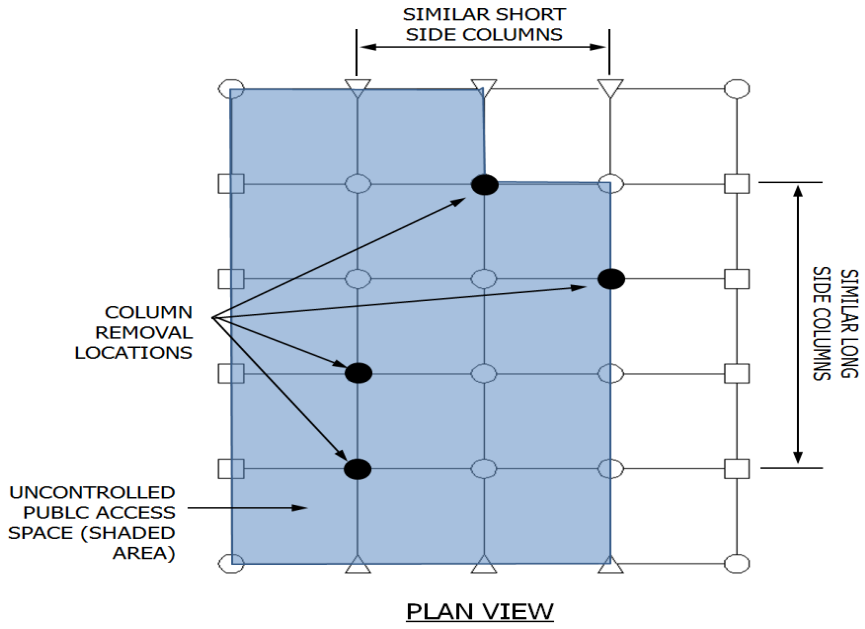

(b) Internal column removal

Figure 2.4: Locations of column removal for assessing collapse (GSA, 2013)

2.5 Experimental studies on progressive collapse

Experimental studies on progressive collapse can be investigated at the entire building level, frame level or sub-assembly level. For the sub-assembly level investigation, only the bay of the removed column is considered and effect of the indirectly affected part on the loss column is simulated using flexible axial restraint. For the present study, only review at the frame level and subassembly level is discussed. Experimental studies on RC frame structures

Yi et al. (2008) investigated the behaviour of a four bay three storey reduced scale RC frame subjected to downward displacement of the middle column. The experiment was aimed at understanding the progressive collapse of RC frame without a ground floor column. The axial force of the first and second floor columns calculated as 109KN was applied to the middle column through servo-hydraulic actuator as shown in Figure 2.5. The ground floor column consisted of a two-mechanical jack stacked together. During the test, the mechanical jack was gradually unloaded to simulate the loss of middle column.

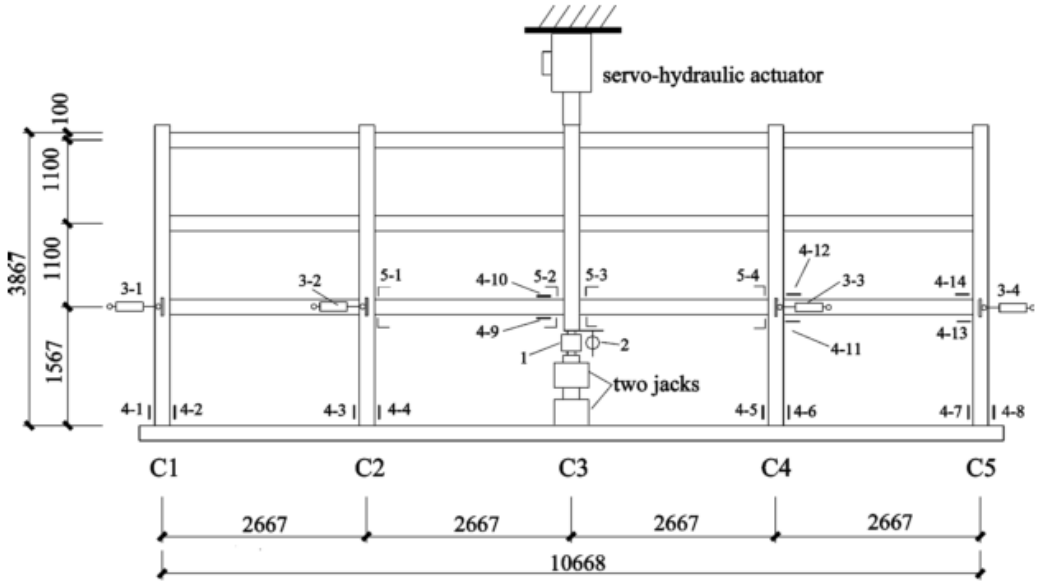

Figure 2.5: Test RC frame detail (Yi et al. 2008)

The load displacement response indicated that the RC frame went through four response stages during the test (see Figure 2.6). These included elastic, elasto-plastic, plastic and catenary action stages. The elastic stage began from the start of unloading until crack initiated at the tensile zone of the critical section (point A). This was followed by the elastic plastic part which ended with the formation of plastic hinges (point B). Between point B and C, the beam behaved in a plastic manner and at point C catenary action started until rupture of the bottom rebar at the ground floor beam-column interface which marked the collapse of the RC frame. It was concluded that the frame did not collapse under its self-weight.

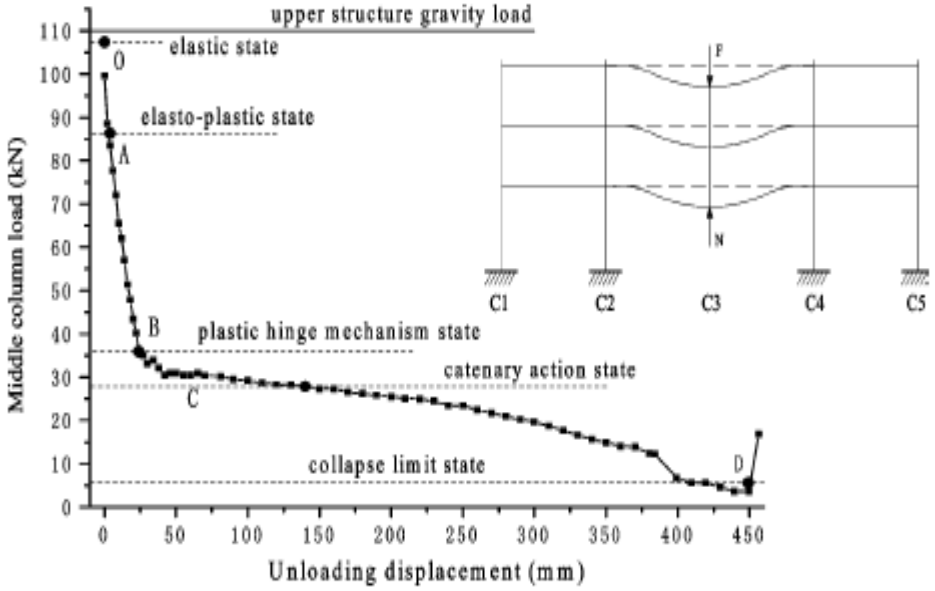

Figure 2.6: Load versus unloading displacement of the middle column (Yi et al. 2008)

In another study, Stinger & Orton (2013) investigated the contribution of compressive action, Vierendeel action and infill action to the collapse resistance of RC frames. The tested specimen was one quarter of a two-bay, two-story prototype building designed according to the ACI 318 requirement. Three different specimens were tested in their study. The first specimen represented a typical existing building without continuous bottom reinforcement at the location of the removed column. The second specimen had continuous reinforcement passing through the location of the removed column and the third specimen was designed with an infill wall. Reaction frames were used at the

end to simulate restraint provided by other part of the building. Figure 2.7 shows the tested RC frame and the reinforcement arrangement. Displacement control loading was applied through an actuator at the middle column location until the frame collapse.

The result indicated that compressive arching action occurred at a smaller displacement. After the attainment of maximum compressive arching action, crushing of concrete occurred at the middle and end beam-column interface until catenary action started at middle column displacement of about one-beam depth. The load-displacement response shows that catenary action developed in both specimens with and without bottom reinforcement and final failure was due to the rupture of bottom rebar.

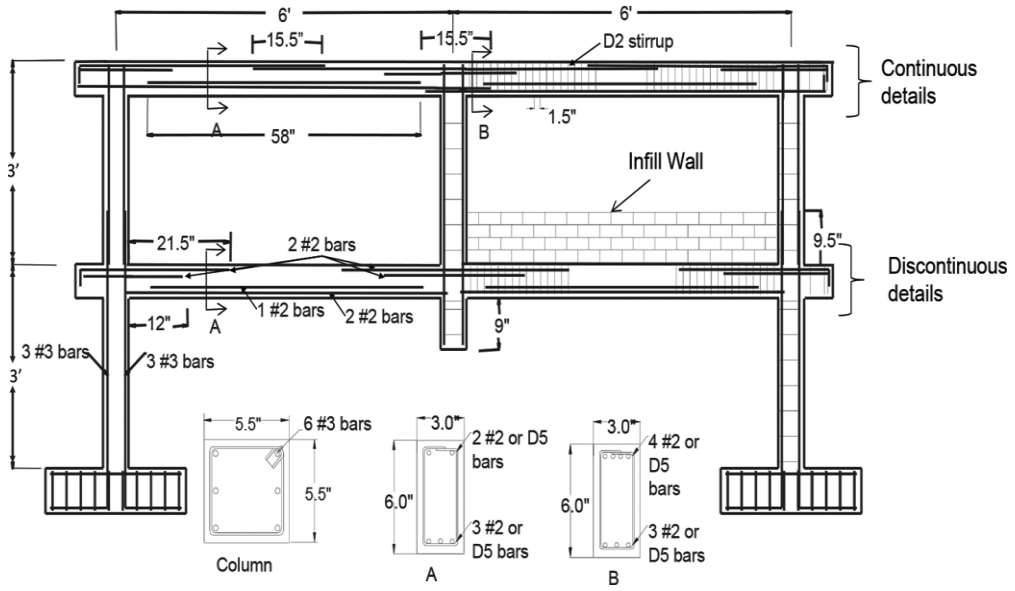

Figure 2.7: Reinforcement arrangement of tested specimen (Stinger & Orton 2013)

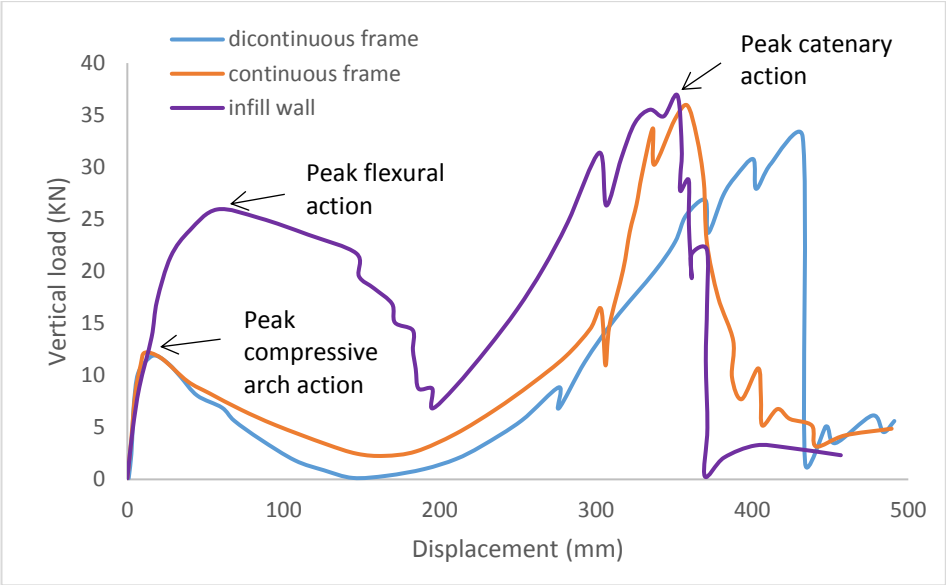

Figure 2.8: Vertical load-displacement relationship for the specimen (Stinger & Orton 2013)

2.5.1 Studies on RC subassemblies

Su et al. (2009) conducted series of tests on twelve RC beam-column sub assemblages to investigate the capacity of compressive arching action in axially restrained beam. Variables investigated in the test were reinforcement ratio, span-depth ratio and loading rate. Each of the tested beam consisted of a two-bay beam and three column stubs simulating middle column removal. Three span-depth ratios of 4.08, 6.12 and 9.08 were used and reinforcement ratio ranged between 0.55 to 1.3% representing light to moderately reinforced section.

The end columns were both connected to a steel socket which was further connected to a rigid support to achieve the axial and rotational restraint. To avoid rotation of the middle column, two roller bearings were placed at each face close to the middle column. The middle column was subjected to displacement controlled loading until the beam collapse.

The result showed that the ultimate strengths of the specimens were greater than the flexural capacities implying that compressive forces developed due to the axial restraint at the end columns and this helped increase the load capacity. The capacity of

compressive arching action was between 50 to 160% greater than the flexural capacity of beam calculated without considering the presence of axial restraint. After the maximum compressive action capacity was reached, with further deflection, concrete crushed at the end and middle beam column interface. This was accompanied by reduction in the applied load until the load started to increase again due to catenary action.

It was observed that compressive arching capacity increases with decreases in reinforcement ratio in specimens with symmetrical and unsymmetrical reinforcement arrangements (see Figure 2.9). This is because the compressive depth for arching depends on the compressive depth used up for yielding of tensile rebar. Thus, the higher the tensile reinforcement, the higher the compressive depth required for tensile rebar yielding and the lower the depth left for arching.

It was further noticed that specimen with low span-depth ratio gave a higher compressive arching capacity than beams with large span-depth ratio. Specimens with low span-depth ratio are more susceptible to concrete crushing than specimen with larger span-depth ratio (see Figure 2.10)

Although the investigation was targeted at studying the compressive arching behaviour, catenary action kicked in when the axial force changed from negative to positive. In all tested specimens, failure was due to rupture of bottom rebar at the interface between the beam and middle column stab.

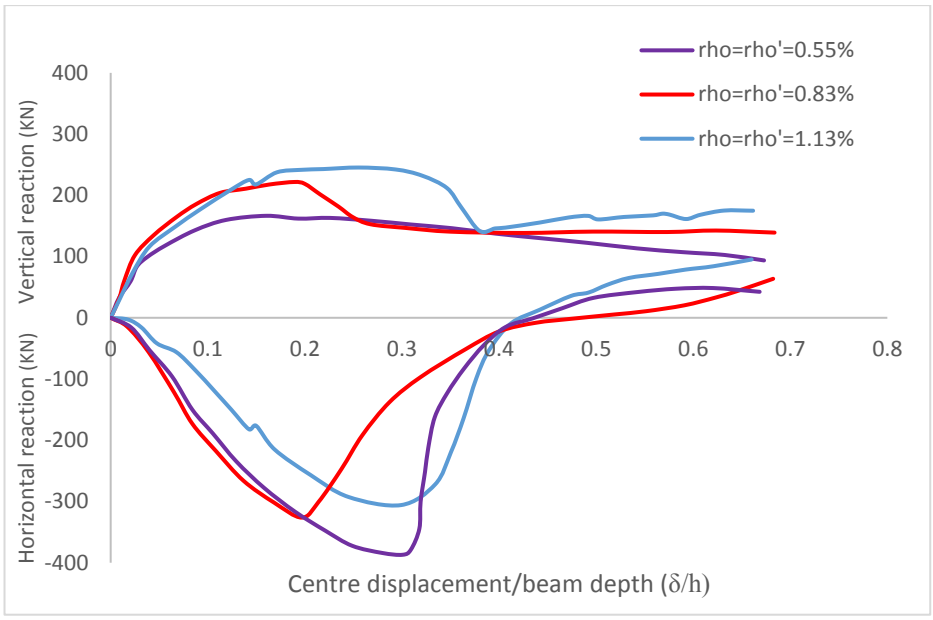

(a) symmetrical reinforcement

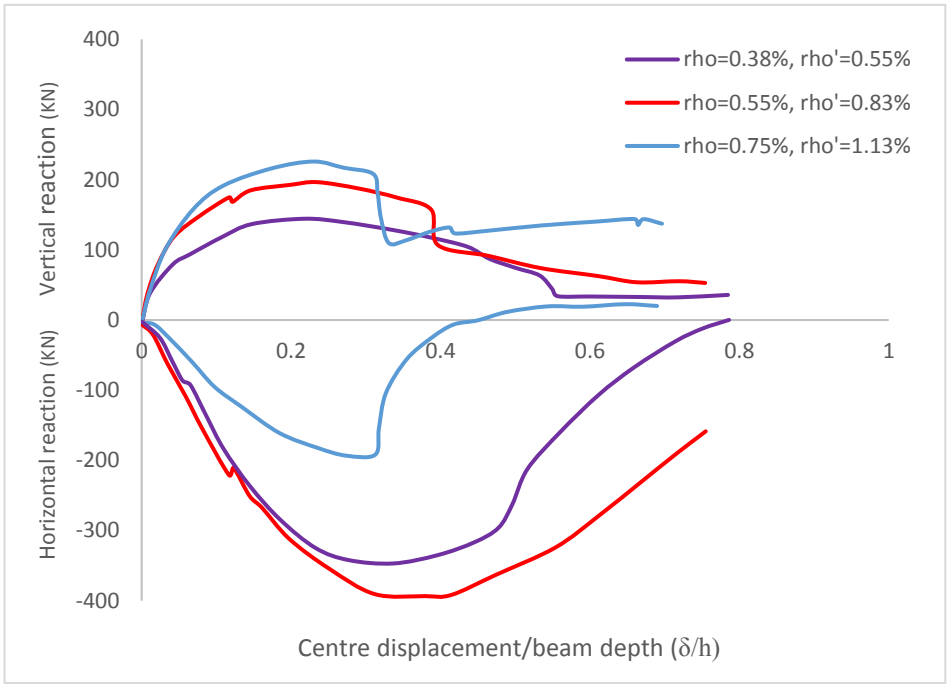

(b) unsymmetrical reinforcement

Figure 2.9: Effect of reinforcement ratio on compressive arching action in RC subassemblies (Su et al. 2009)

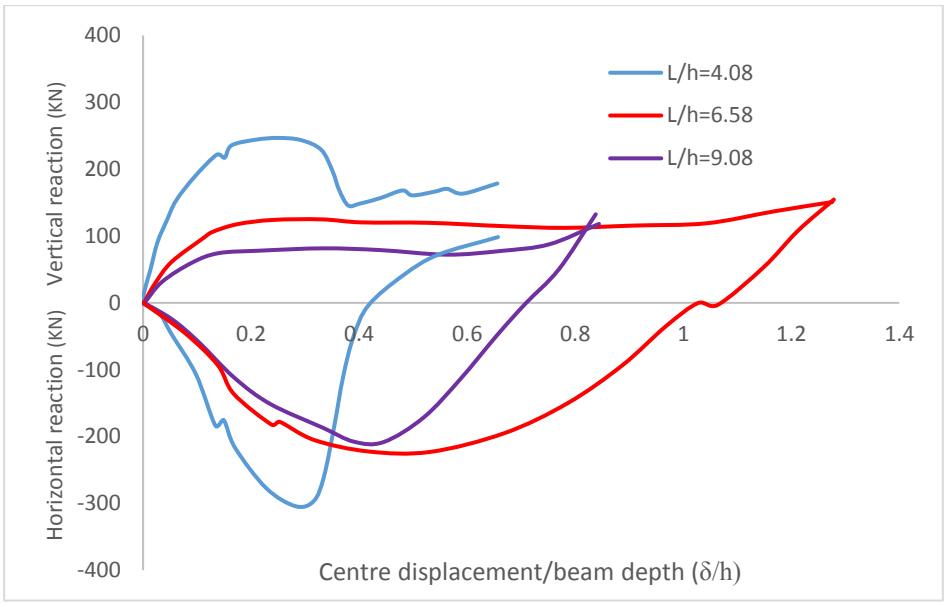

(a) symmetrical reinforcement

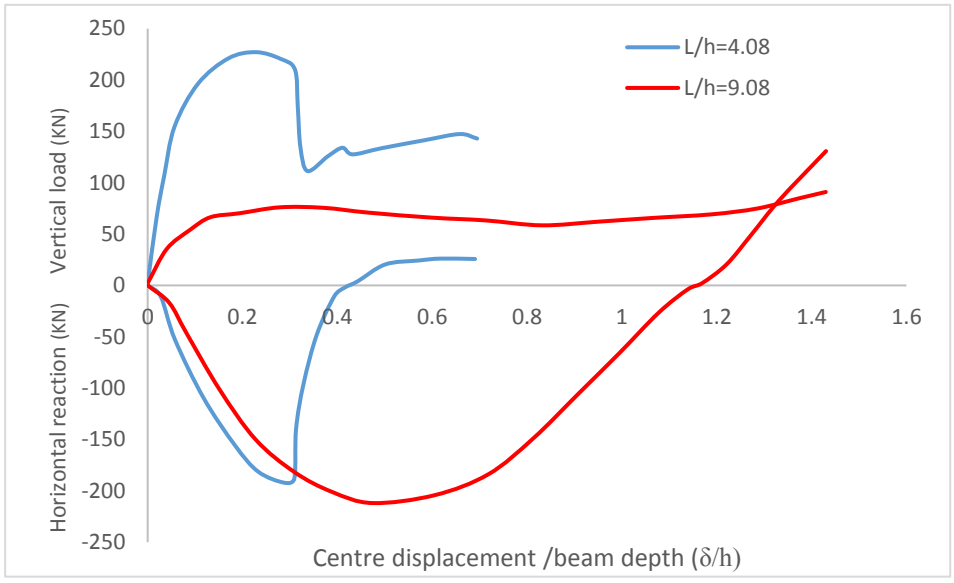

(b) unsymmetrical reinforcement

Figure 2.10: Effect of span-to-depth ratio on compressive arching action in RC subassemblies (Su et al. 2009)

Sasani & Kropelnicki (2008) investigated the behaviour of a 3/8 scaled model of a perimeter reinforced concrete frame structure. The tested beam had a depth of 7.5 inches (190.5mm) with clear span of 65.25inches (1657.4mm) between the edge and centre column. Reinforcement was made of Grade 500MPa and concrete compressive

strength was 41MPa. The reinforcement arrangement of the tested beam is shown in Figure 2.12. Loading was applied on the middle column in a displacement controlled manner devoid of any dynamic effect.

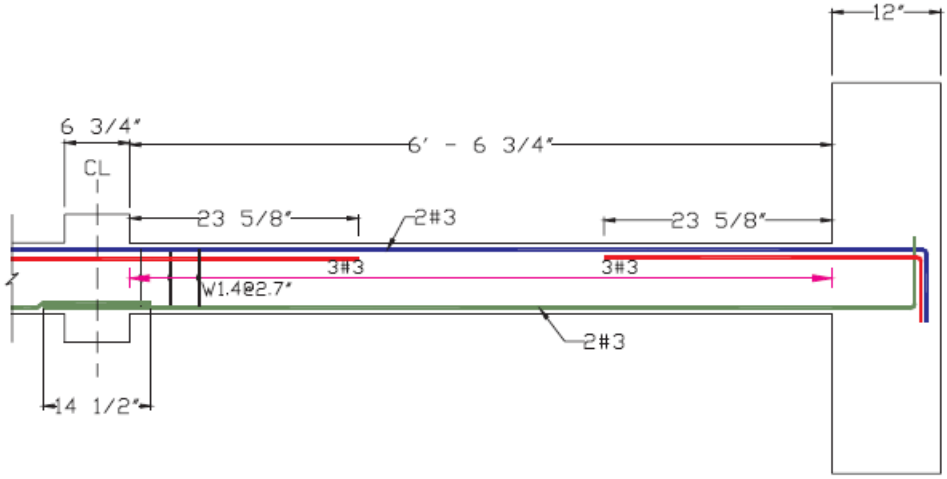

Figure 2.11: Reinforcement detailing of tested beam (Sasani and Kropelnicki, 2008)

The result in Figure 2.12 indicated that with increasing loading, bottom rebar at the middle beam-column interface ruptured. After the rupture of bottom rebar, tensile force in the top rebar caused catenary action to develop. Although the longitudinal reinforcement within the middle column was lap spliced, there was no splice failure in the test. This was attributed to the use of splice type B which is 1.3 times longer than splice type A as per ACI 318 code.

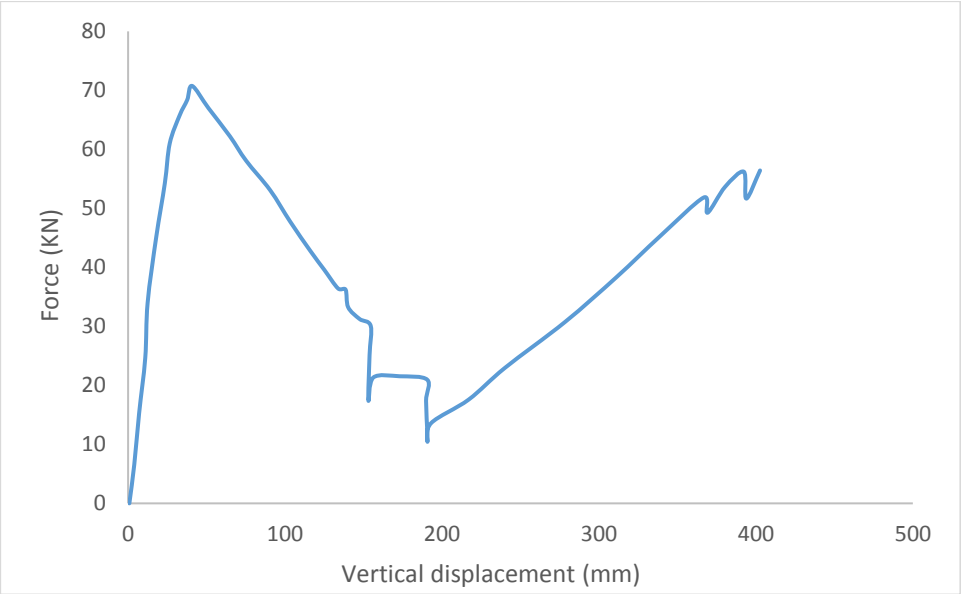

Figure 2.12: Load-middle column displacement relationship (Sasani and Kropelnicki, 2008)

Eight specimens were tested to determine if CFRP material can provide continuity and help prevent progressive collapse in RC frame bridging over a lost column (Orton, 2007). Two of these specimens were made of RC with no CFRP retrofitting. One of the non-retrofitted specimens had discontinuous bottom reinforcement while the other had continuous reinforcement at the middle column (column removal point).

The result showed that catenary action developed in both specimens with and without continuous reinforcement. The development of catenary action in the specimen with discontinuous bottom rebar was attributed to the transfer of tensile forces from the positive moment through the stirrups to the negative moment (Figure 2.13).

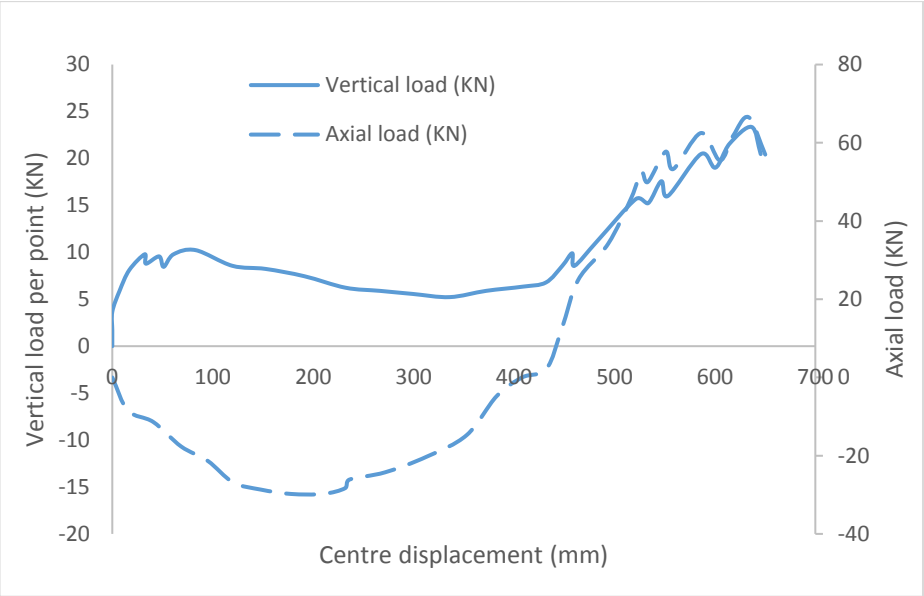

(a) discontinuous reinforcement

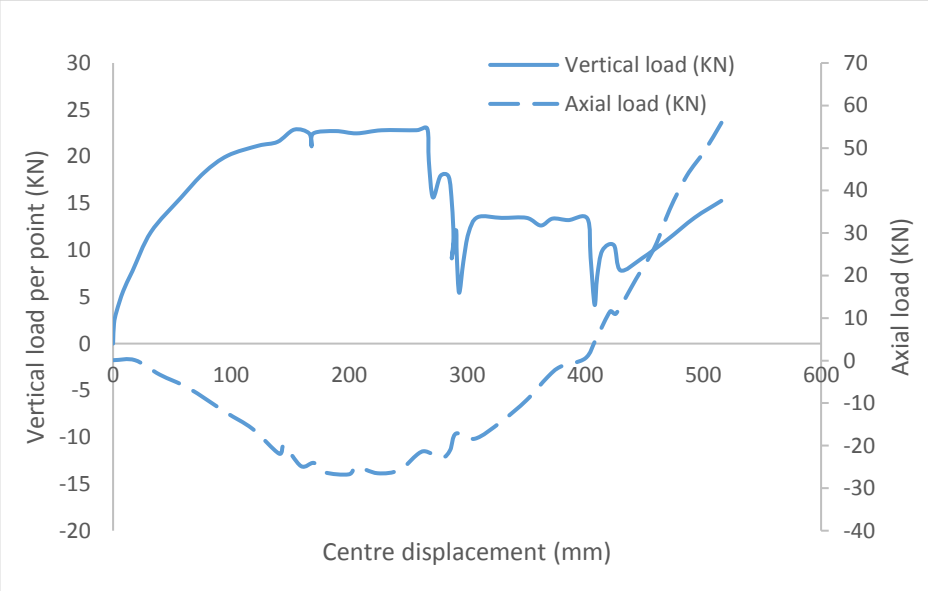

(b) continuous reinforcement

Figure 2.13: Vertical and axial load against middle column displacement for RC specimens (Orton 2007)

Yu and Tan (2013a) investigated the effect of seismic and non-seismic detailing on the behaviour of RC beam column sub-assemblage bridging over a removed column. The prototype frame was part of a 5-storey commercial building designed in accordance

with the ACI 318-05 code. One-half scaled version of the prototype frame consisting of two beams and three column stubs was used for the experiment. The end columns were larger than the middle column to avoid damage. One end of the column was connected to a steel frame and the other end was connected to a reaction wall to simulate axial restraint by the surrounding structure. The end columns were supported in the vertical direction by a pin support placed on three steel rollers. Load was applied to the specimen by pushing the middle column in a displacement controlled manner with the help of the actuator.

The load-displacement characterisation of the seismic and non-seismic detailing specimen was similar and the advantage of seismic detailing was not noticed (Figure 2.14). The maximum compressive arching capacity were 20 and 30% higher than the flexural capacity for specimen with seismic and non-seismic detailing. With further loading catenary action kicked in at a displacement of 300mm when axial force changed from negative to positive. For specimen with seismic detailing, at catenary action stage the first bottom bar ruptured at the middle column joint interface. This was followed by rupture of the second bottom bar leaving the section with only top bars. Final failure occurred after the rupture of top bars at one of the end joint interface. Similar observation was made for specimen with non-seismic detailing.

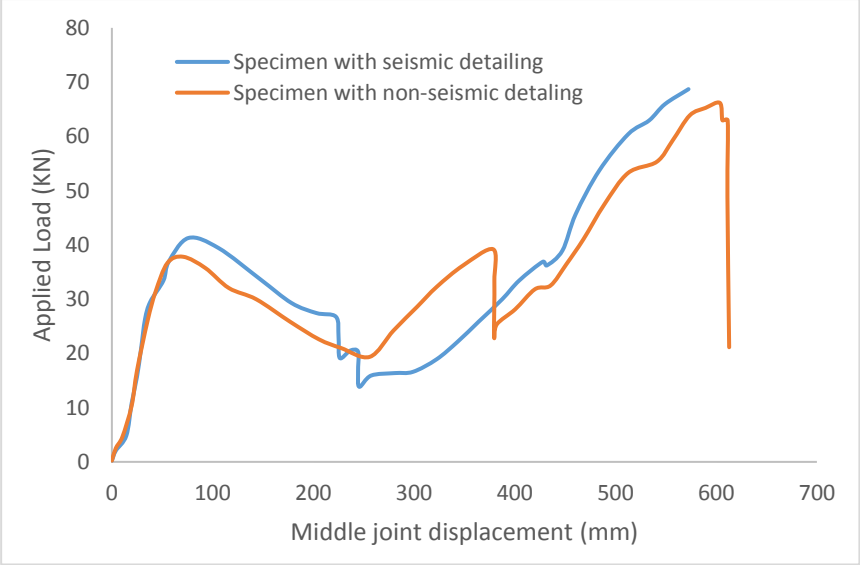

(a) applied load-displacement response

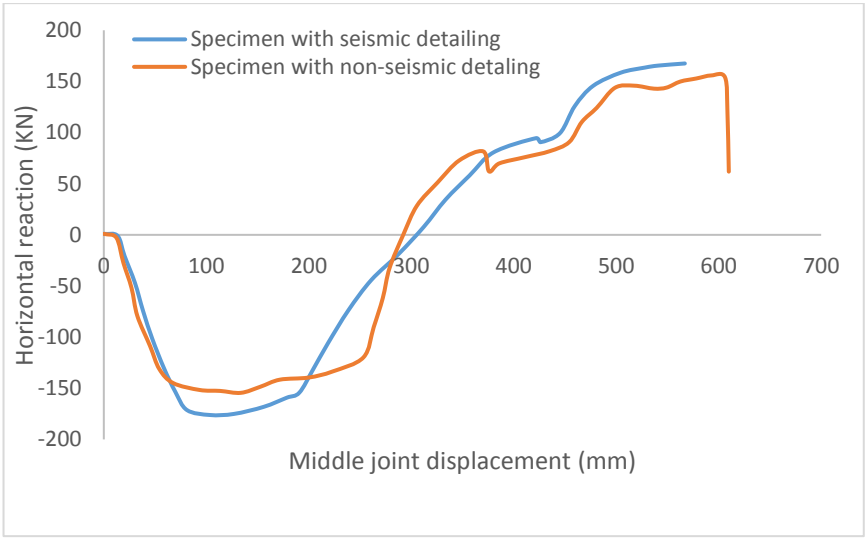

(b) horizontal force-displacement response

Figure 2.14: Relationship of load- displacement and horizontal force-displacement of the middle column (Yu & Tan 2013a)

Yu & Tan (2013b) further performed a parametric study on beam-column sub-assemblies to investigate the effect of reinforcement ratio, span-depth ratio and reinforcement detailing at joint on the structural behaviour of RC sub assemblage. The tested specimens were one-half scaled version of prototype RC frames designed according to ACI 318-05 code provision. Top reinforcement varied from 0.9 and 1.87% at the column position while bottom reinforcement varied from 0.49 to 0.82%. Span-depth ratio of the specimens ranged from 13.4 to 23 (defined here as total net length of actually two beams to the section depth). Two of the tested specimens were lap spliced to study its effect on the development of catenary action. Grade 500 steel was used for the test and concrete compressive strength was 38MPa. Axial restraint was provided by a reaction wall on one end of the column and a steel frame at the other end. Twisting of the centre column at large deformation was prevented by two out-of-plane restraints at the middle column and load was applied through a hydraulic actuator with displacement control at 0.1mm/s rate.

Results of the test were considered at structural, sectional and fibre levels. It was observed that specimen with higher bottom reinforcement ratio had higher structural resistance with top reinforcement ratio remaining constant. Similarly, with the same

bottom reinforcement ratio, specimens with higher top reinforcement ratio had higher structural resistance. However, a higher bottom reinforcement ratio was only beneficial to the structural resistance at initial catenary stage prior to the rupture of bottom bars whereas a higher top reinforcement ratio was beneficial both at the initial catenary action where bottom bars ruptured and at the final stage of the catenary action which was provided by the top reinforcement. Figures 2.15 and 2.16 show effects of the reinforcement ratio while Figure 2.17 shows the effect of span-depth ratio. All but one specimen failed by rupture of reinforcement. It can be seen that the test agree well with findings from Su et al. (2009). The specimen with L/d ratio of 13.4 failed in shear due to the short span-depth ratio which caused stirrups to fracture at the beam column interface.

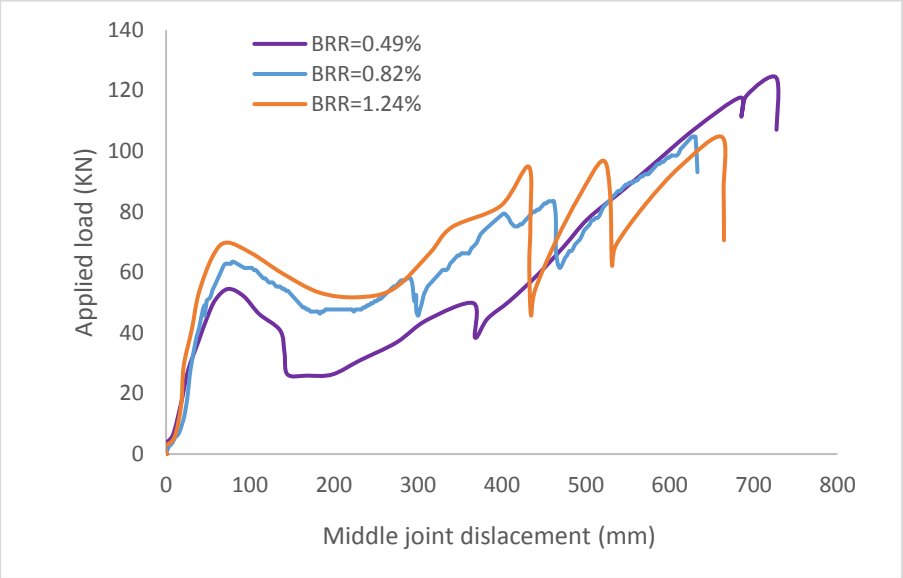

(a) load-middle joint displacement

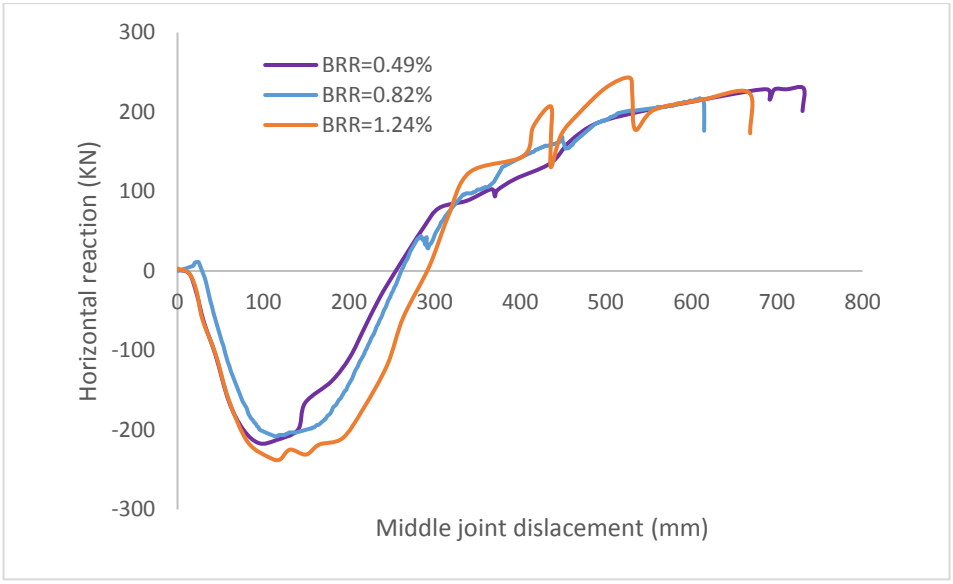

(b) horizontal reaction-middle joint displacement

Figure 2.15: Effect of bottom reinforcement ratio on structural behaviour of subassemblies (Yu and Tan, 2013b)

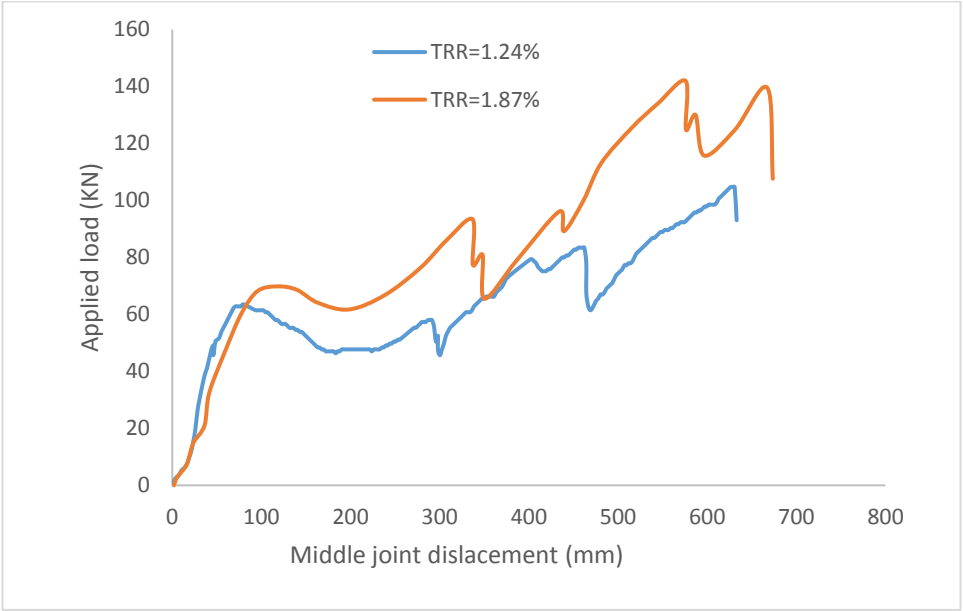

(a) load-middle joint displacement

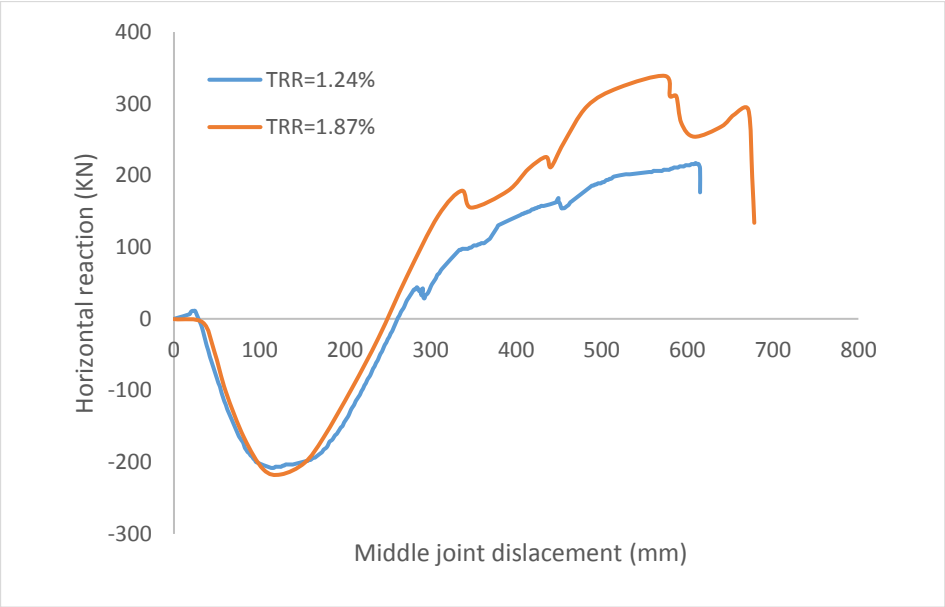

(b) horizontal reaction-middle joint displacement

Figure 2.16: Effect of top reinforcement ratio on structural behaviour of subassemblies (Yu and Tan, 2013b)

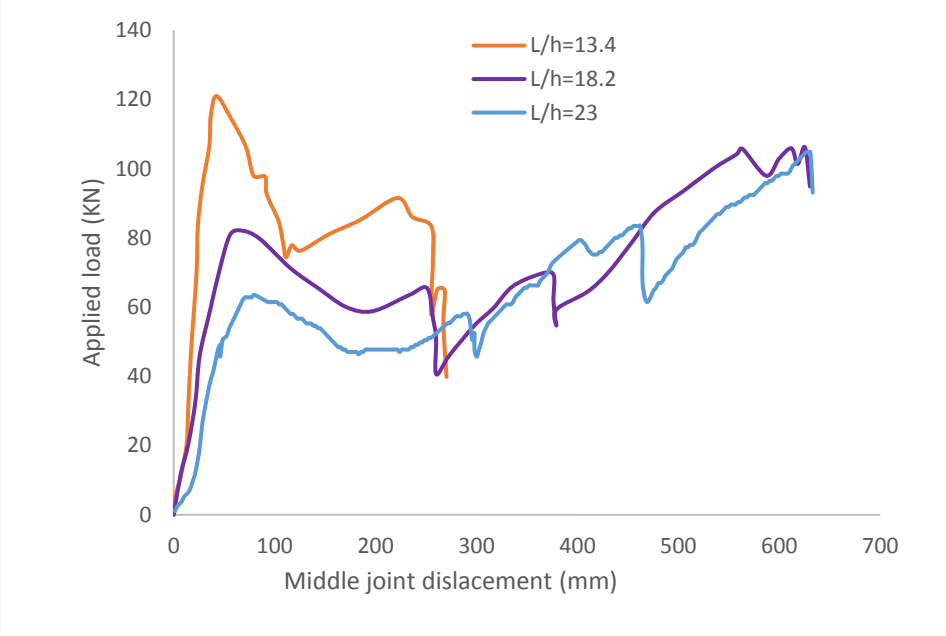

(a) load-middle joint displacement

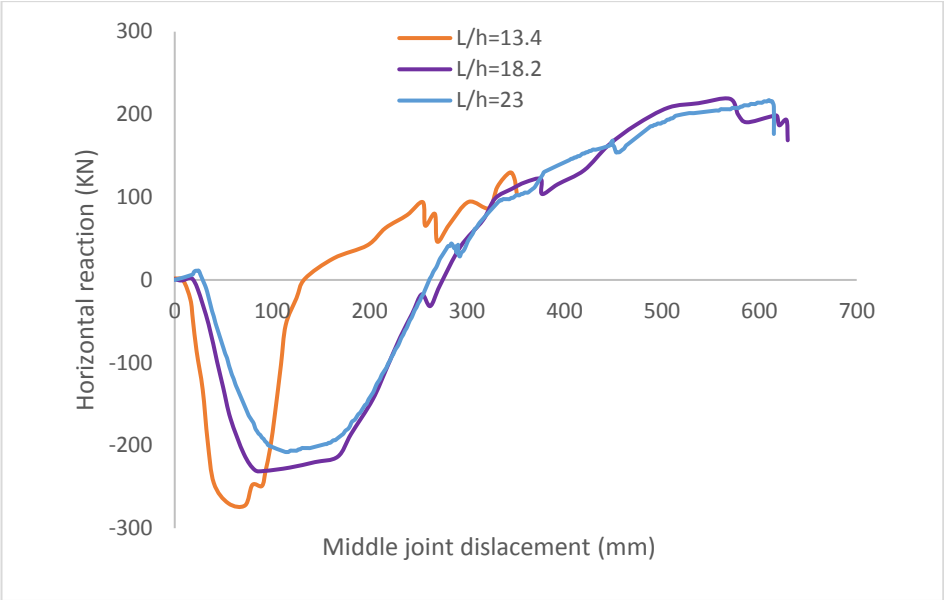

(b) horizontal reaction-middle joint displacement

Figure 2.17: Effect of span-depth ratio on structural behaviour of subassemblies (Yu and Tan, 2013b)

In a study to investigate the effect of seismic design and detailing on progressive collapse of RC structures, two reinforced concrete sub-assemblies were tested (Lew et al. 2011). The two assemblies were part of a 10-storey building designed according to the codes from American Concrete Institute (ACI 318-02), American Society of Engineers (ASCE 2002) and International Code Council (ICC 2003). One of the sub-assemblies was designed for Seismic Design Category C and the other was designed for Seismic Design Category D. For the seismic design Category C, Intermediate Moment Frame (IMF) was used while Special Moment Frame was used for the Seismic Category D.

The IMF specimen had a beam size of 508 by 711mm (height by width) and reinforcement consisted of 4no. Φ25mm (0.65%) top bars and 2no. Φ29mm (0.43%) bottom bars at the support section. For the SMF specimen, the beam size was 660 by 864mm and reinforcement at the support were 7no. Φ25mm (0.69%) for top and 6no. Φ25mm (0.59%) for bottom section. The geometric and reinforcement detail for IMF specimen is shown in Figure 2.18. The load was applied to the middle column using a displacement controlled approach.

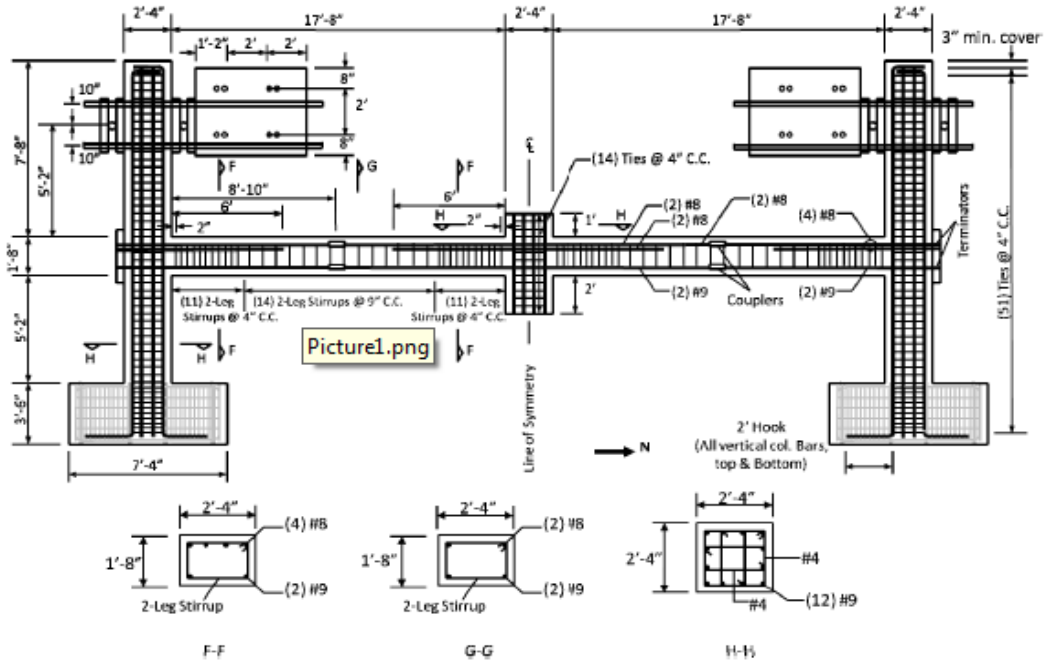

Figure 2.18: Geometric and reinforcement details for IMF specimen (Lew et al. 2014)

Figure 2.19 shows the middle column load versus displacement relationship of the two specimens. The behaviour and failure modes of both specimens were similar. With increasing loading, flexural cracks formed at the end and middle column interface. The authors noted that these cracks were more uniform throughout the length of the beam when the beam entered into catenary action stage which implies that the beam was in tension. In both specimens, the final failure load was greater than the maximum compressive arching action capacity and rotation at fracture of bottom rebar was 0.18 and 0.2 for IMF and SMF specimens respectively.

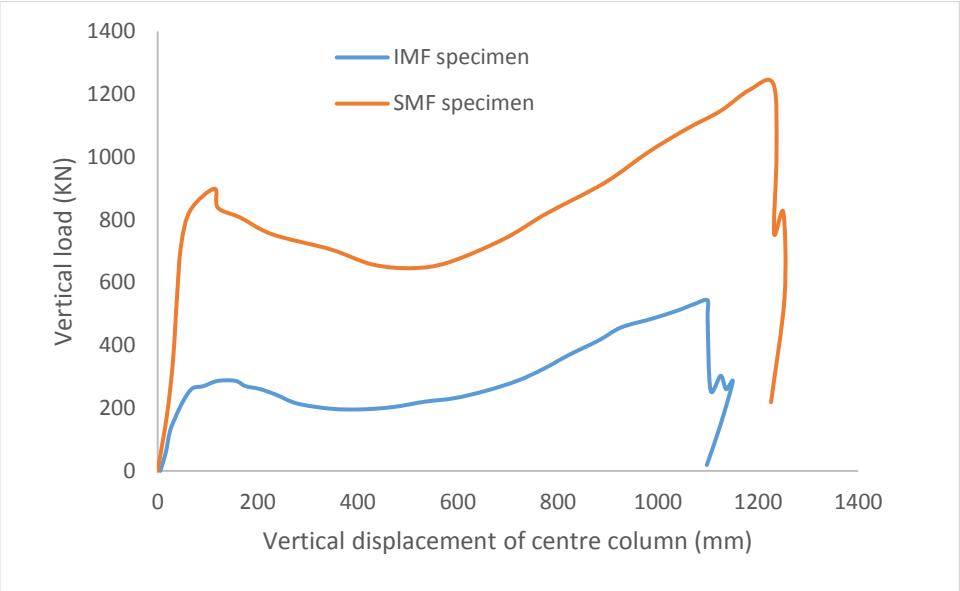

Figure 2.19: Vertical load against centre column displacement of tested specimens (Sadek et al. 2011)

2.6 Parameters affecting compressive arching action in axially restrained reinforced concrete beams

The experimental test in Section 2.5 shows that compressive arching action capacity is affected by reinforcement ratio, span depth ratio, axial restraint and concrete compressive strength. In this section, the review of the effect of each of these parameters are presented.

2.6.1 Effect of axial restraint on compressive arching action capacity

The influence of axial restraint on compressive arching action (CAA) capacity was studied in Yu & Tan (2014) using a theoretical model. In their study, a non-dimensional relative axial stiffness (γ_a) was used to study the axial restraint stiffness effect on CAA capacity and it was defined as:

$$\gamma_a = \frac{K_a}{(E_c A)/L_t} \tag{2.3}$$

where K_a is the axial restraint stiffness, E_c is the elastic modulus of concrete, A is the cross-sectional area and L_t is the total net length of the double-span beam and the middle column stub. Three different specimens were used for this purpose. These included specimen A5 from test by Su et al. (2009) and specimen S5 and S7 from tests by Yu & Tan (2013). It should be mentioned that the three specimens considered in their investigation had different geometrical and reinforcement properties.

For each of the specimens considered, the axial restraint stiffness (K_a) was varied while other parameters were kept constant. Their result showed that a larger axial stiffness (K_a) increases the CAA capacity when $\gamma_a < 1$, whereas for a strong axial restraint ($\gamma_a \geq 1$), further increase of the axial stiffness (K_a) only has a marginal effect on CAA capacity. Their classification of weak and strong restraint was based on the lower rate of increase in CAA capacity for $\gamma_a \geq 1$ compared to when $\gamma_a < 1$ as can be observed in Figure 2.20.

The same trend was observed in all three specimens considered, however the increase in CAA was more pronounced in specimen A5 compared to specimens S5 and S7. This was attributed to the short L/d ratio of specimen A5 compared to other two specimens. They suggested that CAA capacity should only be considered as one of the load path for resisting progressive collapse, when there is a strong axial restraint which was defined in their study as $\gamma_a \geq 1$.

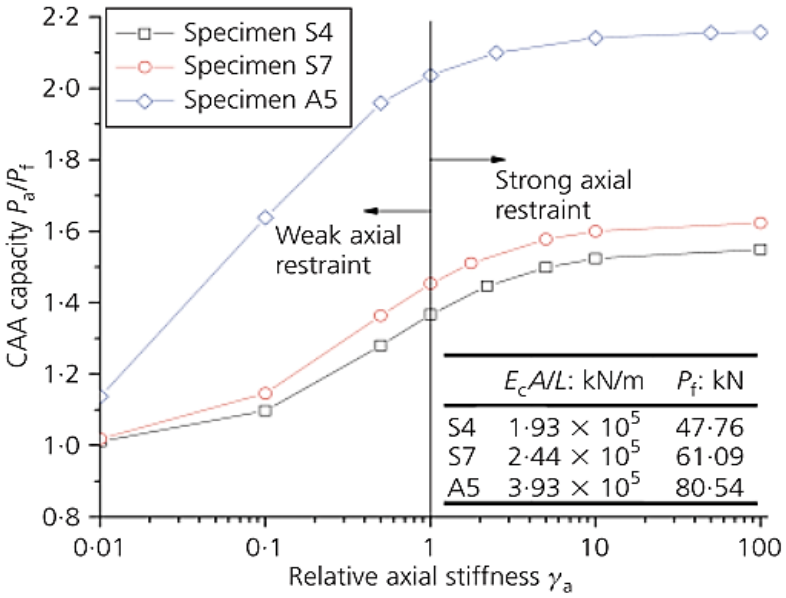

Figure 2.20: Effect of axial restraint stiffness on normalized CAA capacity (Yu & Tan 2014)

2.6.2 Effect of reinforcement ratio on compressive arching action capacity

In separate studies, Su et al. (2009) and Yu and Tan (2013) investigated the effect of reinforcement ratio on compressive arching action (CAA) capacity. Both studies were performed by varying the bottom reinforcement while keeping the top reinforcement constant and in turn varying the top reinforcement while keeping the bottom reinforcement constant. Yu and Tan (2013) reported from their findings that increase in bottom reinforcement reduces the normalized CAA capacity. The same trend was also observed when the top reinforcement was varied. Similar findings were made in the test by Su et al. (2009). In the case of Su et al. (2009), the tensile reinforcement ratio at the middle and end sections were used to investigate the effect of reinforcement on CAA capacity. They concluded that when the reinforcement ratio decreased from 1.13 to 0.46%, the normalized increase in load increased linearly from 1.91 to 2.63. Yu and Tan (2013)-also arrive at the conclusion that increase in reinforcement ratio decreases the CAA capacity.

The reinforcement ratio effect on CAA capacity was investigated in a more elaborate detail in Yu and Tan (2014) using analytical model on compressive arching action. In the study, the effect of reinforcement ratio and concrete strength was defined using a single non-dimensional factor ω defined as:

$$\omega = \frac{\rho f_y}{f_c} \tag{2.4}$$

Where ρ is the sectional reinforcement ratio in the RC beam. f_y is the yield strength of reinforcement and f_c is the compressive strength of concrete. The choice of the use of sectional reinforcement ratio stems from the fact that during the arching action stage, the bottom reinforcement at the middle joint and the top reinforcement at the end section are in tension, Hence the total tension reinforcement in the beam can well be represented using the sectional reinforcement. The reinforcement ratio was varied to obtain different ω for a given L/d ratio and the enhancement factor (α) was determined in each case. The concrete compressive strength in the study was 38.2MPa while the yield strength for 10 and 13mm diameter bars were 511 and 494MPa respectively. Figure 2.21 shows the plot of enhancement ratio (α) against the arching mechanical reinforcement ratio (ω). It can be observed that the normalized increase in load capacity decreases with increase in the reinforcement ratio (ω).

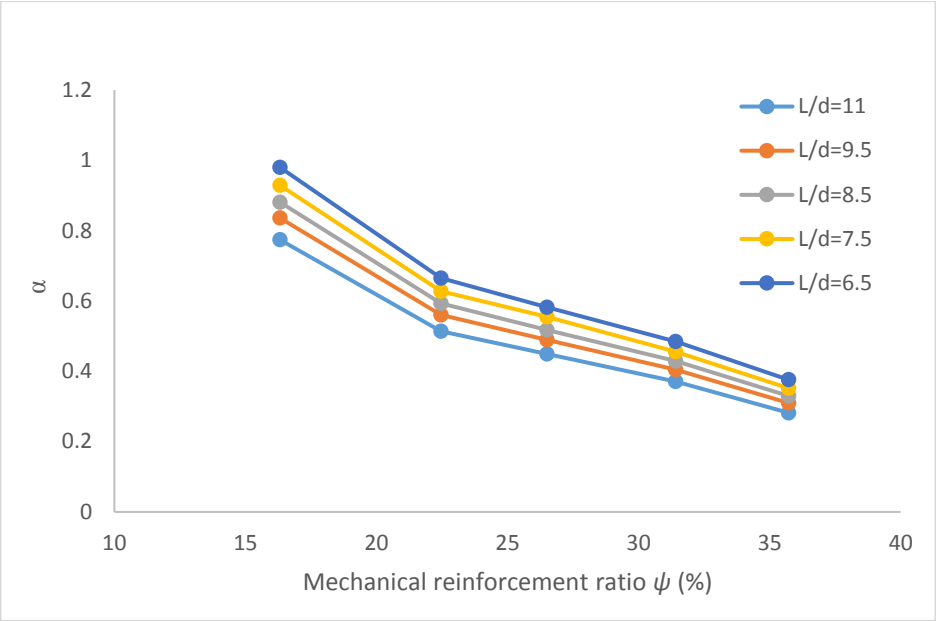

Figure 2.21: Effect of reinforcement ratio on enhancement factor for different L/d ratio (Yu & Tan 2014)

2.6.3 Effect of span depth ratio on compressive arching action capacity

The effect of L/d ratio was investigated in the Su et al. (2009) and Yu & Tan (2013). In Su et al.(2009), three different L/d ratio including 4.08, 6.58 and 9.08 were considered. The reinforcement ratios were kept constant in the three specimens considered although the concrete strength was slightly. Specimen with L/d ratio of 4.08 had concrete strength of 31.2MPa while that of 6.58 and 9.08 were 18.6 and 19.3MPa respectively. In the case of Yu & Tan (2013), three different L/d ratios of 6.2, 8.6 and 11 were used. The concrete compressive strength and reinforcement ratios were kept constant. Figure 2.22 shows the effect of L/d ratio on the enhancement ratio (α) in the two existing studies considered. It can be seen from the figure that the enhancement ratio ranges between 0.49 and 0.89 for L/d ratios of 4.08 to 9.08 in Su et al. (2009). In Yu & Tan (2013), the difference was slightly lower ranging from 0.33 to 0.43. As mentioned previously, the concrete strength in Su et al. (2009) was not constant. The difference in concrete strength between specimens with L/d of 4.08 and the other two specimens may have contributed to higher increase in load capacity in L/d of 4.08 compared to that of 6.58 and 9.08.

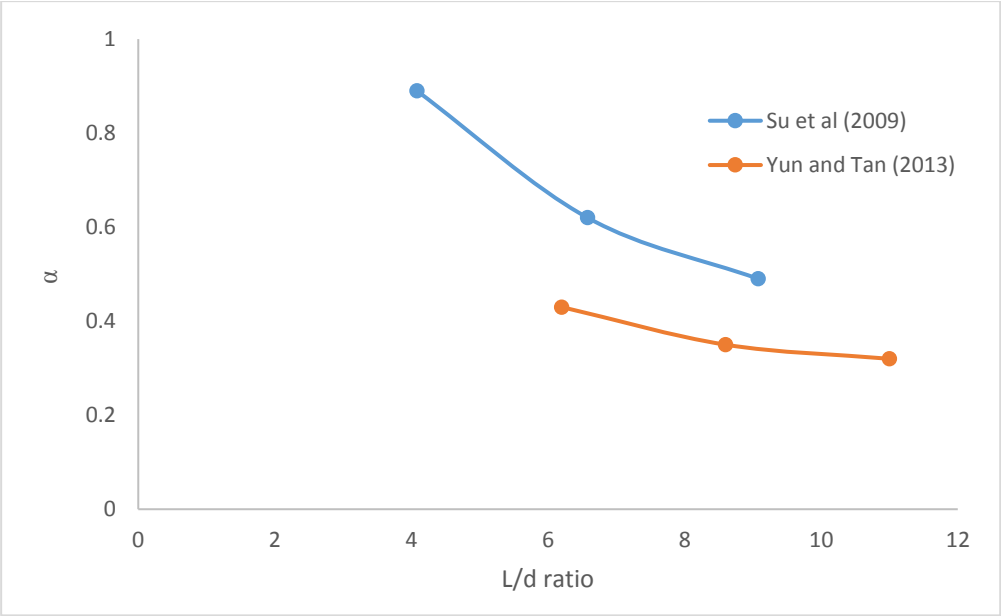

Figure 2.22: Effect of L/d ratio on enhancement factor from experimental test

2.6.4 Effect of concrete compressive strength on compressive arching capacity

Only Vali *et al.* (2015) investigated the concrete strength effect on CAA capacity. In their study, three different concrete compressive strengths including 18, 48 and 67MPa were considered while keeping other parameters constant. Figure 2.23 shows the variation of enhancement factor with concrete strength as observed in their test. It could be seen from here that enhancement factor increases as the concrete strength increases.

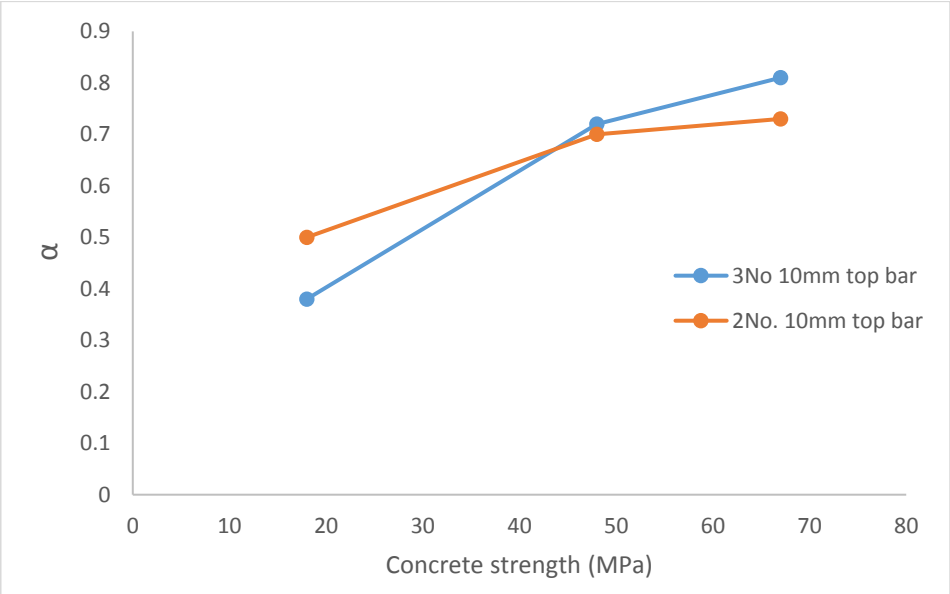

Figure 2.23: Effect of concrete strength on enhancement factor (Vali et al. 2015)

2.7 Analytical studies

The analytical studies on axially restrained beams can be classified into two groups: a) compressive arching action, and b) catenary action. In this section, the selected analytical studies for compressive arching action and catenary action are reviewed and the underlying assumption and limitations are also discussed.

2.7.1 Analytical studies on compressive arching action

In the 1950's, experimental studies on one-way and two-way RC slabs showed that the maximum load was greater than the capacity calculated by yield line theory (Christiansen 1963; Park 1964; Wood 1961). This increase in load capacity compared to the flexural capacity was attributed to the development of compressive membrane action in the slab. Since then a number of analytical studies to predict the capacity of axially restrained RC slabs and beams have been performed.

Christiansen (1963) developed an analytical model for the prediction of the ultimate strength of laterally restraint one-way RC slabs and beams. In his study, the ultimate strength was considered to comprise of bending and membrane stresses. The bending

capacity was determined using the yield line theory. For the arching contribution, the depth available for arching was determined by equating the outward movement of the end support with the extension of beam due to rotation minus the elastic and plastic shortenings of one-half of the beam. This is expressed mathematically as:

$$a_1 = h - \Delta - \frac{(T_1 + T_2 + 2C)}{f_c} \tag{2.5}$$

where a_1 is the depth available for arching, h is the depth of beam. T_1 and T_2 are the tensile force for per unit width in the tensile reinforcement at the support and middle section and C is the additional compressive force per unit width due to arching. These parameters are represented schematically in Figure 2.24. The analytical model prediction correlated well with the experimental test result. However, the mid-span deflection at maximum compressive membrane force in the model was less than observed in the experiment. This discrepancy was attributed to the additional bending that occurred close to the hinges which was due to the increased compression.

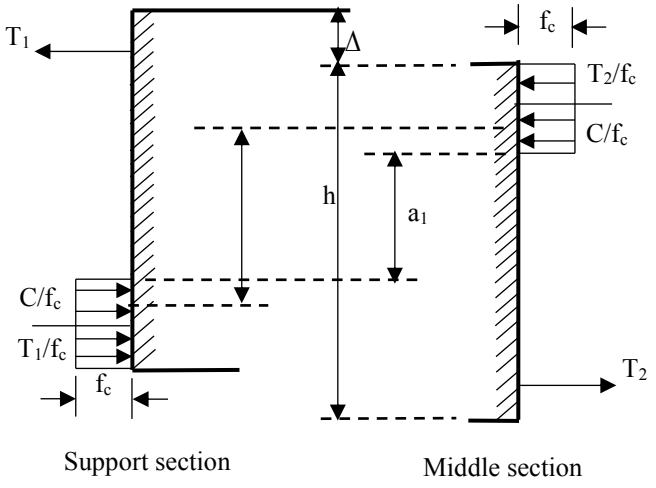

Figure 2.24: Horizontal forces at support and mid-span (Christiansen 1963)

By treating the contribution from bending and arching similar to Christian's approach, Rankin and Long (1997) developed analytical model for the determination of maximum compressive arching action capacity in laterally restrained slab. The study was based on McDowell's research work in a laterally restrained masonry walls

(McDowell, 1956). By adopting the stress distribution from McDowell's work, the arching moment of resistance was determined for elastic and elastic-plastic cases. The flexible boundary condition was taken into consideration by considering equilibrium between a rigid beam and equivalent three-hinge arches with axial stiffness (K_a).

It should however be noted that both Christiansen (1963) and Rankin & Long (1997) treat the bending and arching deformation separately. In reality, arching and bending coexist in the beam and deformation compatibility needs to be fulfilled. More so Rankin model was developed for slab and did not take into consideration the compressive reinforcement which may affect the arching capacity in a laterally restrained RC beam.

Rankin and Long (1997) developed a theoretical model to predict the compressive arching action in slabs using the theory of McDowell et al (1956). The idealised geometry of the slab is shown in Figure 2.25.

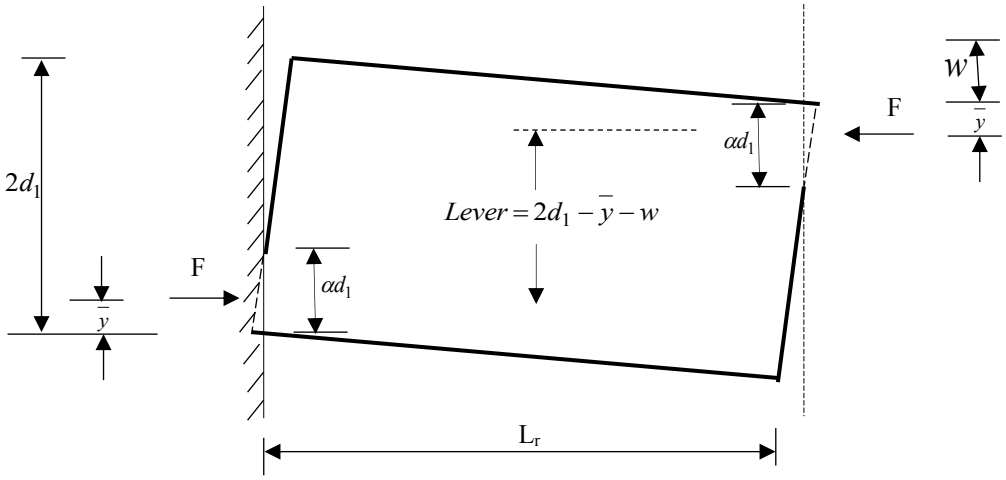

Figure 2.25: Plan and elevation view of RC assemblages with idealised geometry for half span laterally restrained slab after McDowell et al (1956) (Rankin & Long 1997b)

In McDowell et al (1956), the moment ratio (M_r) for elastic and elastic-plastic stress distribution was given as:

$$M_r = \frac{8u}{3R}\left(1 - \frac{5u}{4}\right)\left(1 - \frac{u}{2}\right)^2 \quad \text{for elastic stress distribution} \tag{2.6}$$

$$M_r = 4\left(1 + \frac{R}{2} + \frac{3u^2}{4} - 2u - \frac{R^2}{3u^2}\right) \quad \text{for elastic-plastic stress distribution} \tag{2.7}$$

where R and u are non-dimensional parameters defined as:

$$R = \frac{\varepsilon_c L^2}{4d_1^2} \tag{2.8}$$

$$u = \frac{w}{2d_1} \tag{2.9}$$

Differentiating Equation (2.6) and (2.7) resulted in:

$$20u^2 - 32u + 8 = 0 \tag{2.10}$$

$$20u^2 - 32u + 8 = 0 \tag{2.11}$$

The deflection corresponding to the maximum arching action is determined for the elastic stress distribution. However, for elastic-plastic stress distribution, the expression depends on R and by solving the expression numerically at discrete point, the arching moment ratio was obtained for the following range of R:

for $R > 0.26$

$$M_r = \frac{0.3615}{R} \tag{2.12}$$

and for $0 < R < 0.26$

$$M_r = 4.3 - 16.1\sqrt{(3.3*10^{-4} + 0.1243R)} \tag{2.13}$$

The arching moment of resistance is then calculated as:

$$M_a = \frac{0.85 f_c^{'} d_1^2 M_r}{4} \tag{2.14}$$

The arching moment of resistance in Equation (2.14) assumes that the depth (d_1) is used by arching only. Considering that part of the depth is used to balance the tensile yielding at support and middle section, Rankin and Long adopted Christiansen's approach (Christiansen 1963) to determine the effective depth for arching only as:

$$2d_1 = h - (\rho + \overline{\rho})\frac{f_y d}{0.85 f_c^{'}} \tag{2.15}$$

where ρ and $\overline{\rho}$ are the tensile reinforcement ratio at the support and middle section of the slab.

The above expression was based on RC slab with full axial restraint. By considering the equilibrium of equivalent three-hinged arch shown in Figure 2.26, the length of the rigidly restraint RC slab was expressed in terms of elastic length as:

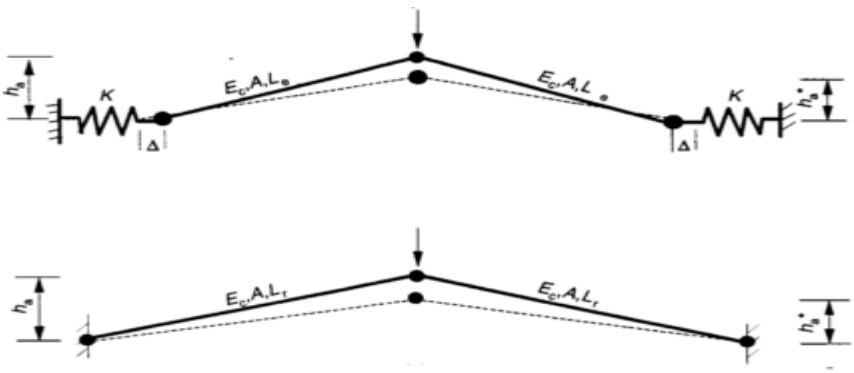

Figure 2.26: Equivalent three hinge arches (a) with flexible restraint (b) rigid restraint (Rankin & Long 1997b)

$$L_r = L_e\left[\frac{E_c A}{KL_e} + 1\right]^{1/3} \tag{2.16}$$

where L_e is the length of the RC slab with elastic restraint

E_c is the elastic modulus of concrete

K is the axial stiffness of restraining spring and

A is the cross-sectional area of the compression zone

The maximum moment due to arching of RC slab with elastic restraint can be expressed as:

$$M_a = M_{ar} \frac{L_e}{L_r} \tag{2.17}$$

Finally, the enhanced ultimate capacity due to bending and arching is calculated as:

$$P_b = k(M_{b1} + M_{b2}) \tag{2.18}$$

$$P_a = kM_a \tag{2.19}$$

where k = 4/L for RC slab with load applied at middle joint.

The proposed model was validated with experimental test on slabs from Christiansen (1963), Birke (1975), and Roberts (1969) and the results correlated well. The model was also used to predict the strength enhancement in T-beams and good agreement was obtained (Ruddle et al. 2003).

It should however be noted that both Christiansen (1963) and Rankin and Long (1997) treat the bending and arching deformation separately. In reality, arching and bending coexist in the beam and deformation compatibility needs to be fulfilled. More so Rankin and Long's model ignores the compression reinforcement which for a RC beam may increase the arching compression.

Yu and Tan (2014) developed an analytical model for the prediction of the compressive arching capacity of RC beams. The model is an advancement of Park and Gamble's model (1960) in that it considers the partial rotational and axial restraint and the stress state of reinforcement. The model is based on plane section assumption and also assumes that the maximum compressive strength in concrete at the critical section is a constant equal to 0.003. The deformation of one-half of the beam is shown in Figure 2.27. Based on compatibility relation, the neutral axis at the end is related to the neutral axis at the middle section as:

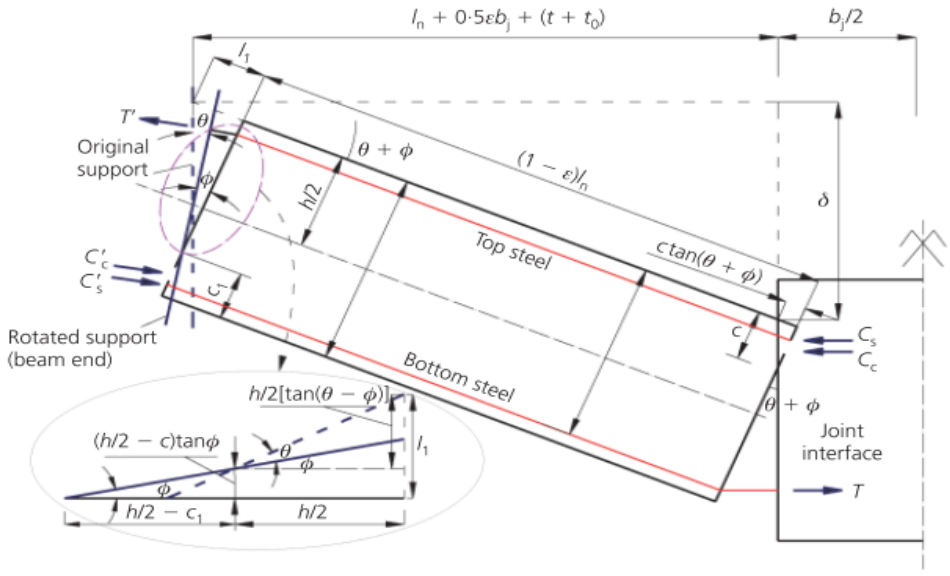

Figure 2.27: Compatibility condition of one-half of RC beam (Yu and Tan, 2014)

$$c = \frac{h}{2} - \frac{\delta}{2} - \frac{\beta l^2}{2\delta}\left(\frac{1}{E_c A} + \frac{2}{lK_a}\right)N - \frac{\beta l t_o}{\delta} + \left(\frac{h}{2} - c_1\right)\left(1 - \frac{M_{u1}\beta l}{K_r \delta}\right) \qquad (2.20)$$

where c and c_1 are the neutral axis at the end and middle section respectively.

M_{u1} and N bending moment at the beam end and axial force in the beam respectively. K_a and K_r are the axial and rotational stiffness of the end restraint respectively.

The neutral axes c and c_1 cannot be solved by Equation (2.20) only. The second equation was determined by considering equilibrium of forces for the end and middle section as:

$$N_{u1} = C_c' + C_s' - T' \qquad \text{for end section} \qquad (2.21)$$

$$N_u = C_c + C_s - T \qquad \text{for middle section} \qquad (2.22)$$

where C_c and C_c' are determined using equivalent rectangular stress block as:

$$C_c' = 0.85 f_c' b \beta_1 c_1 \qquad (2.23)$$

$$C_c = 0.85 f_c^{'} b \beta_1 c \tag{2.24}$$

Compressive force in steel was determined based on the strain in the rebar.

By considering compatibility and equilibrium equations explained above, the neutral axis depth c and c_1 were determined for a given value of middle column displacement using an incremental procedure and the forces and moment and the compressive arching capacity were determined.

2.7.2 Analytical studies on catenary action

Izzuddin (2005) proposed an analytical model for catenary action in axially restraint beams. The response of the beam was classified into four stages as shown in Figure 2.28.

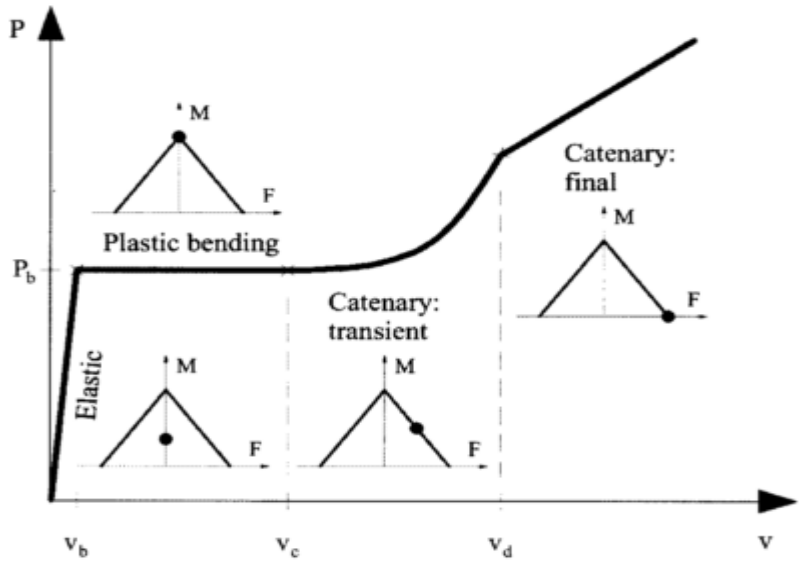

Figure 2.28: Four response stages (Izzuddin 2005)

The load-displacement response at the elastic stage was considered to be linear and depends on the flexural rigidity of the beam. The load at any given displacement during the elastic stage was defined as:

$$P = \alpha \frac{EI}{L} v, \quad \left(\alpha = \begin{cases} 48 \text{ for } MPL \\ 76.8 \text{ for } UDL \end{cases} \right) \tag{2.25}$$

For the plastic bending stage, the load was assumed to be constant and depends on the plastic moment capacity of the section with the load and displacement expressed as:

$$P_b = \beta \frac{M_p}{L}, \quad \left(\beta = \begin{cases} 4 \text{ for } MPL \\ 8 \text{ for } UDL \end{cases} \right) \tag{2.26}$$

$$v_b = \frac{\beta}{\alpha} \frac{M_p L^2}{EI} \tag{2.27}$$

where M_p is the plastic moment capacity of the section, L is the length of the double span beam and v_b is the mid-span displacement.

In the transient stage, in addition to bending, the beam also elongates causing axial tension forces to develop. The extension of the beam including the elastic axial support was given as:

$$\Delta = 2 \frac{v^2}{L} \tag{2.28}$$

Using the principle of Hooke's law, the deformation of elastic axial restraint was related to the axial force in the beam by the expression:

$$F = K_e (2 \frac{v^2}{L} - \Delta_p) \tag{2.29}$$

With the flow rule theory, Izzuddin (2008) obtained an expression relating the incremental plastic axial deformation and rotation at the plastic hinge. The incremental axial force in the beam was then obtained as:

$$\delta F = K_e (4 \frac{v \delta v}{L} - 4 \frac{r_p \delta v}{L}) \tag{2.30}$$

where r_p is the ratio of the moment and axial force capacities of the section.

Integrating Equation (2.30) with starting displacement (v_c) corresponding to maximum of (v_b and r_p), the axial force during the transient stage was calculated as:

$$F = K_e \frac{2(v - v_c)(v + v_c - 2r_p)}{L} \tag{2.31}$$

The corresponding moment was determined from the moment-axial force yield function and the load was obtained considering equilibrium of forces in the beam and expressed as:

$$P = \frac{\beta}{L}\left[M_p + K_e \frac{2(v - v_c)(v + v_c - 2r_p)(v - v_p)}{L} \right] \tag{2.32}$$

The end of the transient stage is reached when the axial force equals the axial capacity of the beam and the load at this stage was calculated as:

$$v_d = v_c + \sqrt{(v_c - r_p)^2 + \frac{F_p}{2K_e}} \tag{2.33}$$

After the axial capacity of the beam is reached, for subsequent displacement greater than v_d, the load was determined as:

$$P = \beta \frac{F_p v}{L} \tag{2.34}$$

where F_p is the axial capacity of the beam

Although the model can represent the catenary action in axially restraint beams, it does not consider strength degradation which may occur due to partial failure at critical region or connection, for example for a typical steel connection this may be fracture of bottom weld, and for an RC section this could be rapture of part of tensile reinforcing bars. This leads the prediction from the model to be unreliable in some cases.

2.8 Concluding remarks

From the review presented in this chapter, it is seen that Alternate Load Path is arguably the most commonly accepted method, as recommended by design guidelines, for the progressive collapse assessment of structures. For laterally restrained RC assemblies, the different load path which could develop in a column loss scenario are flexural, compressive arching and catenary action. Different researchers have agreed that the maximum compressive arching action in RC assemblies occur at a lower displacement (within about 0.6 times of the section depth) and is affected by reinforcement ratio, axial restraint, span depth ratio and concrete compressive strength, however there are question that are yet to be addressed. Furthermore, the existing analytical model for catenary action does not consider strength degradation and may therefore lead to over estimation of the prediction. Based on the research gap existing in the literature, the questions the present research seeks to address includes:

- To perform a detailed quantitative study to ascertain the proportion of additional load due to arching that can be attributed the factors affecting the arching compression.
- To develop a more detailed analytical model for compressive arching action that will consider the compounding effect of bending and arching and the deformation state of the concrete.
- To develop a generic analytical model for catenary action in a lateral retrained subassembly with incorporation of strength degradation. The generic model can be used to predict the load-displacement response in both RC and steel assemblies.

Chapter 3: Critical evaluation of compressive arching action - a semi empirical study

3.1 Introduction

Chapter two presented a general review of both theoretical and experimental studies in the field of progressive collapse of reinforced concrete assemblies and structures. In this chapter, the focus is on the compressive arching action with particular interest in the relative increase in the compressive arching capacity taking into consideration the various parameters that affect this relative increase, based primarily on existing experimental data in the literature. Despite a number of experimental studies on this topic, a systematic scrutiny covering a sufficient variation range of parameters from the various test programmes has not been conducted before. To this end, a detailed account of existing experimental studies on compressive arching action in RC sub-assemblage is first presented. This includes test set-up, geometric details and the results concerning particularly the arching action. Subsequently, a critical analysis of all the experimental studies with particular focus on the parameters affecting the relative increase in the compressive arching action is presented. Finally, a semi-empirical set of equations for predicting the compressive arching action is proposed.

3.2 Existing experimental studies

A number of studies on compressive arching action of RC subassemblies are available in the literature. Herein, a critical review of five (5) group of studies on compressive arching action of RC subassemblies are presented. These five studies investigated in total 32 different specimens with differing geometric, support conditions, reinforcement ratio and concrete compressive strength.

Lastly, the normalized increase in arching is evaluated for each of experimental test. Although, the flexural capacity was calculated in some of the test herein, the flexural

capacities are recalculated based on formation of plastic hinges at the mid-span and end sections. An illustration of the determination of flexural capacities is shown below.

Consider the cross-section details of the beam as shown in Figure 3.1. Assuming that compression steel has not yielded and tension steel has yielded, equilibrium of forces can be written as:

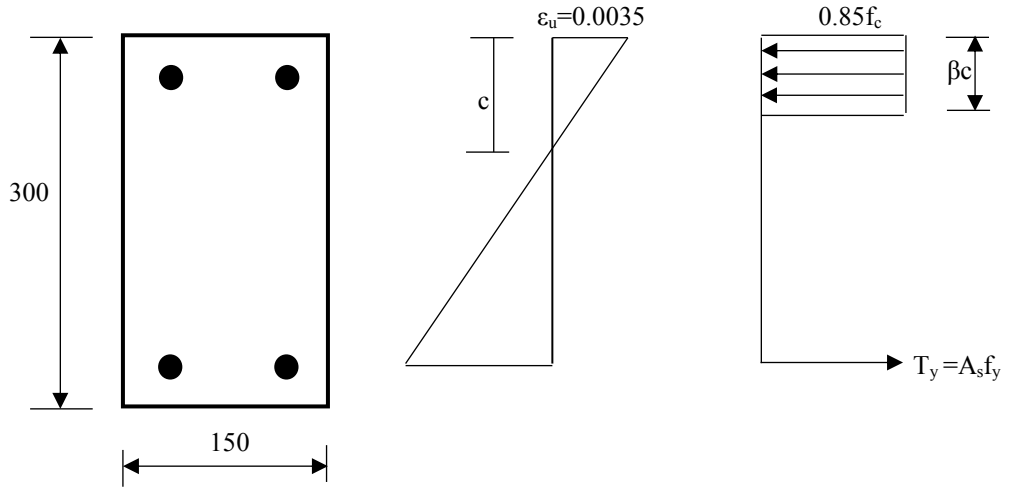

Figure 3.1: Cross section showing the assumed stress distribution at the middle and end section in specimen A1

$$A_s f_y = 0.85 f_c b \beta c + 0.0035 A_{sc} E_s \frac{(c-35)}{c} \tag{3.1}$$

Substituting the geometric and material parameters into Equation (3.1), the neutral axis (c) can be determined and subsequently the corresponding moment capacity of the section can be calculated.

Let the moment capacity at the end and middle section be represented as M_e and M_m. The load capacity (P_f) due to flexure can then be determined as:

$$P_f = 2(M_e + M_m)/L \tag{3.2}$$

where L is the half-span length of the beam.

The normalized increased in load due to arching is then calculated as:

$$\Delta\omega_N = \frac{P_a - P_f}{P_f} \tag{3.3}$$

Where P_a and P_f are the maximum arching compression and flexural capacities respectively. Equation (3.3) is used to determine the normalized increased in load for the different experimental test considered in this study as shown in subsequent sections.

3.2.1 Test by Su et al. (2009)

This experimental study investigated the load capacity of axially restrained RC beam assemblage under gravity loading in a column removal scenario and the effect of reinforcement ratio, span depth ratio and loading rate on the compressive arching behaviour of the beam. A total of 12 test specimens were considered in the study, which were further divided into three groups. The first group (group A), with specimens identified as A1 to A6, investigated the effect of reinforcement ratio. In the second group (B), the effect of span depth ratio was studied while the third group (C) investigated the effect of loading rate on the compressive arching action capacity. Each of the specimen consisted of three column stubs and two beams with load applied at the middle column stub. The test geometry is shown in Figure 3.2 while the reinforcement details are shown in Table 3.1. Each of the key parameters considered in the study are discussed in the section that follows.

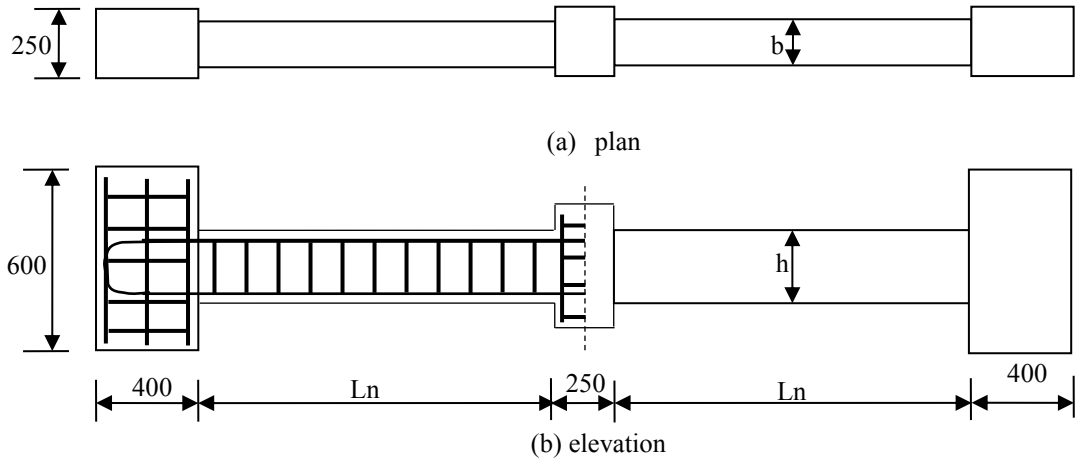

Figure 3.2: Plan and elevation view of RC assemblages (after Su et al., 2009)

Table 3.1: Geometric and reinforcement details of tested specimens by Su et al. (2009)

Specimen ID	b x h (mm)	L_n (mm)	f'_c (MPa)	Longitudinal reinforcement ratio		Ties
				top	bottom	
A1	150 x 300	1225	25.8	2ϕ12 ρ = 0.55%	2ϕ12 ρ = 0.55%	Φ8 @ 100
A2	150 x 300	1225	28.2	3ϕ12 ρ = 0.83%	3ϕ12 ρ = 0.83%	Φ8 @ 80
A3	150 x 300	1225	31.2	3ϕ14 ρ = 1.13%	3ϕ14 ρ = 1.13%	Φ8 @ 80
A4	150 x 300	1225	23.0	2ϕ12 ρ = 0.55%	1ϕ14 ρ = 0.38%	Φ8 @ 100
A5	150 x 300	1225	26.5	3ϕ12 ρ = 0.83%	2ϕ12 ρ = 0.55%	Φ8 @ 80
A6	150 x 300	1225	28.6	3ϕ14 ρ = 1.13%	2ϕ14 ρ = 0.75%	Φ8 @ 80
B1	150 x 300	1975	18.6	3ϕ14 ρ = 1.13%	3ϕ14 ρ = 1.13%	Φ8 @ 100
B2	150 x 300	2725	19.3	3ϕ14 ρ = 1.13%	3ϕ14 ρ = 1.13%	Φ8 @ 120
B3	150 x 300	2725	21.1	3ϕ14 ρ = 1.13%	2ϕ14 ρ = 0.75%	Φ8 @ 120
C1	100 x 200	1225	15.9	2ϕ12 ρ = 1.30%	2ϕ12 ρ = 1.30%	Φ8 @ 80

3.2.1.1 Boundary condition

The schematic representation of the boundary condition used in the study is shown in Figure 3.3. It consisted of a steel socket and a rigid support. The end columns were connected to the steel socket with the help of high strength bolts and steel plate. The steel socket was in turn connected to a rigid support on a steel test bed using a pin located 150mm away from the beam end. Using vertical and horizontal strut, these sockets were then connected to the support such that axial and rotational restraint were obtained. Figure 3.4 shows the test set-up for the test.

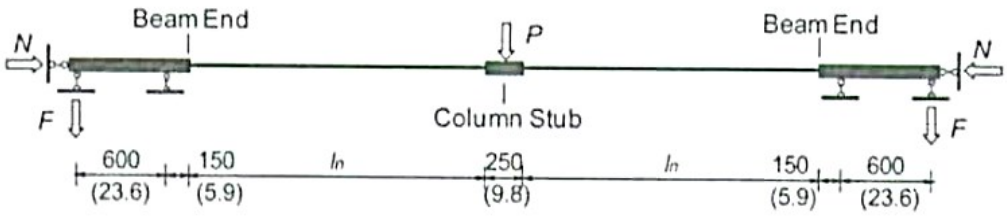

Figure 3.3: Schematic representation of the test set up and tested specimen (after Su et al., 2009)

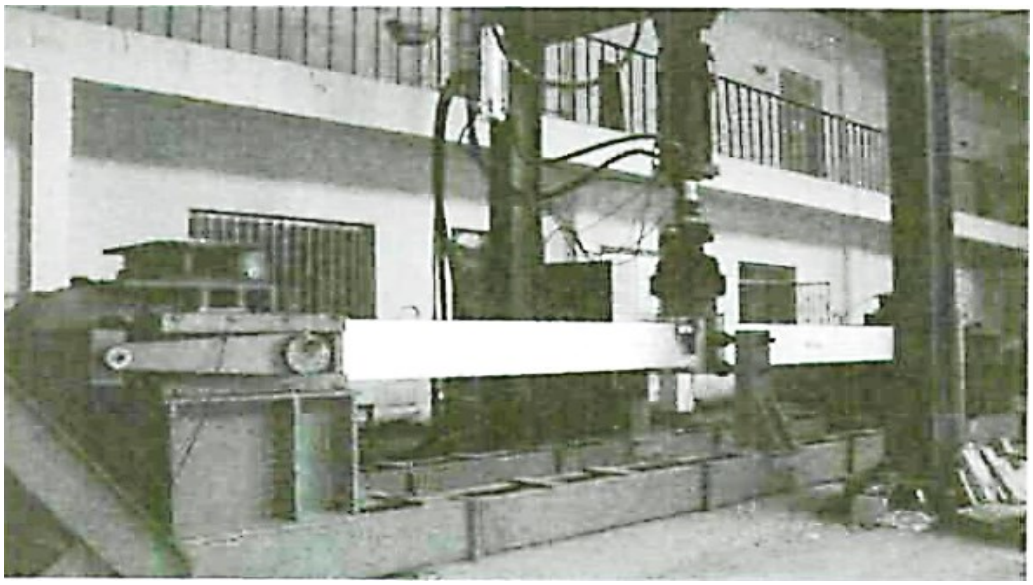

Figure 3.4: Test set up (after Su et al., 2009)

3.2.1.2 Span depth ratio

The span depth ratio (L/d) considered in the study included 4.08, 6.12, 6.58 and 9.08. It could be argued that the tested specimen's L/d ratio ranged from very short to moderate spans. In practice L/d ratio up 15 may be used. It should be mentioned that L/d ratio of 4.08 is rarely used in practice and the behaviour may be dominated by shear rather than bending due to the short span.

3.2.1.3 Reinforcement ratio and rebar strength

The reinforcement ratio at the support and mid-span section varied between 0.55 and 1.30%. This range of reinforcement ratio falls within the range commonly used in practice, thus the reinforcement in the tested specimens may be classified as light to heavily reinforced sections. Two different reinforcement sizes of Φ12 and Φ14mm were used for the longitudinal rebar and Φ8mm was used for the transverse reinforcement. The yield strength of the reinforcements was 350, 340 and 290MPa for 12, 14 and 8mm diameter rebar respectively.

3.2.1.4 Concrete strength

According to the authors, concrete strength was not among the variables investigated in the test. Nevertheless, the concrete strength in all the tested specimens differed slightly. This was attributed to the different batches of concrete used in casting the specimens. The concrete cubic strength used in different specimens varied between 19.9 to 39.0MPa. It should be mentioned that in the test, concrete strength was measured using cubic strength, herein the cubic strength is converted to cylinder strength by multiplying with a factor of 0.8 (BS EN 206-1)

3.2.1.5 Damage patterns

The authors noted that during the loading process, cracking of concrete first initiated at the middle beam-column interface and subsequently at the end interface. Due to the presence of axial restraint, there was no noticeable reduction in concrete stiffness after cracking of concrete and almost a linear stiffness was obtained up to the yielding of tensile reinforcements. It was observed that crushing of concrete occurred in specimen A2 at a much smaller middle column displacement. This was attributed to the in-plane rotation of the middle column stub. For other specimens crushing of concrete occurred after the maximum compressive arching action was reached. This crushing of concrete led to the sudden reduction in the horizontal reaction and applied force and was more severe in specimens with shorter L/d ratio than specimens with longer L/d ratio.

3.2.1.6 Maximum compressive arching action capacities

Following the approach explained in Section 3.2, the normalized arching effect is calculated and presented in Table 3.2.

Table 3.2: Compressive arching and recalculated flexural capacities of specimens tested by Su et al. (2009)

Specimen ID	Axial stiffness (KN/m)	Rotational stiffness (KNm/rad)	L/d ratio	P_a (KN)	P_f (KN)	$\Delta\omega_N = \frac{P_a - P_f}{P_f}$
A1	1.00E+06	1.75E+04	4.08	168	66	1.55
A2	1.00+E06	1.75E+04	4.08	221	97	1.28
A3	1.00+E06	1.75E+04	4.08	246	130	1.89
A4	1.00+E06	1.75E+04	4.08	147	56	1.62
A5	1.00+E06	1.75E+04	4.08	198	81	1.44
A6	1.00+E06	1.75E+04	4.08	226	106	1.13
B1	1.00+E06	1.75E+04	6.58	125	77	0.62
B2	1.00+E06	1.75E+04	9.08	82.9	55.8	0.49
B3	1.00+E06	1.75E+04	9.08	74.7	47	0.59
C1	1.00+E06	1.75E+04	6.12	60.9	37.9	0.61

As can be observed in Table 3.2, the normalized increase in load due to arching compression varies from 0.49 to 1.89. A closer look at the results further shows that the maximum normalized increase in load occurred in specimen with minimum bottom reinforcement ratio. It should however be mentioned that the baseline for normalization herein refers to the bending capacity of the beam which depends on the reinforcement ratio and yield strength. For specimens in group A, the L/d ratio was 4.08 and as can be observed in Table 3.2, the effect of arching is more pronounced in RC beams with shorter L/d ratio which leads to higher increase in normalized load compared to longer L/d ratio.

3.2.2 Test by Yu & Tan (2013a) and Yu & Tan (2013b)

The authors conducted two different studies on the compressive arching action capacity on RC sub-assemblies using the same beam geometry and test setup, hence the details of the two studies are discussed together in this section.

Yu & Tan (2013a) investigated the effect of seismic and non-seismic detailing on the behaviour of RC beam column sub-assemblage bridging over a removed column. The prototype frame was part of a 5-storey commercial building designed in accordance with the ACI 318-05 code. One-half scaled specimen of the prototype frame was used for the study. In the tested beam, clear span between the outer columns was 5750mm, depth and width of the beam was 250mm and 150mm respectively. Enlarged column stubs of 400mm wide by 450mm deep were used at the end to simulate continuity. A total of two (2) specimens were tested. In the seismic detailed specimen, the bottom reinforcement was lapped at some distance away from the middle column while in the non-seismic detailing it was lapped within the middle column location.

In a follow-up study, Yu & Tan (2013b) investigated the effect of reinforcement ratio and span depth ratio on the compressive arching behaviour of RC subassemblies. A total of six (6) specimens with varying reinforcement and span depth ratios were considered. The same test geometry and set up used in Yu & Tan (2013a) was adopted in the study. The geometric detail of the tested specimens is shown in Figure 3.5 while the reinforcement details in the two tests are shown in Table 3.3.

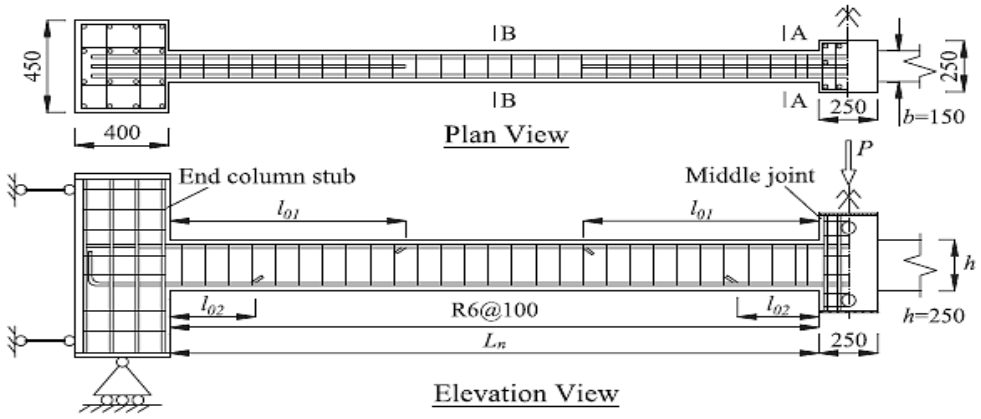

Figure 3.5: Reinforcement detail of sub-assemblage (Yu & Tan 2013b)

Table 3.3: Geometric and reinforcement detail of test specimens (Yu & Tan 2013a; Yu & Tan 2013b)

ID	Reference	L_n (mm)	L_n/h	Longitudinal reinforcement details			
				Section A-A		Section B-B	
				Top	Bottom	top	Bottom
S1	(Yu & Tan 2013a)	2750	11	1T13+2T10 (0.9%)	2T10 (0.49%)	2T10 (0.49%)	2T10 (0.49%)
S2		2750	11	3T10 (0.73%)	2T10 (0.49%)	2T10 (0.49%)	2T10 (0.49%)
S3	(Yu & Tan 2013c)	2750	11	3T13 (1.24%)	2T10 (0.49%)	2T13 (0.82%)	2T10+1T13 (0.9%)
S4		2750	11	3T13 (1.24%)	2T13 (0.82%)	2T13 (0.82%)	2T13 (0.82%)
S5		2750	11	3T13 (1.24%)	3T13 (1.24%)	2T13 (0.82%)	3T13 (1.24%)
S6		2750	11	3T16 (1.87%)	2T13 (0.82%)	2T16 (1.25%)	2T13 (0.82%)
S7		2150	8.6	3T13 (1.24%)	2T13 (0.82%)	2T13 (0.82%)	2T13 (0.82%)
S8		1550	6.2	3T13 (1.24%)	2T13 (0.82%)	2T13 (0.82%)	2T13 (0.82%)

3.2.2.1 Boundary condition

In the test, axial restraint was provided by reaction frame at one end of the specimen and a reaction wall at the other end as shown in Figure 3.6. The vertical support was provided by pin connection placed on top of three rollers. The use of the roller support system was to ensure vertical and horizontal reactions were obtained independent of each other. The reactions were measured with load cells and horizontal movement of the end connection were measured with linear variable displacement transducers (LVDT). The recorded horizontal movement and reaction on either side of the assemblies were used to calculate the restrain stiffness for the assemblies. Due to imperfection, reaction and movement at the two ends were different. The equivalent stiffness reported in Table 3.4 was calculated using the restrained stiffness at both ends (Yu 2012).

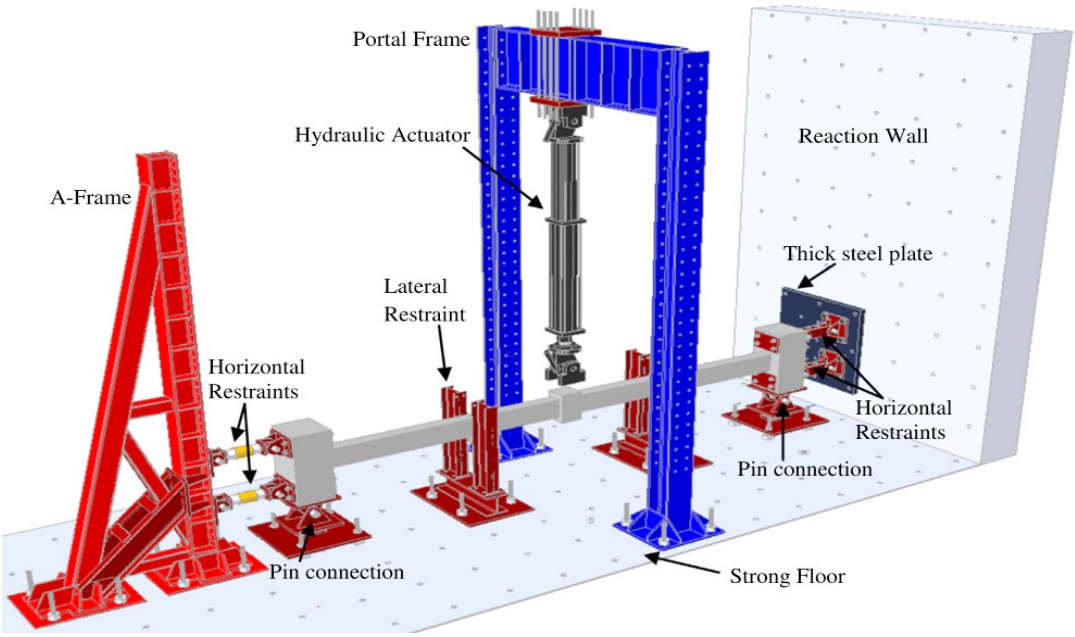

Figure 3.6: Reinforcement detail of sub-assemblage (Yu & Tan 2013a)

3.2.2.2 Span depth ratio

Three span depth ratios including 11, 8.6 and 6.2 were considered in the study. This test covered a much wider range of L/d ratio compared to test by Su et al. (2009). The span to depth ratio of 11 can be a representative of larger span depth which may be commonly found in practice.

3.2.2.3 Reinforcement ratio and rebar strength

A much wider range of reinforcement ratio was considered in this study compared to Su et al. (2009). The reinforcement at the support section ranged from 0.9 to 1.87% and 0.49 to 1.24% for top and bottom section respectively. Similarly, at the middle section of each beam span, the reinforcement ranged from 0.49 to 1.25% and 0.49 to 1.24% respectively. Thus, the specimen tested in this study can be said to range from lightly reinforced to heavily reinforced section with reinforcement ratio of 1.87%. As shown in Table 3.3, different reinforcement sizes were used for the longitudinal reinforcement. The yield strengths were 511, 494 and 513MPa respectively for 10, 13 and 16mm diameter reinforcements respectively.

3.2.2.4 Concrete strength

Similar to the test Su et al. (2009), concrete strength was not a variable, thus its effect on the compressive arching action was not investigated. In the first test, the concrete compressive strength was 31.24MPa in the two specimens tested while in the second test, one batch of concrete with concrete strength of 38.15MPa was used in all six (6) specimens.

3.2.2.5 Damage pattern

The authors noted that damage pattern of the specimens S3 to S7 with L/d ratio of 11 was the same and as such only damage pattern of specimen S5 was studied in detail. Figure 3.7 shows the damage pattern of specimen S5 at the maximum compressive arching action capacity. Concrete crushing occurred at the middle joint interface and cracks with approximately equal spacing also occurred near the middle and end column stubs.

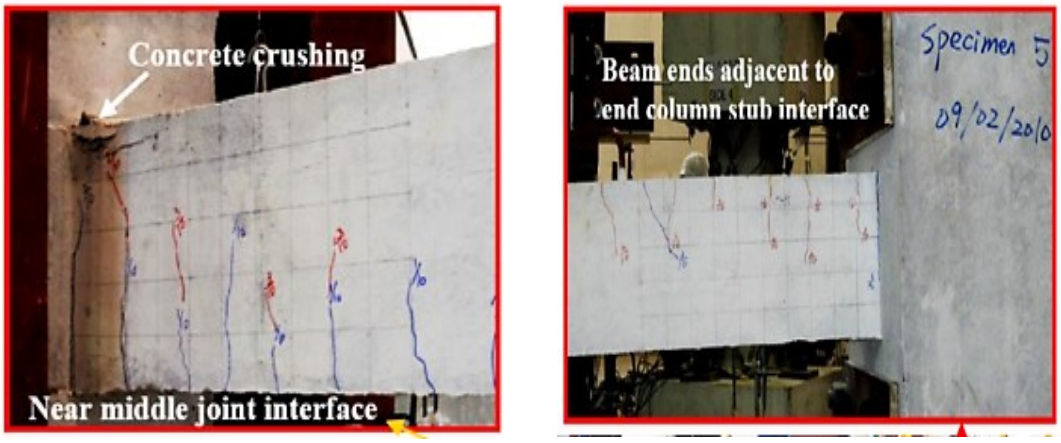

(a) near middle joint interface (b) near end joint interface

Figure 3.7: Damage pattern of specimen S5 at compressive arching capacity with middle joint displacement of 75mm (Yu & Tan 2013b)

Damage pattern of specimen S8 was marked by severe crushing of concrete near the middle and end joint interface due to the reduced L/d ratio 6.2. Figure 3.8 shows damage pattern of specimen S8 with more severe crushing compared to specimen S5.

A close look at Figure 3.7 and 3.8 further shows that crushing of concrete only occurred close to the middle joint interface at a displacement of 75mm in specimen S5 with L/d ratio of 11 whereas in specimen S8 with L/d ratio of 6.2, concrete crushing occurred at both end and middle joint interface at a displacement of 75mm. From these observations, it could be argued that the probability of crushing of concrete during arching action increases as the L/d ratio decreases.

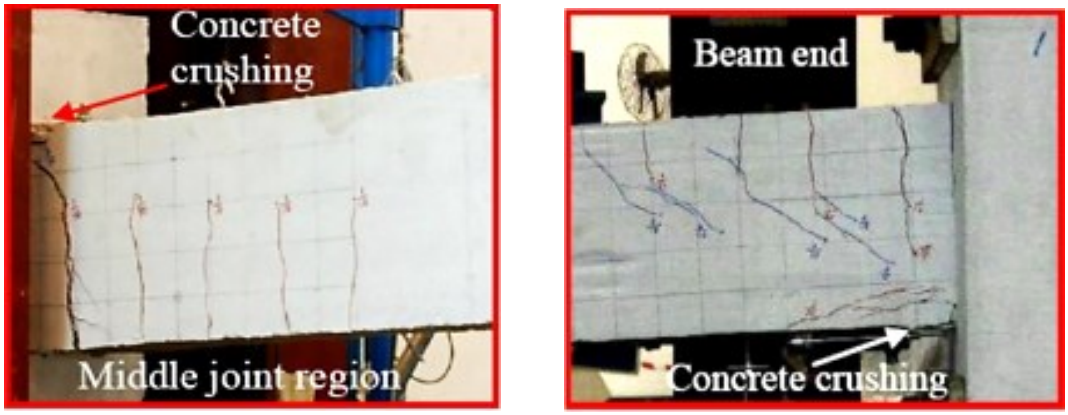

(a) near middle joint interface (b) near end joint interface

Figure 3.8: Damage pattern of specimen S8 at compressive arching capacity with middle joint displacement of 75mm (Yu & Tan 2013b)

3.2.2.6 Maximum compressive arching action capacities

Following the approach explained in Section 3.2, the normalized arching effect is calculated and presented in Table 3.4. The flexural capacities for the specimens are recalculated for each specimen as shown in the table.

The range of normalized increased in load is 0.13 to 0.44 compared to the wider range observed in test by Su et al. (2009). The reason for this low normalized increase in load capcity could be attributed in part to the smaller axial restraint compared to the axial retraint in test by Su et al. (2009). The detail study on these variation will be investigated in detail in Section 3.3.

Table 3.4: Compressive arching and recalculated flexural capacities of specimens tested by (Yu **& Tan 2013c)**

Specimen ID	Axial stiffness (KN/m)	Rotational stiffness (KNm/rad)	L/d ratio	P_a (KN)	P_f (KN)	$\Delta\omega_N = \frac{P_a - P_f}{P_f}$
S1	1.06E+05	1.0E+04	11	41.64	33.2	0.25
S2	1.06+E05	1.0E+04	11	38.38	29.68	0.32
S3	4.29+E05	3.0E+04	11	54.47	40.43	0.33
S4	4.29+E05	3.0E+04	11	63.22	47.36	0.32
S5	4.29+E05	3.0E+04	11	70.33	56.29	0.24
S6	4.29+E05	3.0E+04	11	70.33	61.57	0.13
S7	4.29+E05	3.0E+04	8.6	82.82	60.58	0.36
S8	4.29+E05	3.0E+04	6.2	121.34	84.03	0.44

3.2.3 Test by Vesali *et al*. (2013) and Vali *et al.* (2015)

Vesali et al. (2013) investigated the effect of longitudinal reinforcement ratio and stirrup spacing on RC beams using six scaled reinforced concrete beam assemblages. The sub assemblages consisted of 2 bay beam and 3 columns stubs with enlarged end column stubs similar to the test by Yu & Tan (2013b). The geometry and reinforcement arrangement of the tested beams is shown in Figure 3.9.

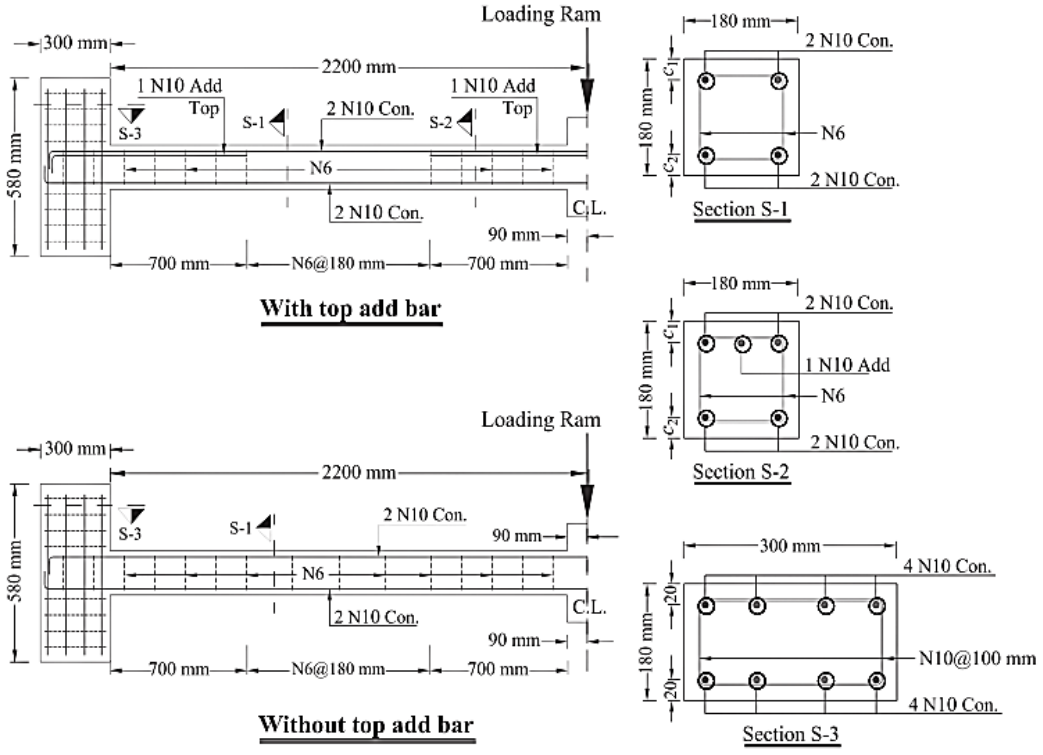

Figure 3.9: Geometric and reinforcement arrangement of the test specimens (Vesali et al. 2013)

In a follow up study by Vali et al. (2015), the effect of concrete compressive strength on compressive arching capacity of RC subassemblies was investigated. The same geometry and test set-up used in the previous test was adopted in the study.

3.2.3.1 Boundary condition

In the test, axial and rotational restraint were provided by two steel bollards. The end columns were anchored to these bollards boards using a 20mm diameter Mac alloy. The bollard board was in turn bolted to a strong floor using a 36mm diameter Mac alloy bar as shown in Figure 3.10. The bottom of the beam was supported by a C-channel section which was bolted to the vertical bollard board at each end of the beam-column assembly.

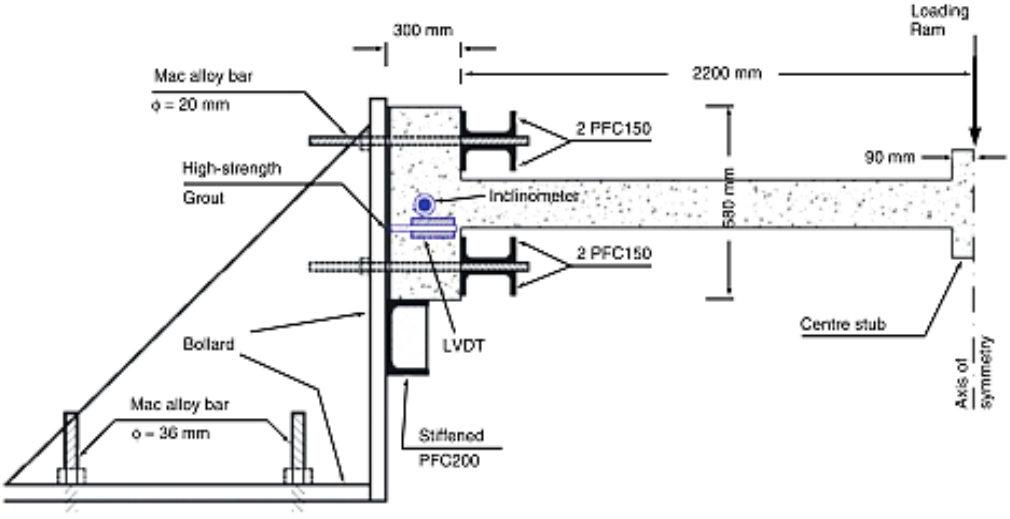

Figure 3.10: Anchoring of subassembly to test set up (Vali et al. 2015)

3.2.3.2 Span depth ratio

The span-to-depth ratio in the two separate studies were kept the same with L/d ratio of 11.72. This is almost the same L/d ratio used in the study by Yu & Tan (2013b).

3.2.3.3 Reinforcement ratio and rebar strength

In the study by Vesali *et al.* (2013) six specimens were tested. In three (3) of these specimens, reinforcement consisted of 3no. Φ10mm (0.87%) and 2no. Φ10mm (0.58%) at the top and bottom sides of the section of the beam. The remaining three (3) specimens had 2no. Φ10mm at top and bottom section. The essence of one (1) additional top reinforcement at the support was to investigate if it has any effect on the compressive arching behaviour of the subassemblies. The transverse reinforcement at critical section (near the middle and end beam-column interface) consisted of Φ6mm at 60, 120 and 180mm spacing for the different specimens. The essence of the variation in the spacing of transverse reinforcement was to study if it has effect on the compressive arching behaviour of the beam.

In Vali *et al*. (2015), six specimens were also tested and the reinforcement ratio was similar to that used in Vesali *et al.* (2013). The results of the test by Vesali *et al.* (2013)

showed that transverse reinforcement did not affect the compressive arching behaviour and hence transverse reinforcement was provided by Φ6mm at 180mm spacing. The nominal yield strength for longitudinal and transverse reinforcements was 500 and 250MPa respectively.

3.2.3.4 Concrete strength

Concrete compressive strength of specimens in the first study (Vesali et al. 2013) varied between 26-30.5MPa. This slight variation in concrete strength was due to the use of different batch of concrete in casting the specimens. In the second test (Vali et al. 2015), the objective was to investigate the effect of concrete strength on compressive arching behaviour. For this reason, a wider range of concrete strength was considered. The specimens had concrete compressive strength of 18, 48 and 68MPa, respectively.

3.2.3.5 Damage pattern

The damage pattern around the maximum arching action was not shown in the literature. The authors only showed the damage pattern at the rupture of bottom which was almost the end of effective arching stage. According to the authors, the crushing of concrete concentrated at about 150mm at the end and middle section of the beam (see Figure 3.11). This corresponds to about 0.85d (d being the depth of the cross-section).

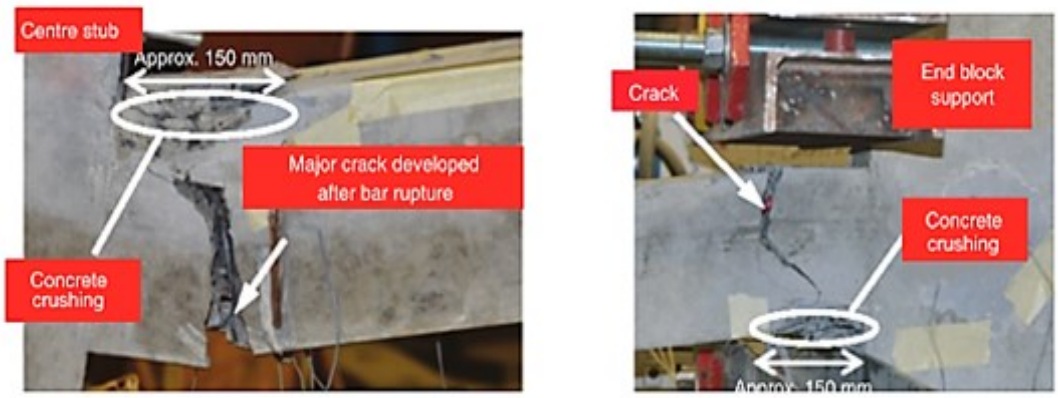

(a) near middle joint interface (b) near end joint interface

Figure 3.11: Damage pattern of the tested specimen (Vali et al. 2015)

3.2.3.6 Maximum compressive arching capacities

Based on the reported test data, the normalized increase in load due to arching and the flexural capacities are recalculated and the results is presented in Table 3.5 for the twelve specimens considered in the two studies. It can be observed that the normalized increase in load range from 0.36 to 0.81. Comparing the result in this study with that in Yu and Tan (2013b) which is about the same L/d ratios, it can be observed that the normalized increase in load is larger in the specimens in this study than in Yu and Tan (2013b). One reason for this may be because of the difference in the axial restraint between the two studies. Although the axial restraint in the present study was not recorded, a close look at the test set up shows that the axial restraint is closer to rigid restraint. Further analysis of these series of results together with the results from other test programmes will be discussed later in Section 3.

Table 3.5: Compressive arching and recalculated flexural capacities of specimens tested by Vesali et al. (2013) and Vali et al. (2015)

Specimen ID	Reference	P_a (KN)	P_f (KN)	$\Delta\omega_N = \frac{P_a - P_f}{P_f}$
V1	(Vali *et al.*, 2013)	40.5	22.8	0.78
V2		35.7	24.5	0.46
V3		41.4	25.0	0.66
V4		40.1	29.4	0.36
V5		41.6	26.5	0.57
V6		39.4	27.0	0.46
V1*	(Vali et al. 2015)	51.3	28.4	0.81
V2*		42.5	24.6	0.73
V3*		47.4	27.5	0.72
V4*		38.5	22.7	0.68
V5*		33.2	24.0	0.38
V6*		28.3	18.9	0.50

3.2.4 Test by Sadek et al. (2011)

This test programme investigated the effect of seismic design and detailing on the progressive collapse of two reinforced concrete sub-assemblies. One of the tested beam was designed for Seismic Design Category (SDC) C and the other was designed for Seismic Design Category (SDC) D. In the former, Intermediate Moment Frame (IMF) was used to resist lateral loads while in the latter, Special Moment Frame (SMF) was used. Each of the specimens consisted of two beams and two end columns with a short column stub at the middle. The geometry and reinforcement arrangement for the two tests are shown in Figure 3.12.

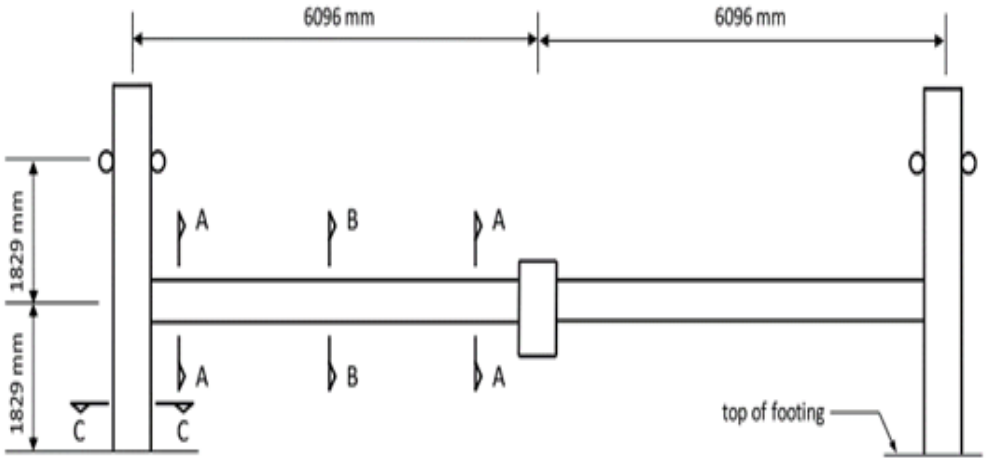

(a) Evelavtion view of the test specimen

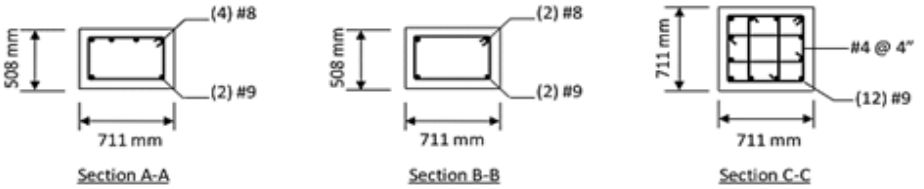

(b) section details for IMF specimen

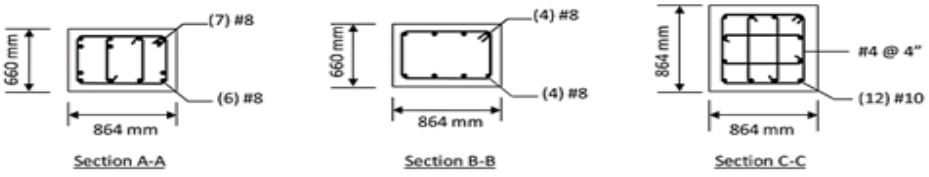

(c) section details for SMF specimen

Figure 3.12: Geometric and reinforcement details of the test assemblies

3.2.4.1 Boundary condition

The end columns were monolithically cast to enlarged concrete footings which were further anchored to a strong test floor to avoid any rotation and translation. The top sides of the columns were restrained from horizontal movement using two rollers, one on either side of the column. Since the tested beam assembly was supposedly part of a larger frame, the beam longitudinal reinforcements at the end of the column were

anchored using a treaded mechanical device to mimic continuity of reinforcement. The test setup for the experiment is shown in Figure 3.13.

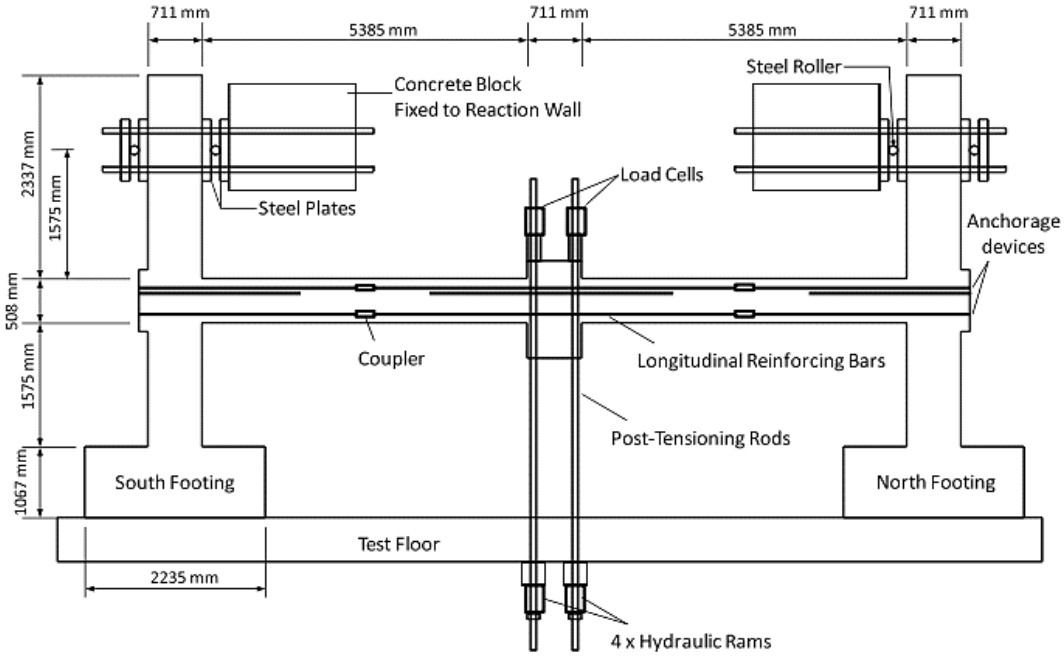

Figure 3.13: Test set up (Sadek et al. 2011)

3.2.4.2 Span depth ratio

The span depth ratio for the IMF and SMF specimens were 10.6 and 8 respectively. These span ratios are within the range used in practice and can be classified as moderate to large spans. It should however be noted that unlike in the other tests where the depth was larger than the width of the beam, herein the beam depth was smaller than the width of the beam.

3.2.4.3 Reinforcement ratio and rebar strength

The reinforcement at all the support sections for IMF specimen as shown in Figure 11 consisted of 4no. Φ25mm (0.65%) top bars and 2no. Φ29mm (0.43%) bottom bars. For the SMF specimen, reinforcement at the support were 7no. Φ25mm (0.69%) and 6no Φ25mm (0.59%) for top and bottom section respectively. The percentage of reinforcement is within the range used in practice.

The yield strength of 25 and 29mm diameter rebar was 476 and 462MPa respectively and that of transverse reinforcement was 524MPa.

3.2.4.4 Concrete strength

Concrete strength was not a variable in the test, hence the concrete strength for the IMF and SMF specimens were 32.4 and 35.9MPa respectively. The concrete strengths for the two tests.

3.2.4.5 Maximum compressive arching action capacities

The normalized increase in load due to arching and the calculated flexural capacities for the two specimens are shown in Table 3.6. It can be seen that increase in load due to arching was very minimal in the test specimens with a maximum normalized increase ratio of only 0.36. However, as a general trend, it is seen that the normalized increase in load capacity was lower in specimen IMF which has a larger L/d ratio compared to specimen SMF.

Table 3.6: Compressive arching and recalculated flexural capacities of specimens tested by Sadek et al. (2011)

Specimen ID	L/d ratio	P_a (KN)	P_f (KN)	$\Delta\omega_N = \frac{P_a - P_f}{P_f}$
IMF	10.6	296	248	0.19
SMF	8.0	900	664	0.36

3.3 Critical analysis of all the experimental results

In the preceding sections, each of the tests concerning compressive arching action has been scrutinised and discussed in detail. The examination clearly shows that the tests conducted by different authors covered a wide range of variables including the boundary conditions, geometric and reinforcement details. In this section, the results of all individual test specimens are analysed together to further shed more light on the general trend of the normalized increase in load due to arching compression and the effects of key parameters, namely the span-to-depth ratio (L/d), condition of the end

support (axial stiffness of the support), reinforcement ratio and concrete compressive strength on compressive arching capacity.

As the arching effect is directly associated with the depth of the beam, the L/d ratio is chosen as a primary parameter affecting the arching effect. The L/d ratio has been generally recognised as a key factor from individual experimental studies. For example Su et al. (2009) tested a set of beam specimens with a span-to-depth ratio (L/d) of 4, 6.58 and 9.12. Yu & Tan (2013) considered L/d ratios of 6.2, 8.6 and 11. Their results both showed that compression arching capacity decreased with increase in L/d ratio as general trend. However, due to the limited cases covered in each individual study, a systematic examination in a more quantitative manner has not been carried out.

In this section, the variation of the arching capacity with different L/d ratio is scrutinised in detail in an attempt to establish more clearly the specific effect of the L/d ratios, as well as the effects that may be attributed to other parameters mentioned earlier. On the basis of the analysis of the experimental results, a simplified theoretical model is put forward to facilitate the interpretation of the influences of the key parameter, especially the L/d ratio, on the arching action. Finally, through calibration with the experimental data, a semi-empirical model is proposed for the prediction of the arching effect in RC beam assemblies.

Without discriminating the differences in the other parameters first, Figure 3.14 shows the plot of normalized increase in strength due to arching against L/d ratio in all the specimens considered herein.

Not surprisingly, it can be observed that for the same L/d ratio there exist a marked difference in the enhancement factor, due apparently to variations in some other conditions as will be discussed later. For instance, with L/d ratio of 4 the highest enhancement factor is 1.63 while the lowest is 0.88. The same can be said about the specimen with L/d ratio of 11 and 12.

Nevertheless, the general trend of decrease in the enhancement factor as L/d increases can be seen up to an L/d ratio of 11 where the enhancement factor is approaching zero which indicate that arching action tends to become negligible. However, for the

particular series of tests with L/d ratio of 12, the enhancement factor appears to be higher than that for the lower L/d ratio of 11, and some data points are even above those for L/d ratio of 6 and 8.

As mentioned earlier the above differences and the discrepancy in the case of L/d ratio equal to 12 may be the results of several parameters, but let us take a look of the crucial axial support condition, or more precisely the magnitude of the axial restraint provided first. For the particular L/d ratio of 12 group, although the axial stiffness of the end support was not measured during the test, taking a close look at the set up for these tests shown in sub-section 3.2.3 (Vesali et al., 2013; Vali et al., 2015), it could be argued that the axial restraint in the test is very close to the upper bound region and can therefore be classified as rigid. It should also be pointed out that some of the test specimens had a higher concrete compressive strength (e.g. 48 and 67MPa) as compared to the rest of the test data in the current collection where the concrete strength was around 30MPa. As shown in Table 3.5 there was a slight increase in the normalised net increase in load capacity as the concrete strength increases.

Considering all L/d ratio except L/d ratio of 12 (for the time being), a trend line can be drawn through the data points as shown in Figure 3.15. It should however be noted that the trendline drawn in Figure 3.15 is just to show to trend of variation in normalized increase in load as the L/d ratio increases but it is not in the simplified empirical formulation to be presented later.

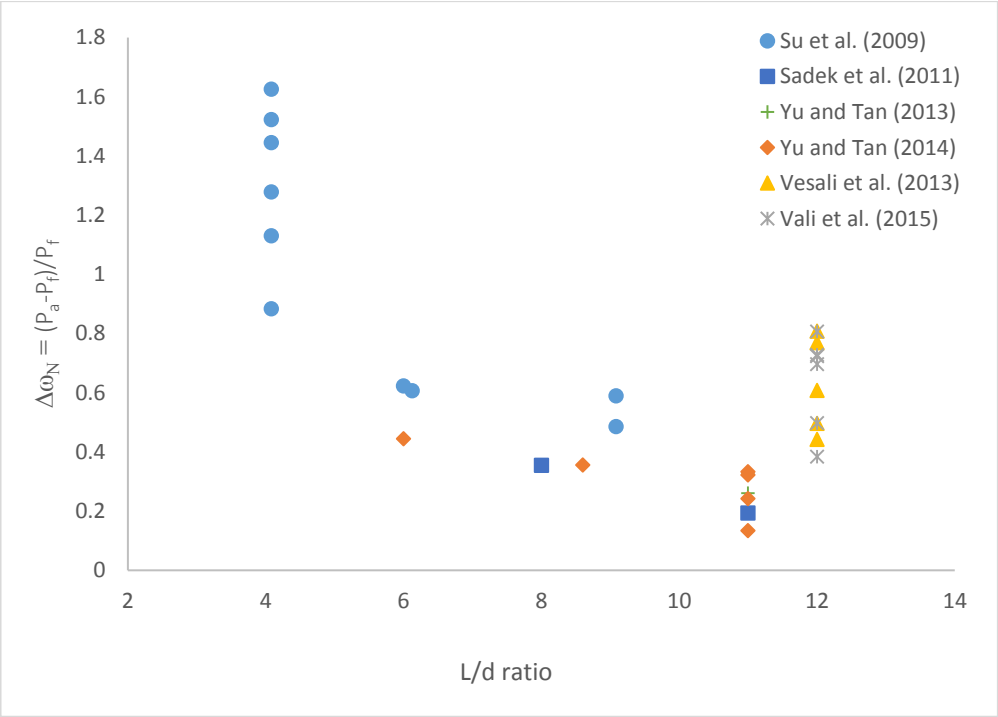

Figure 3.14: Variation of normalized increase in load due to arching with span depth ratio for all specimens

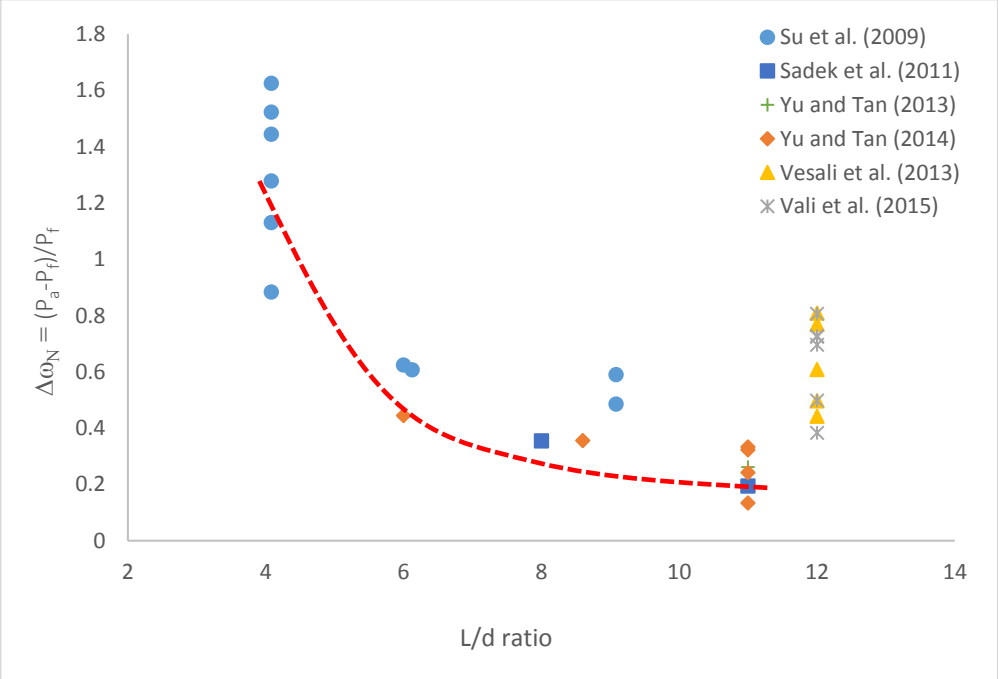

Figure 3.15: Trend line through the data points

It should be mentioned that for some L/d ratios mentioned above such as 4, same boundary condition was used for each case, only the concrete strength or reinforcement ratio was varied. This implies that even for a fixed L/d ratio and axial restrained stiffness, the normalized increase in arching can vary a lot with the variation caused by the reinforcement ratio or concrete compressive strength, keeping in mind of inherent uncertainties in a reinforced concrete specimen.

To investigate the effect of parameters affecting the normalized increase in arching load ($\Delta\omega_N$), each of the following parameters; axial restrained stiffness, reinforcement ratio, span depth ratio and concrete compressive strength will be further looked at in detail. For this purpose, a simplified version of the theoretical model for arching action which takes into consideration the key parameters affecting arching action is derived in the section that follows.

3.4 A simplified formulation for arching action

As shown in the preceding sections, the trend of the maximum compressive arching action varies in test from different researchers, due to the wide range of geometric and material properties considered. This variation is mainly due to the span depth ratio, reinforcement ratio, concrete strength and axial restraint of the supporting end. To have an in depth understanding of the effect of these parameters requires extensive experimental studies which may be costly. On the other hand, the trends of the effect of these parameters on arching capacity may be established more generally with the assistance of a mechanics-based simplified model. To this end, a simplified theoretical model for arching compression is presented in this section. This model follows the approach by Rankin and Long (1997) in that it considers the maximum arching action capacity to be contributed by bending and arching actions, but further considers the contribution from compressive reinforcement which is ignored in Rankin and Long's model.

The scope of the formulation here is confined to the maximum compressive arching capacity. A more comprehensive theoretical model on compressive arching action

which takes into consideration the compounding effect of bending and arching and able to predict the complete load-displacement response within the arching effective regime is presented in Chapter 5.

Consider the rigid body rotation analogy shown in Figure 3.16. Based on compatibility, the relationship between the compression zone depth and middle displacement can be expressed as shown. The definitions of the relevant geometric parameters are also illustrated in the figure.

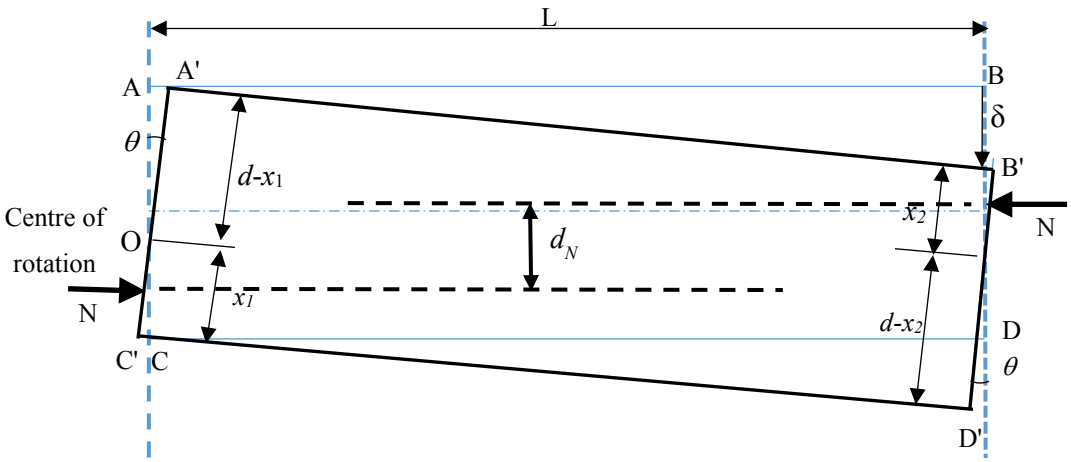

Figure 3.16: "Rigid" body rotation analogy for arching deformations

$$(A'B')^2 = (A'B)^2 + (B'B)^2 \tag{3.4}$$

$$\Rightarrow \quad (L-\theta\times x_2)^2 = [(L-\theta\times(d-x_1)]^2 + \delta^2 \tag{3.5}$$

Expanding Equation (3.5) and ignoring second order increment (θ) terms,

$$-2L\theta x_2 = 2L\theta x_1 - 2L\theta d + \delta^2 \tag{3.6}$$

Noting $\theta = \delta / L$, it can be found that

$$x_1 + x_2 = d - \frac{\delta}{2} \tag{3.7}$$

Assuming the compression depths at the end and middle section are the same,

$$x_1 = x_2 = \frac{d}{2} - \frac{\delta}{4} \tag{3.8}$$

Using a reference block distribution of compressive stress at f_c, the arching compressive force on each side is:

$$N_r = f_c b(\frac{d}{2} - \frac{\delta}{4}) \tag{3.9}$$

Now consider that from the beginning up until maximum arching effect, the concrete compressive stress distribution changes from a "linear" distribution (and magnitude "zero") to the final rectangular block, it is reasonable to introduce a proportioning factor to define the development of the equivalent arching axial force, as:

$$N = N_r(\frac{\varepsilon_c}{\varepsilon_r}) = f_c b(\frac{d}{2} - \frac{\delta}{4})[(\frac{\delta}{L}\lambda)/\varepsilon_r] \tag{3.10}$$

where λ is a compressive strain factor relating the rotation (δ/L) to the concrete compressive stress. ε_c is the current compressive strain (corresponding to δ), ε_r is a reference edge strain marking the attainment of a full plastic compression zone. For detail analysis, coefficient for λ and ε_r may be obtained through FE simulation studies. However, in the present illustration the exact values of these coefficient are not required.

Thus, the additional moment due to arching compression can be written as:

$$\Delta M_{N(rigid)} = N \times d_N = f_c b(\frac{d}{2} - \frac{\delta}{4})(\frac{\delta}{L})(\frac{\lambda}{\varepsilon_r})[d - \delta - \frac{x_1 + x_2}{2}] \tag{3.11}$$

Substituting the expression for x_1 and x_2 into equation (3.11) assuming they are equal gives:

$$\Delta M_{N(rigid)} = f_c b(\frac{d}{2} - \frac{\delta}{4})(\frac{\delta}{L})(\frac{\lambda}{\varepsilon_r})[\frac{d}{2} - \frac{3\delta}{4}] \tag{3.12}$$

$$\Rightarrow \quad \Delta M_{N(rigid)} = f_c b(\frac{\lambda}{\varepsilon_r})(\frac{1}{L})[\frac{d^2}{4}\delta - \frac{d}{2}\delta^2 + \frac{3}{16}\delta^3] \tag{3.13}$$

The "maximum" arching effect may be found by setting the derivative of Equation (3.13) with respect to δ equal to zero:

$$\frac{\partial \Delta M_{N(rigid)}}{\partial \delta} = 0 \tag{3.14}$$

$$[\frac{d^2}{4} - d\delta + \frac{9}{16}\delta^2] = 0 \tag{3.15}$$

Rearranging Equation (3.15) gives:

$$9(\frac{\delta}{d})^2 - 16\frac{\delta}{d} + 4 = 0 \tag{3.16}$$

Solving the quadratic Equation (3.16):

$$\frac{\delta}{d} \cong 0.3 \quad \text{or} \quad \delta \cong 0.3d \tag{3.17}$$

Substituting $\delta \cong 0.3d$ in Equation (3.13), the additional moment due to arching can be obtained as:

$$\Delta M_{N(rigid)} = f_c b(\frac{\lambda}{\varepsilon_r}) \times 0.035 d^2 (\frac{d}{L}) \tag{3.18}$$

With Equation (3.18), the additional moment due to arching can be calculated. However, the above expression was derived considering a rigid body rotation of beam with full axial restraint. More so, the compression reinforcement at the end and middle section of beam was not considered in the formulation. This will lead to the inaccurate prediction of the additional moment due to arching.

Now, consider again the rigid body rotation same as that shown in Figure 3.16 but with flexible axial restraint.

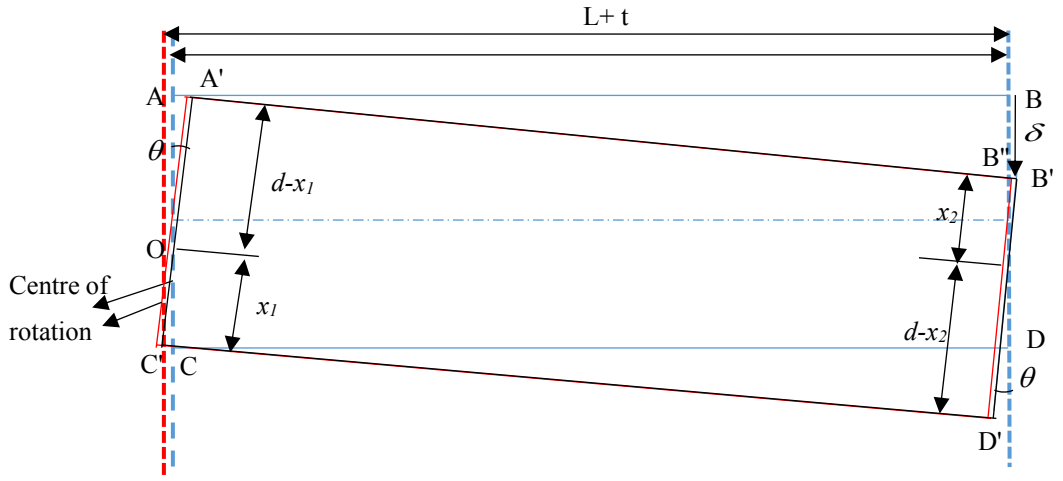

Figure 3.17: "Rigid" body movement of beam with consideration of flexible restraint

Following similar approach as before, the compatibility conditioned yields:

$$(A'B'')^2 = (A'B)^2 + (B''B)^2 \tag{3.19}$$

$$\Rightarrow \quad (L - \theta \times x_2)^2 = [(L + t) - \theta \times (d - x_1)]^2 + \delta^2 \tag{3.20}$$

Expanding, ignoring second order increment (θ) terms

$$-2L\theta x_2 = 2L\theta x_1 - 2L\theta d + 2Lt + \delta^2 \tag{3.21}$$

Noting that $\theta = \delta / L$ and $t = N / K_a$

$$x_1 + x_2 = d - \frac{\delta}{2} - \frac{N}{K_a} \cdot \frac{L}{\delta} \tag{3.22}$$

Comparing Equations (3.7) and (3.22) it is seen that the presence of flexible axial restraint stiffness manifest as a reduction in the compression zone depth. For very large value of K_a, Equation (3.22) reduces to Equation (3.7).

Now, noting that part of the compression zone depth has been used up by bending, the compression zone depths for arching alone at the end and middle section can be expressed as:

$$x_1^{'} + x_2^{'} = d - \frac{\delta}{2} - \frac{N}{K_a} \cdot \frac{L}{\delta} - x_{bp1} - x_{bp2} \tag{3.23}$$

where $x_1^{'}$ and $x_2^{'}$ are the depth attributed to arching at the end and middle section and, x_{bp1} and x_{bp2} are the compression zone due to bending at end and middle section which is simplified as:

$$x_{bp1} = \frac{f_y A_{st'}}{0.85 f_c b} \tag{3.24}$$

$$x_{bp2} = \frac{f_y A_{st}}{0.85 f_c b} \tag{3.25}$$

Equilibrium of forces in the arching effective regime assuming compression rebar yields may be expressed as:

$$0.85 f_c b x_1^{'} + A_{sc'} f_y = 0.85 f_c b x_2^{'} + A_{sc} f_y \tag{3.26}$$

Substituting the expression for N (using end section) into Equation (3.23) and simplifying further yields:

$$x_1^{'}(1 + \frac{0.85 f_c b L}{K_a \delta}) + x_2^{'} = d - \frac{\delta}{2} - \frac{A_{sc'} f_y L}{K_a \delta} - x_{bp1} - x_{bp2} \tag{3.27}$$

The depth of arching compression $x_1^{'}$ and $x_2^{'}$ can be determined by solving Equations (3.26) and (3.27) to give:

$$x_1^{'} = \frac{d - \frac{\delta}{2} - \frac{A_{sc'} f_y L}{K_a \delta} - x_{bp1} - x_{bp2} + \frac{f_y (A_{sc} - A_{sc}^{'})}{0.85 f_c b}}{2 + \frac{0.85 f_c b L}{K_a \delta}} \tag{3.28}$$

$$x_2^{'} = \frac{d - \frac{\delta}{2} - \frac{A_{sc'} f_y L}{K_a \delta} - x_{bp1} - x_{bp2} + \frac{f_y (A_{sc} - A_{sc}^{'})}{0.85 f_c b}}{2 + \frac{0.85 f_c b L}{K_a \delta}} - \frac{f_y (A_{sc} - A_{sc}^{'})}{0.85 f_c b} \tag{3.29}$$

Taking the arching compression zone at the end section as reference point, the additional moment due to arching may be calculated as:

$$\Delta M_N = [0.85 f_c b x_2^{'}][d - \delta - x_{bp1} - x_{bp2} - \frac{x_1^{'} + x_2^{'}}{2}] + A_{sc} f_y (d - \delta - a - x_{bp1} - 0.5 x_1^{'}) + A_{sc}^{'} f_y (0.5 x_1^{'} + x_{bp1} - a) \quad (3.30)$$

The additional moment due to arching can be determined using Equation (3.30). It should however be noted that the expression for additional moment is a function of middle column displacement (δ), thus the vertical displacement corresponding to the maximum arching compression needs to be determined. One way of doing this is to differentiate Equation (3.30) with respect to the displacement (δ) and solve the differential to determine the displacement which corresponds to the maximum arching moment. Due to the complexity of the expression, this approach may not be visible. Since only the maximum additional moment is required in the present study, the displacement can be incremented within a given range to obtain the additional moment.

From experimental studies on RC assemblies with axial restraint, the displacement corresponding to maximum arching capacity varies between 0.16 and 0.46d. Thus, using Equation (3.30), the displacement (δ) can be varied within the range of 0.5d and the maximum additional moment due to arching is extracted from the incremental analysis.

After determining the maximum moment based on the approach explained above, the additional load due to arching compression is then given as:

$$\Delta P_N = \frac{\Delta M_N}{L} \quad (3.31)$$

For the determination of bending capacity, herein the sectional bending moment strength is approximated based on standard RC section analysis as:

$$M_b = f_y A_s (d - a - \frac{f_y A_s}{1.7 f_c b}) \quad (3.32)$$

For a general case with unsymmetrical reinforcement arrangement at end and middle sections and considering one-half of beam, pure bending capacity can be calculated as:

$$P_b = \frac{(M_{be} + M_{bm})}{L} \tag{3.33}$$

The ratio between the additional load capacity due to arching and the pure bending load capacity can therefore be expressed as:

$$\Delta\omega_N = \frac{\Delta P_N}{P_b} \tag{3.34}$$

The flow chart showing the implementation of above procedure is shown in Figure 3.18.

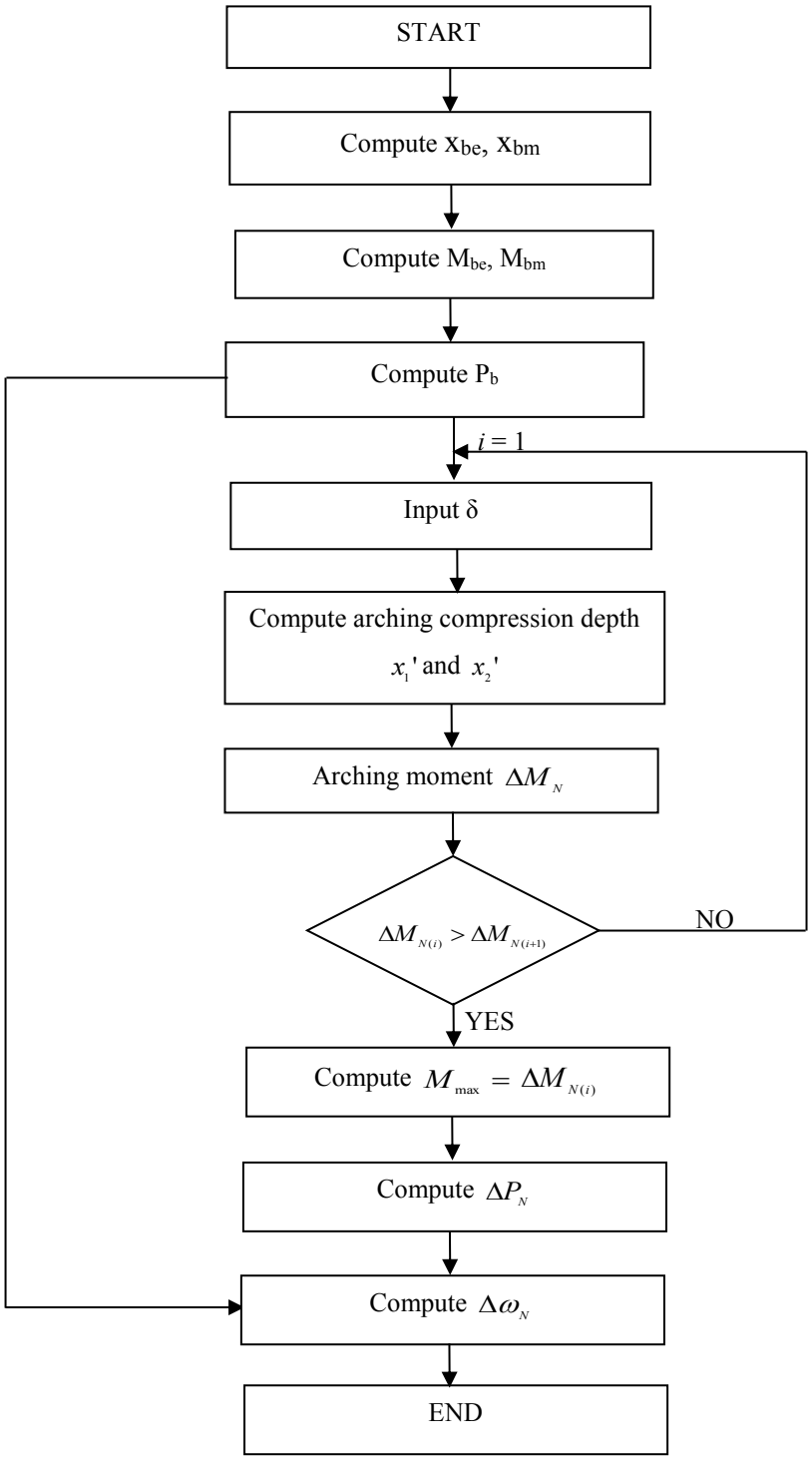

Figure 3.18: Flow chart for the incremental procedure

3.5 Effect of parameters affecting relative increase in load due to compressive arching action

With the simplified formulation presented in Section 3.4, the effect of parameters affecting relative increase in load due to compressive arching action can be looked at in a more rigorous manner. In this section, the effect of each of the parameters on compressive arching action as observed from the existing experiments is analysed and then followed by the detailed examination using the developed simplified model.

3.5.1 Effect of axial restraint on compressive arching action capacity

Using the simplified formulation in Section 3.4 and experimental data in Section 3.2, the effect of axial restraint on the normalized increase in load capacity is further investigated in more detail. To enable a consistent comparison regarding the influence of boundary condition on this normalized increase from different tests, it is necessary to express the axial constraint by a common factor. One obvious way of achieving this is to normalize the axial restraint stiffness by the axial stiffness of the beam, as also considered in Yu and Tan (2014). Herein we shall write the normalized axial support stiffness in the following expression:

$$\alpha_K = \frac{K_a}{K_s} \tag{3.35}$$

where K_a is the axial stiffness of the end support and K_s is the axial stiffness of the beam which is defined in this study with respect to the axial stiffness of a single bay beam (to be corresponding to each of the two end supports considering symmetry) as:

$$K_s = \frac{EA}{L} \tag{3.36}$$

where E is the elastic modulus of concrete, A is the cross-sectional area of the beam and L is the length of one-bay beam. For experimental tests where Young's Modulus (E) is not stated, it is assumed to be $4730\sqrt{f_c}$ according to ACI 318 code, where f_c is the uniaxial compressive strength of concrete in MPa. With this simplification, the

different boundary conditions can be classified as strong (rigid) moderate or weak axial restraint, as will be elaborated in detail later.

It should be noted that in some of the tests, the axial restraint stiffness of the support system was not stated. For instance, in the tests by Vesali et al. (2013) and Vali et al. (2015) the axial stiffness was not mentioned. However, looking at the test set up previously shown in Section 3.2 it could be argued that such support system provided a high axial restraint to the specimen hence support system is considered as strong axial restraint. On the other hand in the test by Sadek et al. (2011), the test set up was not enough rigid, hence axial movement of the beam-end could not be prevented thus such restraint can be classified as weak.

Based on the above explanation, the axial restraint stiffness coefficients for all the specimens are calculated and presented in Table 3.7. For comparison purposes, the axial restraint stiffness coefficient calculated in Yu and Tan (2014) is also presented. Specimens for which the axial restraint stiffness were not provided such as in Vesali et al. (2013) and Vali et al. (2015) are assigned a high axial stiffness of 1.0×10^6 KN/m because the support system is close to rigid. A marked variation in the axial stiffness can be observed in this Figure with stiffness ratio ranging between 0.3 and 3.5.

Table 3.7: Comparison of axial restraint stiffness from experimental data set

Spec. ID	Reference	Axial stiffness (KN/m)	L_t (mm)	L (mm)	E_c (MPa)	A (mm^2)	$\gamma_a = \frac{K_a}{(E_c A)/L_t}$	$\alpha_a = \frac{K_a}{(E_c A)/L}$
A1	(Su et al. 2009)	1.00E+06	2700	1225	22857	45000	2.50	1.19
A2			2700	1225	23897	45000	2.39	1.14
A3			2700	1225	25135	45000	2.27	1.08
A4			2700	1225	21581	45000	2.65	1.26
A5			2700	1225	23165	45000	2.46	1.18
A6			2700	1225	24065	45000	2.37	1.13
B1			4200	1975	19407	45000	4.58	2.26
B2			5700	2725	19769	45000	6.10	3.06
B3			5700	2725	20670	45000	5.83	2.93
C1			2700	1225	17943	20000	7.16	3.41
S1	(Yu & Tan 2013a)	1.06E+05	5750	2750	25152	37500	0.62	0.31
S2			5750	2750	25152	37500	0.62	0.31
S3	(Yu & Tan 2013c)	4.29E+05	5750	2750	27813	37500	2.25	1.13
S4			5750	2750	27813	37500	2.25	1.13
S5			5750	2750	27813	37500	2.25	1.13
S6			5750	2750	27813	37500	2.25	1.13
S7			4550	2150	27813	37500	1.78	0.88
S8			3350	1550	27813	37500	1.31	0.64
V1	(Vesali et al. 2013)	1.00E+06	4400	2110	24852	32400	5.2	2.49
V2			4400	2110	23383	32400	5.53	2.65
V3			4400	2110	24648	32400	5.24	2.51
V4			4400	2110	22946	32400	5.63	2.70
V5			4400	2110	24441	32400	5.29	2.53
V6			4400	2110	24648	32400	5.24	2.51
V1*	(Vali et al. 2015)	1.00E+06	4400	2110	36834	32400	3.51	1.68
V2*			4400	2110	36834	32400	3.51	1.68
V3*			4400	2110	31177	32400	4.14	1.99
V4*			4400	2110	31177	32400	4.14	1.99
V5*			4400	2110	19091	32400	6.77	3.25
V6*			4400	2110	19091	32400	6.77	3.25

To further investigate the effect of axial restraint herein the simplified theoretical formulation derived in the Section 3.4 is used. The beam geometry for the study is 150 by 300mm with the original span length (half of the test double-span specimen) of 1.2m giving L/d ratio of 4. Reinforcement consisted of 2 no. Φ12mm top and bottom. Concrete compressive strength is 30MPa and yield strength of reinforcement is 500MPa. The only variable is the axial restraint stiffness (K_a) which is varied between 5000 to 10^{10} KN/m representing very small to very large axial restraint. For each axial restraint stiffness (K_a) considered, the normalized axial support stiffness (α_K) is calculated according to Equation (3.37) the corresponding normalized increase in load capacity is determined.

The results of the analysis are presented in Table 3.8, and the relationship between the normalized increased in load due to arching and the normalized axial stiffness is shown in Figure 3.20. The rate of increase in load decreases as the axial stiffness increases. This is similar to the findings by Yu and Tan (2014).

Table 3.8: Effect of axial stiffness coefficient on the normalized increase in load due to arching

K_a (KN/m)	K_s (KN/m)	α_K	$\Delta\omega_N$
5000	971520	0.0051	0.16
10000	971520	0.0103	0.32
20000	971520	0.0206	0.51
50000	971520	0.0515	0.77
100000	971520	0.1029	0.95
200000	971520	0.2059	1.08
500000	971520	0.5147	1.22
10000000	971520	1.0293	1.28
20000000	971520	2.0586	1.3
50000000	971520	5.1466	1.36
100000000	971520	10.2931	1.4
1000000000	971520	102.9315	1.4

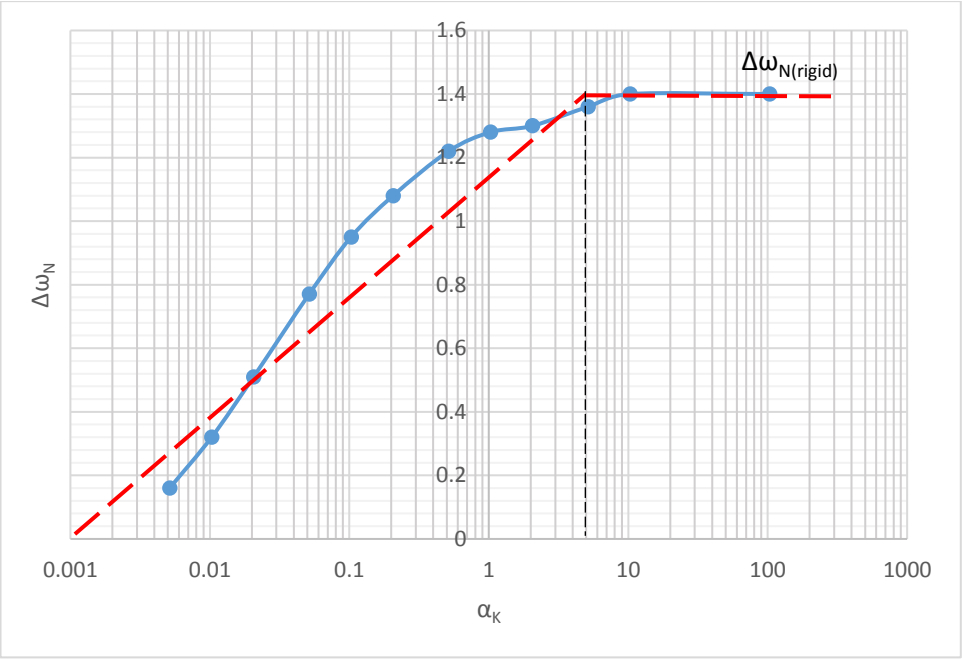

Figure 3.19: Effect of axial restraint stiffness on normalized CAA capacity

Using a coarse approximation as indicated by the dash red line, the expression for the effect of flexible axial support on arching effect can be written as:

$$\Delta\omega_N \cong \frac{\lg\alpha_k - \lg 0.001}{\lg 5 - \lg 0.001}\Delta\omega_{N(Rigid)} \tag{3.37}$$

This simplifies to:

$$\Delta\omega_N \cong \frac{\lg\alpha_k + 3}{\lg 5 + 3}\Delta\omega_{N(Rigid)} \quad \text{for } 0.001 \le \alpha_K \le 5 \tag{3.38}$$

and

$$\Delta\omega_N \cong 0 \qquad \text{if } \alpha_k < 0.001, \tag{3.39}$$

$$\Delta\omega_N \cong \Delta\omega_{N(Rigid)} \qquad \text{if } \alpha_k > 5. \tag{3.40}$$

The implication of the above expression is that if the $\Delta\omega_N$ coefficient for all the specimens are calculated and converted to rigid $\Delta\omega_{N(rigid)}$ the converted all "rigid" support cases will follow the fit shown in blue dashed line in Figure 3.19 (obviously

for the L/d = 9 and 12 groups the original $\Delta\omega_N$ will remain. The trend now should indicate a clearer and consistent relationship.

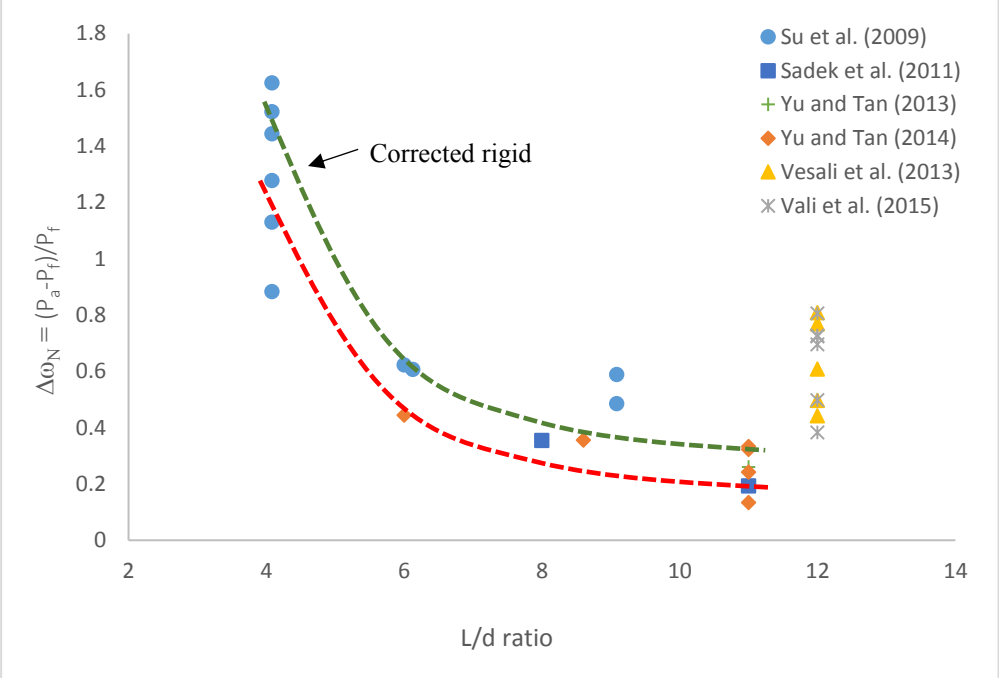

Figure 3.20: Illustration of the arching effect vs. L/d with all data "corrected" to rigid end supports.

3.5.2 Effect of reinforcement ratio on compressive arching action capacity

The effect of reinforcement is considered in a broader sense using a common normalising factor. From the semi-empirical view point, there may be different ways to consider the effect of reinforcement ratio on CAA capacity. One approach is to consider the absolute difference in the tension and compression reinforcement. The shortcoming of this approach is that for a symmetrical reinforcement arrangement, the difference between tension and compression reinforcement becomes zero. Thus, two different RC assemblies with different symmetrical reinforcement arrangement having different enhancement factor will have the same difference in reinforcement ratio (zero in this case). An alternative approach is to consider the geometric area of tension reinforcement at the support and middle sections as used in Su et al. (2009) and Yu & Tan (2014). This approach could be justified in the sense that the compression zone

available for arching is deducted by the amount of compression zone used for balancing the tension yielding of reinforcement. Although, this gives a consistence indication of the effect of reinforcement on arching capacity, it may not be applicable in the case with very high compressive rebar compared to tension rebar. However, it could be argued that in a typical buildings design, the support reinforcement is either equal to or greater than the span reinforcement hence this approach is suitable within the range of reinforcement ratio commonly used in practice. Thus, this approach is adopted in the present study.

The analysis is performed using the simplified model presented in section 3.4. The geometry of the beam is 150 by 300mm and length of one-half beam is 1800mm. Concrete and reinforcement strength are 30 and 500MPa, respectively. Different combinations of reinforcement ratios are considered such that the machanical reinforcement ratio (ψ) as defined by Equation (3.39) ranges from 10 to 55%. The axial restraint in the analysis is defined 10^6 KN/m.

The result of the analysis is presented in Table 3.9 and the plot of normalized increase in load against the mechanical reinforcement ratio is shown in Figure 3.21. It can be seen that the trend is similar to that reported in Yu & Tan (2014) and it shows that the normalized increase in load due to arching reduces as the reinforcement ratio increases.

A key observation herein is that while the normalised increase in load due to arching shows a very wide margin of variation (0.52 to 1.81), the absolute difference between maximum arching capacity (P_a) and bending capacity (P_f) shows minimal variation ranging from 79.1 to 70.9KN for a wide range of mechanical reinforcement ratio considered in this study (ψ =13.3 to 47.5%). This means that reinforcement ratio has less effect on the absolute difference between arching and bending capacities but a very considerable effect when this difference is normalised by the bending capacity. This is very much due to the increase in bending capacity with increase in reinforcement ratio keeping other factors constant.

Table 3.9: Effect of mechanical reinforcement ratio on normalized increased in load

Reinforcement ratio		$\psi = \frac{\rho f_y}{f_c}$ (%)	P_f (KN)	P_a (KN)	P_a–P_f (KN)	$\Delta\omega_N$
Top	Bottom					
2T10 (0.4%)	2T10 (0.4%)	13.3	43.6	122.7	79.1	1.81
3T10 (0.59%)	2T10 (0.4%)	16.5	53.7	131.6	77.9	1.45
3T12 (0.85%)	2T10 (0.4%)	20.8	66.6	142.3	75.7	1.14
3T12 ((0.85%)	2T12 (0.57%)	23.6	75.6	152.3	76.7	1.01
3T12 (0.85%)	3T12 (0.85%)	28.3	89.6	167.2	77.6	0.87
3T16 (1.52%)	3T12 (0.85%)	39.5	118.7	194.4	75.7	0.63
4T16 (2.0%)	3T12 (0.85%)	47.5	137.5	208.4	70.9	0.52

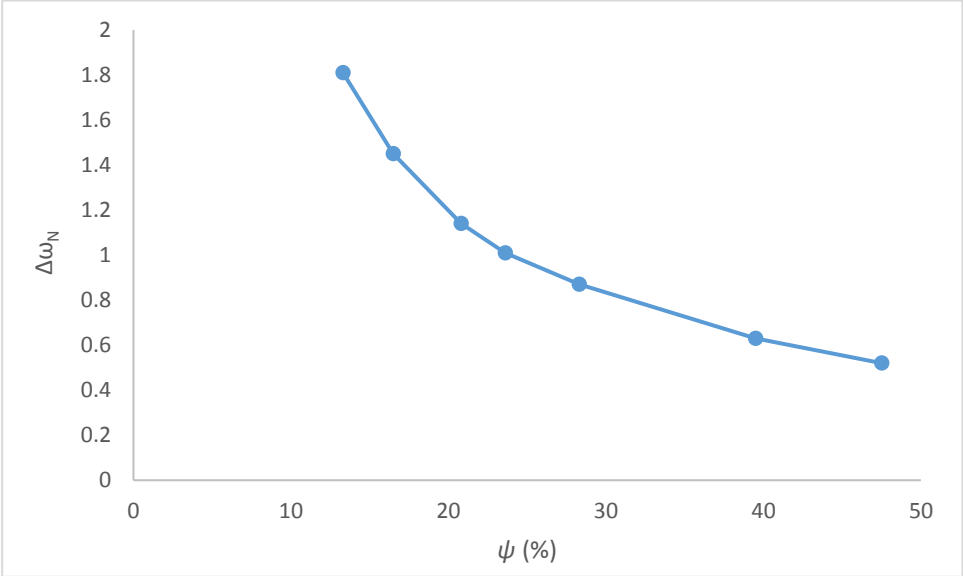

Figure 3.21: Effect of reinforcement ratio on relative increase/decrease in normalized increase in load capacity (normalized with bending capacity)

To consider the effect of mechanical reinforcement ratio in a semi empirical manner as would be shown later, it may be necessary to expressed Figure 3.21 in terms of relative factor. Herein a mechanical reinforcement ratio of 20% is adopted as a base reference and the factor for other mechanical reinforcement ratios are determined from this reference point.

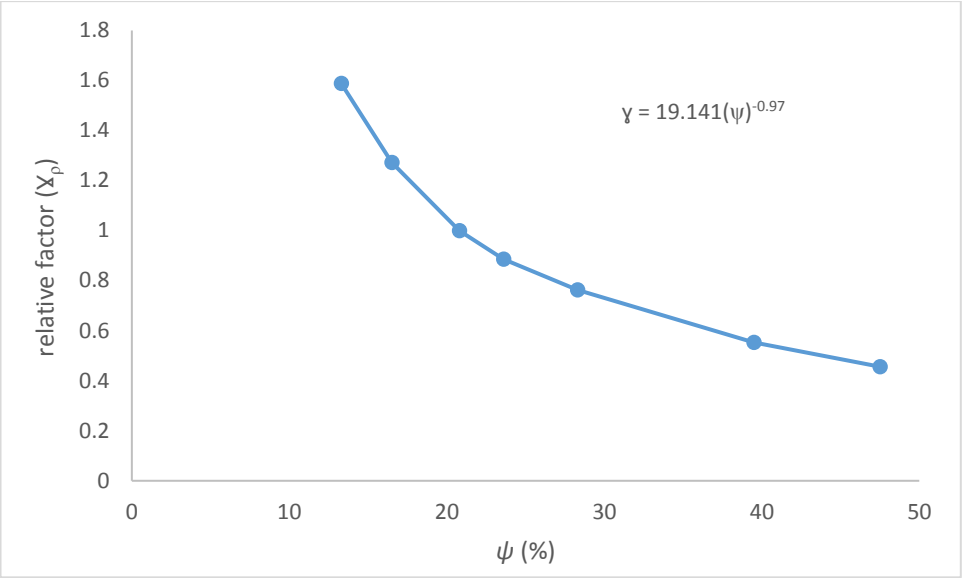

Figure 3.22: Effect of reinforcement ratio on relative increase/decrease in $\Delta\omega_N$

From Figure 3.22, a simple expression relating the arching factor to the mechanical reinforcement ratio correction factor can be expressed as:

$$\Delta\omega_N\big|_{\psi} = \gamma_{\psi} \times \Delta\omega_N \tag{3.41}$$

where $\gamma_{\psi} = 19.14(\psi)^{-0.97}$

3.5.3 Effect of span depth ratio on compressive arching action capacity

To further investigate the effect of L/d ratio on normalized increase in load due to arching, the simplified theoretical model developed in Section 3.4 is used. There may be two different approaches to obtaining the effect of L/d. One approach is adopting a constant depth and varying the beam length to obtain different L/d ratios. Another approach is fixing the beam length and varying the section depth to get different L/d ratio. Noting that arching effect is more sensitive to the depth than the length, the second approach is adopted in investigating the L/d ratio.

The length of the beam is fixed at 3600mm while the width is 150mm. Reinforcement consist of 3no and 2no ϕ14mm top and bottom section respectively and concrete

strength is 30MPa. Full axial restraint is assumed for the end supports. Five different depths of 300, 360, 450, 600 and 900mm are used which result in L/d ratio of 4, 6, 8, 10 and 12. The plot of the normalized increase in load ($\Delta\omega_N$) and the respective L/d ratio is shown in Figure 3.23. It can be seen that effect of L/d ratio on normalized increase in load decreases as the L/d ratio decreases. The result is in line with the experimental result from literature for the effect of L/d.

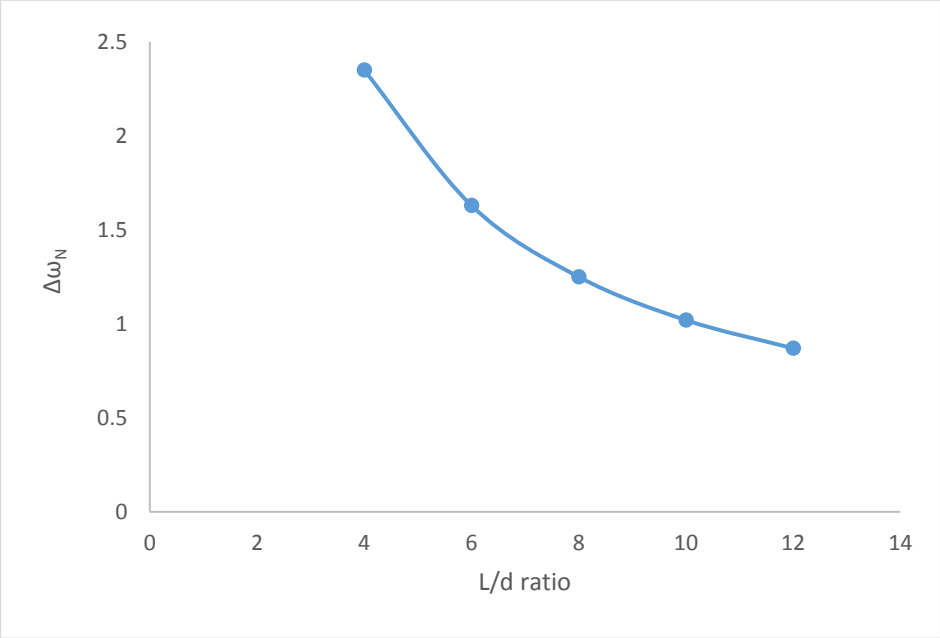

Figure 3.23: Effect of L/d ratio on $\Delta\omega_N$ from simplified model

To consider the effect of L/d in the simplified empirical form it may be reasonable to express the L/d effect in terms of a relative factor taking L/d ratio of 4 as a base reference as shown in Figure 3.24.

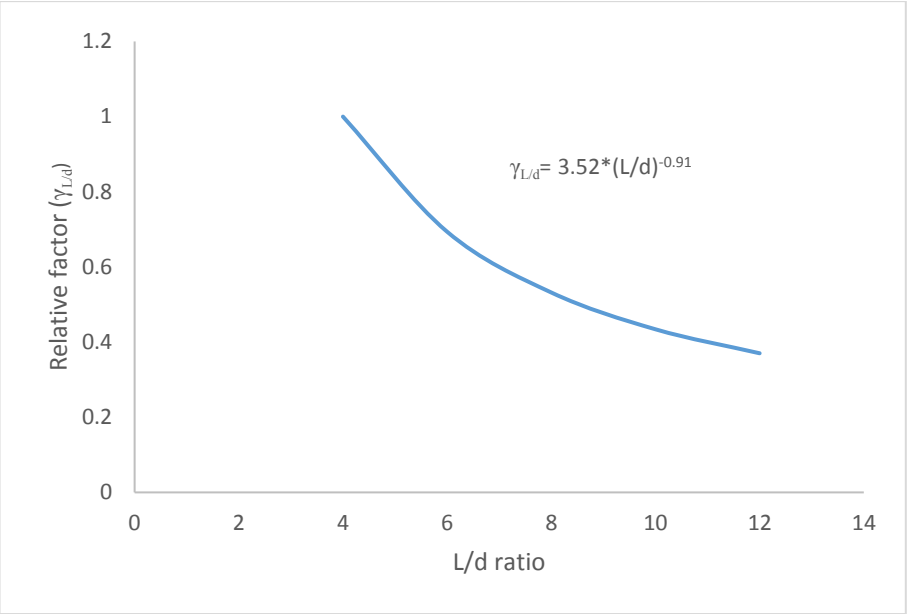

Figure 3.24: Effect of L/d ratio relative factor with L/d=4 as a base reference

From Figure 3.24, the expression for the effect of L/d ratio on normalised load can be expressed as:

$$\Delta\omega_N\big|_{L/d} = \gamma_{L/d} * \Delta\omega_N \tag{3.42}$$

where $\gamma_{L/d} = 3.52*(L/d)^{-0.91}$

3.5.4 Effect of concrete compressive strength

Concrete has a slight effect on compressive arching action as shown in Section 2.6.4 of Chapter 2, However, it could be argued that effect of concrete strength has already been considered indirectly in the axial stiffness effect and reinforcement ratio factor. Hence, concrete effect is not considered separately.

3.6 Empirical method for the prediction of the arching effect

3.6.1 Consideration of effect of the parameters

Given the above evaluation on the L/d ratio, axial stiffness ratio, and reinforcement factors it would be possible to generate empirical prediction formulas for the prediction of the arching effects, at least for the correction factors to take into account of the span depth ratio (L/d), axial support stiffness and reinforcement factor effect, assuming the arching action for a standard reference case of a given L/d is available.

Herein the standard reference case is considered as axially rigid RC beam with L/d ratio of 4. The beam geometry is 150 by 300mm and reinforcement of 2no ϕ12mm at top and bottom sides of cross section, respectively. Yield strength of reinforcement is taken as 500MPa.

i) The compressive arching capacity of this reference beam is determined using the simplified theory developed in Section 3.4 as:

$$P_a = 222KN \tag{3.43}$$

Bending moment of the section is calculated as:

$$M_b = f_y A_s (d - a - \frac{f_y A_s}{1.7 f_c b}) = 28\text{KNm} \tag{3.44}$$

Flexural capacity is calculated as:

$$P_b = 2 * 2M_b / L = 93.3\text{KN} \tag{3.45}$$

Normalized increase in load capacity for the reference RC beam ($\Delta\omega_{N(\text{Ref})}$) becomes:

$$\Delta\omega_{N(\text{Ref})} = \frac{P_a - P_f}{P_f} = 1.38 \tag{3.46}$$

ii) Bringing in the L/d ratio effect:

$$\Delta\omega_N\big|_{L/d} = \gamma_{L/d} * \Delta\omega_{N(\mathrm{Re}f)} \tag{3.47}$$

Substituting Equation (3.46) in (3.47) gives

$$\Delta\omega_N\big|_{L/d} = 1.38\gamma_{L/d} \tag{3.48}$$

where $\gamma_{L/d} = 3.52*(L/d)^{-0.91}$

iii) Bringing in the axial support flexibility effect:

$$\Delta\omega_N\big|_{\alpha_k} = \frac{\lg\alpha_k + 3}{\lg 5 + 3}\Delta\omega_{N(Rigid)} \quad \text{for } 0.001 \le \alpha_k \le 5 \tag{3.49}$$

Now, Equation (3.49) can be written as:

$$\Delta\omega_N\big|_{\alpha_k} = \frac{\lg\alpha_k + 3}{\lg 5 + 3}(1.38\gamma_{L/d}) \tag{3.50}$$

iv) Bringing in the reinforcement ratio effect:

$$\Delta\omega_N\big|_{\psi} = \gamma_{\psi} * \Delta\omega_N\big|_{\alpha_k} \tag{3.51}$$

where $\gamma_{\psi} = 19.14(\psi)^{-0.97}$

Substituting Equation (3.50) into (3.51) gives:

$$\Delta\omega_N\big| = 19.14(\psi)^{-0.97} * \frac{\lg\alpha_k + 3}{\lg 5 + 3} * (1.38\gamma_{L/d}) \tag{3.52}$$

Equation (3.52) gives an expression that considers the effect of reinforcement ratio, L/d ratio and axial flexibility.

Recalling that;

$$\Delta\omega_N = \frac{P_a - P_f}{P_f} \tag{3.53}$$

The ratio of the maximum arching to the bending capacity (C_a) can then be expressed as:

$$C_a = \frac{P_a}{P_b} = 1 + \Delta\omega_N \tag{3.54}$$

For a given RC beam with a defined geometric and material properties, the ratio of maximum arching compression capacity to the bending capacity can be obtained by Equation (3.54).

3.6.2 Validation of the proposed semi empirical formulae

The series of semi empirical formulas derived in Section 3.6.1 are used to predict the ratio of maximum arching to bending capacities. The result is compared with the experimental result. As shown in Figure 3.25, the discrepancies between the predicted and test values are very small. As can be seen, a strong correlation exists between the predicted and test result with a correlation coefficient of 0.996 which represent a positive correlated result. It should however be mention that part of the discrepancy in the test by Yu & Tan (2013b) may be due to the connection gaps that existed between the test set up and end columns of the specimen during the test which affected the compressive arching action that could actually develop. Notwithstanding these minor differences, the empirical expressions can to reasonable level of accuracy predict the arching capacity in a laterally restrained subassembly.

Table 3.10: Comparison of experimental and predicted result

Specimen ID	Axial stiffness (KN/m)	$\alpha_a = \frac{K_a}{(E_c A)/L}$	$C_a = P_a/P_f$ Predicted	$C_a = P_a/P_f$ (Test)	$\frac{C_{a(test)}}{C_{a(predicted)}}$
A1	1.00E+06	1.19	2.58	2.55	0.99
A2		1.14	2.16	2.28	1.06
A3		1.08	1.97	1.89	0.96
A4		1.26	2.68	2.62	0.98
A5		1.18	2.31	2.44	1.06
A6		1.13	2.07	2.13	1.03
B1		2.26	1.64	1.62	0.99
B2		3.06	1.32	1.49	1.13
B3		2.93	1.43	1.59	1.11
C1		3.41	1.35	1.61	1.20
S1	1.06E+05	0.31	1.35	1.26	0.93
S2		0.31	1.40	1.32	0.94
S3	4.29E+05	1.13	1.42	1.33	0.93
S4		1.13	1.36	1.32	0.97
S5		1.13	1.30	1.24	0.95
S6		1.13	1.28	1.13	0.89
S7		0.89	1.43	1.35	0.94
S8		0.64	1.55	1.43	0.92
Mean value of test to predicted ratios					0.999
Correlation coefficient					0.996

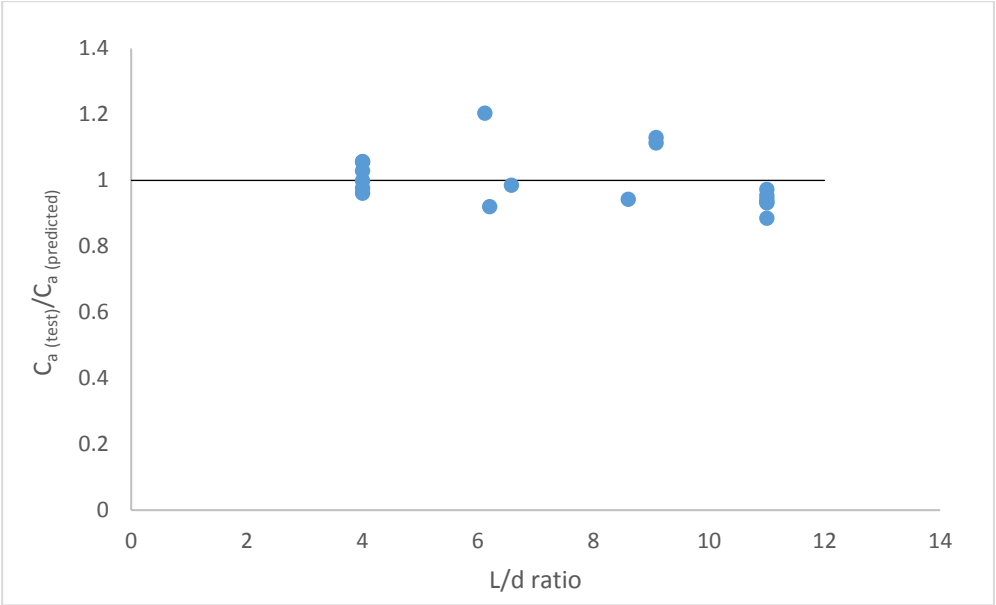

Figure 3.25: Correlation of predictions with test results for different L/d ratios

3.7 Conclusions

On the basis of survey and collection of data on compression arching in a laterally restrained RC beam, the effect of parameters affecting the arching compression have been succinctly studied. Axial restraint stiffness, reinforcement ratio, concrete compressive strength and span depth ratio all have effect on the arching compression. The reinforcement ratio affects the maximum arching compression capacity but has lesser effect on the relative increase in load between the maximum arching and bending capacities whereas L/d ratio and axial restraint stiffness affect both the relative increase due to arching and the maximum arching action that could developed.

A more reliable classification of axial stiffness should be based on the relative rigidity. The results tend to suggest that RC assemblies with an axial stiffness coefficient (α_κ) greater than 5 can reasonably be considered as having a rigid support, and for stiffness coefficients lower than 5, the arching compression should be scaled down accordingly.

Chapter 4: Numerical modelling of reinforced concrete beam assembly under a progressive collapse scenario

4.1 Introduction

To fully understand the behaviour of reinforced concrete subassemblies under column removal, experimental tests are required in which various design parameters may be varied to better understand the governing mechanisms and the influences of the parameters in question. Such test does not only require time for planning and execution, but it is also capital intensive. An alternative to experimental tests may be to use finite element method. In recent years, several studies on behaviour of RC and composite beams under large deformation have been executed using finite element analysis (Yang & Tan 2014; Albrifkani & Wang 2016; Lew et al. 2014; Pham et al. 2016). This is due to the advancement in the finite element method (FEM) and the availability and affordability of high speed computers.

There are numerous finite element codes which can be used to simulate the behaviour of RC structure subjected to extreme event. Example of these codes are ABAQUS/Explicit (Dassault Systèmes, 2007), LS-DYNA (LSTC 2012), ADINA (ADINA 2006), Autodyn (ANSYS 2009). Each of these codes has a large library of material models which can simulate the behaviour of reinforced concrete structural elements under a variety of loading conditions. However, the accuracy of such numerical models depends on the soundness of the material models in capturing the constitutive behaviour of materials under different stress conditions and the interaction between concrete and reinforcement. Due to complexities of the concrete material, there does not exist a material model that is recognised to be capable of describing the behaviour of concrete across different loading and deformation regimes. This means

different applications require dedicated research effort in the development and validation of the finite element model.

In the present study, an explicit finite element code LS-DYNA is adopted to model the behaviour of RC subassemblies. LS-DYNA has a number of constitutive material models which are capable of simulating the behaviour of concrete including cracking and softening. Some of the widely used concrete material models in LS DYNA library include Continuous Surface cap model (MAT_159), Winfrith_Concrete (MAT_84), Riedel-Hiermaier-Thoma model (RHT) and Karagozian and Case Concrete Damage REL3 (KCC) model. A comparative studies of the these models shows that they are capable of capturing the confinement factor, post-peak softening, strain rate effect and shear dilation (Brannon & Leelavanichkul 2009). Herein, the KCC model is selected as the material model for concrete. This model has a user-friendly input setting compared to other three models mentioned above. For modelling longitudinal and transverse reinforcement, a PIECEWISE_LINEAR_PLASTICITY (MAT_024) is adopted.

In this chapter, the background of KCC model is first presented, issues commonly encountered in the simulation of reinforced concrete assemblies under large deformation such as hour glassing effect, mesh size sensitivity and strain localization in rebar at large deformation are discussed. Finally, the developed modelling scheme is validated through benchmarking against available experiment in the literature.

4.2 Background of KCC model

The performances of KCC material model for concrete under different loading and stress condition are well documented in the literature (Magallanes et al. 2010; Crawford et al. 2012; Magallanes 2008; Malvar et al. 1997). To facilitate some more specific discussion into the model behaviour when applied in the simulation of RC beam assemblies under large deformations, a brief overview of the basic formulation of this material model is given in this section.

KCC concrete material model has three independent strength surfaces. These include the yield, maximum and residual surfaces. These surfaces are defined using eight parameters which include; a_{0m}, a_{1m}, a_{2m} for maximum surface, a_{0y}, a_{1y}, a_{2y} for yield surface and a_{1r}, a_{2r} for residual surface. These values are determined and validated using standard test on concrete (Crawford et al. 2012). At each incremental time step, the current strength surface is interpolated between the yield and the maximum surfaces or the maximum and the residual surfaces together with the damage accumulation parameter. A schematic representation of the three surfaces are shown in Figure 4.1. The state of stress at any increment is determined by Equation (4.1).

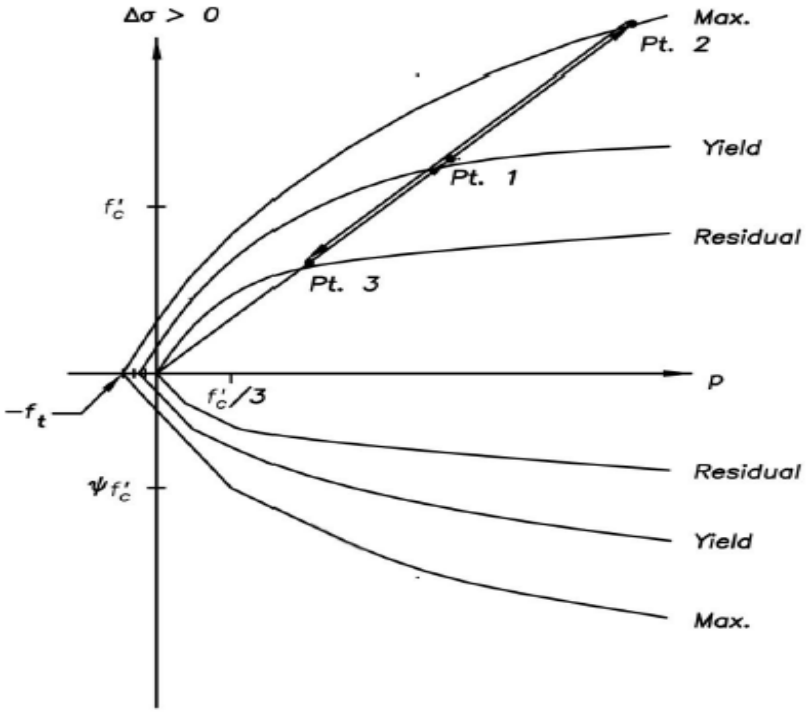

Figure 4.1: Three strength surfaces represented in K&C model (Mat_072R3) (Malvar et al. 1997)

$$\Delta\sigma = \begin{cases} [\eta(\Delta\sigma_m - \Delta\sigma_y) + \Delta\sigma_y] & \Delta \le \lambda_m \\ [\eta(\Delta\sigma_m - \Delta\sigma_r) + \Delta\sigma_r] & \Delta > \lambda_m \end{cases} \tag{4.1}$$

where σ_y, σ_m and σ_r represent the yield, maximum and residual surfaces and are defined by Equation (4.2).

$$\Delta\sigma = \begin{cases} \Delta\sigma_y = \sigma_{0y} + \dfrac{p}{\sigma_{1y} + \sigma_{2y} p} & \textit{yield surface} \\ \Delta\sigma_y = \sigma_{0m} + \dfrac{p}{\sigma_{1m} + \sigma_{2m} p} & \max \textit{imum surface} \\ \Delta\sigma_y = \dfrac{p}{\sigma_{1r} + \sigma_{2r} p} & \textit{residual surface} \end{cases} \tag{4.2}$$

With Equations (4.1) and (4.2), the three surfaces shown in Figure 4.1 are defined. As mentioned previously, the state of stress at each time increment is interpolated between two surfaces: yield and maximum surfaces when hardening occurs and maximum and residual surfaces when concrete enters the softening regime. This is achieved using the eta function (η) in Equation (4.1). η is a function of a variable lambda (λ) which measures the state of damage at a particular time increment and is defined as shown in Equation (4.3).

$$\lambda = h\sqrt{(2/3)\varepsilon_{ij}^{p}\varepsilon_{ij}^{p}} \tag{4.3}$$

where h is defined as:

$$h = \begin{cases} \dfrac{1}{r_f\left(1 + \dfrac{p}{r_f f_t}\right)^{b1}} & \textit{for } p \geq 0 \text{ (compression)} \\ \dfrac{1}{r_f\left(1 + \dfrac{p}{r_f f_t}\right)^{b2}} & \textit{for } p < 0 \quad \text{(tension)} \end{cases} \tag{4.4}$$

In Equation (4.4), r_f is a rate scalar, f_t is the tensile strength, b_1 and b_2 are factors that controls the rate of accumulation of damage in tension and compression. With these parameters different behaviour of concrete in tension and compression can be defined. The default values for b_1 and b_2 are 1.6 and 1.35 and default eta-lambda (η-λ) curve in KCC model is shown in Figure 4.2.

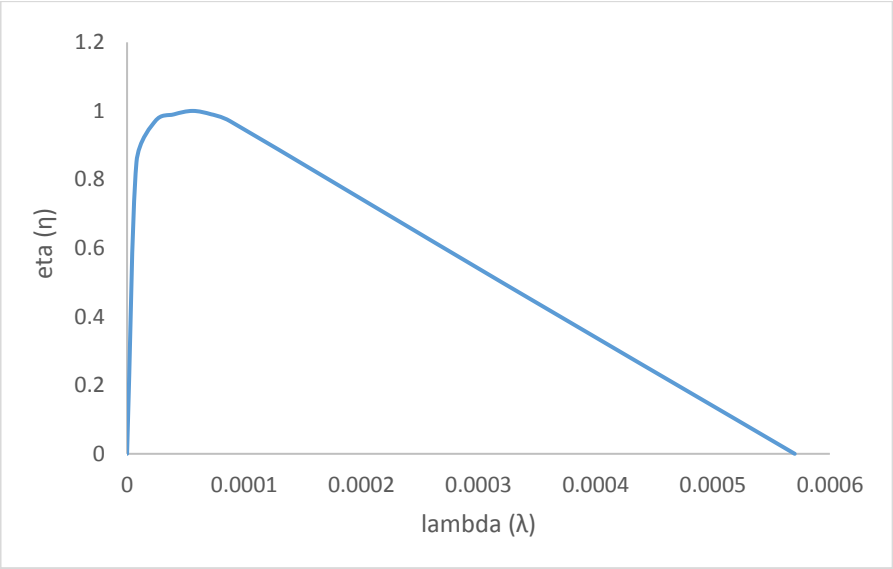

Figure 4.2: Default η-λ curve in KCC model

4.2.1 Performance of KCC model

In Section 4.2, it was shown that damage accumulation in KCC model is determined from the η-λ curve together with the b_1 and b_2 which are parameters that controls the rate of damage accumulation in tension and compression. Previous study by Xu and Lu (2016) however reveals that the concrete modelled by KCC in a RC member subjected to blast load tends to fail abruptly, especially in the region interacting with the reinforcing bars. This was attributed to the quick descending of the tensile strength to zero in the softening regime thereby resulting in a state of no stress in concrete surrounding the rebar.

For relatively simple loading and stress conditions, the default setting of KCC model may give good prediction. However, in a complex stress condition where concrete-rebar interaction (through shear or bond) dominates (Xu and Lu, 2016), the default η-λ curve could fail to capture the behaviour of RC elements. This problem may be more severe in the case of large deformation of RC element during which the rebar anchorage in concrete becomes crucial, particularly in the development of the catenary action. To carter for the need of the present study, a concrete model which is versatile and able to predict the response of the structure under different stress conditions and

loading without the need to explicitly define a bond slip relationship is desired. To achieve this objective, the softening behaviour of concrete in tension and shear is a critical factor, and to ensure a good representation of such properties of the concrete the η-λ curve in KCC model is modified.

The behaviour of concrete is governed by cracking in tension and crushing in compression in a case where adequate confinement is provided. There are numerous ways in which the tensile behaviour of concrete may be depicted. In spite of this, a general practice is that a target fracture energy, which is energy required to propagate a tensile crack of unit area, should be preserved. In this sense, the fracture energy is considered as a material property and therefore should be independent of the mesh size. To ensure the independency of the macroscopic tensile behaviour from the mesh size, the fracture energy is normally tied to the element length, so that the stress-strain relation in the softening regime varies with the element size (h_c) but the integral over the element width remains constant,

$$G_f = \int (\sigma d\varepsilon) h_c \quad \text{or} \quad \int (\sigma d\varepsilon) = G_f / h_c \tag{4.5}$$

Depending on the material models, the softening stage may be represented in different ways, but if a targeted fracture energy is preserved as depicted in (c) to (f) in Figure 4.3, similar results can be achieved, especially in small deflection problems.

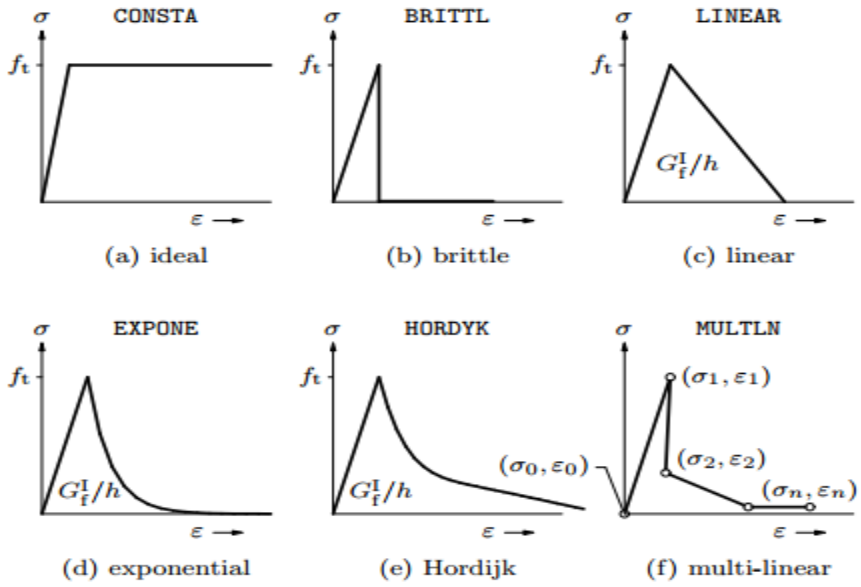

Figure 4.3: Tension softening for modified Maekawa model (adopted from DIANA manual)

However, in the case of extremely large deformation with multiple tension cracks as in the present study, the state of concrete-rebar interaction will tend to play increasingly important role, and without explicit modelling of the bond interface, a robust description of the tensile stress-strain curve is necessary. This is equivalent to an implicit representation of rebar-concrete bond which is generally less brittle than direct tension of concrete, such that a minimal interaction between concrete and steel after cracking of concrete in tension will be maintained. This can be achieved by modifying the softening portion of the tension stress-strain curve of concrete to allow for a prolonged residual capacity.

To achieve this, the η-λ curve is modified to yield a stress-strain relationship similar to that of a power form stress strain relationship proposed by Maekawa et al. (2003) and shown in Figure 4.4. In the Figure, ε_{cr} is the cracking strain and c determines the rate of decrease in tension after cracking and depends on the type of reinforcement used (plain or deformed). Herein, the reinforcements are assumed to be deformed, hence c is selected as 0.4. This approach has been found to give reasonable result in studies on large deformation of reinforced concrete beam (Albrifkani & Wang 2016). Similar stress-strain behaviour of concrete in tension with residual stress gave accurate

result in modelling large deformation behaviour of composite connections (Guo et al. 2013).

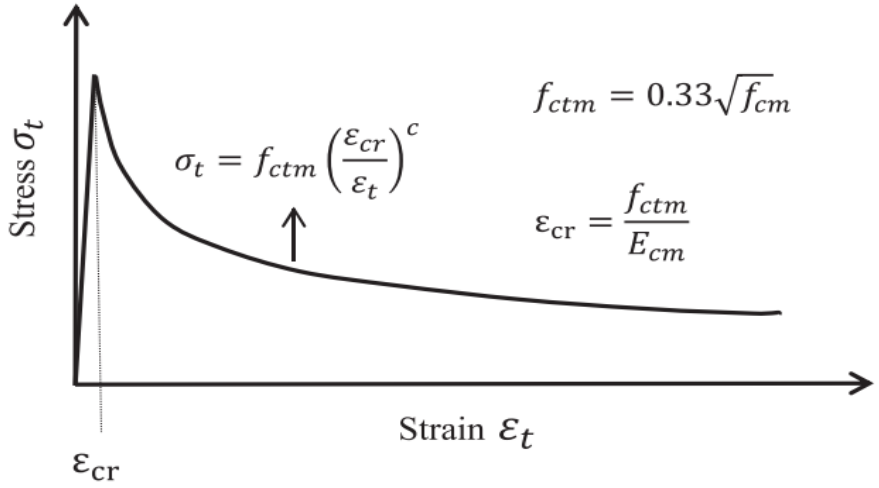

Figure 4.4: Stress strain relationship of concrete in tension (Maekawa et al. 2003)

Unlike in some other concrete models for example the concrete damage plasticity model (CDP), where concrete tensile and compressive behaviour are defined independently, in KCC model the concrete compressive and tensile behaviours are defined in a combined manner. This implies that any modification (enhancement) of tensile behaviour would result in over-ductile behaviour of concrete in compression. To control this, the b_1 and b_2 parameters in the model are modified accordingly thereby allowing the much desired behaviour in tension and compression to be determined. The effect of these parameters on a single element simulation test is investigated in the next section.

4.2.1.1 Single element simulation

A single cubic element of size 25mm is used for the simulation. The compressive strength of concrete is taken as 30MPa. Due to the softening branch, a displacement control loading is adopted. In the study by Xu and Lu (2016), the η-λ curve with maximum λ of 0.004 was found to give reasonable result for blast loading. In this study, the η-λ curve is modified to give a stress-strain response with a prolong residual capacity similar to the stress-strain response by Maekawa et al. (2003) depicted in

Figure 4.4. The η-λ curve used for the single element simulation test is shown in Figure 4.5. Parameters controlling damage accumulation in compression (b_1) and tension (b_2) are taken to be 1.2 and 1.35.

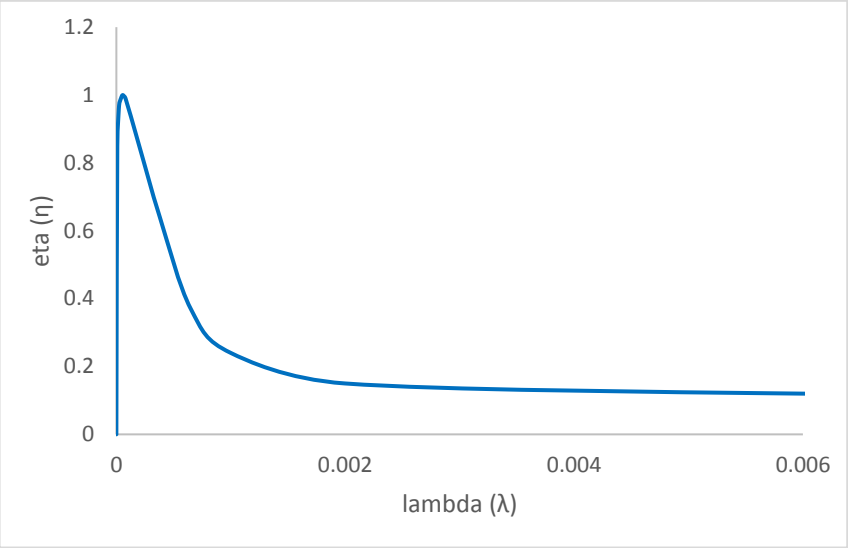

Figure 4.5: Modified η-λ curve with and without residual capacity

The result of the tensile stress-strain response for the single element simulation test and the prediction by Maekawa et al. (2003) is shown in Figure 4.6. In the Maekawa et al. (2003), the critical stress is determined as $0.33\sqrt{f_c}$ but in the comparison shown in Figure 4.6, the critical (maximum) stress from FE simulation test is used in the Maekawa et al. (2003) model to predict the tensile stress-strain behaviour. It can be observed that the descending branch of the curve is similar in both the FE and predicted models. The stress increases up to the maximum value of 3MPa and followed by softening. At a strain of 0.02, the residual stress is around 0.4MPa in both models.

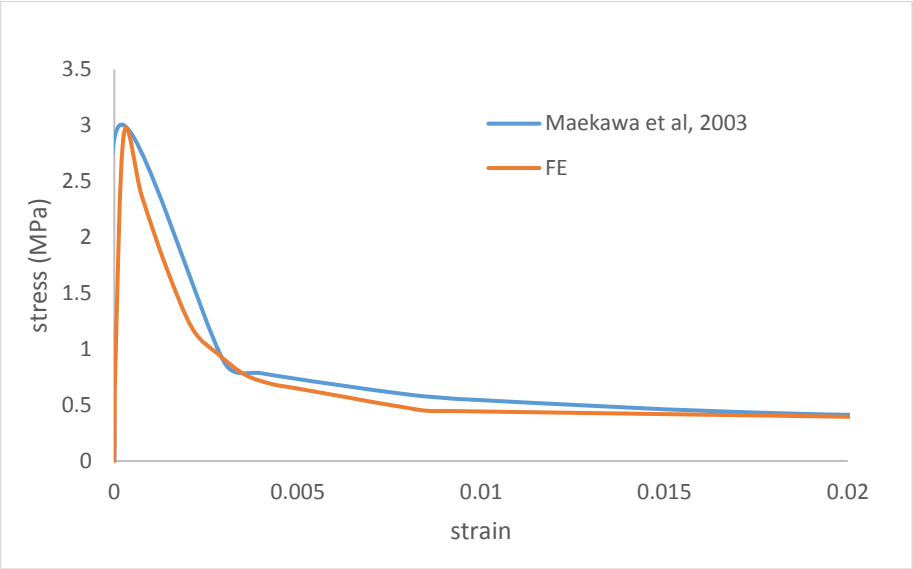

Figure 4.6: Uniaxial stress-strain curve of single element simulation test (element size=25mm)

The compressive stress-strain behaviour for the model is shown in Figure 4.7. A close look at the Figure shows that the peak compressive stress of 30MPa occur at a strain of about 0.0019 which is within the range of values obtain in the experimental tests (Hognested et al. 1955; Popovics 1973). Tests in literature further shows that concrete softens after attaining the maximum compressive strength. This behaviour is exhibited in the simulated stress strain behaviour as shown in Figure 4.7.

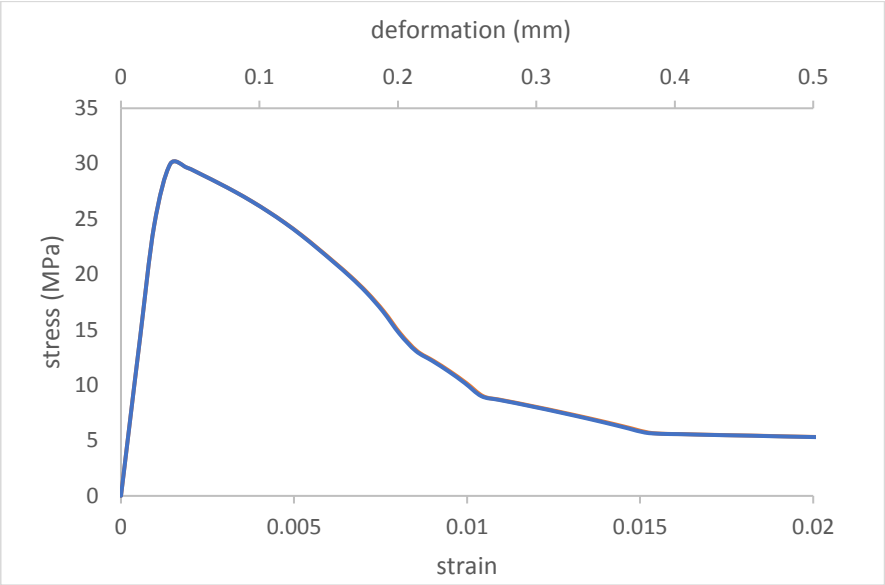

Figure 4.7: Uniaxial compressive stress-strain curve of single element simulation test (element size=25mm)

With confinement, the compressive strength of concrete is enhanced compared to the strength of unconfined concrete. Experimental tests shows that the strength of confined concrete depends on the level of confinement and increases as the confinement increases (Ansari & Li 1998; Imran & Pantazopoulou 1996; Moradi, Saber; Alam 2013). An experimental test showing the effect of confinement on concrete is shown in Figure 4.8. It can be seen that the simulated behaviour (Figure 4.9) well represent the behaviour as observed in the experiment. Thus, in the presence of confinement, concrete strength is enhanced and the magnitude of enhancement depends on the level of confining pressure.

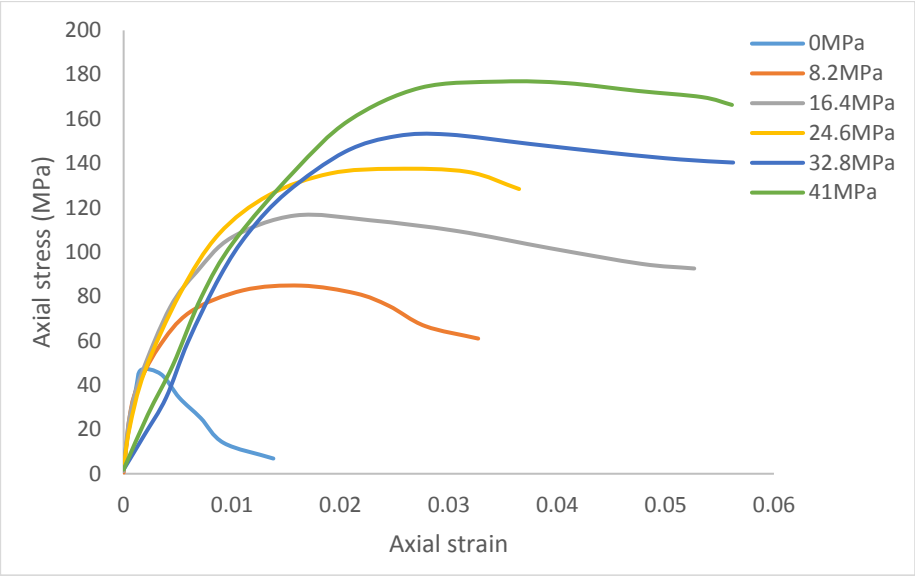

Figure 4.8: Axial stress-strain curves of concrete under different confining pressure (Ansari & Li 1998)

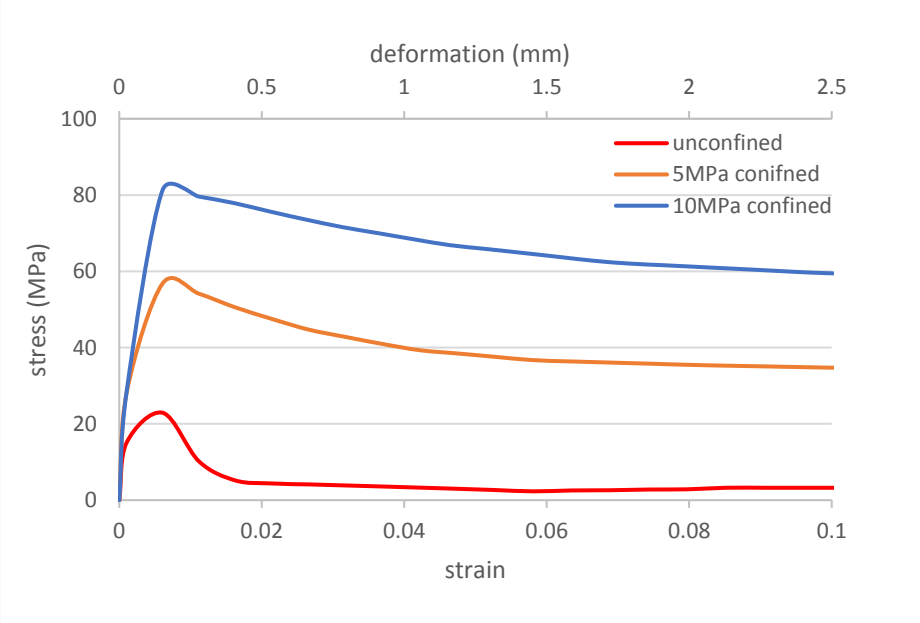

Figure 4.9: Stress-strain curves under confined compression with and without residual capacity (mesh size=25mm)

4.2.1.2 Effect b_2 on stress-strain behaviour

The tensile behaviour of concrete is very important in modelling RC assemblies subjected to large deformation. This is because residual "bond" effect needs to be implicitly represented through tension/shear behaviour of the concrete to allow for accurate representation of RC member behaviour during the large deformation regime. In KCC model, the default value of b_2 is 1.35. In this section, three different values of b_2 are considered to fully understand its effect on the stress-strain behaviour of single element under. The compression damage accumulation factor b_1 is kept constant at 1.2. As shown in Figure 4.10, b_2 has a minor influence in the stress strain curves. This difference occurs within the softening stage of the response. The lower the value of b_2 the higher the area under the stress-strain curve. Since the difference is very minimal, the default value of b_2=1.35 is used in the current study.

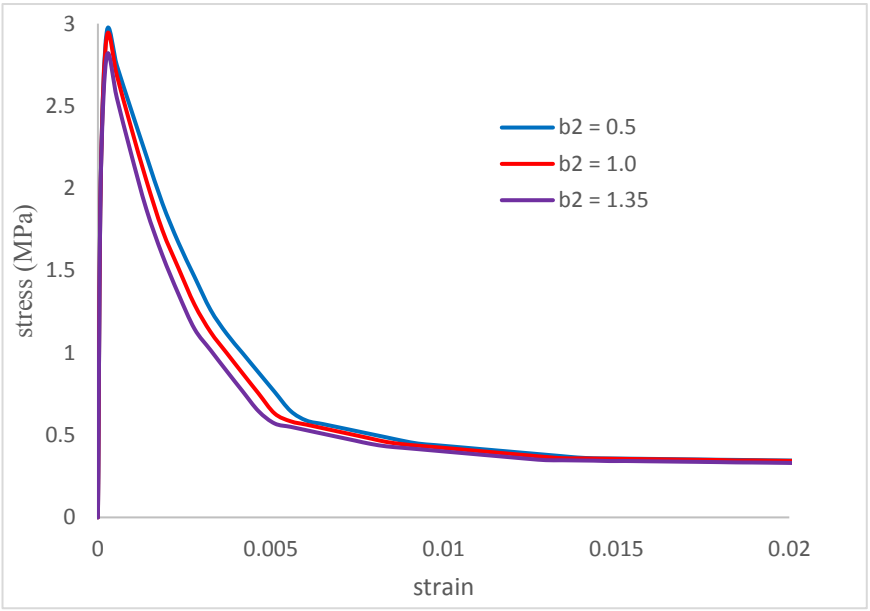

Figure 4.10: Stress-strain curves under confined compression with and without residual capacity (mesh size=25mm)

4.2.1.3 Damage definition

As mentioned previously, the damage index in KCC model is defined as:

$$SDF = \frac{2\lambda}{\lambda + \lambda_m} \tag{4.6}$$

where the range of SDF is from 0 to 2 and λ_m is the value of λ corresponding to the maximum value of eta (η). For 0<SDF<1, the concrete is in the pre-peak stage. When SDF=1, concrete reaches it maximum stress and for 1<SDF<2, concrete enters softening stage with damage continually increasing as λ approaches infinity.

Recent study by Xu and Lu (2016) has shown that the above scaler damage factor (SDF) has a very narrow range of indication of the damage state of concrete. The Scalar damage factor would need to get very close to 2 to correspond to a significant damage state or an advanced softening stage. This is illustrated in Figure 4.11. As can be noticed in this figure, the damage index is already close to 2 even at the early stage of softening but with the index value it would imply that concrete is damaged and cannot transfer stresses. This definition may give false information about the damage accumulation in the KCC model. In view of this problem, Xu and Lu (2016) suggested that one should discriminate severe damage with the damage scalar factor in close range to the limiting value of 2, to be representative of the real severe damage state of concrete. It was recommended that damage index in the range of 1.97-2.0 best represents an advanced damage or softening state of concrete, such as macro-cracking in tension. In the present study, this range is adopted when referring to the damage scale factor for near-failure state of concrete. More so, the strain contour distribution will also be used to represent the damage in concrete.

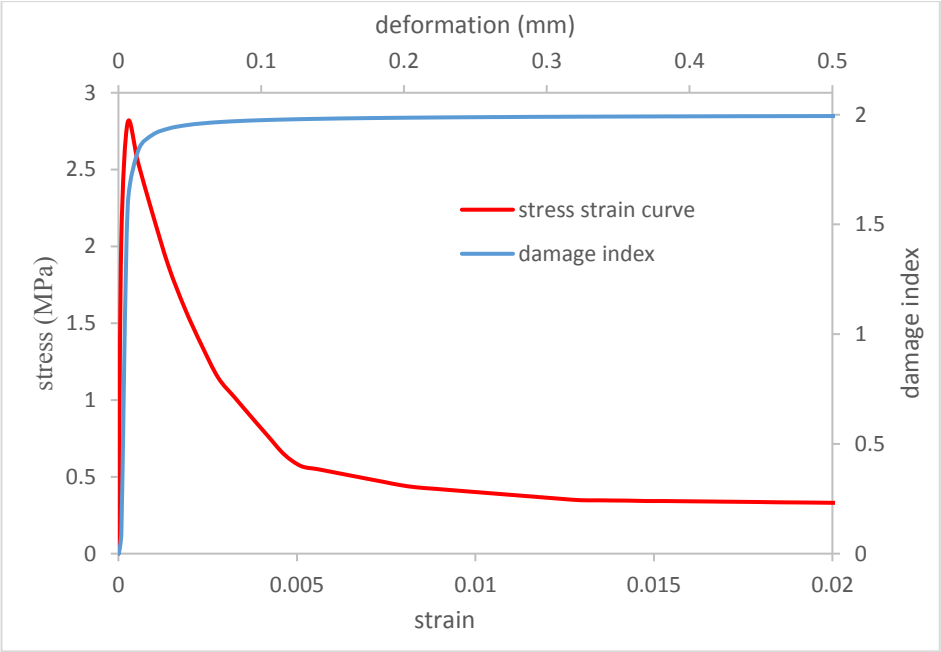

Figure 4.11: Uniaxial tension and damage index

4.3 Modelling of reinforcement

In small deformation problems largely dominated by elastic and limited inelastic responses, reinforcement may be modelled as smeared over concrete. For large deformation problems smeared approach is no longer valid because of geometric and material nonlinearity, and reinforcement needs to be explicitly modelled. There are two methods to explicitly embed reinforcement in concrete in an RC member, these include shared nodes and constraint method. Perfect bond is assumed between concrete and reinforcement in both methods, however the shared nodes option requires that the nodes of concrete and reinforcement be meshed together. This implies that the concrete and reinforcement nodes to be meshed must be coincident or lie within the same proximity. In the constraint method, the reinforcement nodes need not be meshed with the concrete nodes, instead the reinforcing bars are embedded in the concrete such that the motion of the master nodes (concrete) and slave nodes (reinforcement) are the same. In LS-DYNA, reinforcement can be embedded in concrete using the keyword CONSTRAINED_LAGRANGE_IN_SOLID (CLIS). The advantage of the constraint method over the shared nodes is that the reinforcement and concrete can be meshed

independently. Hence the mesh size of reinforcement does not necessarily have to be the same with that of concrete. Herein, rebar effect is simulated using the shared nodes option.

It should be pointed out that, although "perfect" bond is assumed in the RC modelling herein, macroscopic bond-slip can still be observed as the concrete layer interfacing with the rebar (through shared nodes) softens and ultimately fails during the course of response.

4.4 Model checks

When modelling RC assemblies under large deformation, a number of checks is required to ensure the model performs as expected. Issues such as strain localization in rebar, mesh sensitivity and hour glass effect may affect the accuracy of the result. Each of these issues are briefly discussed and the checks for each of them is performed.

4.4.1 Reinforcement strain localization

Strain localisation occurs when plastic strain concentrates in a particular element within the critical section in the post yield response stage. While numerical localisation in concrete modelling is well understood and measures such as preservation of fracture strain energy are available to minimise its effect, localisation in reinforcing bars is seldom examined. This phenomenon is also mesh size dependent and may be very sensitive in the simulation of catenary action behaviour, especially the determination of rebar rupture. As mentioned in Section 4.3, using shared nodes would imply that the rebar element size has to be the same as concrete mesh size, making potential rebar strain localisation less controllable from the meshing point of view.

In the simulation of RC assemblies under column loss scenario, the final failure may be governed by rupture of rebar. The behaviour of RC assemblies during the final stage (catenary stage) is similar to the RC beam subjected to axial tension. For this reason, the effect of strain localisation in rebar is investigated in this section using a simple direct tension simulation test on RC beam.

The beam has a width, depth and length of 40, 200 and 600mm respectively and reinforcement consist of 2 nos. Φ10mm arranged as shown in Figure 4.12. One-half of the beam is modelled with the two end regions modelling with "elastic" concrete to avoid damage to the end of the beam being pulled. The end nodes of the beam on one side are fixed against translation in all directions and all nodes at the other end are pulled in the horizontal direction. Three different mesh sizes of 5, 10 and 20mm are considered in the study. The FE model of the RC element with mesh size of 20mm is shown in Figure 4.12. Concrete is modelled with KCC material model and with concrete compressive strength of 30MPa. Reinforcement is modelled with MAT_24 and three different stress-strain curves including elastic perfect plastic, elastic plastic with linear hardening and real hardening are considered. The three stress-strain curves are depicted in Figure 4.13.

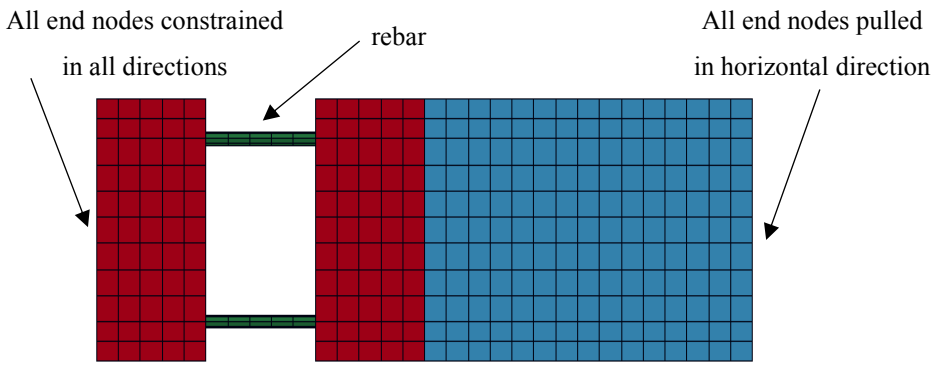

Figure 4.12: FE model of RC beam (mesh size=20mm)

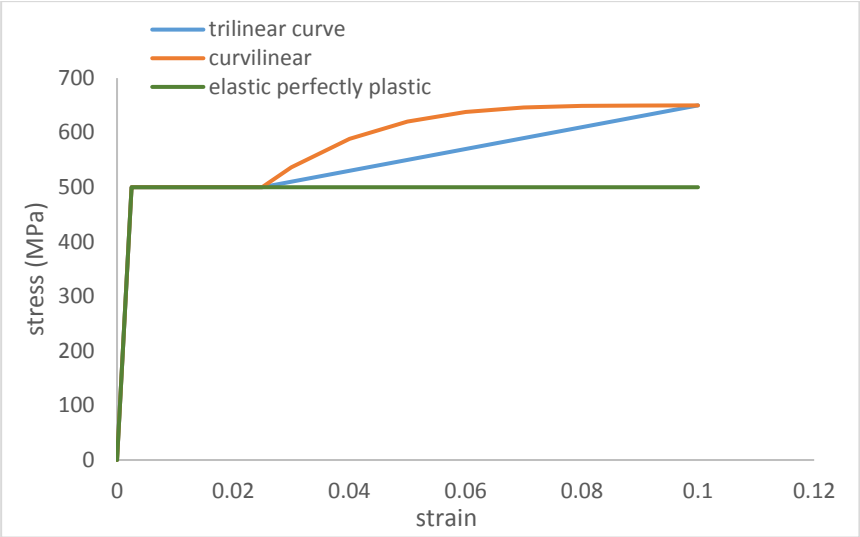

Figure 4.13: Different stress-strain curve used for the study

The load displacement responses of the FE models with different reinforcement stress-strain curves are shown in Figures 4.14-4.16. It can be observed that the effect of strain localisation in rebar is more pronounced in the RC beams with elastic-perfectly plastic stress-strain behaviour. For instance, the difference between the failure displacement of model with mesh size of 5mm and 20mm is 50%. Such big difference could affect the result of the simulation. When hardening is introduced, the difference in failure displacement is reduced to 10 and 27% for models with trilinear and real stress-strain curves respectively.

It could be concluded from this study that when modelling RC assemblies subjected to catenary action, the use of elastic perfectly plastic stress strain behaviour of reinforcement may result in strain localisation causing the failure displacement to be significantly mesh dependent. This problem could be rectified by introducing strain hardening. It is also recommended that the effect of strain localisation may be further reduced by using trilinear stress strain curve as indicated in Figure 4.15.

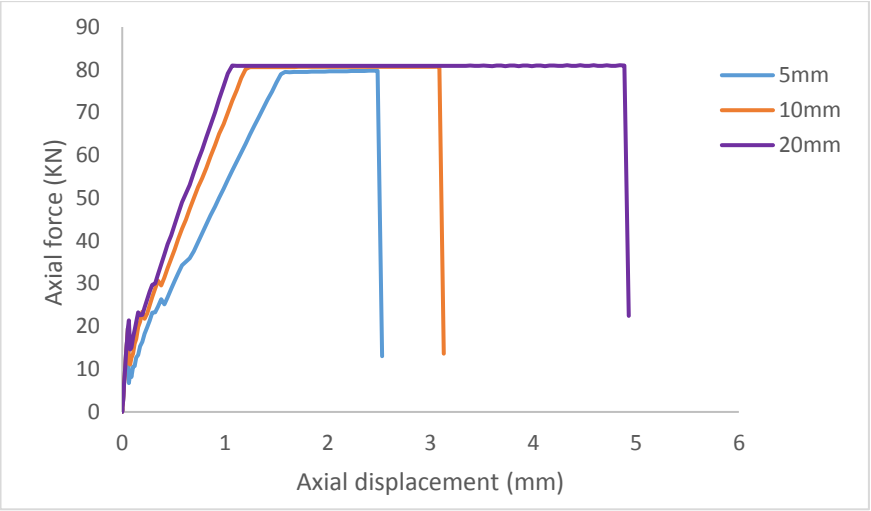

Figure 4.14: Axial load-axial displacement response for model with elastic perfectly plastic stress-strain behaviour of reinforcement

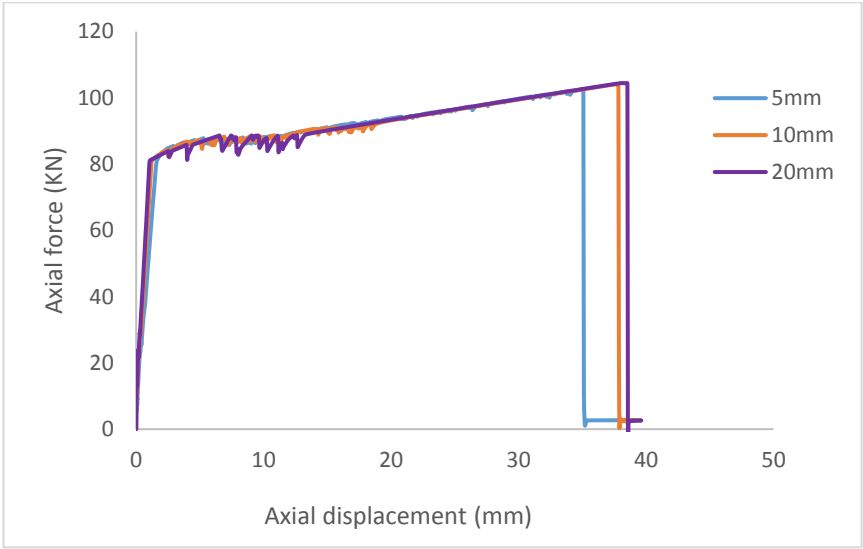

Figure 4.15: Axial load-axial displacement response for model with trilinear stress-strain behaviour (with hardening) of reinforcement

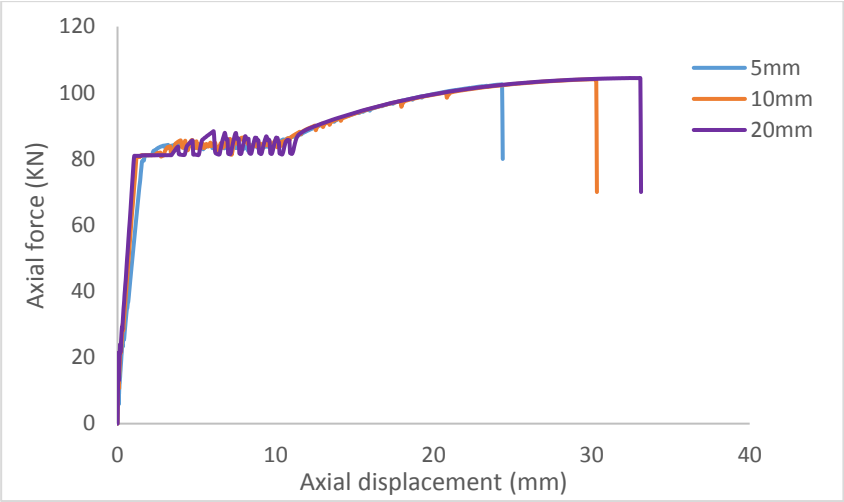

Figure 4.16: Axial load-axial displacement response for model with curvilinear stress-strain (with hardening) behaviour of reinforcement

4.4.2 Mesh sensitivity

FE simulation results are mesh sensitive and this effect may be more pronounced in the simulation of RC assemblies where there is high level of nonlinearity leading to softening of the material. Using a coarse mesh size may result in the stress and strain distributions not being captured properly especially in cases where elements with reduced integration point are used. On the other hand, very small element size will increase the computation cost. Thus, it is important that the sizes of the elements used in the FE model represent to a reasonable accuracy the correct stress and strain distribution and is not overly costly computation wise. To this end, a mesh convergence study is undertaken.

The RC subassemblies tested by Yu and Tan (2013) is used for this exploratory analysis. The beam section was 150 mm by 250 mm and the length of one-half of the beam assembly was 2750 mm giving a length-to-depth ratio (L/d ratio) of 11. Longitudinal reinforcement consisted of 3 nos. Φ13mm and 2 nos. Φ13mm top and bottom at the support section. To simplify the analysis in the present study, the end of the beam is fixed against translation in all directions.

Three different mesh sizes are considered. Since the critical regions are the beam-column interface at the end and middle column regions, the mesh size at these locations are varied and refined but the mesh size in other areas are kept constant. The summary of the mesh size and number of elements for the three different models are presented in Table 1. The FE model is shown in Figure 4.17 for model A as an example. The critical region is assumed to be within 300mm from the end and middle columns.

Table 4.1: Details of mesh size and number of element in the different models

Model ID	Model A	Model B	Model C
Mesh size within critical region	12.5 x 12.5 x 15	12.5 x 12.5 x 20	12.5 x 12.5 x 25
Mesh size in other regions	12.5 x 12.5 x 25	12.5 x 12.5 x 25	12.5 x 12.5 x 25
Number of solid elements	34400	30080	28640
Number of beam elements	1926	1768	1640

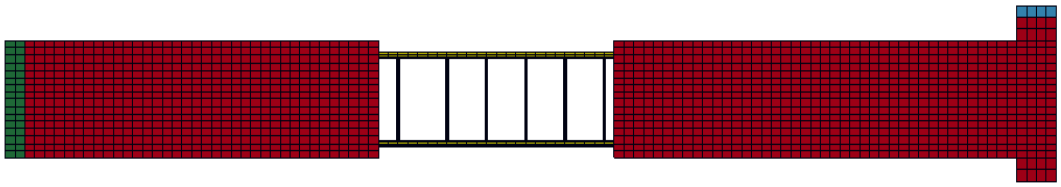

Figure 4.17: Finite element mesh of model C

Concrete is modelled using KCC material model with uniaxial compressive strength of 30MPa. Steel is modelled using mat_24 (PIECEWISE_LINEAR_PLASTICITY). The reinforcement is defined by elastic-plastic behaviour with hardening. Yield and ultimate strength is 500 and 650MPa respectively. The stress-strain relationship of steel used in the study is shown in Figure 4.18. Noting that the stress-strain curve used may have effect on the strain localisation, two different stress strain curves are used. The two stress-strain curves have the same yield and ultimate strain but differs in the hardening properties.

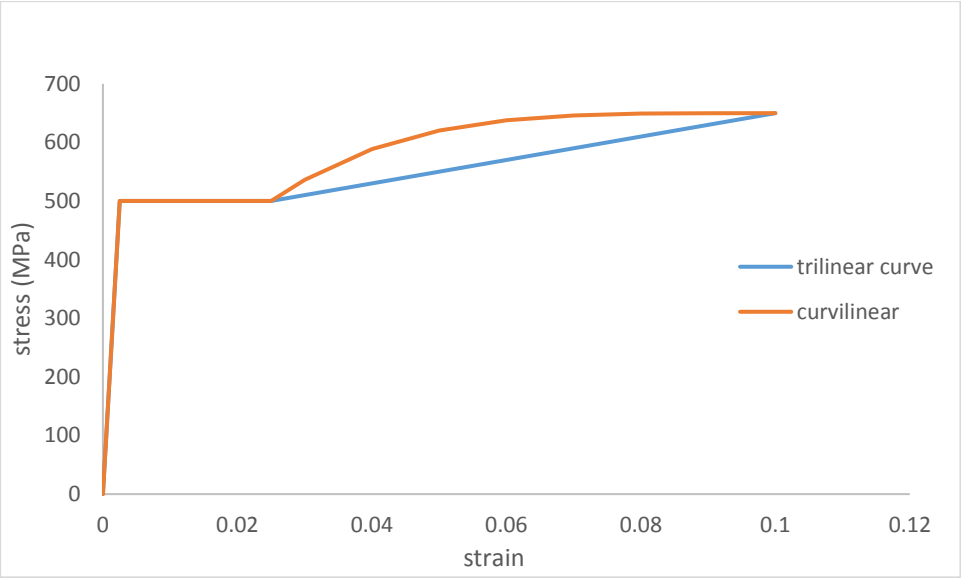

Figure 4.18: Stress-strain curves for reinforcement

The load displacement and axial force-displacement responses for the models with trilinear and curvilinear stress-strain curves are shown in Figures 4.19 and 4.20 respectively. It is seen that the model predictions are similar, however the prediction from model with mesh size of 25mm slightly overestimate the load capacity when compared with predictions from models with mesh sizes of 15 and 20mm respectively. The final failure displacement differs slightly in the models. However, this difference is about 10% and such difference is small hence, failure displacement within these range could be taken as correct failure displacement. Furthermore, the residual strength after rupture of bottom reinforcement could not last for a prolong time before the eventual rupture of top reinforcement near the middle column interface. This is caused by the concentration of strain in single rebar element following the rupture bottom rebar.

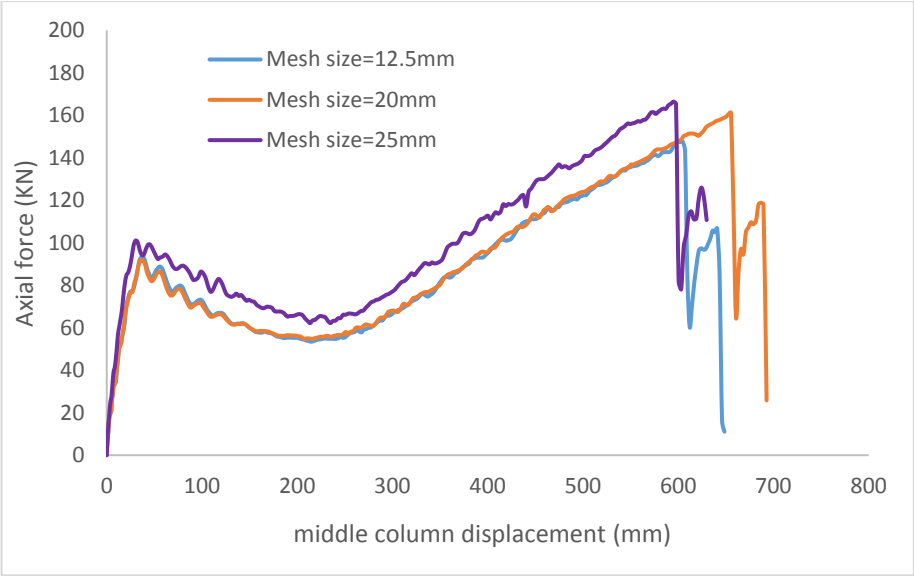

(a) Applied load-middle column displacement response

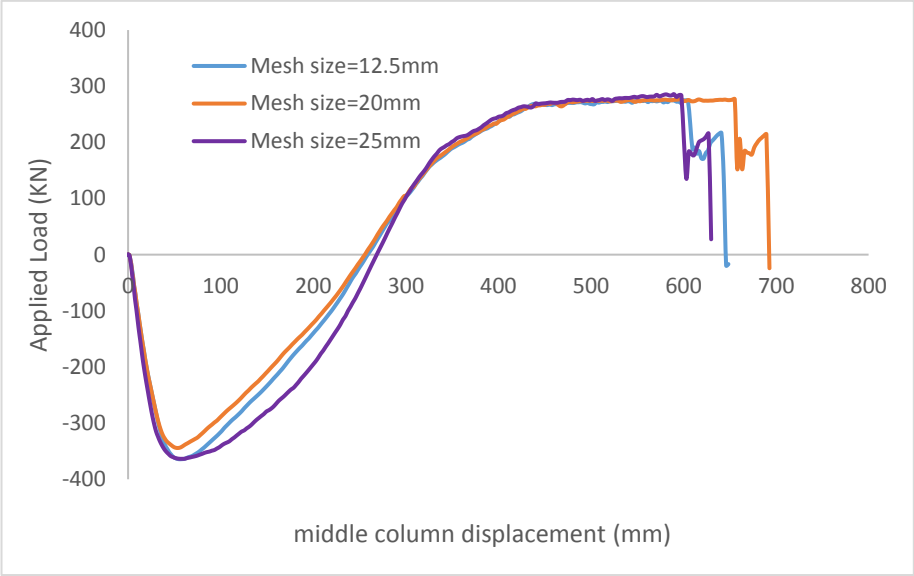

(b) Axial force-middle column displacement response

Figure 4.19: Load and axial force-displacement responses for RC beam with trilinear stress-strain behaviour

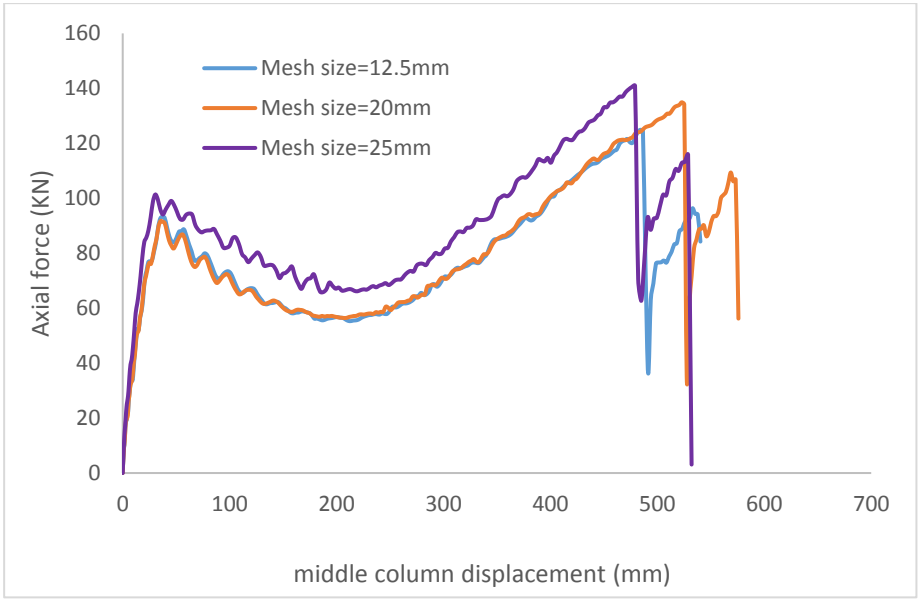

(a) Applied load-middle column displacement response

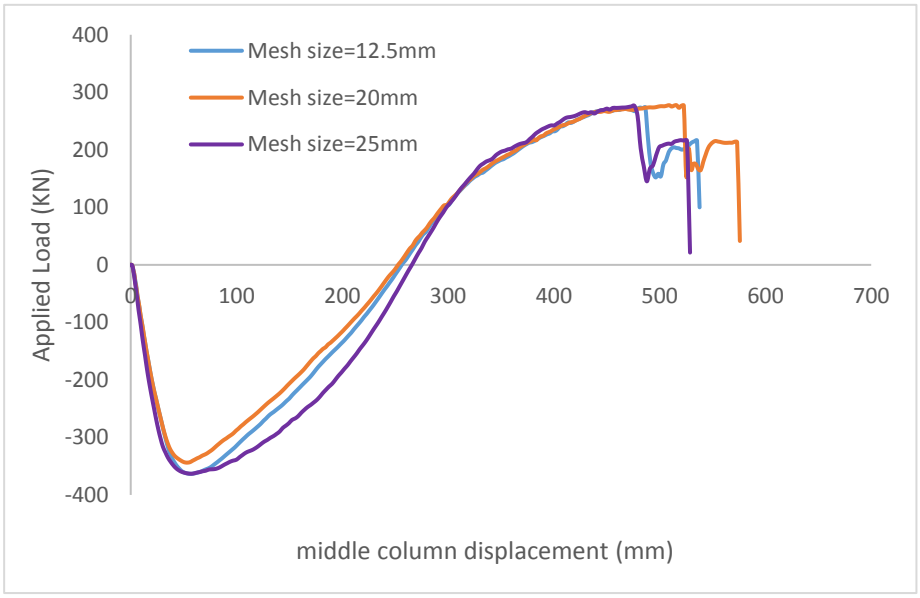

(b) Axial force-middle column displacement response

Figure 4.20: Load and axial force-displacement responses for RC beam with trilinear stress-strain behaviour

The behaviour of the models during the large deformation regime can be further studied using the strain contour distribution. As indicated in Figure 4.21a, the entire beam length was in tension at a displacement of 500mm. A detailed look at the strain contours within the middle column interface (Figure 4.21b) reveals that maximum tensile strain concentrated within a few elements close to the middle column with severe elongation occurring in those elements compared to other elements. The bottom rebar strain distribution along the beam length (Figure 4.22) for models with different meshes shows similar behaviour with strain concentrating within the critical region (around 600mm). It can be concluded that the behaviours are quite similar in the models with different mesh sizes.

From this study, it can be seen that mesh size of 12.5 or 20mm can well capture the behaviour. Hence for the validation study in the next section, mesh size of 12.5mm will be used at the critical section.

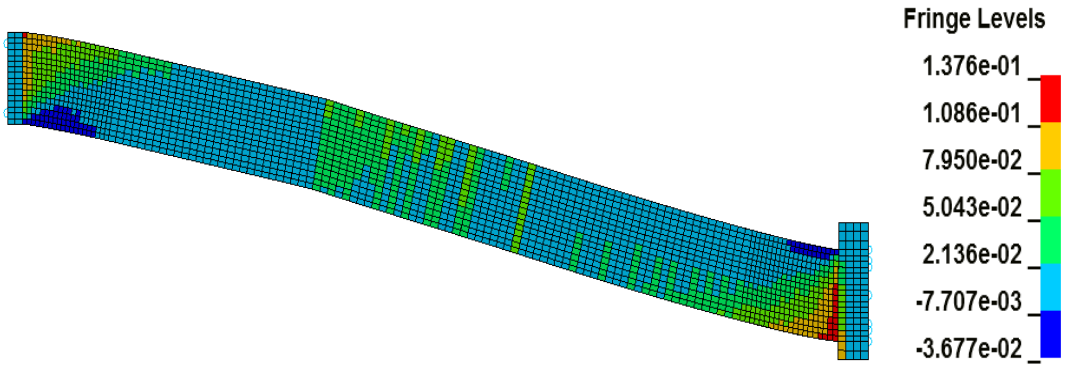

(a) Strain distribution along the beam

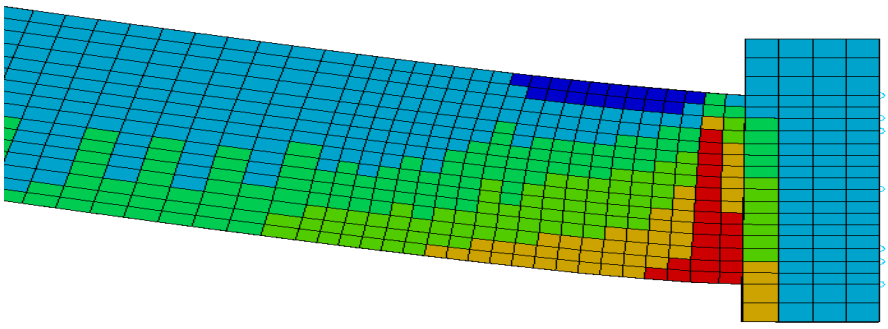

(b) Strain distribution within the middle beam-column interface

Figure 4.21: Strain contour distribution in FE model A at displacement of 500mm

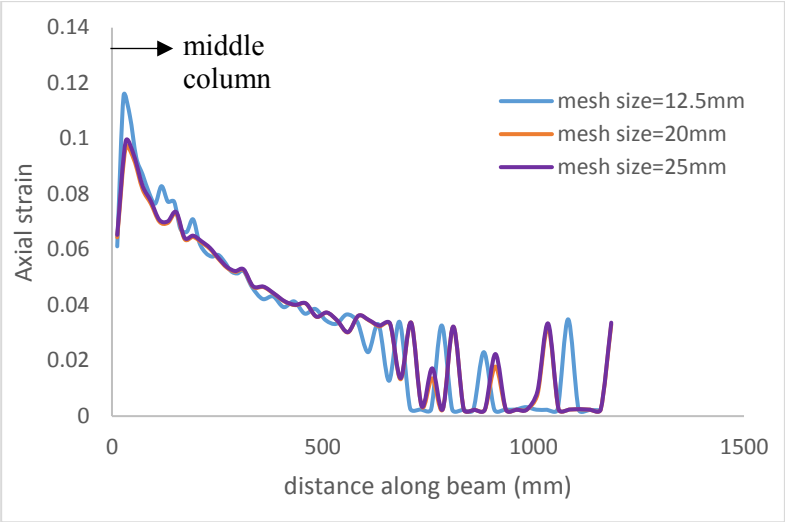

(a) Bottom rebar strain distribution

Figure 4.22: Bottom rebar strain distribution along the beam

4.4.3 Hour glass effect

The use of 8-node elements with reduced integration point offers advantage over fully integrated element in that it reduces the computational cost. However, its disadvantage is that artificial strain energy can be created which may affect the accuracy of the FE model. Hour glassing effect often occurs when there is a distortion in an elements due to force concentration on few nodes. This may be more severe in modelling of RC beam subjected to large deformation. An illustration of the hour glass effect is shown in Figure 4.23.

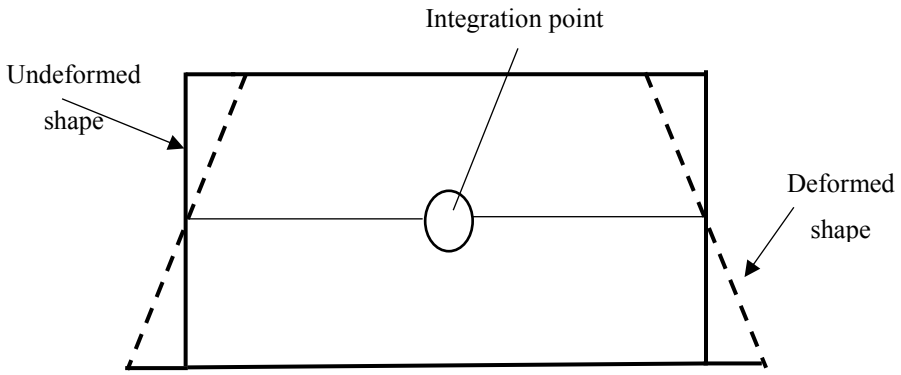

Figure 4.23: Illustration of hour glassing arising from bending deformation with no straining

When hour glassing occurs in FE models, the individual element where the hour glassing occur is severely distorted while the entire section remains undeformed. This will cause the hour glass energy to increase.

In LS DYNA (and similarly in other general-purpose FE codes), the effect of hour glassing can be reduced by using stiffness form of control, among other options, and a factor between 0.03 and 0.1 is recommended. The hour glass effect can be checked by comparing the hour glass energy with internal energy. It is recommended that the hour glass energy should be less than 10% of the internal energy for the FE simulation to be acceptable.

Figure 4.24 shows the comparison of hourglass and internal energy for Model A. The ratio is well below the 10%. Apart from the sudden rise of the energy ratios at the beginning of the loading which is expected, maximum ratio throughout the duration of the simulation was well below 4%.

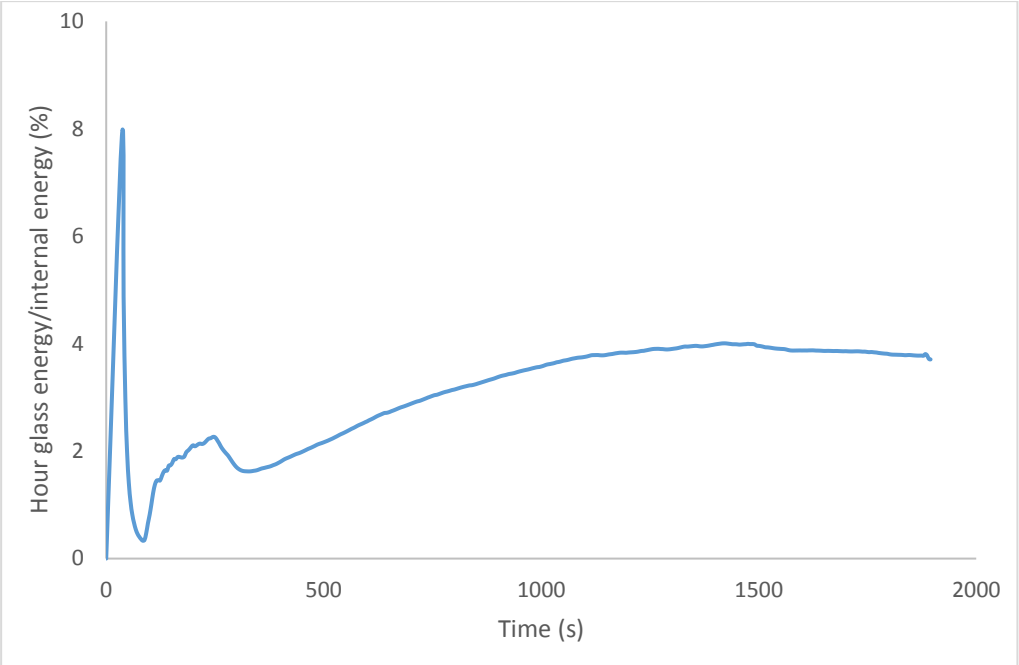

Figure 4.24: Ratio of Hour glass and internal energies during the quasi static loading for model A.

4.5 Validation of numerical models with experimental study by (Yu & Tan 2013b)

4.5.1 Detail of the experiment

In this section the numerical modelling framework is validated using experimental test from Yu and Tan (2013). The experiment was conducted to investigate the effect of reinforcement ratio and span to depth ratio on the structural behaviour of sub-assemblage under column removal scenario. In all, five (5) sub-assemblages were tested. In the present study, two of the tested beams (S4 and S6) are modelled.

The elevation and plan view of the sub-assemblage is shown in Figure 4.25 while the geometric and reinforcement detail of two of the specimens selected for the validation study is presented in Table 4.2. Concrete tensile and compressive strength were 3.5MPa and 38.2MPa respectively. Yield strength of 13 and 16mm reinforcement was

494 and 513MPa while ultimate strength was 594 and 612MPa respectively. The rupture strain for 13mm bar was 0.11 and that of 16mm rebar was 0.13.

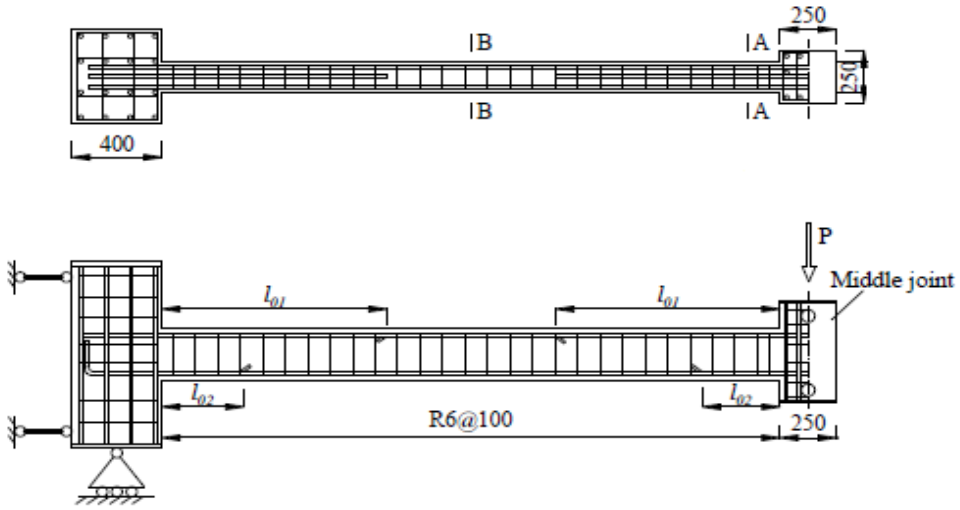

Figure 4.25: Elevation and plan view of the tested specimen (Yu & Tan 2013b)

Table 4.2: Reinforcement detail of beam-column sub-assemblage (Yu & Tan 2013b)

Specimen ID	Ln (mm)	Longitudinal reinforcement				Bottom rebars at middle joints
		A-A		B-B		
		Top	Bottom	Top	Bottom	
S4	2750	3T13 (1.24%)	2T13 (0.82%)	2T13 (0.82%)	2T13 (0.82%)	continuous
S6	2750	3T16 (1.87%)	2T13 (0.82%)	2T16 (1.25%)	2T13 (0.82%)	continuous

The end columns were connected to a reaction wall on one side and steel A-frame on the other side to simulate the axial restraint. The vertical support was provided by a pin connection which rested on a steel roller. This was to avoid the effect of horizontal reaction and therefore make the entire setting independent. To avoid lateral movement of the beam, lateral restraint was provided at each side of the middle column. Displacement controlled loading was provided by an actuator which acted at a rate of 0.1mm/s to avoid any dynamic effect.

4.5.2 Overview of the finite element model for the test beam assemblies

Concrete is modelled with 8-node solid element with reduced integration while reinforcement is modelled with 2-node beam element. Although the stiffness of the two end columns in the test was found to be slightly different, only half of the beam is modelled taking advantage of symmetry. The "beam" elements representing rebar are embedded into the solid element through node sharing. This represents a perfect bond condition between rebar and surrounding concrete and renders the "bond-slip" behaviour to the softening of concrete elements interacting with the rebar, as mentioned in Section 4.3.

As reported in the test, gaps existed between the connection and the end columns. To simulate the sub-assemblage behaviour accurately, such gaps needs to be taken into consideration. In the FE model, nonlinear spring elements (S04) in LS DYNA were used to simulate the axial behaviour. The spring elements were connected to a steel plate with elastic properties (MAT 001) similar to the test set up to avoid stress concentration. To avoid stress localisation, 15 springs with smaller stiffnesses were used to model the end axial restraint as shown in Figure 4.26. Force-displacement behaviour of these springs including the gaps that existed between the end column and connection (as shown in Figure 4.26a) were obtained from the referenced paper.

From mesh sensitivity study, it was shown that concrete mesh size of 12.5 x 12.5 x 12.5mm for the critical region yielded satisfactory accuracy in terms of the mesh. Thus, this mesh size was adopted to model the critical section while the mesh size at the less critical section was 25mm. As noticed in the mesh sensitivity studies, the mesh size of the rebar may cause strain localisation in the top bar after rupture of bottom bar. To avoid this problem, the mesh size of rebar was doubled within the critical section, hence rebar mesh size was 25mm.

Figure 4.26 shows the test and finite element model of the end columns. Similar to the test, steel plate with elastic properties were placed on the middle column to avoid local failure. The top nodes of this plate were push down in a displacement controlled manner.

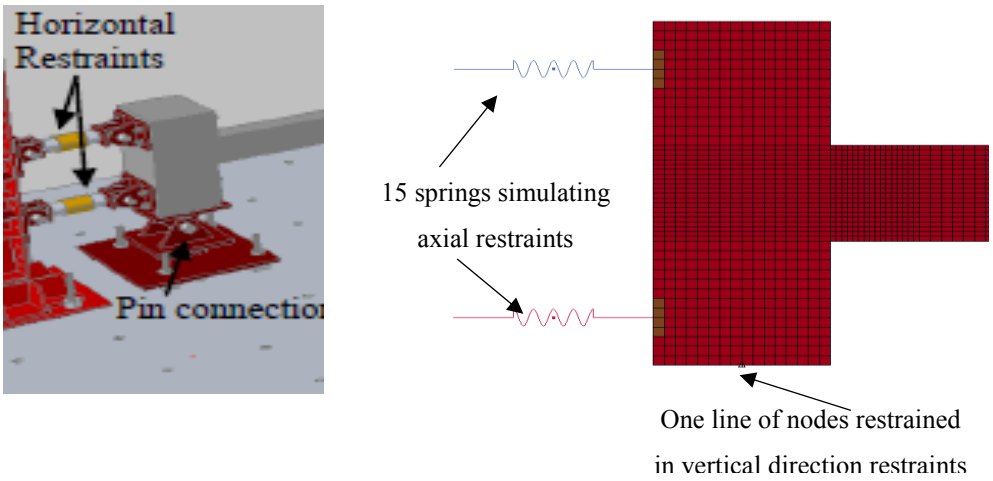

Figure 4.26: Details of boundary condition in the experimental test and FE assemblies

Figures 4.27 and 4.28 shows the load-displacement and horizontal reaction-displacement relationships for the two assemblies modelled in this study. It can be seen that the models predict to a reasonable accuracy the key phenomenon observed in the experiment. However, the maximum compressive arching action capacity is slightly over predicted by the FE models. Also, the FE models under predict the failure displacement in the two specimens. It could however be argued that the actual rupture strain in a rebar may reinforcement vary a lot. For example, two different tests on the same material may yield different rupture strain. Also, the material is not perfect and as can be observed from the experimental load-displacement response in Figures 4.27 and 4.28, the rupture of bottom rebars on either side of the middle column did not occur simultaneously whereas in the FE model it failed at the same time. Regardless of these few differences, the FE model results agrees well with the experimental test results in terms of the over-all response and the failure modes.

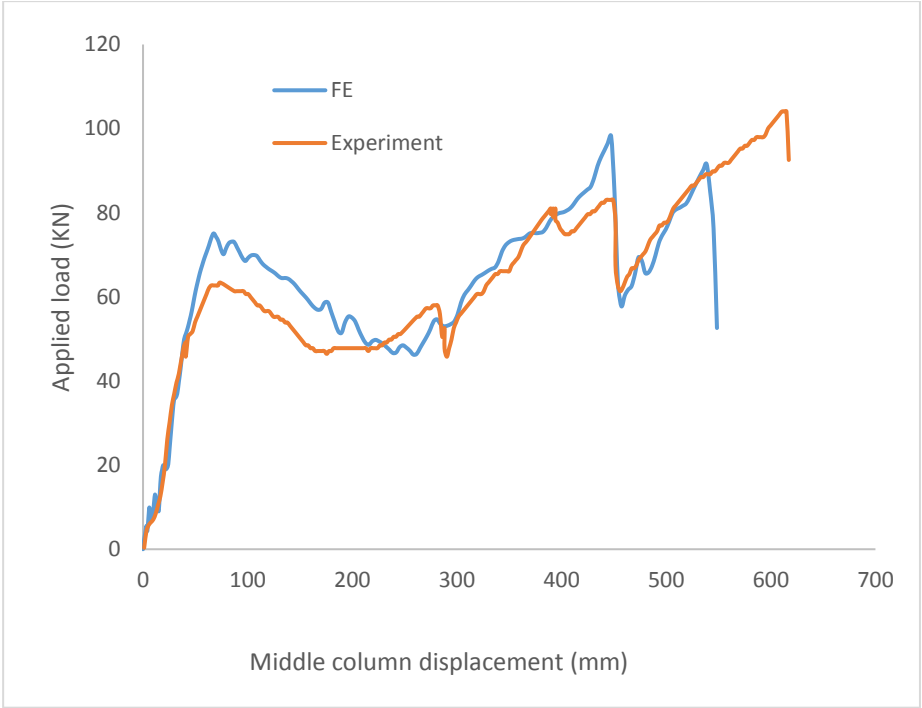

(a) Applied load-middle column response

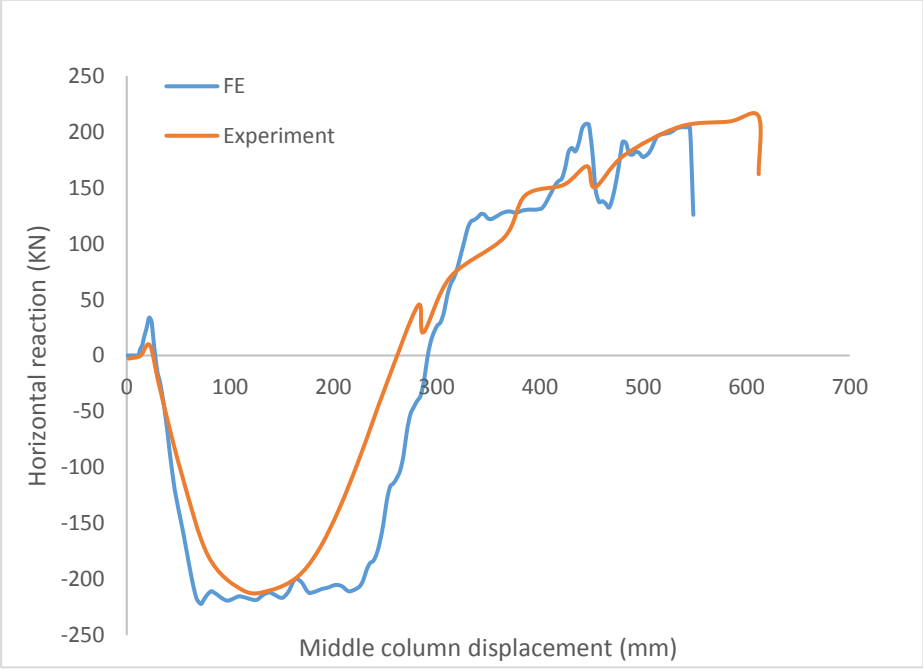

(b) Horizontal reaction-middle column displacement response

Figure 4.27: Comparison of responses from FE and experiment for specimen S4

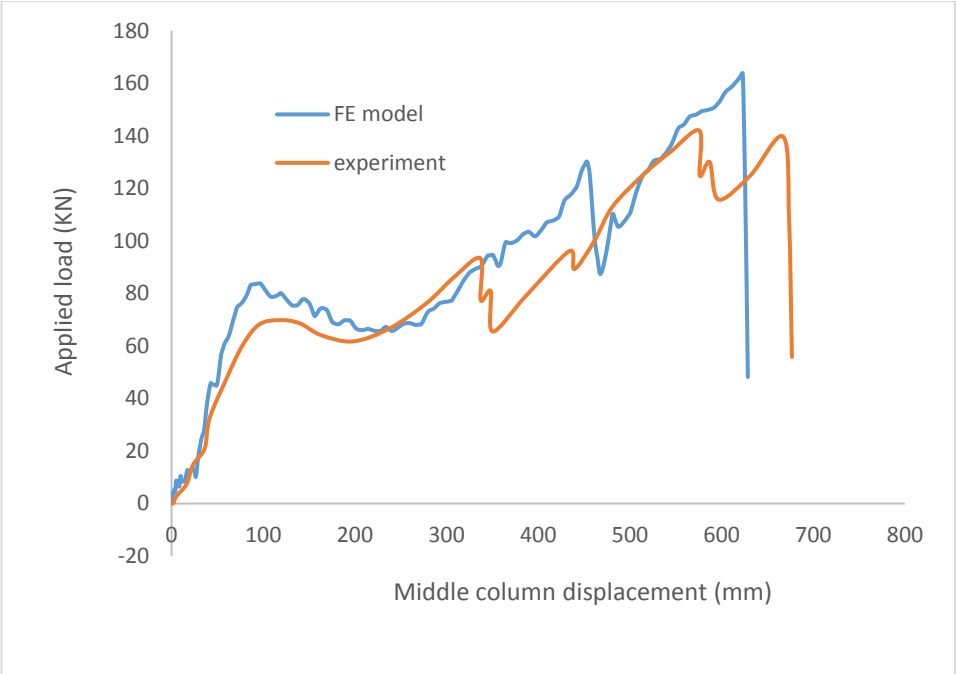

(a) Applied load-middle column response

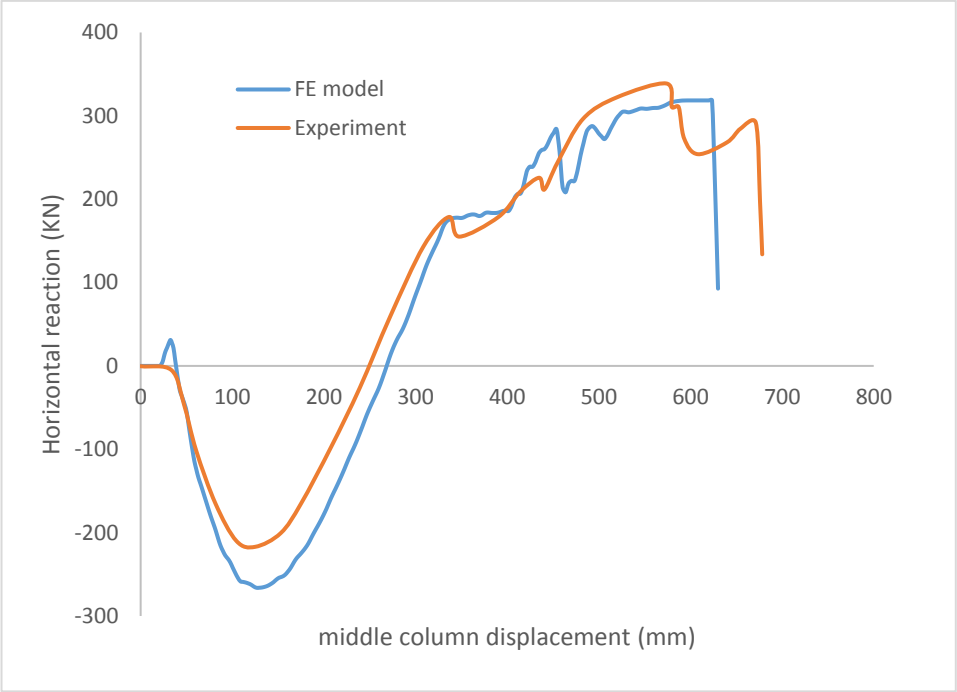

(b) Horizontal reaction-middle column displacement response

Figure 4.28: Comparison of responses from FE and experiment for specimen S6

The damage pattern from experiment and FE models are shown in Figures 4.29 and 4.30 for specimens S4 and S6 respectively. It is seen that in test and FE models, damage concentrated within the middle and end beam column interface. Although element erosion was not considered in the numerical models, it can be observed that concrete near the end and middle column are severely damaged. This is similar to the test where concrete eroded. A close look at the damage pattern from FE models further shows that failure mode was perfectly captured and failure was caused by the fracture of bottom rebar near the middle column which was followed by fracture of top rebar at a much larger middle column displacement.

(a) test

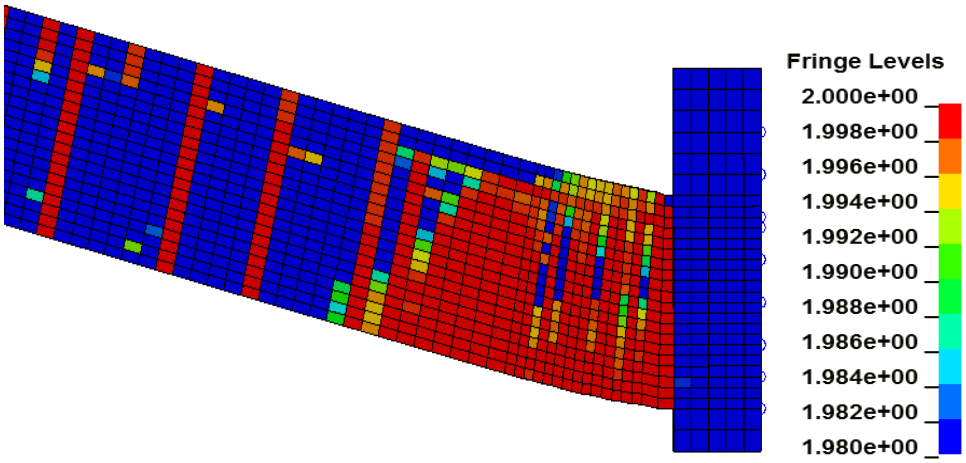

(a) FE model

Figure 4.29: Comparison of damage pattern from FE and experiment for Specimen S4 (SDF=1.98-2.0)

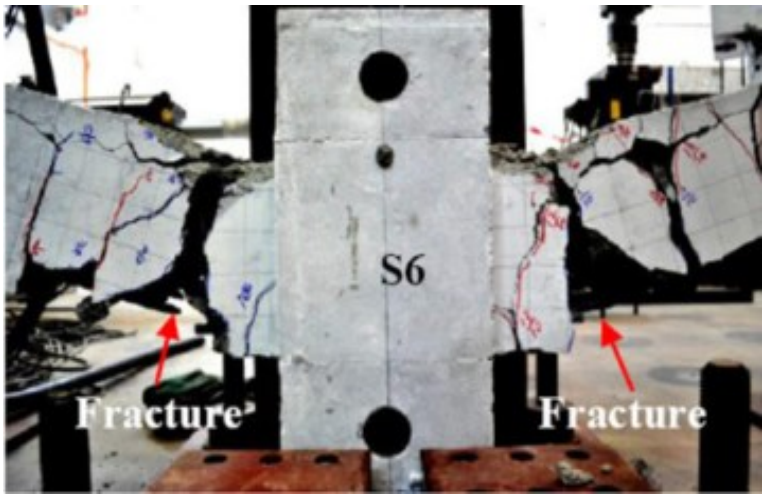

(a) Test

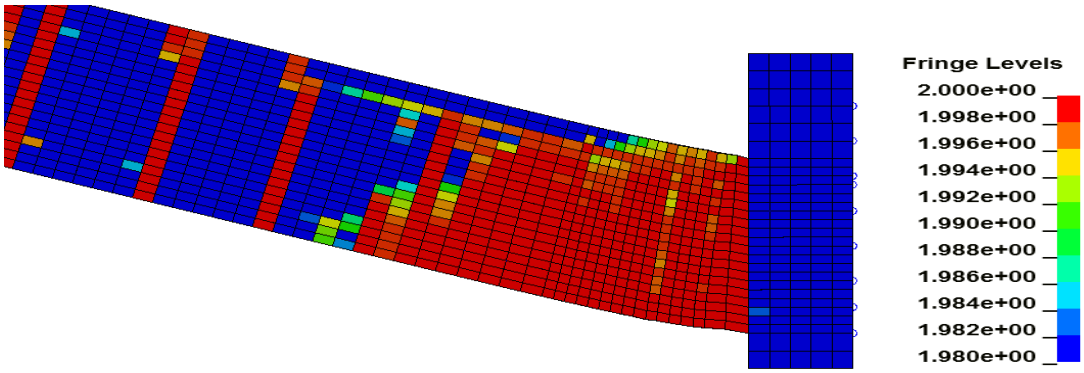

(b) FE model

Figure 4.30: Comparison of damage pattern from FE and experiment for Specimen S6 (SDF=1.98-2.0)

4.6 Concluding remarks

This chapter presents a numerical modelling scheme for simulating the behaviour of RC beam-column assembly under a progressive collapse scenario, with particular attention on the concrete material modelling and rapture of reinforcement bars; these features are crucial in a realistic simulation of the arching effect and the extent to which catenary effects may be developed. Thus, the choice of material model for modelling concrete is presented and essential verification and validation of the material model carried out. Localisation phenomena and the associated mesh sensitivity for rebar are examined and possible approaches to minimise such an effect are discussed.

Other general modelling considerations and possible issues, such as general mesh sensitivity and hour glassing, which can affect the simulation results in modelling of RC assemblies are also discussed.

Finally, the developed model is benchmarked against experiment tests and it is found that the FE models replicates well the key features observed in the experiment. Although for the particular cases examined, the model tends to slightly over predict the response of compressive arching action, it can be observed that the model accurately represented the failure modes which included concrete cracking at the

critical beam-column interface, followed by rupture of bottom rebar and final failure caused by rupture of top rebar.

The FE model will be employed in subsequent chapters to assist in the investigations of progressive collapse behaviour of representative RC designs.

Chapter 5: Theoretical model on compressive arching action and associated deformation limit state in axially restrained reinforced concrete beam

5.1 Introduction

From the critical review and analysis of experimental studies on compressive arching action in Chapter 3, it is seen that the load capacity in axially restrained RC assemblies is greater than its flexural capacity, and this increase in the load capacity is due primarily to the arching compression. The arching effect depends on the reinforcement ratio, span-depth ratio, concrete compressive strength and axial restraint.

Due to the significant magnitude of the arching capacity, it is important to be able to predict the arching capacity more accurately, and this may only be achieved through models that adequately represent the underlying mechanisms. A number of analytical models on compressive arching action have been developed (Yu & Tan 2014; Alogla et al. 2017; Abbasnia & Nav 2016; Rankin & Long 1997b; Christiansen 1963). Some of these models treat the contribution from flexure and arching action in an uncoupled manner (Rankin & Long 1997b; Abbasnia & Nav 2016), while others treat the arching action in a coupled manner such that the axial force causes an increase in the moment capacity of the section, but at the same time a P-delta effect arises which tends to reduce the load capacity (Yu and Tan, 2014; Alogla et al., 2017).

A more detailed review of representative theories in the literature and their formulations, which is presented in Section 5.2 of this chapter, reveals that some limitations exist and consequently the models may not capture realistically the response of RC assemblies in terms of the arching action in certain cases. For example, Tan and Yu's model ignores the bending deformation and as such under-predicts the displacement corresponding to the maximum arching action capacity. More so, there is no provision to check for strain in the critical section in this model. Rankin's model,

which was initially developed for RC slabs, does consider the load resistance to be contributed by bending and arching deformations; however, the effect of compression reinforcement on the arching contribution is not considered. This could result in under-prediction of the response. Also, Rankin's model only predicts the maximum arching capacity. For a comprehensive assessment of progressive collapse resistance of the beam-column assemblies, an accurate determination of both the arching resistance capacity and the range of displacement upon which the arching action is effective, i.e. the energy absorption capacity, is required. However, the deformation aspect associated with the arching effect has seldom been examined in previous studies.

To address these problems, a theoretical model on compressive arching action which takes into consideration of the compounding flexural and arching deformations, and hence the stress-strain and damage state of concrete in the critical compressive zones is proposed.

5.2 Development of the Analytical Model: Basic Considerations

5.2.1 General Concept

Figure 5.1 shows a typical RC sub-assemblage subjected to a concentrated load at the middle column, representing a situation with a double-span beam created due to removal of the middle column. In an idealised condition, the ends are assumed to be fixed against translation and rotation. Due to the restraint at the ends, the tendency of the RC beam to expand with increasing load (P), is prevented. This causes the development of axial compressive force which acts in turn to increase the vertical load bearing capacity of the beam.

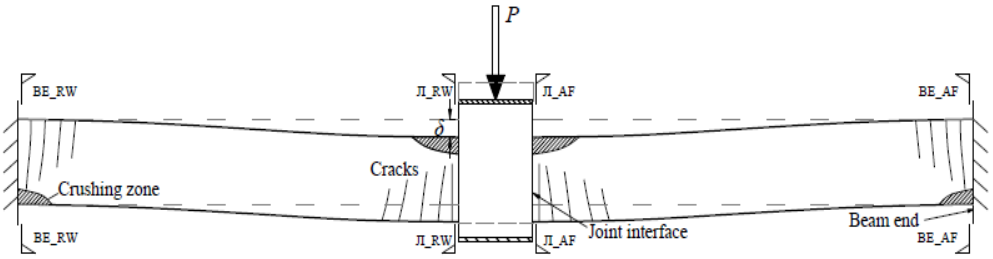

Figure 5.1: A beam-column subassembly under concentrated load at middle column (Yu and Tan, 2014)

Figure 5.2 shows a conceptual illustration of the combined bending and arching effects while an RC beam is deflected. The external load is represented by a point load at the column loss location, but it could also be distributed load over the beam spans. Taking advantage of the symmetry, only the deformed shape of one-half of the beam and the forces acting are shown.

In this model, the bending and arching modes share the same vertical displacement of the middle point, but the flexural mode is associated with a presumable pure bending deformation with no axial force interference. For the sake of analysis, the bending and arching effects are decoupled into two separate mechanisms as shown in Figures 5.3a-b. From these Figures, the overall vertical resistance is comprised of a pure flexural resistance and the compressive arching action.

From the force point of view, this can be separated into two sets of equilibrium systems, namely a) bending, and b) arching action.

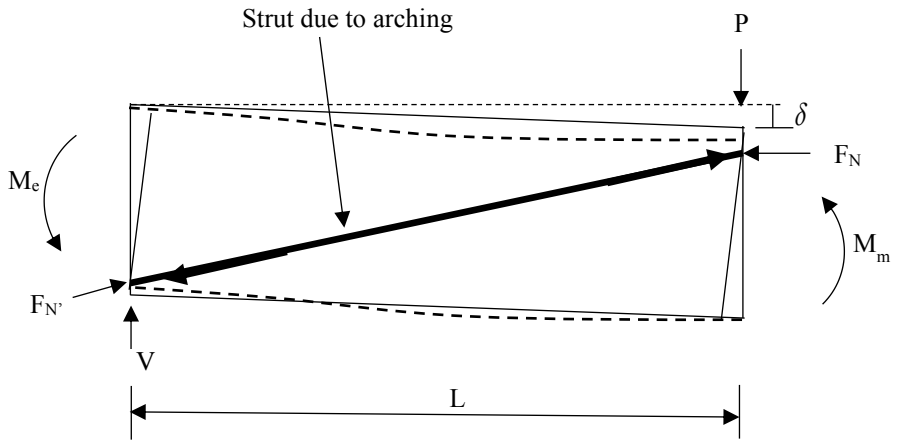

Figure 5.2: Free body diagram showing all forces acting on the beam, and the co-existing bending and arching modes of resistance

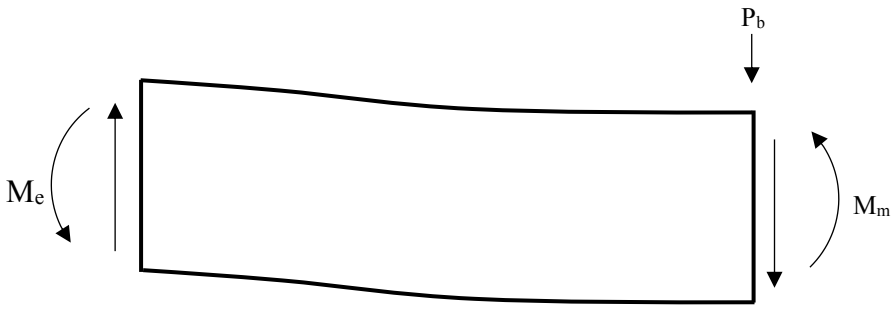

(a) Bending mode

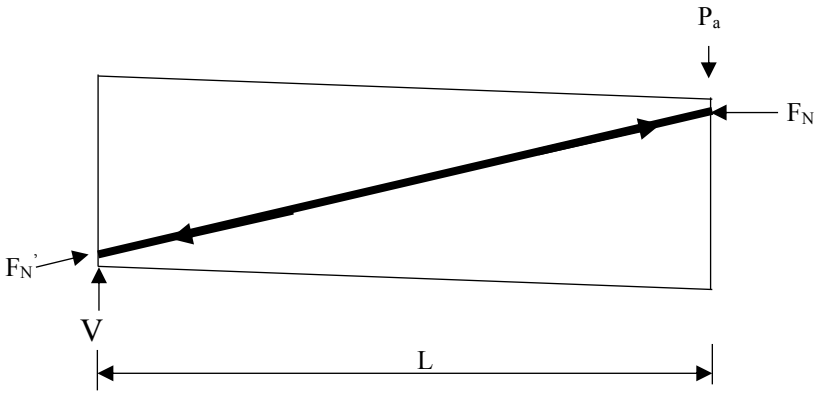

(b) Strut/arching action mode

Figure 5.3: Free body diagram showing the two sets of forces corresponding to bending and arching action modes

For simplicity, the response is divided into elastic and plastic response. Figure 5.4 shows the idealised load displacement response in the proposed model. The response in each of the stages will be discussed in the section that follows.

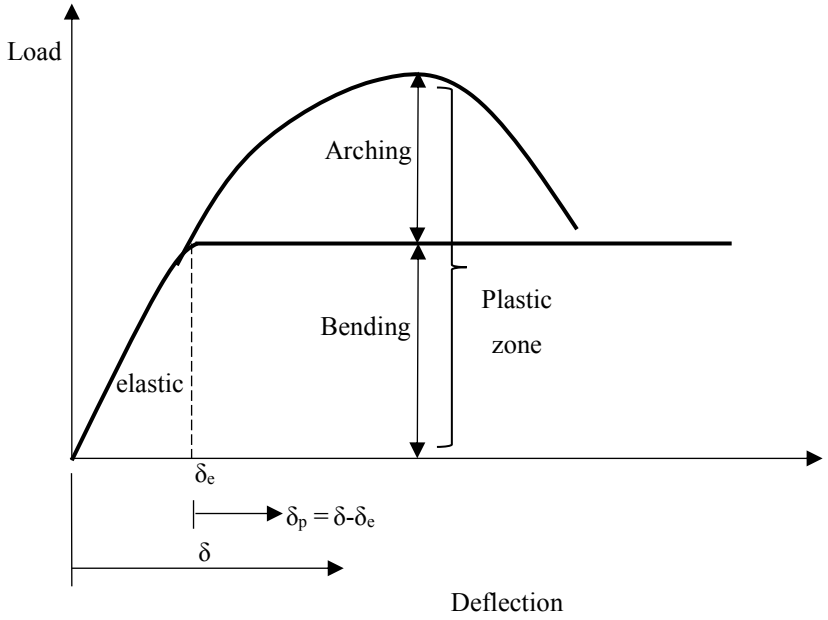

Figure 5.4: Load-displacement response showing the elastic and plastic stages in the proposed model

5.2.2 Different stages of response

5.2.2.1 Pre-arching stage (elastic bending stage)

During the elastic stage of the response it is assumed that only bending deformation occurs. For the present purpose, the elastic response stage ends when tensile reinforcement starts to yield. It should however be noted that for RC beams, there is no perfect elastic stage as yielding occurs from the moment when tensile reinforcement reaches initial yield, and goes on until the stresses over the concrete becomes stabilised.

Let the plastic moment capacities at the end and middle sections be represented by M_e and M_m respectively. Using the strain and stress distribution in Figure 5.5, the load

and the corresponding middle point displacement at the end of elastic stage can be determined as:

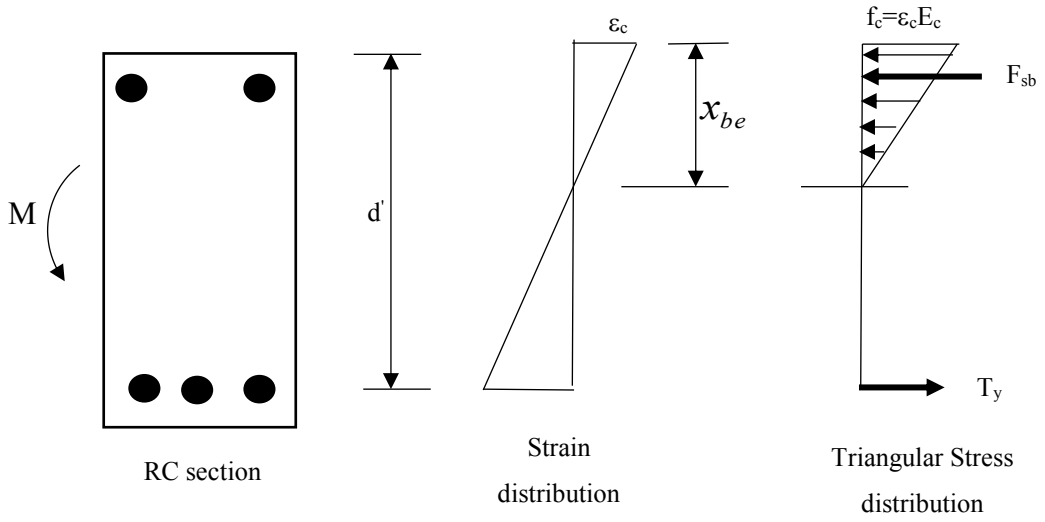

Figure 5.5: Section stress and strain distribution at elastic bending mode

$$P_b = \frac{2(M_e + M_m)}{L} \tag{5.1}$$

$$\delta_e = \frac{P_b(2L)^3}{192E_cI_e} \tag{5.2}$$

Combining equation Equations (5.1) and (5.2) the displacement corresponding to end of elastic bending stage can be expressed in terms of the plastic moment capacities as:

$$\delta_e = \frac{(M_e + M_m)L^2}{12E_cI_e} \tag{5.3}$$

Where I_e is the effective moment of inertia which is calculated as per the ACI 318 requirement. Due to the difference in the moment of inertia at support and mid-span sections, the average moment of inertia according to ACI 318 code and is given as:

$$I_e = 0.5\left(I_{e,\sup} + I_{e,mid}\right) \tag{5.4}$$

Where $I_{e,sup}$ and $I_{e,mid}$ are the effective moment of inertia at the support and mid-span sections respectively and is defined as:

$$I = \left(M_{cr}/M_b\right)^3 * I_g + \left[1 - \left(M_{cr}/M_b\right)^3\right] * I_{cr} \leq I_g \quad (5.5)$$

Where M_{cr} corresponds to the cracking moment, M_b is the moment at the section considered, I_{cr} is the moment of inertia of cracked section and I_g is the gross moment of inertia. The effective moment of inertia corresponding to the yield moment for support and mid-span sections are calculated using Equation (5.5), after which the average moment of inertia for the beam is determined using Equation (5.4).

5.2.2.2 Arching stage ("Plastic stage")

Following major cracking and yielding of the critical sections at the end support and middle column interface, the bending and arching modes occur concurrently. For a given deflection δ, the load resistance is contributed by bending and arching, and at the same time, the strain deformation in the end and middle-column regions is caused by both the bending and arching modes, which in turn affects the magnitude of arching effect which could develop. Each of these modes will be discussed in the section that follows.

5.2.2.2.1 Bending mode

For the pure bending mode of the response at a given deflection, we need to establish the following:

a) the bending strains and stresses at the middle and end sections.
b) Bending moment at the middle and end section and hence the bending resistance (P_b).

However, let us concentrate on the response stages "around" the peak arching effect first. Let's further assume that at this stage both end regions have already developed plastic hinges. The plastic moments at the end and middle section are M_e and M_m respectively assuming symmetry.

Let the deflection under consideration be δ,

Plastic deflection is given as:

$$\delta_p = \delta - \delta_e \tag{5.6}$$

where δ_e is the elastic limit deflection.

Plastic rotation at the end is calculated as:

$$\theta_p = \frac{\delta_p}{L} \tag{5.7}$$

The total plastic strain at the end and middle sections can be evaluated from the above plastic rotation if a plastic hinge length is known. For an indicative purpose in this formulation, let us assume

$$L_p = \alpha \times \delta = 1.0d \tag{5.8}$$

where d is the beam depth.

Plastic strain in the extreme compressive fibre (same as the critical zone due to arching zone) at the "end" and "middle" sections are:

$$\varepsilon_{cp1} = \frac{\theta_p}{L_p} x_{bp1} \tag{5.9}$$

$$\varepsilon_{cp2} = \frac{\theta_p}{L_p} x_{bp2} \tag{5.10}$$

where x_{bp1} and x_{bp2} are the compression zone depths at end and middle sections.

It should be noted that during the plastic response stage, the compression zone due to bending further reduced as the stress distribution becomes parabolic. Hence, the concrete compressive stress distribution can be represented by the equivalent stress block. With this assumption, the compression zone depth for bending (x_{bp}) can be determined for the end and middle sections.

For the determination of the strain in the compressive concrete, which is a key parameter in the new formulation for the analysis of the arching effect, the standard beam analysis can be carried out. Total strain due to bending at the end and middle sections comprised of elastic and plastic strain and equals:

$$\varepsilon_{c1} = \varepsilon_e + \varepsilon_{cp1} \tag{5.11}$$

$$\varepsilon_{c2} = \varepsilon_e + \varepsilon_{cp2} \tag{5.12}$$

where ε_e denotes the compressive strain at the elastic limit stage.

The above concrete compressive strains are to be employed to evaluate the status of the concrete deformation and stresses in the critical regions in relation to the bending deformation.

5.2.2.2.2 Strut/Arching mode

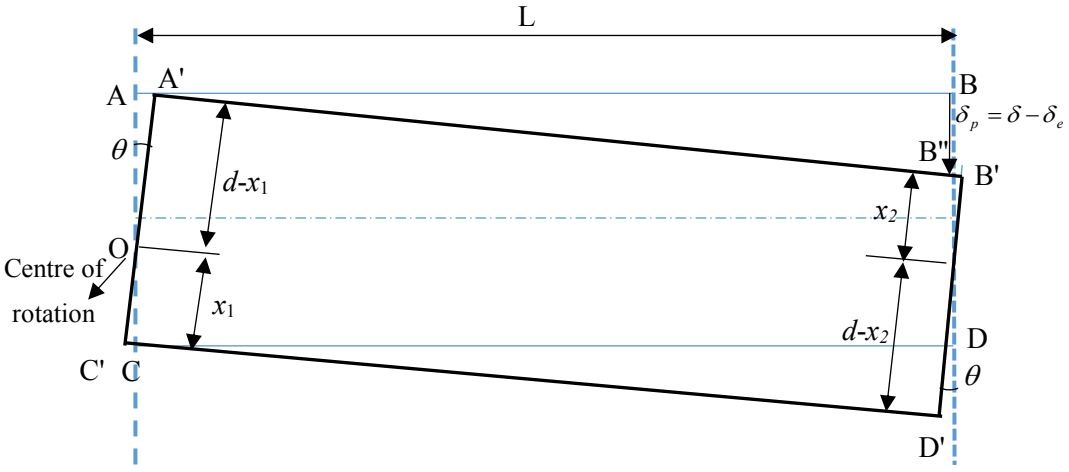

Figure 5.6: Rigid block movement of the beam

For the strut/arching mode of response, including the arching compression forces and the lever arm, and hence the arching moment of resistance, it is necessary to establish the following:

a) Under a given deflection δ, the compressive displacement of the "strut"; this will lead to the evaluation of the compressive strain;
b) The compressive zone depth, at the end and middle sections;

The above will then allow the establishment of the compressive stress and their distribution in the compressive zones, and in combination with the stress and strain states from the bending analysis, will further allow an evaluation of the state of the compressive concrete and the arching (moment) resistance.

As the basic case, the supports (end and middle) are assumed to be rigid firstly. The kinematics can be established by using a rigid body rotation analogue, as illustrated in Figure 5.6. The original beam segment is represented by a rectangular ABCD. Assuming the centre of rotation at the left end of the beam is point O, i.e. the compression zone depth is defined by OC (or OC'), where $OC' = x_1$. The displaced position of the beam is A'B'C'D'. For a given deflection δ, the plastic rotational angle $\theta_p = \delta_p / L$. Where $\delta_p = \delta - \delta_e$

For generality, assume the compression zone at the middle section (right end in Figure 5.6) is x_2. The governing geometric equation can be expressed as:

$$(A'B'')^2 = (A'B)^2 + (BB')^2 \tag{5.13}$$

where:

$$A'B'' = A'B' - B''B' = L - \theta \times x_2 \tag{5.14}$$

$$A'B = AB - AA' = L - \theta \times (d - x_1) \tag{5.15}$$

Substituting Equations (5.14) and (5.15) into (5.13),

$$(L - \theta \times x_2)^2 = [(L - \theta \times (d - x_1)]^2 + {\delta_p}^2 \tag{5.16}$$

Expanding, ignoring second order increment (θ) terms

$$-2L\theta x_2 = 2L\theta x_1 - 2L\theta d + {\delta_p}^2 \tag{5.17}$$

Noting $\theta_p = \delta_p / L$, it can be found that:

$$x_1 + x_2 = d - \frac{\delta_p}{2} \tag{5.18}$$

Equation (5.18) satisfy the geometric requirement of the rigid body rotation.

This also means using the rigid body rotation assumption alone will not lead to a unique solution for the compression zone sizes. For example, if $x_1 \to 0$, $x_2 \to (d - \delta_p / 2)$ as illustrated schematically in Figure 5.7.

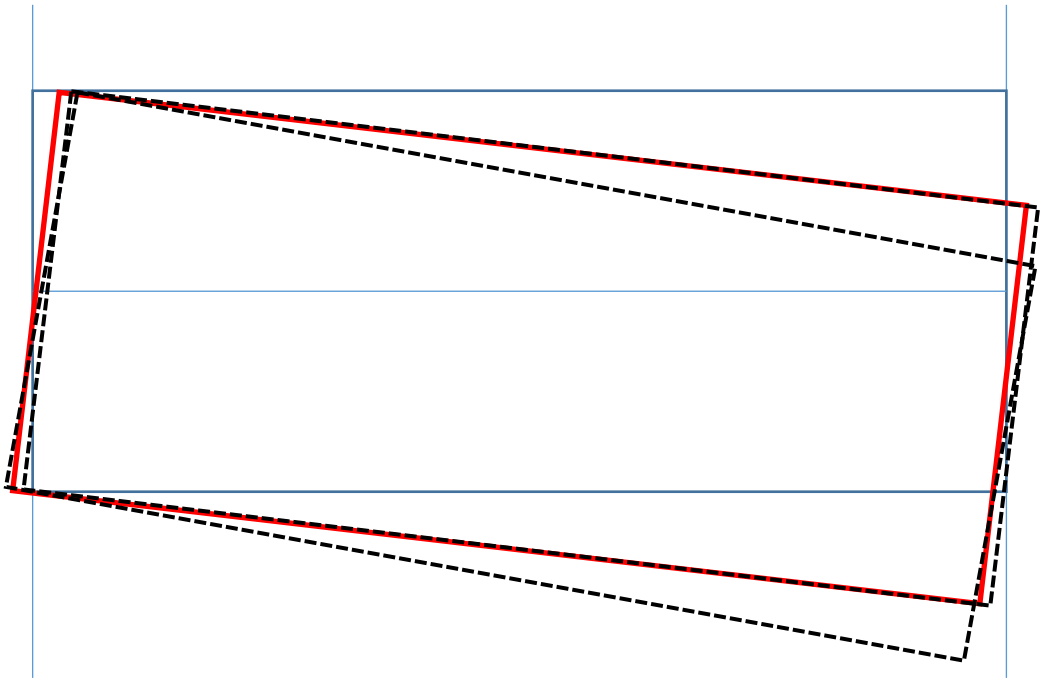

Figure 5.7: Simple illustration of geometrically compatible combinations of compression zone scenarios

A unique solution will require a further equation, and this can be sought from the equilibrium of horizontal compression forces. In the case of uniform design properties, the force equilibrium will imply that equal compression zone sizes at the two ends arise, i.e., $x_1 = x_2$, thus:

$$x_1 = x_2 = \frac{d}{2} - \frac{\delta_p}{4} \tag{5.19}$$

In a more general case with unequal reinforcement between the two compression zones, an equilibrium equation in the following form will arise:

$$F_{CN1} + F_{sN1} = F_{CN2} + F_{sN2} \tag{5.20}$$

Where F_{CN1} and F_{sN1} denote respectively the compressive force in concrete and compressive steel that may be attributed to the aching action at the left support section, F_{CN2} and F_{sN2} are the corresponding counter parts at the middle section (right end in the Figure 5.6).

The actual compressive forces in concrete and steel that may develop from the arching deformation will depend on the strain and stress state in the compressive zones taking into account the concurrent bending deformation in these zones.

For illustration purpose let us assume the compressive stresses from the arching deformation develop independently from bending, i.e. $x'_1 = x_1$ and $x'_2 = x_2$. Let us further assume that compressive steel is at the yield state at both ends, it follows that:

$$f_c b \beta x_1 + f_y A'_{s1} = f_c b \beta x_2 + f_y A'_{s2} \tag{5.21}$$

Thus:

$$x_1 - x_2 = \frac{f_y}{f_c \beta b}\left(A'_{s2} - A'_{s1}\right) \tag{5.22}$$

Solving Equations (5.41) and (5.37) yields:

$$x_2 = \left(\frac{d}{2} - \frac{\delta_p}{4}\right) - \frac{f_y}{f_c \beta b}\left(A'_{s2} - A'_{s1}\right) \tag{5.23}$$

For arching mode of response, the maximum strain in the compressive concrete at the end and middle sections can be related to the compressive deformations of U_1 and U_2

being distributed over an equivalent plastic deformation region of length L_{N1} and L_{N2} as illustrated in Figure 5.8 (for middle section).

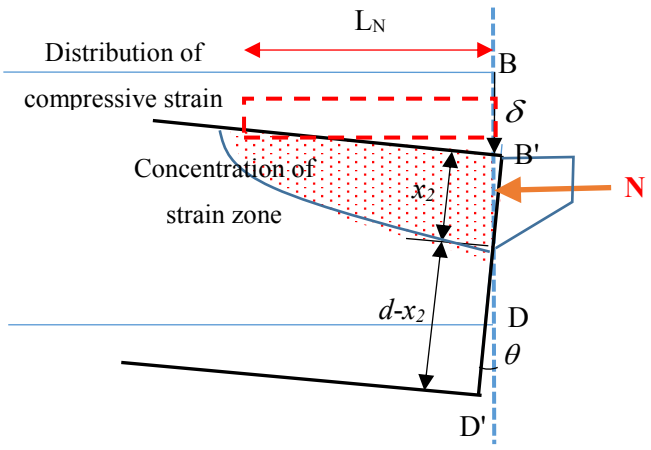

Figure 5.8: Schematic of concrete strain distribution in the compression zone

Edge compression at end section:

$$U_1 = C'C = \theta * x_1 = \frac{\delta_p}{L} x_1 \tag{5.24}$$

Edge compression at middle section (right end):

$$U_2 = B''B = \theta * x_2 = \frac{\delta_p}{L} x_2 \tag{5.25}$$

Compressive strain due to arching at the end and middle sections are given as:

$$\varepsilon_{N1} = \frac{U_1}{L_{N1}} = \frac{\delta_p}{L} * \frac{x_1}{L_{N1}} = \frac{\delta_p}{L} * \lambda_1 \tag{5.26}$$

$$\varepsilon_{N2} = \frac{U_2}{L_{N2}} = \frac{\delta_p}{L} * \frac{x_2}{L_{N2}} = \frac{\delta_p}{L} * \lambda_2 \tag{5.27}$$

Where λ_1 and λ_2 represent the arching compression zone profile and may be determined by semi-empirical approach based on FE simulations.

5.2.3 Stresses and force equilibrium in the arching effective stage

In the previous section, it was shown that the axial compression force that may be developed in arching mode depends on the state of strain and stress in bending mode. To determine the state of compression zone and thus the stress attributed to arching, the total strain due to bending and arching needs to be determined. Since the strain due to bending and arching has been determined already following the procedure explained in section 4.1 and 4.2.1, the bending and arching may be superposed as shown in Figure 5.9.

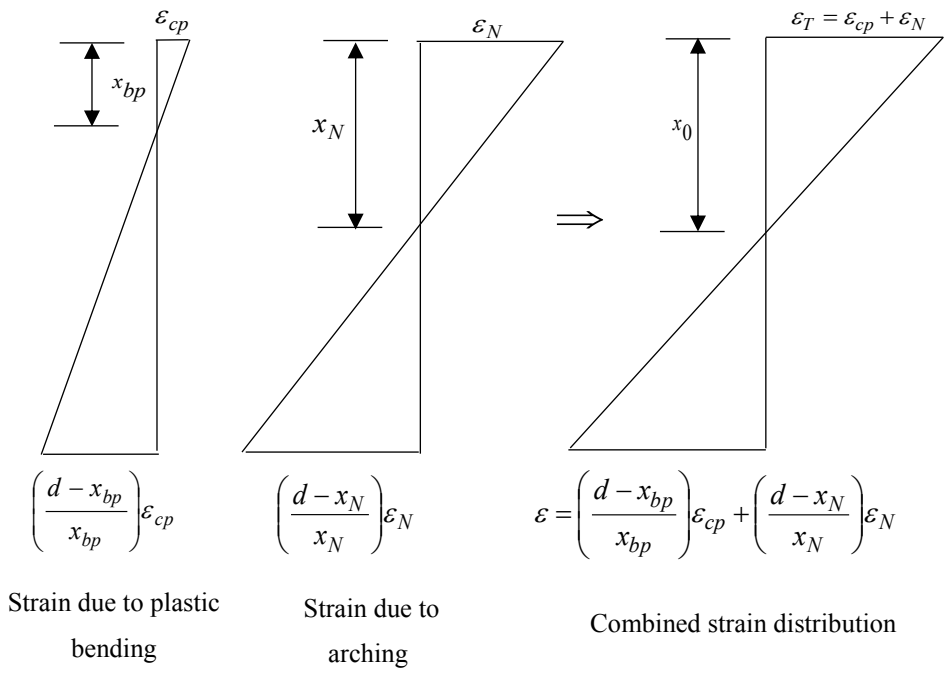

Figure 5.9: Superposition of strain due to bending and arching

Hence, the combined compression depth may be expressed in terms of the arching compression depth as:

$$x_0 = \eta_x x_N \tag{5.28}$$

where:

$$\eta_x = \frac{\varepsilon_{cp} + \varepsilon_N}{\frac{x_N}{x_{bp}}\varepsilon_{cp} + \varepsilon_N} \tag{5.29}$$

ε_{cp} and ε_N are the strain due to bending and arching respectively and can be determined using the formulation in section 5.3. More detailed discussion on the determination of the plastic hinge length for bending (L_p) and the arching compression zone profile (λ) strain values will be given in Section 5.4.

It can be seen in Equation (5.29) that when $x_N = x_{bp}$, $x_0 = x_N$ as expected which implies that arching action will not develop.

With the combined compression zone depth determined as shown above, the stress distribution in the compression zone and thus the equivalent compression zone depth attributed to arching can be determined. For simplicity, let the stress distribution be represented by the equivalent rectangular stress block with uniform stress intensity of f_c. Taking into account the concurrent bending deformation mode, the compression zone depth for arching can be determined as illustrated in Figure 5.13.

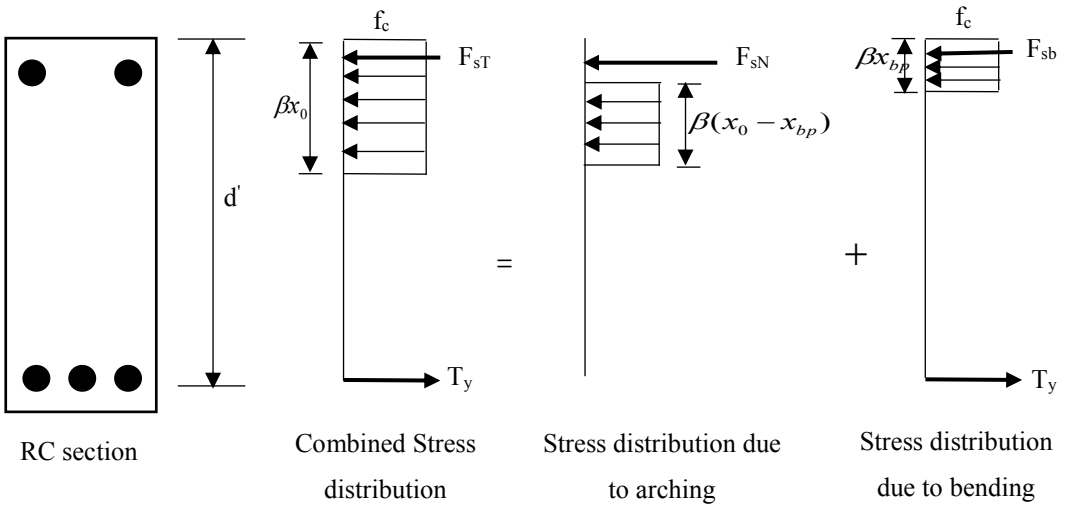

Figure 5.10: Stress distribution considering the concurrent bending and arching deformation modes

Equilibrium of forces attributed to arching at the end and middle section yields:

$$f_c \beta b(x_{01} - x_{bp1}) + F_{sN1} = f_c \beta b(x_{02} - x_{bp2}) + F_{sN2} \tag{5.30}$$

where β is the ratio of equivalent rectangular compressive stress block to neutral axis depth and is taken as 0.85 in this study.

F_{sN1} and F_{sN2} are the axial compressive forces in compression rebar attributed to arching at the end and middle section. For simplicity, assuming that at the arching effective stage the compression bars have yielded, F_{sN1} and F_{sN2} can be calculated as:

$$F_{sN1} = A_{s1}'\left(f_y - \varepsilon_{sb1} E_s\right) \tag{5.31}$$

$$F_{sN2} = A_{s2}'\left(f_y - \varepsilon_{sb2} E_s\right) \tag{5.32}$$

where ε_{sb1} and ε_{sb2} are the strain in compression rebar due to bending deformation

Simplifying Equation (5.30) further yields:

$$x_{01} - x_{02} = x_{bp1} - x_{bp2} + \frac{F_{sN2} - F_{sN1}}{f_c \beta b} \tag{5.33}$$

Substituting Equation (5.28) for x_{01} and x_{02} in Equation (5.33), yields:

$$\eta_1 x_{N1} - \eta_2 x_{N2} = x_{bp1} - x_{bp2} + \frac{F_{sN2} - F_{sN1}}{f_c \beta b} \tag{5.34}$$

Substituting the expression for η_1 and η_2 yields:

$$x_{N1}\left(\frac{\varepsilon_{cp1} + \varepsilon_{N1}}{\frac{x_{N1}}{x_{bp1}}\varepsilon_{cp1} + \varepsilon_{N1}}\right) - x_{N2}\left(\frac{\varepsilon_{cp2} + \varepsilon_{N2}}{\frac{x_{N2}}{x_{bp2}}\varepsilon_{cp2} + \varepsilon_{N2}}\right) = x_{bp1} - x_{bp2} + \frac{F_{sN2} - F_{sN1}}{f_c \beta b} \tag{5.35}$$

The only unknown in Equation (5.35) is x_{N1} and x_{N2}. These unknowns can be determined by solving Equations (5.18) and (5.35) simultaneously.

5.2.4 Kinematics for flexible axial support

The illustration in section 5.2.2 was based on a rigid beam with full axial rigidity. However, experimental result has shown that the end support of the assemblies with loss column are not always rigid, hence for accurate determination of the axial compressive force that can developed the flexibility of the end restraint needs to be considered in the formulation.

Considering again the rigid body movement of beam shown in Figure 5.11. Due to the flexible ends, the end of the beam moves by a displacement (t). The geometric equation can be worked out as:

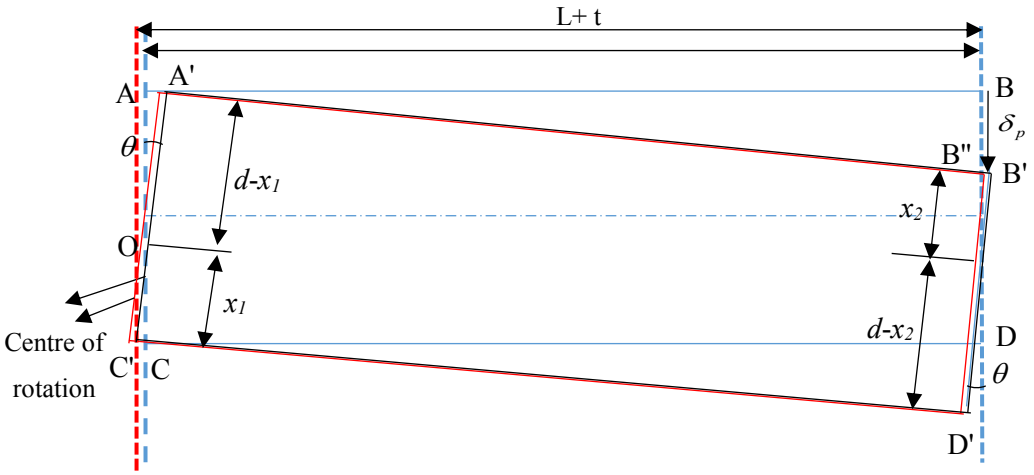

Figure 5.11: Rigid block movement of beam with flexible restraint

$$(A'B'')^2 = (A'B')^2 + (B''B')^2 \tag{5.36}$$

$$(L - \theta \times x_2)^2 = [(L + t) - \theta \times (d - x_1)]^2 + {\delta_p}^2 \tag{5.37}$$

Expanding, ignoring second order increment (θ) terms

$$-2L\theta x_2 = 2Lt + 2L\theta x_1 - 2L\theta d + {\delta_p}^2 \tag{5.38}$$

This simplifies to:

$$x_1 + x_2 = (d - \frac{\delta_p}{2}) - \frac{t}{\delta_p} L \tag{5.39}$$

Equation (5.39) shows that flexible constraint manifest as the relaxation or reduction of the complexion zone depths which reduces the arching action.

For a flexible axial constraint of stiffness K_a, $t = N / K_a$. Equation (5.39) therefore becomes:

$$x_1 + x_2 = (d - \frac{\delta_p}{2}) - \frac{N}{\delta_p K_a} L \tag{5.40}$$

For a flexible boundary condition, Equation (5.40) can be solve simultaneously with Equation (5.35) to determine the depth of compression zone at the end and middle section.

5.2.5 Additional moment of resistance due to arching

The contribution of the arching effect to the vertical load carrying capacity may be looked upon in two different ways: a) treating it as an arching action along the direction of the "strut" and hence its vertical component contributes to the vertical resistance, and b) treating it as a result of the additional moment resistance derived from the arching compression stresses at both ends (left and middle). It can be demonstrated that the two approaches should arrive at the same result. In the present study, the formulation has been focused on the compression stresses due to arching, and hence it is straightforward to adopt the above approach b) in the evaluation of the additional resistance due to arching.

With the depth of compression zone due to arching (x_{N1}, x_{N2}) calculated, along with the stresses in the compression zones that are attributed to arching, the additional moment of resistance due to arching can be obtained. Taking into account the vertical deflection, the additional moment of resistance can be determined by considering the forces at the end and middle sections, as illustrated in Figure 5.15. This approach has been used in the study by Christiansen (1963).

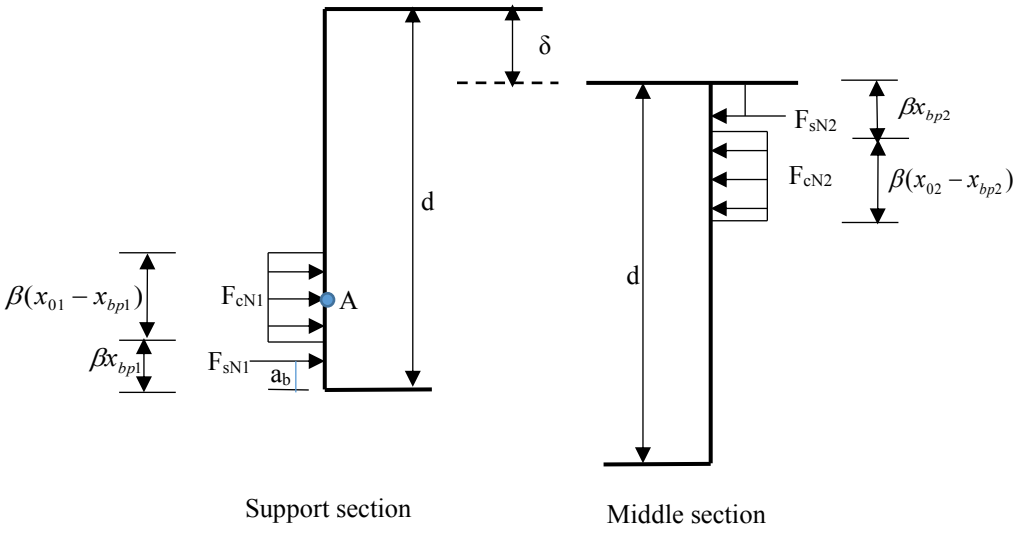

Figure 5.12: Horizontal forces at support and mid-span sections considering only forces attributed to arching

Assuming that the compression forces in the concrete to act at its centroid and taking moment of all the forces about the centroid of concrete compressive zone depth at the support section (point A in Figure 5.12), the additional moment due to arching can be calculated as:

$$\begin{aligned} M_{ar} = {} & F_{cN2}[d-\delta_p-\beta(x_{bp1}+x_{bp2})-0.5\beta(x_{01}-x_{bp1}+x_{02}-x_{bp2})] \\ & + F_{sN2}[d-\delta_p-a_t-\beta x_{bp1}-0.5\beta(x_{01}-x_{bp1})]+F_{sN1}[\beta x_{bp1}+0.5\beta(x_{01}-x_{bp1})-a_b] \end{aligned} \quad (5.41)$$

where a_t and a_b are the distance from the extreme compressive fibre to the centroid of top and bottom reinforcement respectively.

The additional load due to arching can then be calculated as:

$$P_{ar} = M_{ar} / L \quad (5.42)$$

Total load is the sum of load due to bending and arching

$$P_t = P_b + P_{ar} \quad (5.43)$$

5.3 Determination of plastic length due to bending and arching

5.3.1 Introduction

In the proposed model developed in Section 5.2, it was shown that the combined compression zone depth depends on the plastic hinge length due to bending (L_p) and an effective "plastic" arching depth to length ratio (x/L_N). Accurate prediction of compressive arching capacity using this model therefore depends on the plastic lengths of these two modes of deformation.

5.3.2 Plastic hinge length for bending

Regarding plastic hinge length for bending, a number of empirical expressions based on experimental and FE numerical studies on RC beams exist in the literature. Some of the proposed expressions by different researchers are summarised in Table 5.1. It can be seen from Table 5.1 that most of researchers consider the plastic hinge length to depend on the depth of the section (d) and the distance from the critical section to the point of contra flexure (z). However, most of these studies where based on RC beam subjected to normal load and without axial force which may influence the plastic hinge length.

For the present study, the empirical expression by Sheikh & Khoury (1993) is adopted to defined the plastic hinge length because the behaviour of axially restrained beam is dominated by axial compressive forces during the compressive arching stage. Thus, the plastic hinge for bending (L_p) is assumed to be 1.0d where d is the depth of the beam section.

Table 5.1: Expressions for plastic hinge length from different researchers

Researcher reference	Plastic hinge length expression (L_p)	Applicability
(Baker 1956)	$k(z/d)^{1/4}d$	RC Beams and columns
(Corley 1966)	$0.5d+0.2\sqrt{d}$ (z/d)	RC beams
(Mattock 1967)	0.5d+0.05z	RC beams
(Priestley & Park 1987)	$0.08L + 0.022d_bf_y$	RC columns
(Sawyer 1964)	0.25d + 0.075z	RC beams
(Sheikh & Khoury 1993)	1.0h	RC columns under high axial loads

5.3.3 Determination of effective "plastic" arching depth to length ratio (x/L_N)

In the proposed model presented in Section 5.3, the strain attributed to arching is based on the plastic zone ratio expressed as x/L_N. Thus, accurate prediction of the response depends on the x/L_N ratio adopted. There could be different ways of determining a ratio which best describes this arching compression behaviour. In this section, numerical simulation of RC beam is studied to understand the variation of x/L_N for different values of x.

As a basic reference state, a quarter-infinite space is considered, where a block of distributed load is applied on a limited stretch as illustrated in Figure 5.13. For beams under arching action with a relatively small compression zone, the stress condition surrounding the compression area would be analogous to this theoretical reference state and so the analysis of such a scenario provides basic information about the concentration of stress and deformation in this region, and hence the nominal length of L_N.

5.3.3.1 Consideration of an infinitive RC element

Based on the consideration described above, an RC element of 800mm in length and height and width of 200mm is considered. One end and bottom nodes are restrained in all directions and a linearly varying compressive displacement is applied to the top right end as shown in Figure 5.13. The depth of prescribed displacement is varied as

0.1d and 0.3d where d is the depth of the beam. The result of the two cases are analysed to determine the variation of strain in the top fibre for a given compressed depth (0.1d or 0.3d).

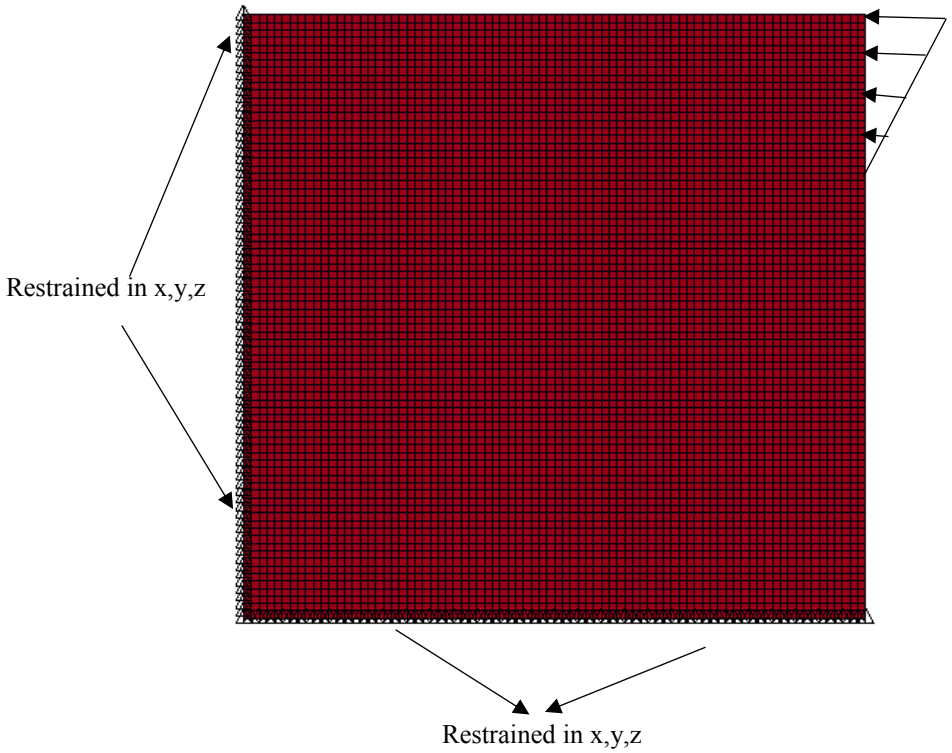

Figure 5.13: An infinitive RC element

5.3.3.2 Applied displacement over a depth of 0.1d (80mm)

The strain distribution along the top fibre of the beam at selected time step is shown in Figure 5.17. It can be observed that nonlinear strain concentrates at the free end and the strain towards the restrained edge is almost elastic. The total strain comprises of elastic and nonlinear strain. The elastic strain may be deducted from the total strain. For simplicity, the elastic deformation may be expressed as:

$$u_e = \frac{NL}{EA} \tag{5.44}$$

where N is the axial force and L is the length of the beam in the loading direction. A is the cross-sectional area of the beam.

With this expression, the nonlinear displacement can be determined and subsequently the plastic zone length can be determined. The results of these analysis are presented in Table 5.2 for three compressed horizontal displacement at the top fibre.

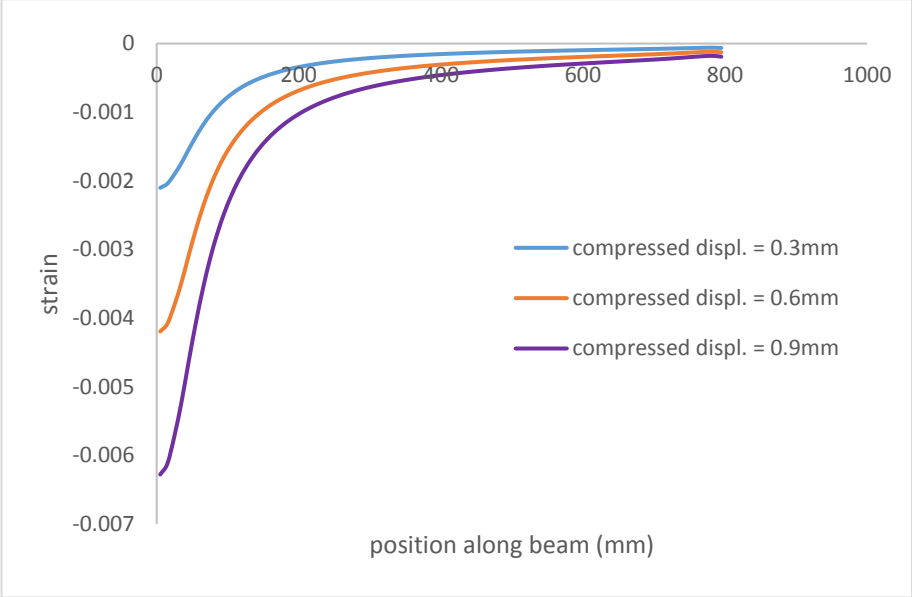

Figure 5.14: Strain variation along top fibre of beam for x=0.1d

The distribution of stress and strain across the depth of the section is shown for three different horizontal displacement. It can be observed that the compressive zone depth is slightly smaller than the depth of applied compression displacement. For instance, the compression zone depth is approximately 50mm whereas the depth of the applied displacement is 0.1d (80mm). The ratio of compression depth to the plastic zone depth for the two different cases (depth from stress/strain distribution and 0.1d) are shown in Table 5.2.

The strain contour at a compressed horizontal displacement of 0.3mm further shows that the compression zone depth is only 50mm although the depth of prescribed displacement was 80mm.

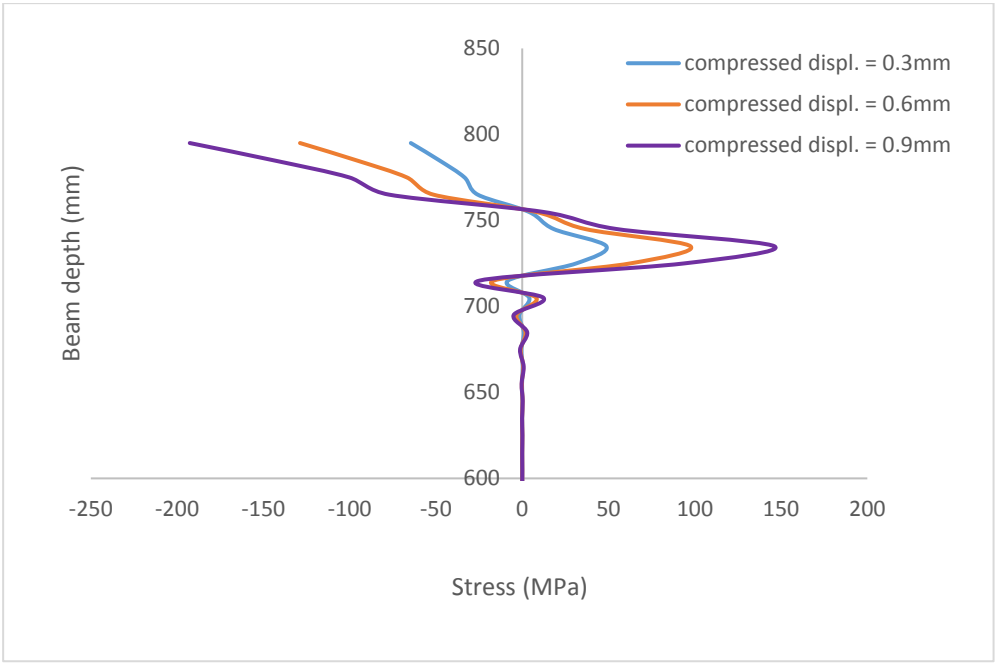

(a) stress distribution

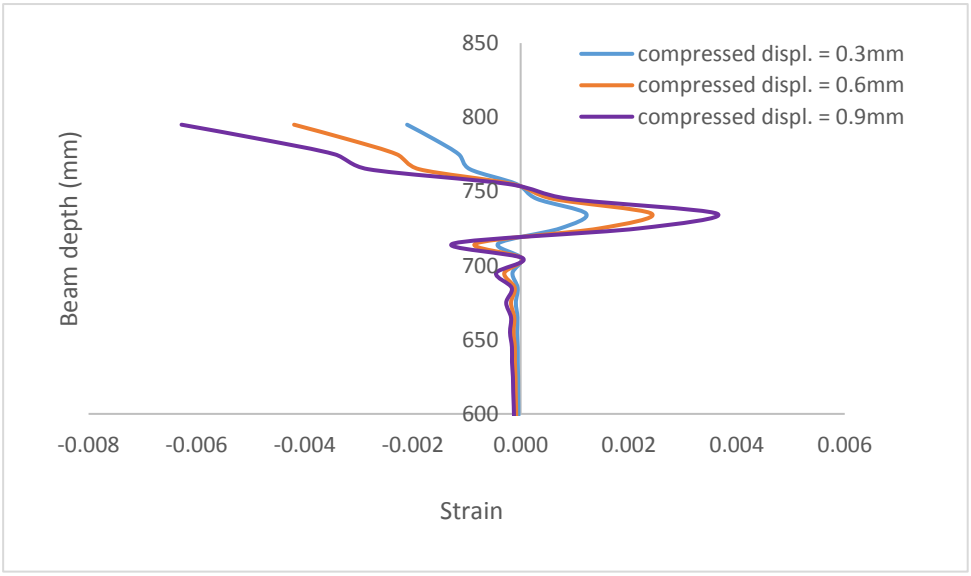

(b) strain distribution

Figure 5.15: Stress distribution and strain distribution across depth for x=0.1d

Table 5.2: Determination of x/L_N for FE model with x=0.1d

displ. (mm)	u_e (mm)	u_{total} (mm)	$u_p=(u_t-u_e)$ (mm)	maximum nonlinear strain (ε_{max})	$L_x = u/\varepsilon_{max}$ (mm)	x/L_N x=0.1d	x/L_N x=50mm
0.3	0.026	0.3	0.274	0.0018	150	0.53	0.33
0.6	0.052	0.6	0.548	0.0038	145	0.55	0.34
0.9	0.078	0.9	0.822	0.0058	142	0.56	0.35

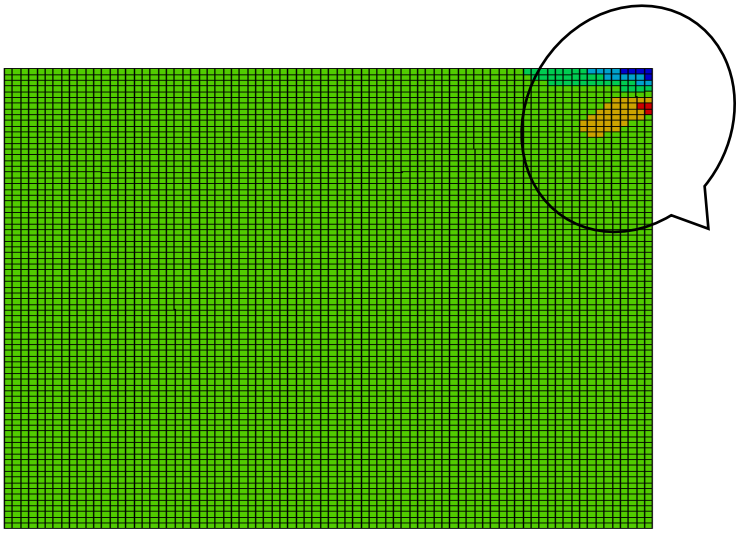

(a)

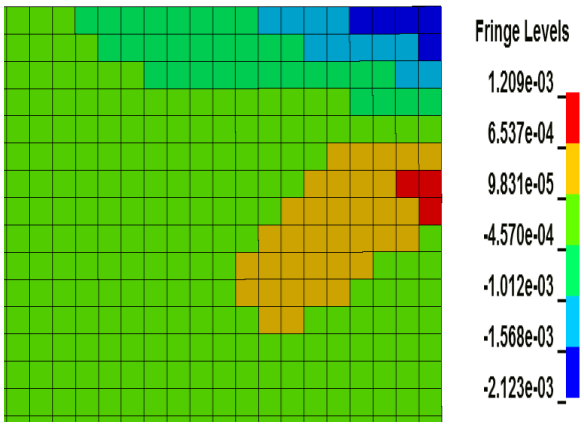

(b)

Figure 5.16: strain contour of (a) RC element (b) compression zone area only at a compressed displacement of 0.3mm

5.3.3.3 Applied displacement over a depth of 0.3d (240mm)

For the case with x=0.3d, the strain distribution along the top fibre of the beam as shown in Figure 5.17 indicates that the strain is much smaller for the same compressed displacement. More so, the strain is not concentrated at the free end but extends almost the entire length of the beam. For a larger compressed displacement (=1.5mm) the maximum compressive nonlinear strain is 0.0045 which is less than the maximum nonlinear strain for compressed displacement of 0.9mm in the model with x=0.1d. This confirms the uniformity of strain as the compressed depth increases. The stress and strain distribution across the depth at a selected compressed displacement is also shown in Figure 5.18. Again, from these distributions, the actual compression zone depth is 175mm not the initially compressed 0.3d (240mm).

The same analysis to determine x/L_N is repeated for the selected time step as shown in Table 5.3. It is seen that the ratio of x/L_N is higher than that of x=0.1d. This again confirms that the more the depth of the compressed zone, the more uniformed the strain will be throughout the beam and x/L_N will increase.

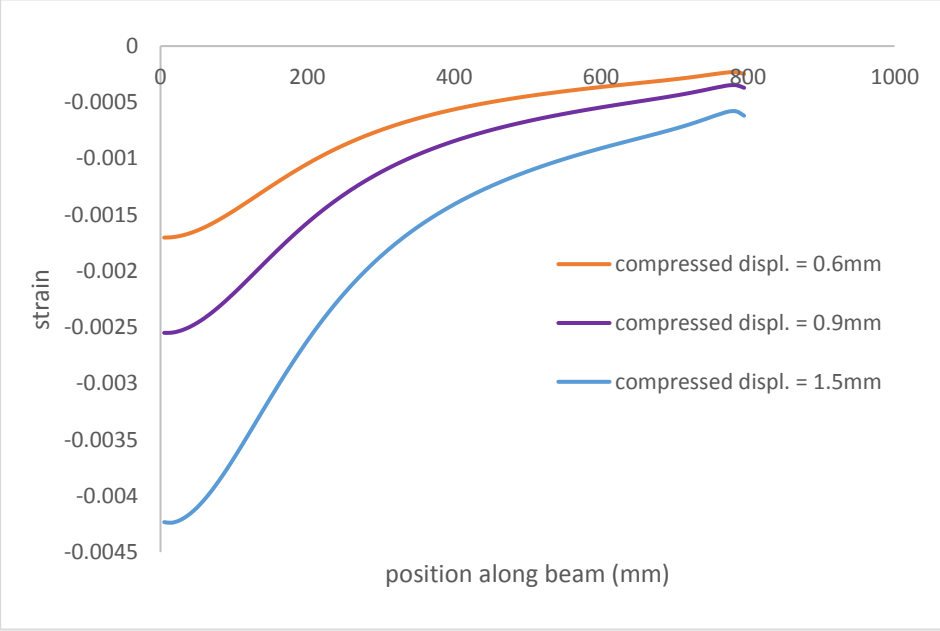

Figure 5.17: strain distribution along top fibre of beam for x=0.3d

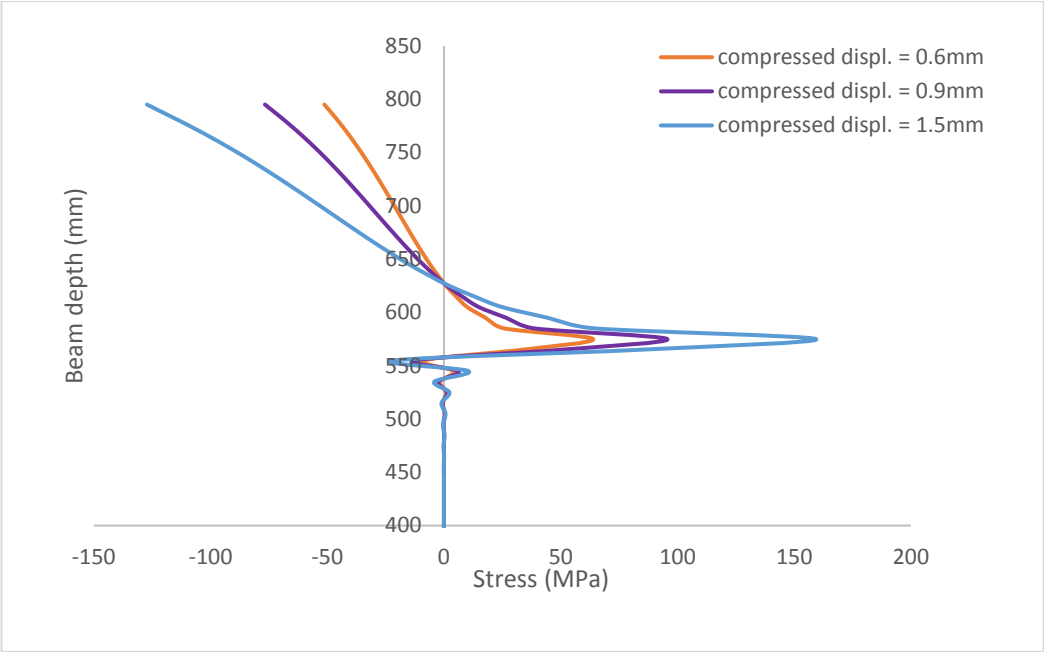

(a) stress distribution

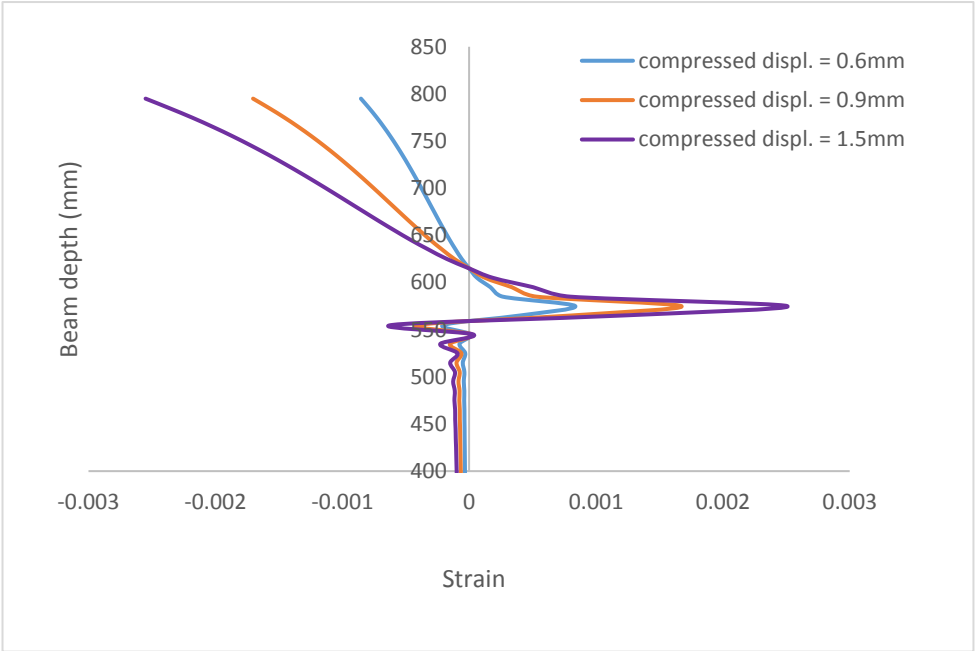

(b) strain distribution

Figure 5.18: Stress distribution and strain distribution across depth for x=0.3d

Table 5.3: Determination of x/L_N for FE model with x=0.3d

displ. (mm)	u_e (mm)	u_{total} (mm)	$u_p=(u_t-u_e)$ (mm)	maximum nonlinear strain (ε_{max})	$L_x = u/\varepsilon_{max}$ (mm)	x/L_N x=0.3d	x/L_N x=175mm
200	0.098	0.6	0.502	0.0014	360	0.6	0.48
300	0.15	0.9	0.75	0.0023	325	0.73	0.54
500	0.25	1.5	1.25	0.0040	312	0.76	0.56

In general, the illustration shows that the x/L_N varies as the depth of compressed zone changes. For the cases considered in this exploration, the ratio varies between 0.3 and 0.56. To be on the conservative side the value of 0.35 is adopted for the ratio x/L_N.

5.4 Validation of the proposed model

In this section, comparisons between the predicted maximum compressive arching action capacities and experimental test results are presented. The geometry and reinforcement details and material properties for each of the tests are presented in Table 5.4. For the experiment by Vesali et al., (2013), the axial restraint stiffness was not provided. The test set up shows that the boundary condition was close to rigid, hence a very large axial stiffness of 1.00E+06KN/m is used. The results from the theoretical analysis and the experiments are also summarised in the table.

As can be seen from the table, the analytical model predicts the arching compression with a reasonable accuracy. The mean value for all the 23 different specimens is 0.966 and the coefficient of correlation is 0.989. This shows that the analytical model can predict the arching effects for beams with a wide range of material, reinforcement and geometrical properties.

Table 5.4: Comparison of experimental and predicted result

ID	Reference	L/d	Restraint stiffness (KN/m)	f_c (MPa)	Reinforcement ratio (%)		Exp.	Theo	Exp/ Theo
					Top	Bottom			
A1	(Su et al. 2009)	4.08	1.00E+06	25.80	0.55	0.55	168.00	147.00	1.14
A2		4.08	1.00E+06	28.20	0.83	0.83	221.00	187.48	1.18
A3		4.08	1.00E+06	31.2	1.13	1.13	246.00	223.88	1.10
A4		4.08	1.00E+06	23.00	0.55	0.38	147.00	123.07	1.19
A5		4.08	1.00E+06	26.50	0.83	0.55	198.00	166.90	1.19
A6		4.08	1.00E+06	28.60	1.13	0.75	226.00	199.51	1.13
B1		6.58	1.00E+06	18.60	1.13	1.13	125.00	116.35	1.07
B2		9.08	1.00E+06	19.30	1.13	1.13	82.90	84.78	0.98
B3		9.08	1.00E+06	21.10	1.13	0.75	74.70	76.50	0.98
S1	(Yu & Tan 2013a)	11.0	1.06E+05	31.24	0.90	0.49	41.64	47.90	0.87
S2		11.0	1.06E+05	31.24	0.73	0.49	38.38	45.10	0.85
S3	(Yu & Tan 2013c)	11.00	4.29E+05	38.15	1.24	0.49	54.47	64.80	0.84
S4		11.00	4.29E+05	38.15	1.24	0.82	63.22	73.10	0.86
S5		11.00	4.29E+05	38.15	1.24	1.24	70.33	85.00	0.83
S6		11.00	4.29E+05	38.15	1.87	0.82	70.33	74.76	0.94
S7		8.60	4.29E+05	38.15	1.24	0.82	82.82	97.20	0.85
S8		6.20	4.29E+05	38.15	1.24	0.82	121.34	137.34	0.88
V1	(Vesali et al., 2013)	11.72	1.00E+06	30.50	0.58	0.58	40.50	43.75	0.93
V2		11.72	1.00E+06	27.00	0.58	0.58	35.70	41.38	0.86
V3		11.72	1.00E+06	30.00	0.58	0.58	41.40	43.60	0.95
V4		11.72	1.00E+06	26.00	0.87	0.58	40.10	45.23	0.89
V5		11.72	1.00E+06	29.50	0.87	0.58	41.60	47.60	0.87
V6		11.72	1.00E+06	30.00	0.87	0.58	39.40	47.89	0.83
Mean for all the specimens									**0.966**
Correlation coefficient									**0.989**

5.5 Conclusions

In this chapter, a theoretical model for the compressive arching action is developed. The model takes into consideration the compounding effect of bending and arching. It is shown that the prediction depends on the plastic zone length for bending and the ratio of arching depth to plastic zone for the arching contribution.

An exploratory study on the variation of the arching depth with the plastic zone length shows that it increases with the increase of the depth of the compression zone. The results indicate that adopting a value of 0.35 for the x/L_N ratio gives a reasonable prediction. Using this ratio yield a stable prediction for the arching action as compared with experimental results for a wide range of beam property parameters.

With the model developed herein the complete load displacement response within the arching stage can be predicted. The model will be used together with the model for catenary action to predict the complete load-displacement response of RC beam assemblies in Chapter 7.

Chapter 6: Simplified theoretical model for prediction of catenary action incorporating strength degradation in axially restrained beams

6.1 Introduction

In the conventional design of steel and reinforced concrete structures, the capacity of beams is governed by the flexural behaviour with formation of plastic hinges at critical locations. However, it has been argued that for axially restraint beams, catenary action may develop and at a much larger displacement and help increase the load capacity of the beam. Accordingly, a number of experimental studies on steel, composite and RC beam-column sub-assemblies with axial restraint has been carried out (Sasani & Kropelnicki 2008; Sadek et al. 2011; Choi & Kim 2011; Yang & Tan 2013a; Yang & Tan 2014; Li et al. 2013; Li et al. 2015). These studies confirm that with adequate axial restraint, following the flexural bending stage, the so-called catenary action can develop causing the beam to behave in a cable-like manner and thus helps improve the resistance against collapse due to gravity loads. However, these experiments are expensive and cannot provide detailed information regarding the mechanism of failure and the reliability of the catenary action. Due to these limitations, the study of catenary action in axially restrained sub-assembly has often been carried out with finite element analysis codes.

With the development of high speed computer and the advancement in the finite element method, the behaviour of structural components and connections at large deformation can be analysed with high degree of accuracy thereby allowing the behaviour of the critical regions at large deformation regime to be investigated in detail. However, the use of finite element method requires a high level of expertise to properly model this behaviour thereby making it unsuitable for routine use by practicing Engineers.

Simplified theoretical model for catenary action may be used in the design, analysis and assessment of progressive collapse resistance of framed structures. For such model to be acceptable, it must be able to capture the key responses as observed in the experiments and the underlying physical mechanisms. These include hardening, degradation, and catenary action. So far, research in the simplified modelling of catenary action has remained at its infant stage. For example, studies by (Izzuddin 2005; Li. et al. 2008) assumed highly idealised sectional strength properties in the formulation of the catenary effect, whereas strength degradation and softening behaviour are not considered in their model. Existing models of this type assume that the plastic strength remains available despite very large deformation, whereas the actual test and FE simulation studies have shown that the behaviour of RC and steel structure depends on the plastic hinge and connection details, and the catenary capacity that may be developed is limited by the failure of connections. The use of existing simplified models may therefore over-predict the collapse resistance in real structures.

In this chapter, a simplified theoretical model which takes into consideration the degradation of strength, which may arise from failure of some of the component of the connection is developed. Although the theme of this thesis is directly associated with reinforced concrete frame structures, the catenary model developed in this chapter is generic and can be used to assess progressive collapse in both steel and reinforced concrete frame assemblies. Consequent upon this, steel and RC subassemblies are used to validate the prediction from the generic model as would be presented in the chapter and the following chapter.

6.2 Scope of the model

1) The model is initially formulated for simply supported beam with flexible elastic axial stiffness. This implies that plastic hinges develop at the mid-span section only. Subsequently, the same principle is extended to beams with development of plastic hinges at mid-span and end sections.

2) Different yield functions (M-N interaction curves) may be used in the proposed model.
3) Response at the cross-sectional level is assumed to be elastic perfectly plastic and hardening is ignored.
4) The axial restraint of beam is assumed to be symmetric.

6.3 Analysis procedure for a simplified beam model without consideration of strength degradation

Consider a simply supported steel beam with an axial restraint, as shown in Figure 6.1. The axial restraint is represented by elastic axial stiffness (K_a). The load-displacement behaviour of this beam with and without strength degradation is schematically shown in Figures 6.2a and 6.2b. Four response stages can be identified in these figures; elastic bending, plastic bending, transient and catenary action stages.

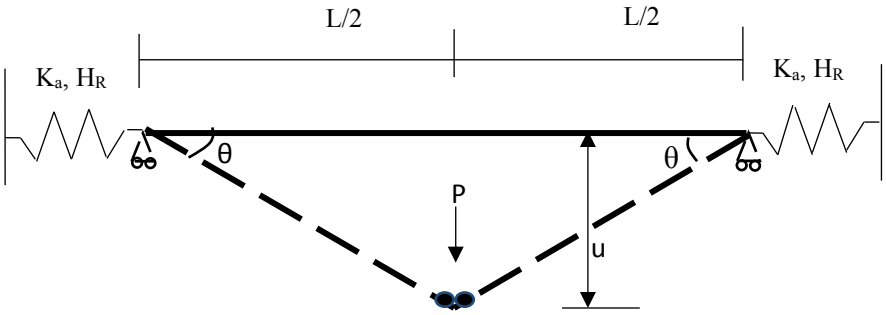

Figure 6.1: Simply supported beam with flexible axial restraint

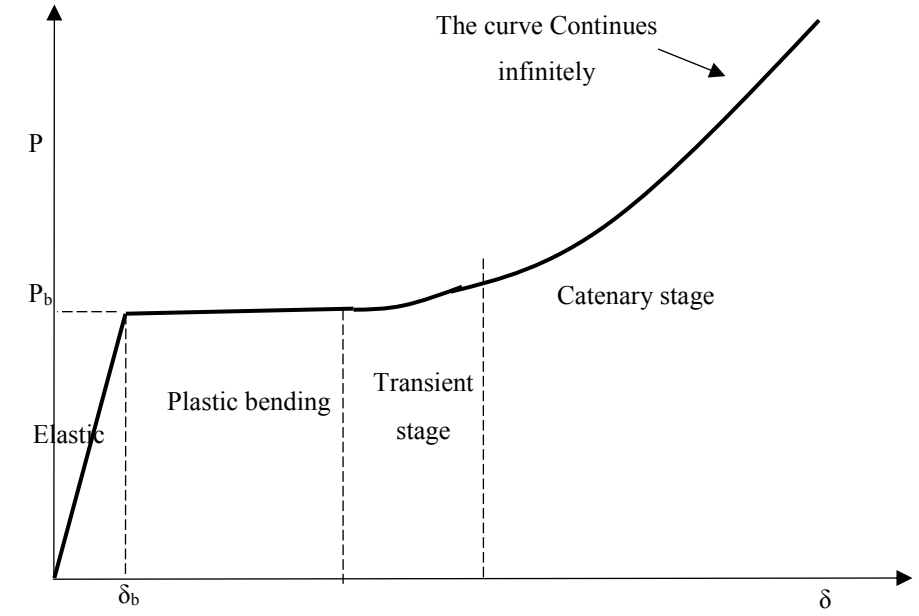

(a) Without strength degradation

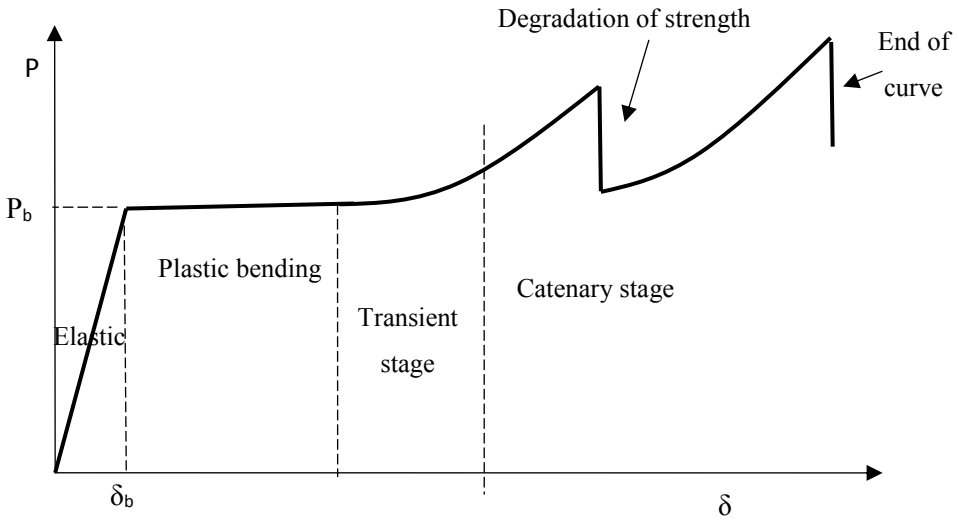

(b) With strength degradation and final failure

Figure 6.2: Schematics of load-displacement curves

As shown in Figure 6.2, during the initial stage of loading, the beam behaves in flexure. After the elastic stage, the displacement further increases but the resistance may remain flat or with some degree of increase depending upon the flexural hardening behaviour in the plastic region until a form. For simplicity, in the present discussion

the plastic flexural stage is assumed to follow immediately the end of the elastic stage and without hardening.

It is worth noting here that in real structures the flexural stage of response will generally involve an elastic-plastic transition stage (see Figure 6.3a) with a nonlinear moment-curvature or moment-rotation relationship at the sectional or plastic hinge level. For example, in a steel section this will result in yielding developing at the outer fibre and gradually extending to the inner fibres until reaching full plasticity. The approximation of the yield point and the yield strength is a separate subject which will not be discussed in detail here. In this model, the elastic-plastic phase i.e. the point between the yield of the outer fibre (denoted as M_y in Figure 6.3a) and the formation of full plastic capacity (denoted as M_p in Figure 6.3a) is assumed to be elastic. Plastic hinge only develops at a full plastic moment capacity M_p. With this assumption, the beam can be simplified into elastic-perfectly-plastic as shown in Figure 6.3b.

The symbol and definition of all the key points in Figure 6.3 are explained as follows:

M_y corresponds to the moment at which the outer fibre first yield.

M_p is the plastic moment capacity of the section

$\emptyset_y$ is the curvature corresponding to the yield moment and

Φ_p is the curvature corresponding to the plastic moment capacity of the section

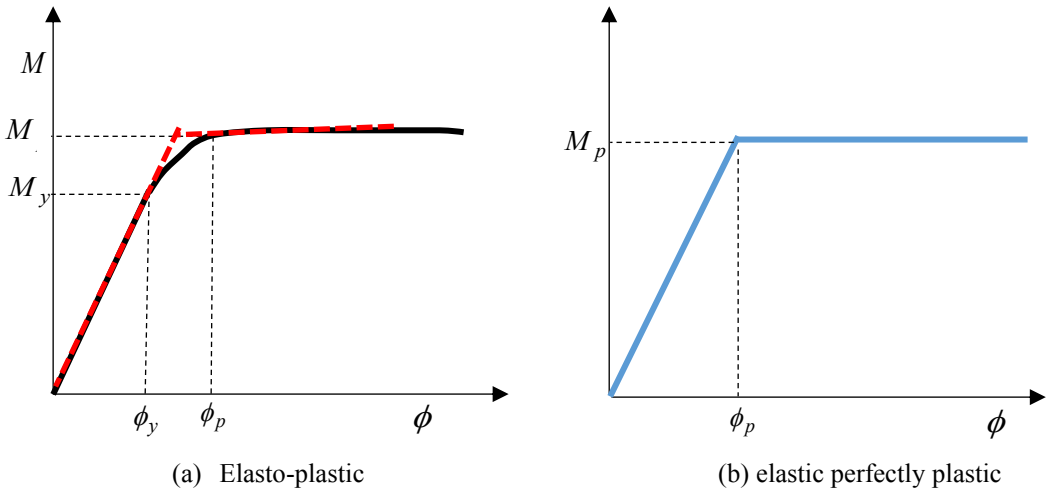

(a) Elasto-plastic (b) elastic perfectly plastic

Figure 6.3: Moment-curvature behaviour at section and plastic hinge

6.3.1 Elastic stage

The beam behaves in a flexural manner and depends on the flexural rigidity and rotational restraint of the beam. In the basic case, axially restraint simply supported beam is considered. Plastic hinge will only develop at the middle as shown in Figure 6.1. Since this stage involves elastic bending, small deflections are expected, and hence axial force is negligible at this stage. The end of the elastic stage is reached once the plastic moment capacities in the middle and end sections are reached (as illustrated in Figure 6.3), which also implies the formation of hinge. The load and the displacement at the idealised yield point are given by:

$$P_b = \frac{4M_p}{L} \tag{6.1}$$

$$\delta_b = \frac{P_b L^3}{48EI} \tag{6.2}$$

Substituting Equations (6.1) into (6.2), the deflection at the end of elastic stage can be expressed as:

$$\delta_b = \frac{M_p L^2}{12EI} \tag{6.3}$$

Where M_p is the plastic bending capacity at the plastic hinge. E and I are the Young's modulus of the material and second moment of area of the section respectively.

6.3.2 Transient stage/catenary action stage

In the transient stage, the behaviour of the beam at the plastic regions can be said to be elastic-perfectly plastic. Thus, there is the stretching of the beam in addition to bending. Axial force effect needs to be considered. The load-displacement behaviour in this stage is determined incrementally by considering these three key areas; (Izzuddin 2005)

a. Interaction between the internal forces i.e. bending moment and axial force (yield function) at the critical section (plastic hinge).
b. Compatibility relationship i.e. the relationship between deformation (incremental axial deformation and plastic rotation) at the plastic hinge and the internal forces (moment and axial force) which is determined by a flow rule.
c. Equilibrium of the external and internal forces.

Each of these three areas are discussed in the section that follows.

6.3.2.1 Interaction equation

The plastic interaction between axial force (N) and bending moment (M) is generally nonlinear. For simplicity, a linear approximation of the interaction between these internal forces may be assumed and this assumption has been used in previous studies (Izzuddin 2005). An example of nonlinear interaction between the internal forces at critical section (plastic hinge) is schematically shown in Figure 6.4, and they may be expressed as (Yin & Wang 2005):

$$\frac{M}{M_p} + \psi\left(\frac{N}{N_p}\right)^2 = 1 \tag{6.4}$$

$$\frac{M}{M_p} + \frac{N}{N_p} = 1 \tag{6.5}$$

where M and N are the moment and axial force, M_p and N_p are the maximum plastic bending capacity and maximum axial capacity of the section. ψ is a coefficient which depends on the sectional properties. For a rectangular section with perfect plastic condition ψ is 1 (Jirasek & Bazant 2001). The derivation of the equation for a perfectly plastic rectangular section is given in Appendix 1. The interaction of forces (bending moment and axial force) in RC section is much more complex than the case illustrated in this section, however an expression similar to Equation (6.4) can also be derived.

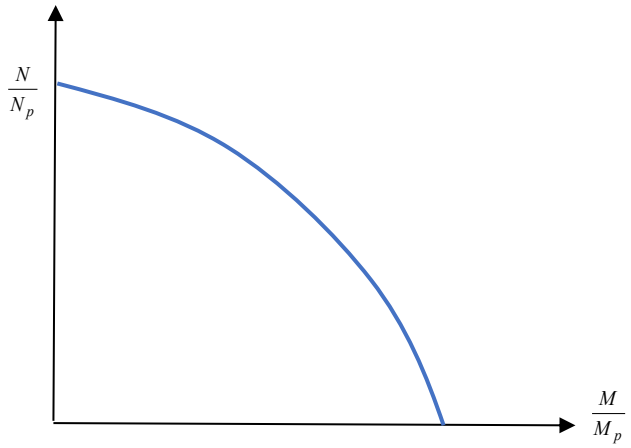

Figure 6.4: Moment-curvature behaviour at section and plastic hinge

6.3.2.2 Constitutive relationship between internal forces and deformation

In the theory of plasticity, it is known that for perfectly plastic material, the yield surface remains fixed. Once yielding condition is fulfilled, an infinitesimal increase in stress will lead to plastic flow. Von Misses in 1928 proposed the concept of plastic potential function. In his case, he used associated flow rule (i.e. the yield function and the plastic potential function coincide with each other). According to the flow rule theory, the vector of plastic deformation increment has direction normal to the yield surface. More detail on this can be found in Chen & Han (1988). This concept has been extended to relate internal forces (M, N) to deformation $(d\Delta, d\theta)$ at the plastic hinge zone (Izzuddin 2005; Long & Hung 2008).

Referring to Figure 6.4, let φ define the yield function, where φ is a function of bending moment and axial force. Since any combination of internal forces (bending moment and axial force) must always lie on the yield surface, it implies that;

$$\varphi = f(M, N) = 0 \tag{6.6}$$

For each incremental displacement δ_i, the corresponding elongation of (U_i) can be determined as:

$$U_i = 2*\left(\sqrt{(L/2)^2 + \delta_i^2} - (L/2)^2\right) \tag{6.7}$$

Equation (6.7) can be simplified further and neglecting smaller terms, gives:

$$U_i = 2\frac{\delta_i^2}{L} \tag{6.8}$$

The elastic elongation then becomes:

$$U_{ei} = U_i - U_{pi} \tag{6.9}$$

From Hooke's law, the axial force can be related to the effective axial stiffness and elastic axial deformation of the beam as:

$$N = K_e(U_i - U_{pi}) \tag{6.10}$$

where K_e is the effective axial stiffness which is defined as:

$$K_e = \frac{1}{\frac{1}{K_a} + \frac{1}{K_s} + \frac{1}{K_a}} \tag{6.11}$$

where K_a is the elastic axial stiffness of the end spring and K_s is the axial stiffness of the beam ($K_s = EA/L$).

Applying flow rule theory to Equation (6.6), the incremental axial deformation (dU_p) and rotation ($d\theta_p$) occurring at plastic hinge can be expressed as (Long & Hung 2008):

$$\begin{Bmatrix} d\theta_p \\ dU_p \end{Bmatrix} = \lambda \begin{Bmatrix} \partial\varphi/\partial M \\ \partial\varphi/\partial N \end{Bmatrix} \tag{6.12}$$

where $\partial\phi/\partial N$ is the partial derivative of the yield function with respect to N and $\partial\phi/\partial M$ is the partial derivative of yield function with respect to M. λ indicates the magnitude of plastic deformation.

Equation (6.12) can be further simplified to:

$$dU_p = \frac{\partial\varphi/\partial N}{\partial\varphi/\partial M} d\theta_p \tag{6.13}$$

Since the normality condition holds for infinitesimal increments in elongation and rotation, Equation (6.10) can be re-written in incremental form as:

$$dN = K_e \left(dU - \frac{\partial\varphi/\partial N}{\partial\varphi/\partial M} d\theta_p \right) \tag{6.14}$$

Noting that for a rigid-plastic beam, the incremental plastic hinge rotation at the mid-span is given as:

$$d\theta_{pm} = 4\frac{d\delta}{L} \tag{6.15}$$

Also, from Equation (6.8)

$$dU = 4\frac{\delta . d\delta}{L} \tag{6.16}$$

Substituting Equations (6.15) and (6.16) into (6.14):

$$dN = K_e(4\frac{\delta.d\delta}{L} - \frac{\partial\varphi/\partial N}{\partial\varphi/\partial M}.4\frac{d\delta}{L}) \tag{6.17}$$

Integrating Equation (6.17) and assuming starting deflection as the deflection at the end of elastic bending stage (δ_b), the axial force at any given deflection δ_i can be expressed as:

$$N = K_e\left[\frac{2}{L}(\delta^2 - \delta_b^2) - \frac{4}{L}(\delta - \delta_b)\frac{\partial\varphi/\partial N}{\partial\varphi/\partial M}\right] \tag{6.18}$$

Thus, for a given deflection, the corresponding axial force can be calculated using the expression in Equation (6.18) and subsequently the moment can be determined from the yield function (Equation 6.6).

6.3.2.3 Equilibrium of forces

To determine the load at each incremental deflection, one-half of the beam and the forces acting on it are considered as shown in Figure 6.5. Although the axial force in the beam may slightly differ from the horizontal reaction, experimental test (Yu & Tan 2013c) shows that the difference is negligible hence herein the horizontal reaction (H_R) is assumed to be the same as the axial force at plastic hinge which is denoted as (N).

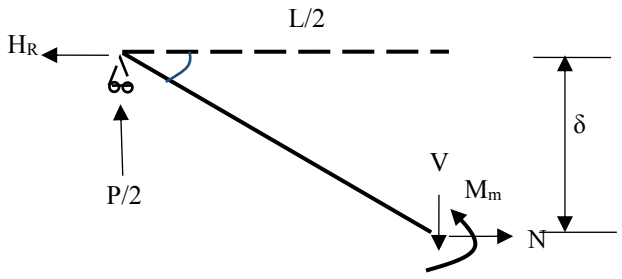

Figure 6.5: Free body diagram showing forces acting on the beam

Taking moment about the middle point,

$$M_m + H_R\delta - PL/4 = 0 \tag{6.19}$$

The load P can be obtained as:

$$P = \frac{4H_R\delta}{L} + \frac{4M_m}{L} \tag{6.20}$$

It should be mentioned that the formulation above is in terms of axial and rotational deformation (U and θ). In reality, the deformation is concentrated in a small section of the beam called plastic hinge zone with finite length (L_p). In other cases, such as steel connection, the deformation may be concentrated within a small area in which case, the behaviour is only determined by the rotation of the beam. In the later section, the application of this model to different connection types and transformation of the axial deformation and rotation to strain measures based on assumed plastic hinge length will be discussed.

The flow chart for the determination of load displacement response based on the above outline procedure is shown in Figure 6.6.

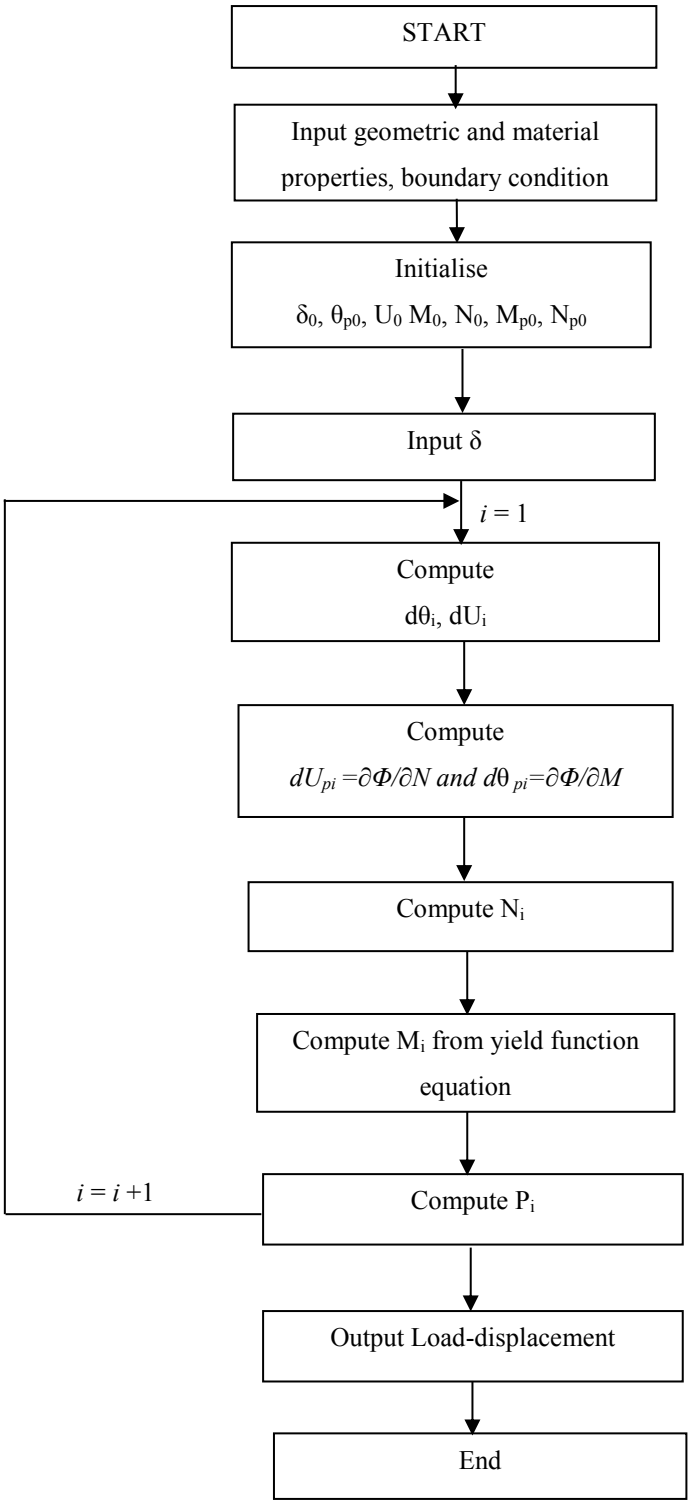

Figure 6.6: Flow chart for calculating internal forces and vertical resistance without considering strength degradation

6.4 Illustrative example of finite element simulation and theoretical prediction of load-displacement response of beam without considering strength degradation

In this section, a rectangular hollow section steel beam is modelled using finite element code (LS-DYNA) and the result is compared with theoretical prediction without strength degradation.

6.4.1 Finite element model description

The model consists of a two-span beam made of steel rectangular hollow section. Steel hollow section is selected for the study to avoid lateral torsional buckling which may increase the complexity of the problem. The overall span of the beam is 9.2m (4.6m single span) and depth and width is 300mm by 150mm with wall thickness of 10mm. Young's modulus and Poisson's ratio of steel are 200GPa and 0.3 respectively while the yield strength is 300MPa.

The beam is modelled with constant stress solid element with reduced integration. This type of solid element has only one integration point and to ensure accurate result is obtained, a mesh convergence study was performed and a mesh size of 10 x 5 x 10mm was used across the beam thickness, and 10 x 10 x 10mm was used within the hollow session area. Taking advantage of symmetry, only one-half of the beam is modelled and appropriate boundary condition is applied at the middle column stub of the subassembly.

Pin boundary condition is applied at the end section to simulate the presence of axial restraint from the surrounding structures. To achieve this boundary condition, the end section is modelled with elastic element to avoid damage that may increase the complexity of the problem. A hole of 20mm diameter is created within the elastic end section with centre of hole located at mid-depth of the beam. A rigid rod with the same diameter is created having the same centre as that of the hole. The elastic end is modelled with MAT_001_ELASTIC and the rod is modelled with rigid element MAT_020_RIGID in LS DYNA. The choice of rigid element for the rod is to avoid

any deformation. The ends of the rods are constrained in all direction using CONSTRAINED_SPC_SET Keyword in LS DYNA. Interaction between the rod and elastic beam end is defined by the contact type available in LS-DYNA AUTOMATIC_SURFACE_TO_SURFACE_TIEBREAK, where the rod surface is defined as the master surface and the elastic beam is defined as slave surface. The FE model of the end section is shown in Figure 6.7b. The top surface nodes of middle column are push down in a displacement controlled loading manner. The load curve is defined using CURVE_SMOOTH and the loading rate is small enough to represent a quasi-static loading scheme and thereby avoid any dynamic effect.

For the theoretical model, the same material and geometric properties used in the FE model is adopted. The plastic moment (M_p) and axial force capacity (N_p) is calculated as 248kNm and 2580kN respectively. The axial stiffness (K_a) in the theoretical model is 10e+20N/mm. This stiffness is greater than the axial stiffness of the beam section (EA/L) (191KN/mm), hence the model beam is rigidly restrained axially.

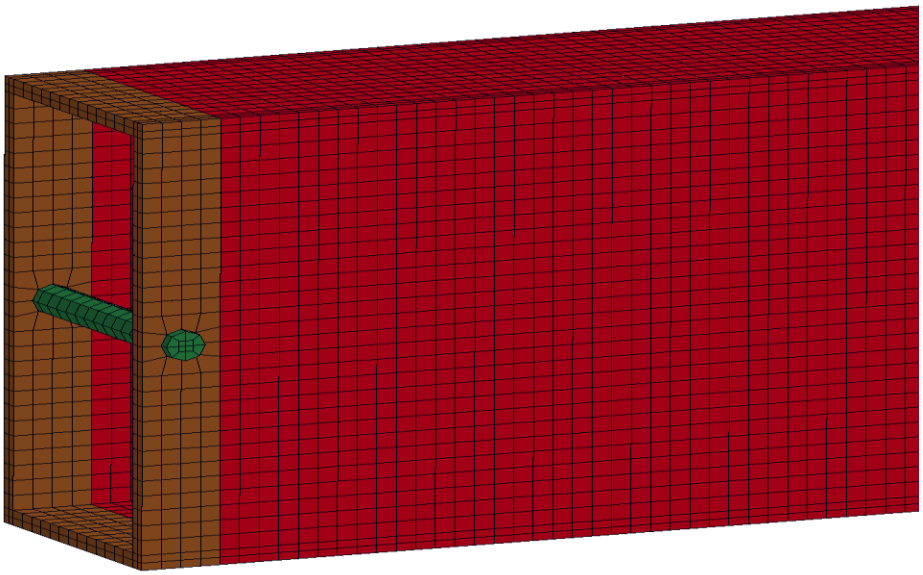

(a) Elevation view of the end section of FE model

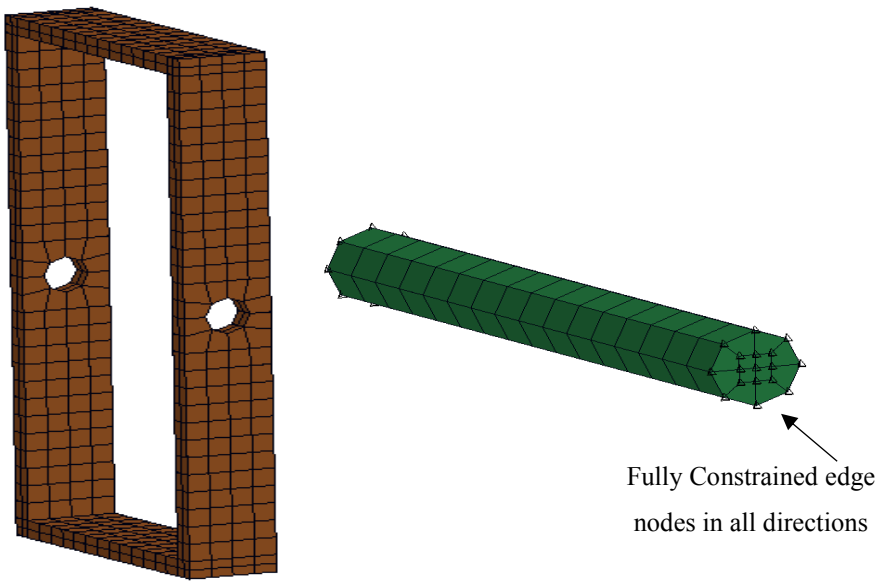

(b) Enlarged view of elastic end section showing the bolt hole and rigid rod with applied boundary condition

Figure 6.7: Geometric and boundary Details of the FE model

6.4.2 Result and discussion for FE and theoretical models with no strength degradation

The load-displacement response for the FE and theoretical models is presented in Figure 6.8. The FE model slightly over-predicts the response compared to the theoretical models and the axial capacity of the beam section is reached at a lower displacement compared to the theoretical model. This is because in the FE model, axial force develops at an early stage prior to formation of plastic hinge whereas in the theoretical model, axial force is assumed to start after formation of plastic hinge. For instance, the axial force in the FE model at the formation of plastic hinge is 294KN whereas axial force is yet to develop in the theoretical model at the same displacement.

The M-N relationship at a section near the middle column for FE and theoretical models are shown in Figure 6.9. It could be seen from this Figure that there is a residual moment capacity when the axial capacity of the section is reached whereas in the theoretical model, the moment is zero once the axial capacity is reached. Aside these

minor differences, the theoretical model prediction is comparable with FE model result with reasonable accuracy.

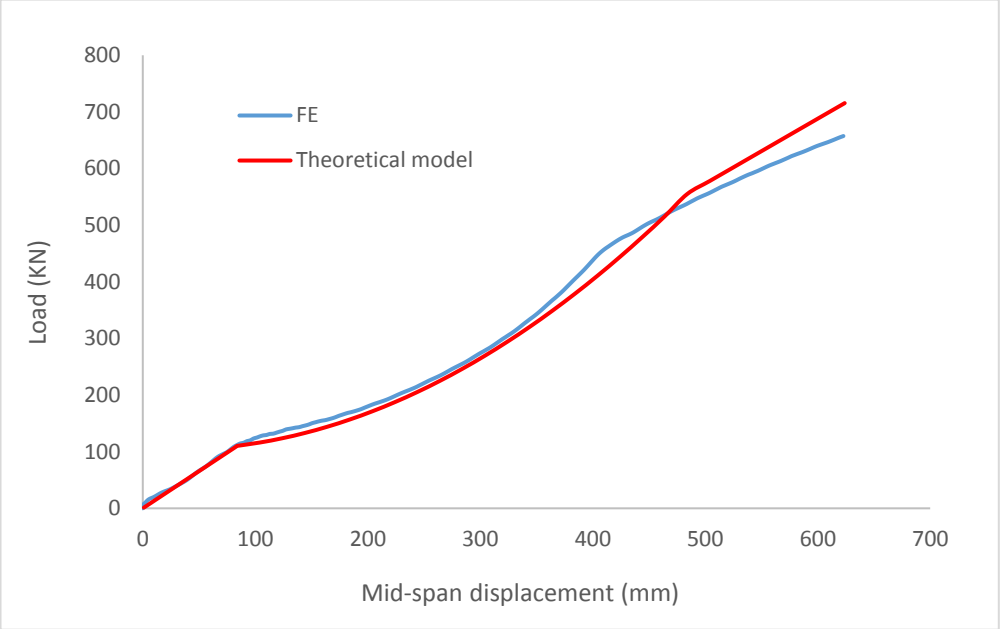

Figure 6.8: Load-displacement curve for FE and theoretical model without consideration of strength degradation

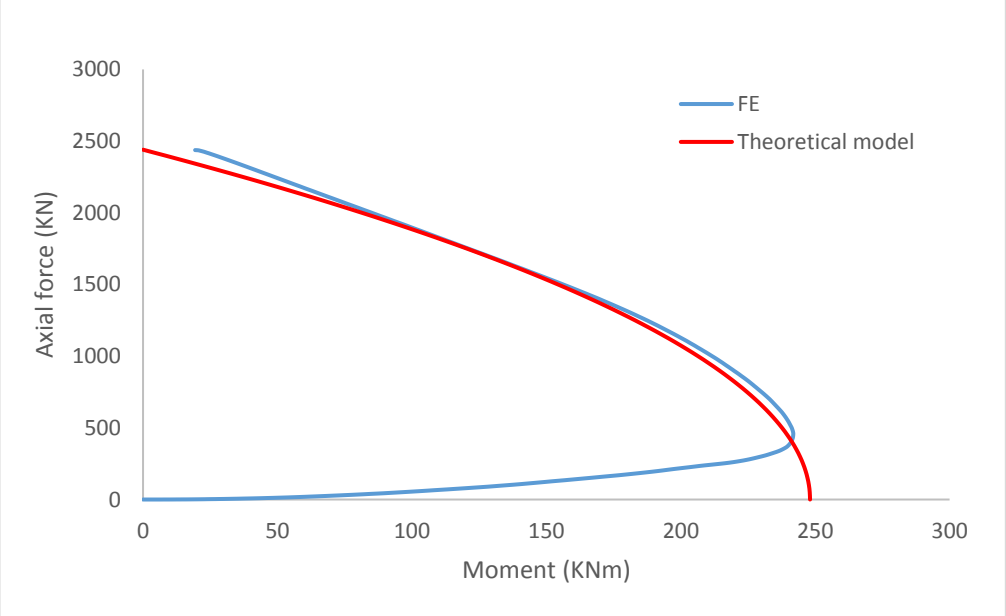

Figure 6.9: Moment-axial force relationship comparison for FE and theoretical model

The plastic strain distribution along the bottom fibre of the beam at three different middle column displacements of 90, 300 and 500mm which corresponds to start of yielding, transient stage and pure catenary action stage are also shown in Figure 10 to shed more light into the evolution of plastic strain and the plastic zone at the middle section of beam.

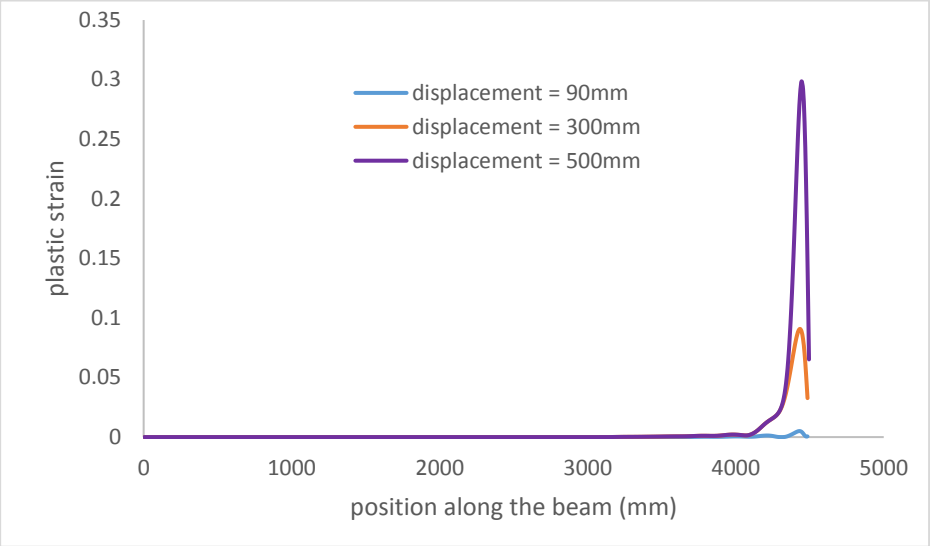

Figure 6.10: Plastic strain distribution along the bottom fibre of the beam

As illustrated in Figure 6.10, at a middle column displacement of 300mm, the maximum plastic strain is about 0.1. For a typical steel connection with welded flange and bolted web (e.g. Li et al. 2013; Li et al. 2015; Yang & Tan 2013b) some of the connection components e.g. bottom flange weld may have fractured causing a reduction in strength. More so the final failure of the connection may occur well before the displacement of 500mm is reached. In such cases, using existing model (Izzuddin 2005) with no consideration of strength degradation and eventual failure limit will overestimate the load capacity of the steel assembly under column removal. For the real behaviour to be captured, it is imperative to consider the degradation of the internal forces (axial force and bending moment) caused by the failure of some of the components of the connection and the eventual failure limit. It is on this premise that

degradation of the strength is considered in the next section to reflect the actual behaviour as observed in the experiments.

6.5 Degradation of yield surface

6.5.1 Concept of strength degradation and implications on catenary effect

The illustration in Section 6.4 clearly shows the need to incorporate strength degradation in the theoretical model for accurate prediction. In this section incorporation of strength degradation is explained in detail.

To illustrate the concept of degradation of strength, consider a steel connection in Figure 6.11a, which is subjected to large deformation. The connection represents a typical semi-rigid steel connection where the beam flange is welded to the column and the beam web is bolted to the column through the web cleat on each side of the connection. At the start of the loading, the beam behaves in flexure with the top flange in compression and bottom flange in tension. As the load increases, the flexural capacity is reached. Further loading will lead to the fracture of the bottom weld. Once this happens, the flexural and axial capacity of the section is significantly reduced and it is limited by the bolts connecting the beam to column in the web section and the top flange weld. This reduction in the flexural and axial capacities of the connections need to be considered to ensure a more reliable prediction of the global load-displacement response.

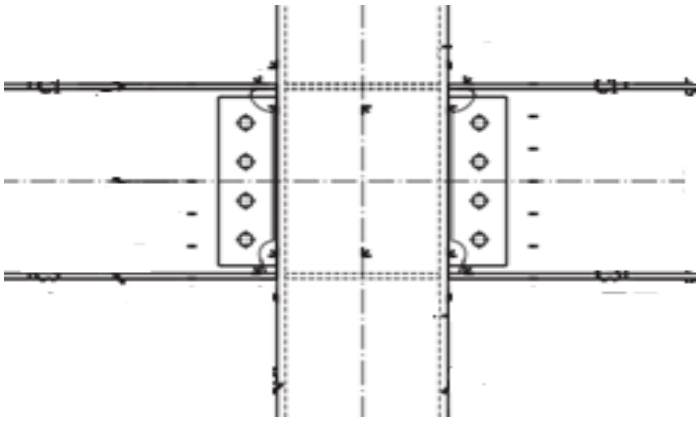

(a) Typical semi rigid steel connection (Li et al. 2015)

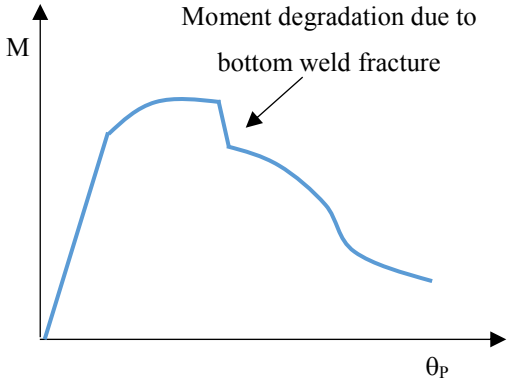

(b) Bending moment-rotation curve

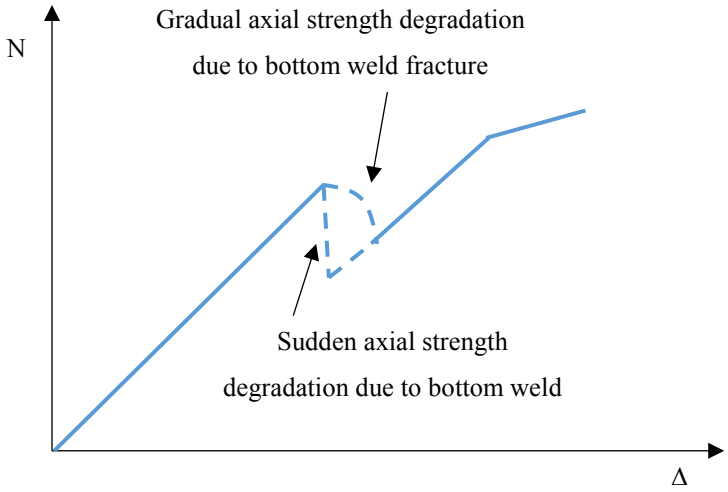

(c) Axial force-axial displacement relationship

Figure 6.11: A representative joint connection and process of strength degradation

As shown in Figures 6.11b and c, due to the failure of the bottom flange weld, the bending moment and axial force is reduced. The reduction of axial force may be steep or less steep (as shown in Figure 6.11c) depending on the ductility of the welded area. The M-N curve corresponding to the ultimate and degraded surfaces after failure of the bottom weld are shown in Figure 6.12. In this theoretical model, the equilibrium is sought for on the degraded surface once the failure criteria are met. The way and manner in which this is done in the model is explained in Section 6.5.2.

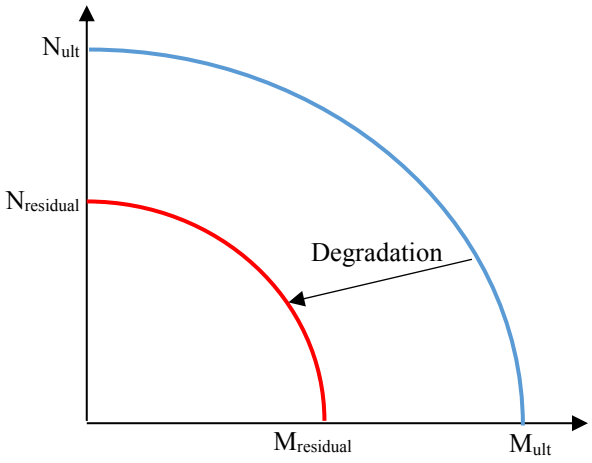

Figure 6.12: Ultimate and residual yield surfaces

6.5.2 Implementation of degradation of yield surfaces in the beam analysis procedure

6.5.2.1 General rules

Given the ultimate and residual yield surfaces, the reduction of internal forces (bending moment and axial force) can be obtained once the specified failure criteria is reached. As an illustration, Figure 6.13 is reconsidered. Let A be a point (on the ultimate surface) at which specified condition for degradation is fulfilled. For further increment, equilibrium is sought for using the residual yield surface. Before seeking for equilibrium on the residual surface, the internal forces need to be reduced such that a combination of axial force and bending moment lies on the new residual yield surface.

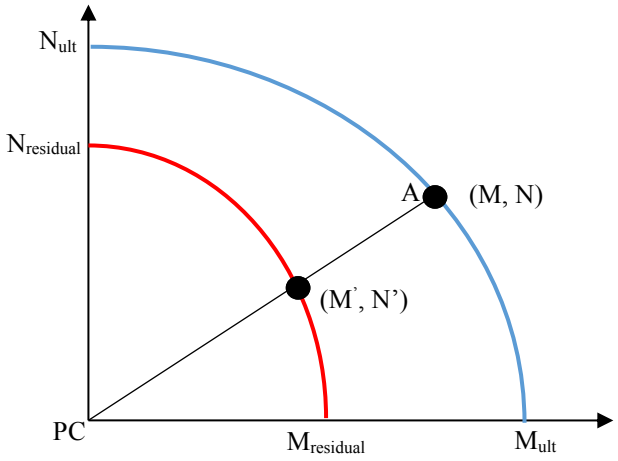

Figure 6.13: Illustration of migration between ultimate and residual surfaces

The method of reducing these internal forces belongs to the plasticity theory and there have been different methods to determine the new position on the residual surface depending on the hardening rule used. In this model, the radial method is adopted (Dafalias & Herrmann 1986; Seidalinov & Taiebat 2014). According to this method, every point on the ultimate yield surface (or bounding surface) has a corresponding image point on the degraded surface. Any mapping rule adopted must satisfy the identity condition (Seidalinov & Taiebat 2014). By identity condition, it means that the new internal forces must lie on the degraded surface.

Using the radial mapping rule, the image of point (M, N) on the ultimate surface is projected onto the degraded surface (M', N'). This image point can be determined using the following expression (Seidalinov & Taiebat 2014).

$$M' = M_c + \mu(M - M_c) \tag{6.21}$$

$$N' = N_c + \mu(N - N_c) \tag{6.22}$$

where μ is the ratio between internal forces on the degraded and ultimate yield surfaces. M_C and N_C corresponds to the projecting centre (PC). M and N are the internal forces on the ultimate yield surface and M' and N' are the corresponding image point on the degraded surface.

In this model, isotropic hardening is assumed. This means that the yield surface can expand or contract (hardened or softened) but cannot translate. Therefore, the projection centre (PC) is fixed. With this assumption, Equations (6.21) and (6.22) can be further simplified to:

$$M' = \mu M \tag{6.23}$$

$$N' = \mu N \tag{6.24}$$

where M_C and N_C are zero as shown in Figure 6.13.

The value of μ can be determined by substituting Equations (6.23) and (6.24) into the degraded surface function. An example of generalised representation of degraded nonlinear yield function is given in Equation (6.25) as:

$$\frac{M}{\rho_M M_p} + \psi\left(\frac{N}{\rho_N N_p}\right)^2 = 1 \tag{6.25}$$

where ρ_M and ρ_N are the reduction factors for axial force and bending moment.

6.5.2.2 Condition for activating strength degradation

The formulation presented in Section 6.3 is in terms of axial deformation and rotation. For steel connection, the rotation of the connection may be taken as the governing criteria for determining when strength degradation may occur. This could be argued on the fact that connection zone is small compared to the entire beam and while the beam remains elastic, only the connection zone elongates. On the other hand, for a RC structure, the plastic hinge is much larger and this plastic hinge elongates and also rotates. To relate the axial elongation and rotation of the beam in this case to physical behaviour of the plastic hinge, the combined effect needs to be considered. There may be different ways to measure the combined effect, depending on the details of the plastic regions and the damage mechanisms. But in general, the combined maximum strain may be indicative of the local demands and hence the degree of degradation. For this reason, herein we employ the maximum strain as a limiting criterion for the development into degradation phase.

To relate the strain criterion to the plastic deformation in the beam model, it is necessary to express the two components; axial deformation and rotation in terms of the maximum strain in the critical cross section (plastic hinge zone). It is known that rotation is related to the curvature of the section and axial deformation is related to the axial strain through the following expressions:

$$U_p = \varepsilon_{\max} L_p \text{; and } \theta_p = \varphi L_p \tag{6.26}$$

where $\varphi = \frac{2\varepsilon_{\max}}{d}$ (assuming bending neutral axis is at the section centre).

Resolving the above equations, the total strain becomes;

$$\varepsilon_{\max} = \frac{\sigma_y}{E} + \frac{U_p}{L_p} + \frac{\theta_p d}{2L_p} \tag{6.27}$$

where;

σ_y is the yield strength of the material

$\varepsilon_{\max}$ is the maximum strain in the plastic hinge

U_p is the axial elongation at each increment

θ_p is the angular rotation at each increment

d is depth of the section

L_p is the theoretical plastic hinge length.

Although the yield strain is very small compared to the total strain, it should be considered to achieve a more accurate prediction. In this illustrative work, the theoretical plastic hinge length is assumed a certain value. In subsequent stage of this study where the behaviour of reinforced concrete beam will be investigated, an equivalent plastic hinge length will be used. A flow chart showing the implementation of the strength degradation is shown in Figure 6.14.

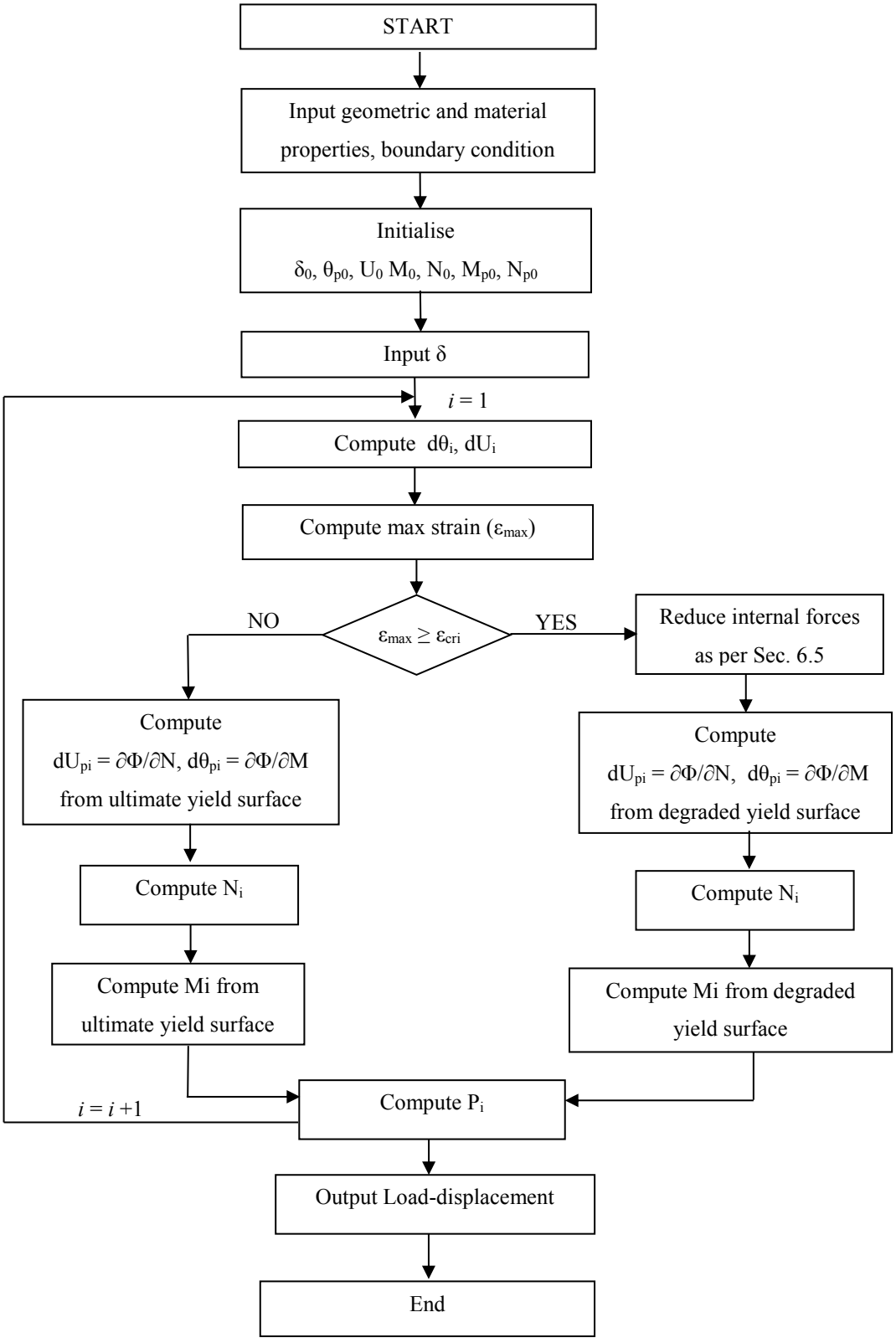

Figure 6.14: Flow chart for calculating internal forces and vertical resistance with consideration of strength degradation

6.6 Verification of the theoretical model for prediction of load-displacement resistance function with strength degradation

6.6.1 Validation with a conceptual FE simulation

The same beam modelled in Section 6.4 is considered here. The entire beam is modelled with elastic properties. The strength degradation is conceptually represented as follows. A section near the middle column which is 50mm in depth and 100mm in length is modelled with another material (elastic) such that at specified maximum strain of 0.1, the element in this section will be eroded which leads to degradation of strength. Figure 6.15 shows the FE model, the critical section with failure strain of 0.1 is shown in the highlighted area. The schematic representation of the section before and after strength degradation is shown in Figure 6.16.

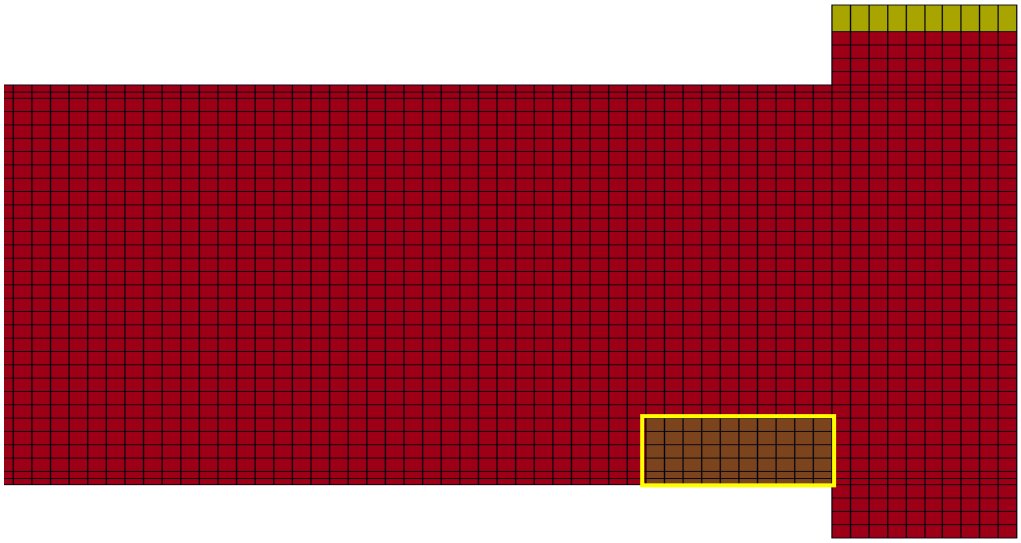

Figure 6.15: Section near middle column with the degraded section shown in the highlighted area

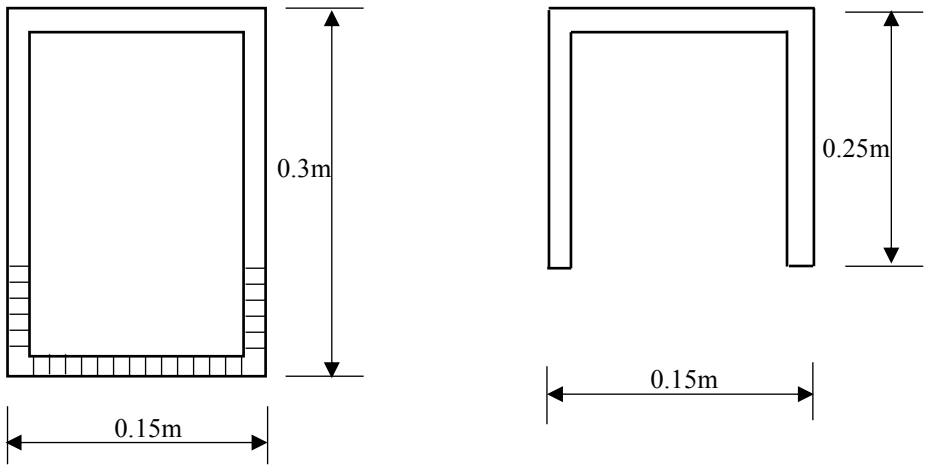

(a) Intact Section (b) Section after partial failure

Figure 6.16: Schematic showing the sections before and after degradation

For the undamaged section used in this analysis, the bending moment-axial force interaction is governed by the equation:

$$\frac{M}{M_p} + \psi\left(\frac{N}{N_p}\right)^2 = 1 \tag{6.28}$$

To determine the degraded yield surface, three points were selected to calculate the axial force and bending moment using the degraded section in Figure 14b. These included;

1) Section in pure bending (no axial force).
2) Section subjected to axial force without bending and,
3) A combination of certain amount of axial force and bending moment

Based on these three points, interaction curve for the full and degraded yield surfaces are shown in Figure 6.17. It can be seen that the degradation has a pronounced effect on the moment capacity of the section compared to the axial capacity. While the axial capacity reduced by only 27% percent, the moment capacity reduced by 46%.

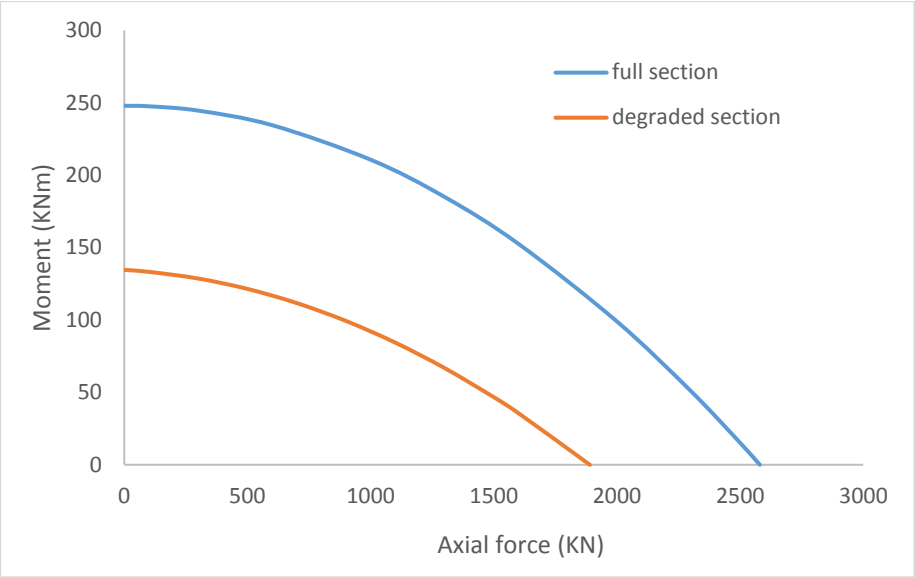

Figure 6.17: Moment-axial force interaction curves for full and degraded sections

The equation for the normalised relationship between bending moment and axial force for the degraded surface can be expressed as:

$$\frac{M}{M_{p1}} + 0.86\left(\frac{N}{N_{p1}}\right)^2 + 0.14\left(\frac{N}{N_{p1}}\right) = 1 \qquad (6.29)$$

where M_{p1} and N_{p1} are the moment and axial force capacities for the degraded section calculated as 134.6KNm and 1890KN respectively. Noting that the moment (M_p) and axial force (N_p) capacities for the full section are 248KNm and 2580KN, the moment - axial force interaction in Equation (6.28) can be expressed in terms of capacities of the full section (M_p and N_p) as:

$$\frac{M}{\rho_M M_p} + 0.86\left(\frac{N}{\rho_N N_p}\right)^2 + 0.14\left(\frac{N}{\rho_N N_p}\right) = 1 \qquad (6.30)$$

where ρ_M and ρ_N are 0.54 and 0.73 respectively.

The comparison of load-middle column displacement between the proposed theoretical model and FE model is shown in Figure 6.18. It can be seen that the proposed theoretical model captures accurately the reduction in the global strength caused by the failure of elements in the critical section. It should however be noted that the spread of damage zone has an effect on the global load-deformation behaviour.

Nevertheless, the exploration herein shows the accuracy of the proposed theoretical model in capturing the degradation of strength in the critical region on the global behaviour of the beam assembly.

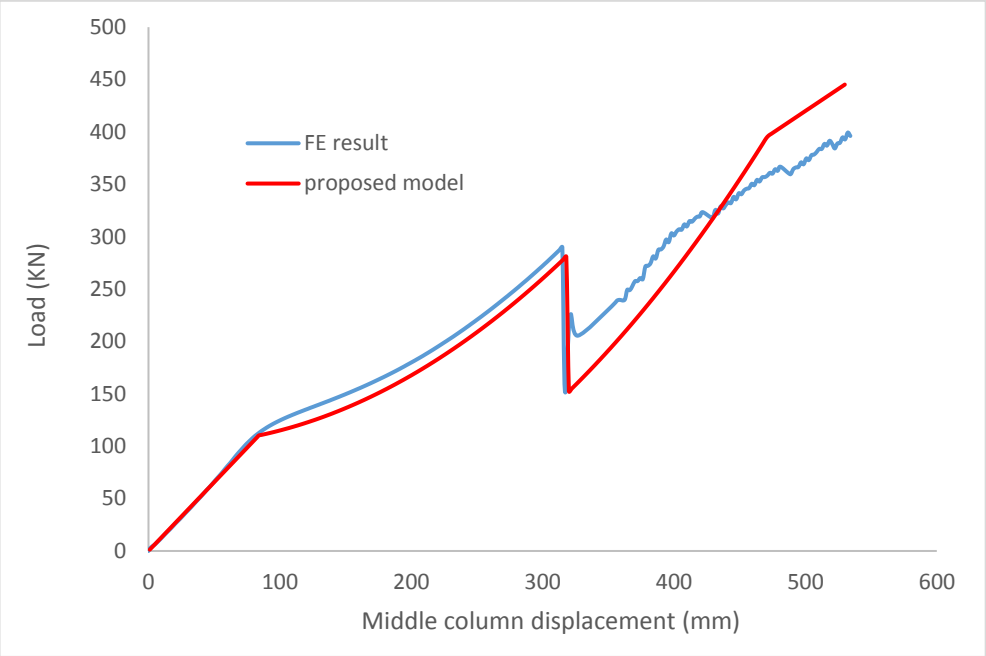

Figure 6.18: Comparison of load-displacement response from FE and proposed model with strength degradation

6.6.2 Validation with existing experiment

The reliability of the theoretical model with strength degradation is further checked using experimental studies by Li *et al.* (2015) . The steel subassembly tested in their studies was extracted from a building with the two ends assumed to be the points of contra-flexures and middle column was removed. The detail of the middle beam-column connection as shown in Figure 6.19 consisted of a beam web bolted to the column and the beam flange welded to the column. Pin boundary condition was applied at the beam ends to simulate the axial restraint and the total length of the beam assembly was 4500mm. The beam was made of standard H section H300 x 150 x 6 x 8 (H x B x t_w x t_f) and the middle column section dimension was square hollow section (SHS) of size 250 x 14 (D x t). Four rows of bolt were used to connect the beam web

to column. The yield and ultimate strength of the beam section was 407 and 653MPa respectively. More details about the experiment can be found in Li *et al.* (2015).

As stated previously, the failure criteria for steel subassembly may be well represented by the rotation of the connection. The rotation at rupture of weld and rotation at eventual failure for a given type of joint details may be determined using more detailed studies including physical experiments. Such data from experimental and other studies on limiting criteria can be easily employed in the proposed theoretical model for the evaluation of the load-displacement resistance function. Since such general data is not currently available, herein the rotation corresponding to the rupture of bottom weld and final failure reported in the test is used.

For a more accurate determination of moment-axial force strength curves, a detailed analysis may be performed for the connection before and after the failure of the bottom flange weld taking into consideration of the bolt arrangements. In the present purpose, a simplified analysis of the M-N relationship is performed using an equivalent beam section. The assumed beam section for the calculation of M-N curve before and after the rupture of bottom flange weld is shown in Figure 6.20. The assumption here is that after the failure of the weld, the bottom flange no longer contributes to the resistance and the section can be assumed to comprise of the web and the top flange.

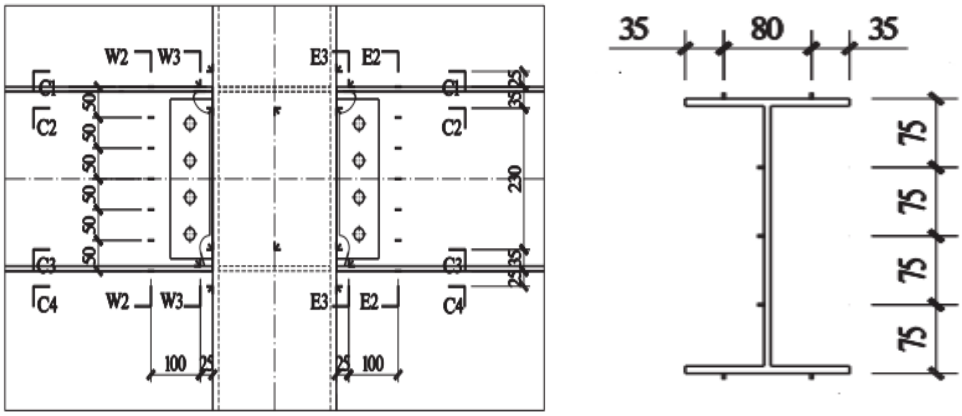

Figure 6.19: Middle beam-column joint and section details of tested specimen (Li et al. 2015)

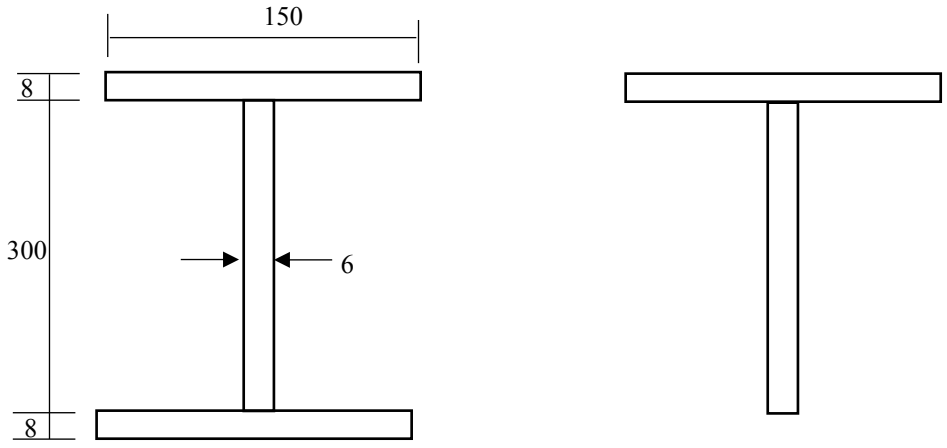

(a) before bottom weld failure (b) after bottom weld failure

Figure 6.20: Determination of M-N curves for the critical region of the tested beam (dimensions in mm)

The M-N interaction curve for the section before and after bottom weld rupture based on the simplified approach explained above and the section geometry in Figure 6.20 is shown in Figure 6.21.

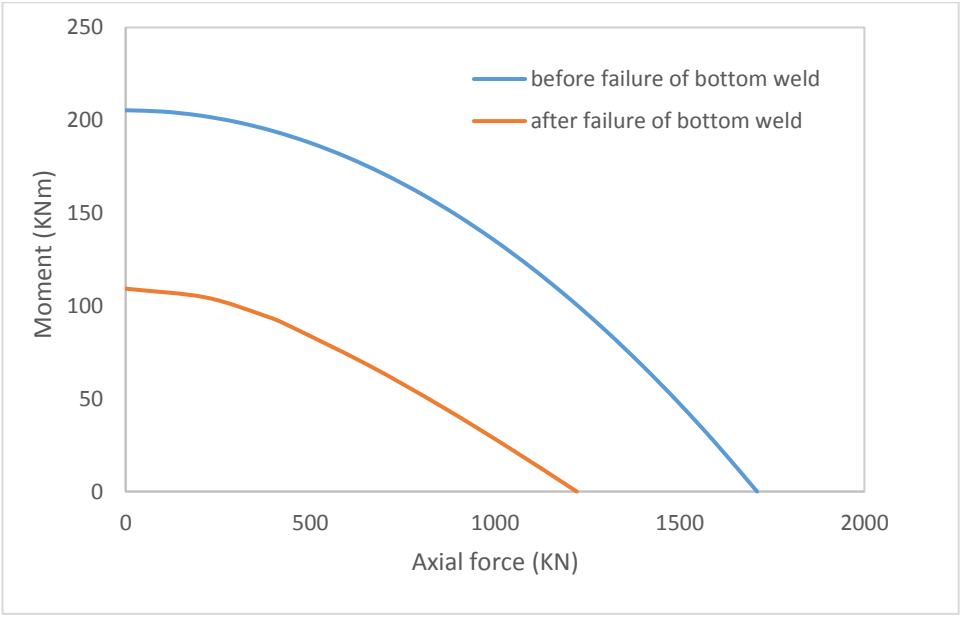

Figure 6.21: Moment-axial force curves before and after fracture of bottom weld

From Figures 6.20 and 6.21, the moment-axial force interaction equations for the full and reduced section following bottom weld fracture can be expressed as:

$$\frac{M}{M_p}+\left(\frac{N}{N_p}\right)^2=1 \tag{6.31}$$

$$0.98\frac{M}{M_{p1}}+0.69\left(\frac{N}{N_{p1}}\right)^2+0.33\left(\frac{N}{N_{p1}}\right)=1 \tag{6.32}$$

where M_{p1} and N_{p1} are the moment and axial force capacities for the reduced section calculated as 109KNm and 1221KN respectively.

The Moment (M_p) and axial force (N_p) capacities for the full section is calculated as 205KNm and 1709KN respectively, hence the moment-axial force interaction in Equation (6.32) can also be expressed in terms of capacities of the full section (M_p and N_p) as:

$$0.98\frac{M}{\rho_M M_p}+0.69\left(\frac{N}{\rho_N N_p}\right)^2+0.33\left(\frac{N}{\rho_N N_p}\right)=1 \tag{6.33}$$

Where ρ_M and ρ_N are 0.53 and 0.71 respectively.

Using the actual and degraded yield surfaces, the load-displacement response is predicted and Figure 6.22 shows the comparison between the experimental and proposed theoretical predictions. It is seen that the theoretical prediction match well with the experimental load-displacement curve. As mentioned previously, information about the rotation at failure of the bottom weld was adopted from the experiment. If such information is available for a given type of connection, it can be used in the model to predict the response with accuracy.

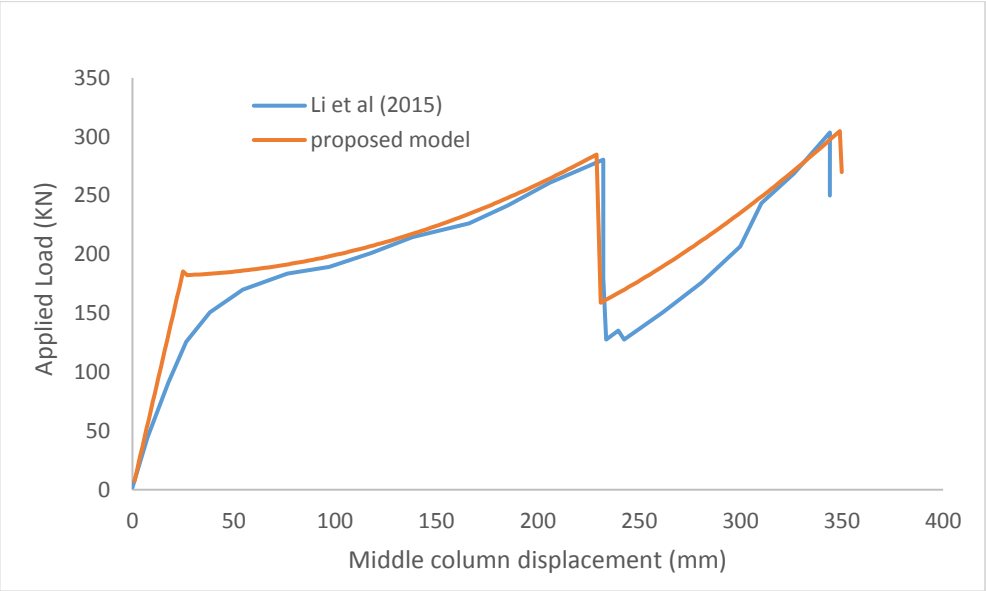

Figure 6.22: Comparison of load-displacement response from experimental result and proposed model

6.7 Application of the proposed model to reinforced concrete beam-column assemblies

6.7.1 General assumptions

The model can be applied to predict the load-displacement response of RC assemblies. From available experimental studies on RC assemblies catenary action start at a middle column displacement of about one beam-depth (Yu & Tan 2013b; Sadek et al. 2011). Prior to the displacement of one-beam depth, the assemblies traverse through the flexural and compressive arching response stages. A schematic representation of the complete load-displacement response including the different stages of response is shown in Figure 6.23. The model for compressive arching action developed in Chapter five can be used to predict the load-displacement response till the deflection of one-beam depth. For simplicity, it is assumed in this model that the load at the start of catenary action is determined by the flexural capacity of the beam. In certain instances, concrete may be severely crushed such that the bending capacity prior to catenary action stage is lower than the actual bending capacity; however as observed from

majority of the available tests and from FE simulation tests, assumption of flexural capacity is not too far away from the actual behaviour.

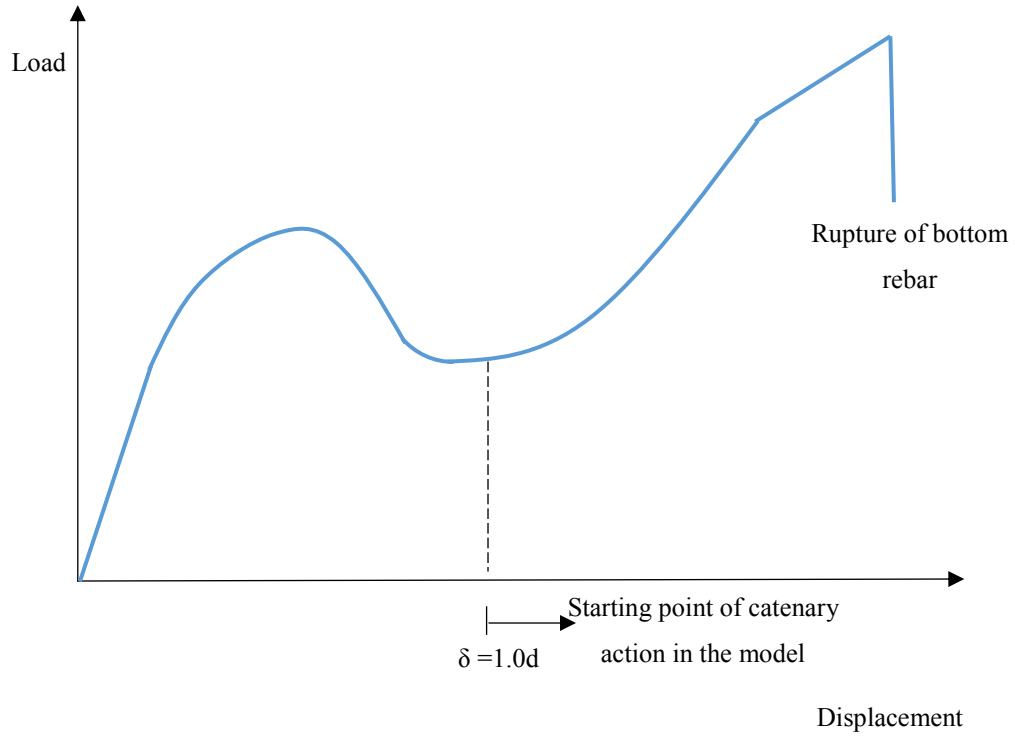

Figure 6.23: Idealised load-displacement resistance function for RC assemblies in the proposed model

6.7.2 Formulation for fixed end RC beams with plastic hinges at support and middle sections

The formulation presented in Section 6.3 only considered plastic hinge developing at middle section of the beam. For a typical reinforced concrete assembly located in the middle of the RC building, plastic hinges will form at the middle and end section, hence the constitutive equations of all the plastic hinges needs to be considered in determining the axial force in the beam.

Let the constitutive behaviour of the plastic hinges at the middle and end sections be φ_m and φ_e.

where:

$$\varphi_m = f(M_m, N) = 0 \quad \text{for middle section} \tag{6.34}$$

$$\varphi_e = f(M_e, N) = 0 \quad \text{for end section} \tag{6.35}$$

As shown previously, the overall elongation of the beam for a given displacement was calculated as:

$$U = \frac{2\delta^2}{L} \tag{6.36}$$

For a small increment in elongation and rotation, the axial force in the beam can be expressed as:

$$dN = K_e(dU - 2dU_{pe} - dU_{pm}) \tag{6.37}$$

where dU_{pm} and dU_{pe} are the incremental elongation of the plastic hinges at the middle and end sections respectively, assuming the beam is symmetrical about the middle section such that plastic hinges at both ends are the same.

Applying flow rule theory to Equations (6.34) and (6.35), the incremental axial deformation dU_{pm} and dU_{pe} can be worked out as done previously. Hence equation (6.37) can be expressed as:

$$dN = K_e\left(dU - 2.\frac{\partial\varphi/\partial N}{\partial\varphi/\partial M_e}d\theta_{pe} - \frac{\partial\varphi/\partial N}{\partial\varphi/\partial M_m}d\theta_{pm}\right) \tag{6.38}$$

where:

$$d\theta_{pm} = 4\frac{d\delta}{L} \text{ and } d\theta_{pe} = 2\frac{d\delta}{L} \tag{6.39}$$

Substituting Equations (6.39) into (6.38) and integrating with deflection of u_c as the starting deflection, where u_c=1.0d, gives:

$$N = K_e \left(2\frac{(\delta^2 - \delta_c^2)}{L} - 4\frac{(\delta - \delta_c)}{L}\frac{\partial\varphi/\partial N_e}{\partial\varphi/\partial M_e} - 4\frac{(\delta - \delta_c)}{L}\frac{\partial\varphi/\partial N_m}{\partial\varphi/\partial M_m} \right) \tag{6.40}$$

Thus, for each incremental displacement, the axial force can be calculated using the expression in Equation (6.40) and subsequently the moment at the middle and end sections can be determined from the yield function in Equations (6.34) and (6.35) respectively.

6.7.3 Equilibrium of forces

To determine the load at each incremental displacement, one-half of the beam and the forces acting on it is considered as shown in Figure 6.24. Similar to the assumption stated in Section 6.3, the horizontal reaction (H_R) is assumed to be the same as the axial force at plastic hinge which is denoted as (N).

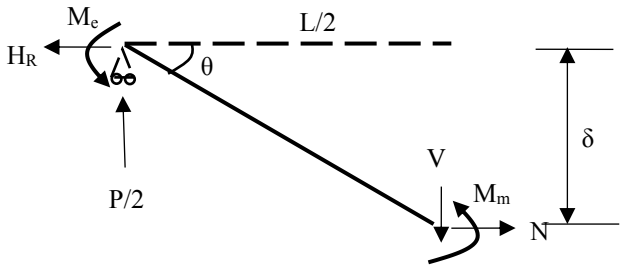

Figure 6.24: Free body diagram showing force acting on a fixed end beam

Taking moment about the middle point,

$$M_e + M_m + H_R\delta - PL/4 = 0 \tag{6.41}$$

The load vertical load P can be obtained as:

$$P = \frac{4H_R\delta}{L} + \frac{4M_m}{L} + \frac{4M_e}{L} \tag{6.42}$$

6.7.4 Failure criteria during catenary action

In terms of failure criteria, the rupture of reinforcement during catenary action stage depends on the strain in the reinforcement at the critical sections. The strain in the reinforcement (at end and middle section) at the start of catenary action can be determined using the compressive arching model. Thus, the total strain at the critical section at any stage of the catenary action can be expressed as:

$$\varepsilon_{total} = \varepsilon_y + \varepsilon_{com} + \varepsilon_{cat} \tag{6.43}$$

where ε_y is the yield strain of reinforcement at the end of elastic stage defined as:

$$\varepsilon_y = \frac{\sigma_y}{E} \tag{6.44}$$

ε_{com} is the strain in the tensile reinforcement at the end of compressive arching stage (deflection of 1.0d) which is determined using the compressive theoretical model in Chapter 5 as:

$$\varepsilon_{com} = \delta_p \frac{(d - a - x_{bp})}{0.5 * L_p L} \tag{6.45}$$

where:

δ_p is the displacement at the end of compressive arching action

d is the depth of the beam

L is the length of double bay beam

a is the cover to reinforcement

L_p is the plastic hinge length used in the theoretical model for compressive arching action

x_{bp} is the compression zone depth for bending at the critical section (middle or end section)

ε_{cat} is the strain in reinforcement during the catenary action stage which can be expressed as:

$$\varepsilon_{cat} = \frac{0.5U_p}{L_{pc}} + \frac{\theta_p d}{2L_{pc}} \tag{6.46}$$

where L_{pc} is the plastic zone length in the catenary action stage.

Comparing Equation (6.27) and (6.46) it can be seen that the strain due to elongation of the beam is reduced by half. The assumption herein is that plastic hinge length at the end and middle section are similar. Thus, damage due to elongation of the beam is divided into two each being taken by plastic hinges at the end and middle section as represented in Equation (6.46).

During the catenary action stage, the entire beam behaves in a cable like manner. Severe cracks occur at the end and middle column section with cracks also developing along the beam at approximately equal spacing (Yu & Tan 2013b; Sadek et al. 2011). This damage may be lumped within the plastic zone at the end and middle column section. For this reason, a plastic zone needs to be defined to reflect the behaviour. It should be noted that the plastic hinge length in the theoretical model on compressive arching action may be different from the plastic hinge length during the catenary model. Hence, they are represented by different symbols herein referred to as L_p and L_{pc} for compressive arching action and catenary models respectively. Thus, with selected plastic hinge length for compressive arching and catenary action stages, the displacement at which the reinforcement ruptures can be determined.

Figure 6.25 shows the flow chat for the implementation of the procedure outlined above. The application of the model in predicting the load-displacement response of RC assemblies will be presented in Chapter 7.

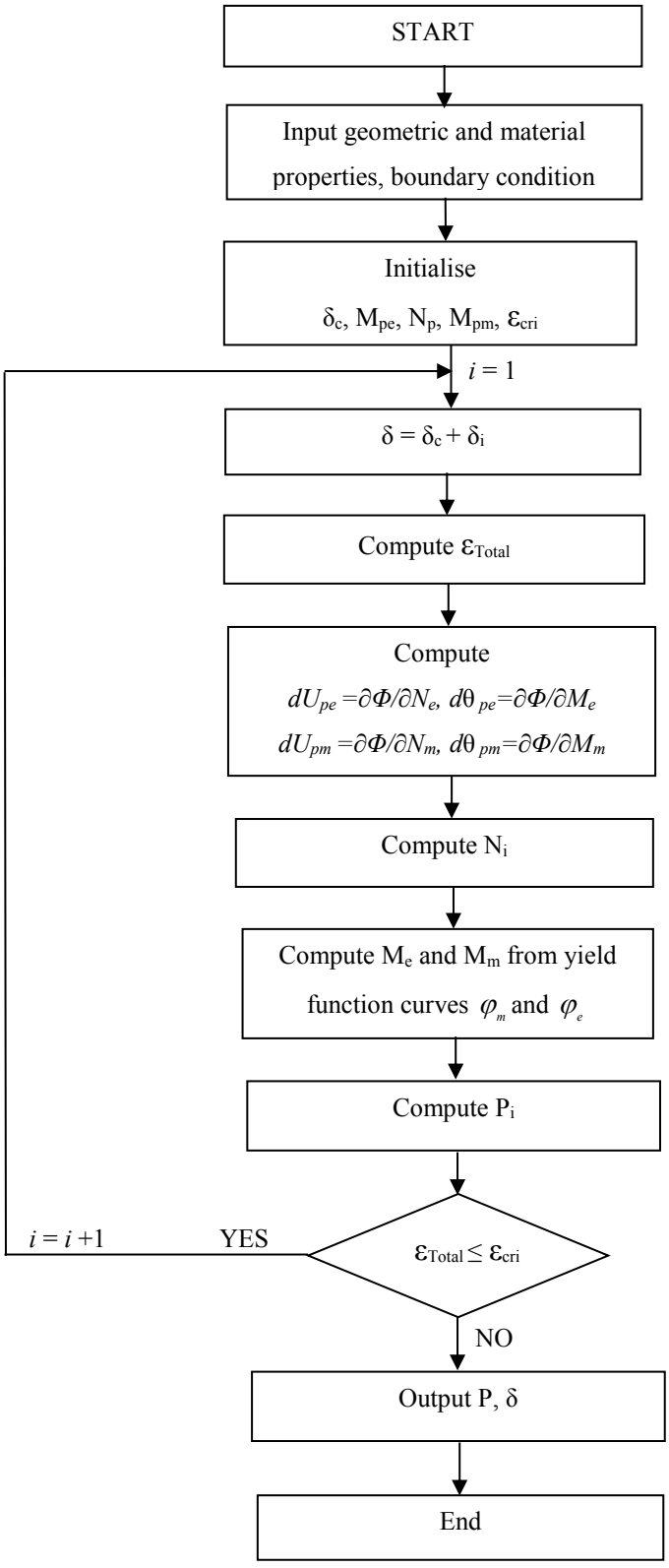

Figure 6.25: Flow chart for calculating internal forces and vertical resistance without considering strength degradation

6.8 Conclusions

An analytical model for catenary action in axially restrained beam is proposed in this Chapter. The model takes into consideration strength degradation which can occur due to failure of some connection components. The proposed model is initially formulated for a simply supported beam and is also extended to cover fixed-end beam with axial restraint. It takes into account the plastic interaction between axial force and bending moment at the plastic hinges for each incremental displacement.

Comparison of experimental test result and predictions from the proposed model shows that the model is capable of predicting correctly the load-displacement response of steel and RC subassembly including the strength degradation which may occur due to failure of some connection components like failure of bottom weld. The model can be used for RC assembly and with a starting displacement after which overall tension in the beams develops (around the order of the depth of the beam). Different criteria for activating the strength degradation in steel and RC assemblies has been discussed. The generic proposed model is simple and can give reliable result which can be used for quick assessment of progressive collapse in steel and RC frame structures.

Chapter 7: Assessment of progressive collapse of RC frame using the developed model framework

7.1 Introduction

In the preceding Chapters, it was shown that for a laterally restrained RC beam assemblage, compressive arching and catenary actions develop to a varying degree, and these actions add onto the general flexural action and in combination they could provide the necessary structure bridging over a loss column and prevent the progressive collapse of the frame structure. Accordingly, theoretical models on compressive arching action and catenary action have been developed and validated.

Although, beam-column fibre element can be used in modelling the response of progressive collapse of RC buildings, it still presents some challenges in modelling accurately the response under column removal. For instance, accurate material model for modelling the confine and unconfined concrete needs to be selected to be better represented the compressive arching action. More so, the beam-to-column joint interface needs to be correctly modelled to obtained accurate result. All this present additional difficulties hence, the simplified model presented in this study can produce accurate result with less effort.

Using the developed theoretical models, the complete resistance function (load-displacement curve) for a critical RC assemblage with a loss of vertical member can be obtained.

In a conventional design, the compressive arching and catenary actions are not considered. In general, the capacity of an RC beam is governed by the flexural behaviour with formation of plastic hinges marking the load capacity of the beam. Assessing progressive collapse of a laterally restraint beam-assemblage based on the flexural capacity may therefore considerably underestimate the progressive collapse resistance capacity of the RC frame as a whole. On the other hand, inaccurate

estimation of the arching and catenary effects without considering adequately the degradation mechanisms could lead to overestimate of the collapse resistance. With the models developed in this thesis, the compressive arching and catenary actions can be well predicted and with improved accuracy.

The resistance functions (load-displacement curves) in the models are determined under static conditions. Without any significant effects due to strain rate, which is not expected to be very high in the progressive phase of the structural response, such resistance functions should represent the constitutive behaviour, which can subsequently be employed in a dynamic response analysis procedure. Indeed, progressive collapse is a dynamic event, and thus an accurate assessment of the amplitude of the response needs to take into consideration the dynamic effect arising from the sudden loss of column.

Many researchers have considered different approaches in assessing progressive collapse using static nonlinear load-displacement curve. GSA (2003) recommended a dynamic amplification factor of 2 to be used with the nonlinear static approach. However, a dynamic load factor of 2 has been argued to be too conservative especially in structures with realistic hardening after initial yielding where the dynamic factor could be much less than 2, consequently in the current edition of GSA (2013), a factor which is based on ductility of the member is used in an equivalent nonlinear static approach.

Izzuddin (2008) proposed a method of assessing progressive collapse using the energy balance principle. The method involves (1) determination of nonlinear static resistance function of the structure without the loss column, (2) determination of maximum dynamic response under sudden column removal using simplified dynamic assessment i.e. converting the nonlinear static resistance function to pseudo static curve, and (3) ductility assessment of the connections. The pseudo static curve is determined on the assumption that part of the building bridging over a loss column has a dominant deformation mode and respond like a single degree of freedom systems. The accuracy of this method depends on the accuracy of the nonlinear static resistance function. The

method has been used in assessing progressive collapse of steel structures (Izzuddin et al. 2007; Izzuddin et al. 2008; Vlassis et al. 2009; Jahromi et al. 2012)

This chapter therefore presents an investigative study into the importance of including realistic compressive arching and catenary actions in the assessment of progressive collapse resistance of RC subassemblies bridging over a loss column. The resistance functions of the structure with the loss column is determined using the compressive arching and catenary models developed in this thesis. Using the established energy method (Izzuddin 2008), the nonlinear resistance function is converted to a pseudo static response which is then used to assess the potential of collapse. The subassembly of the directly affected part of the frame structure is also modelled in LS DYNA, and the nonlinear static and dynamic responses obtained from the analytically predicted and FE modelling results are compared.

7.2 Design of the building frame

For this analysis, a four-storey office building is designed according to Eurocode 2. The plan dimension of the building is 35m by 20m and the gross floor thickness is assumed to be 200mm. The ground storey height is 4m and other storeys are uniformly 3m high, and the spacing between columns in both directions is 5m which is common in practice. The dead load was determined as 5KN/m^2 with an imposed load of 5KN/m^2 which is adequate for an office building. In addition to the dead load from the slab, it is assumed that the periphery frame carries an additional load of 10KN/m due to cladding and parapet walls. The unfactored dead and live load on the periphery frame are 22.5KN/m and 12.5KN/m respectively. Applying the appropriate factor of safety according to Eurocode 2, the maximum design load on the periphery frame is 50KN/m. Figure 7.1 and 7.2 shows the plan of the building and the bending moment distribution on the periphery frame (grid line A/1-7) based on the maximum design load of 50KN/m.

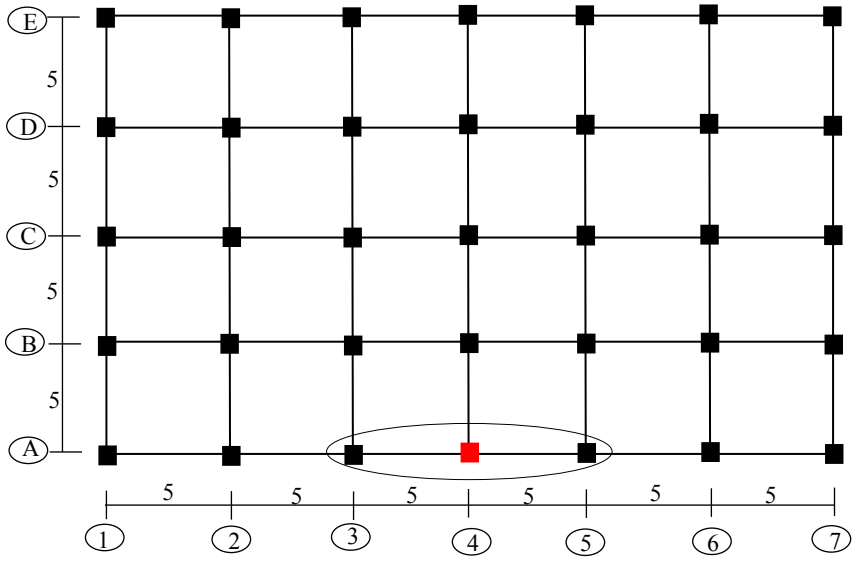

Figure 7.1: Plan view of the building (dimension in metres)

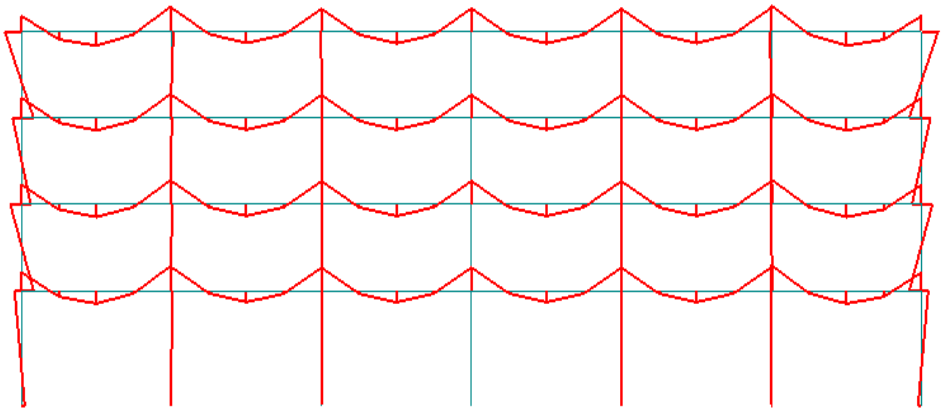

Figure 7.2: Bending moment distribution of the periphery frame

The RC beams are designed according to Eurocode 2. When designing RC structures, the structural designer has the choice of minimizing reinforcement or section size to achieve the desired design moment capacity. In this investigative study two different designs having approximately the same flexural load capacity but different section sizes and reinforcement ratios are considered. A summary of the design details for the two designs are shown in Table 7.1. For simplicity, the reinforcement is assumed to

be continuous within the bay of the removed column. In practice, this could be achieved by using mechanical couplers.

Table 7.1: Summary of design data

Properties/Design ID	Model A (L/d=13)	Model B (L/d=9)
Beam dimensions (mm)	250 x 350	250 x 500
Longitudinal beam reinforcement at support	2T20+2T16 (top) 3T16 (bot)	3T16 (top) 2T16 (bot)
Longitudinal beam reinforcement at mid-span	2T16 (top) 3T16 (bot)	2T16 (top) 2T16 (bot)
Shear reinforcement in beam	Φ8 @ 100mm	Φ8 @ 75mm
Column dimensions	400 x 400	400 x 400
Longitudinal reinforcement in columns	12T16	12T16
Shear reinforcement in columns	Φ8 @ 150mm	Φ8 @ 150mm

7.3 Simplified column loss representation

As mentioned previously, the periphery columns are more exposed to accidental load or an attack. In this study, column A4 (shown in red in Figure 7.1) is assumed to be loss. If the indirectly affected bay can provide adequate restraint to the directly affected bay where column is loss, then damage may be confined within the directly affected bay. As shown in Figure 7.3, the bending moment in the directly affected bay reverses sign with amplified magnitude because of the missing column.

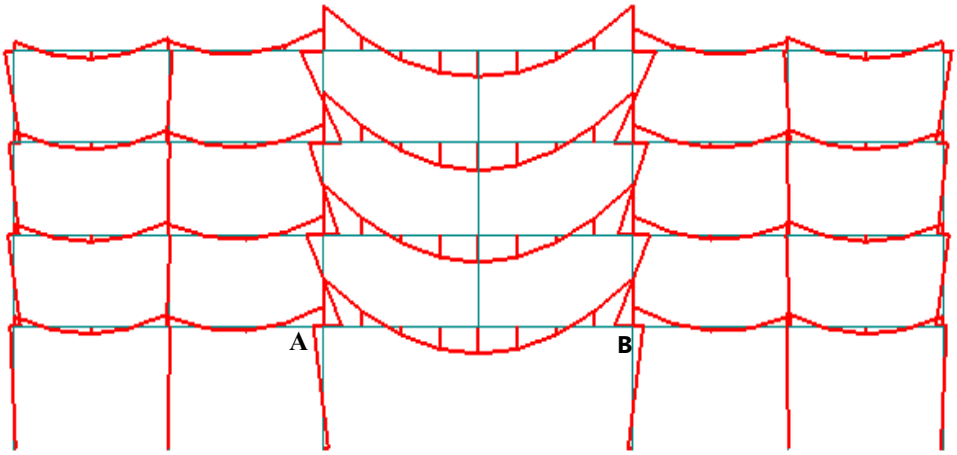

Figure 7.3: Bending moment distribution of Periphery frame without the missing column

For progressive collapse assessment, the frame without the missing column may be modelled to assess the potential of bridging over the missing column. The most comprehensive analysis will involve modelling the entire structure to ensure that interaction across the structural system is fully taken into account. However, modelling the entire frame will be computationally expensive.

For this reason, a key substructure, in this case the ground floor beam and column in the directly affected part, may be modelled while appropriate boundary conditions are applied at point A and B as shown in Figure 7.3 to simulate the lateral restraint provided by the remaining part of the building. The axial restraint can be determined by performing an elastic analysis on the entire frame without the loss column with a (unit) horizontal force applied at point A and B in Figure 7.3. Previous studies shows that including floor slab increases the axial restraint considerably (Yu 2012; Sasani et al. 2011). However, in the present analysis it is assumed that the floor slab is precast and hence does not contribute to the axial restraint. Figure 7.4 shows the deformed shape of the frame under a unit load of 1N at point A and B. It can be seen that swaying of column occurs at the ground and first floor and the other floor columns are less affected by the swaying.

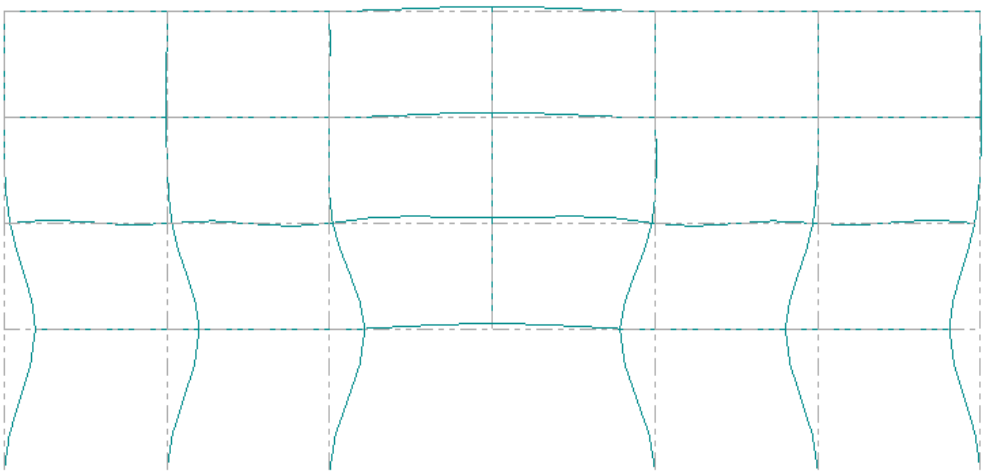

Figure 7.4: Deformation shape of the frame under a unit horizontal at points A and B

For a quick estimation of the axial restraint provided by the indirect bay of the building, the contribution from column/beam members on either side of the directly affected bay may be considered. Since the building is symmetrical about the removed column, the axial restraint will be the same. Considering only the left part of the RC frame and assuming that all upper joints on the right side are restrained in the horizontal directions as shown in Figure 7.5, the axial restraint stiffness may be calculated as:

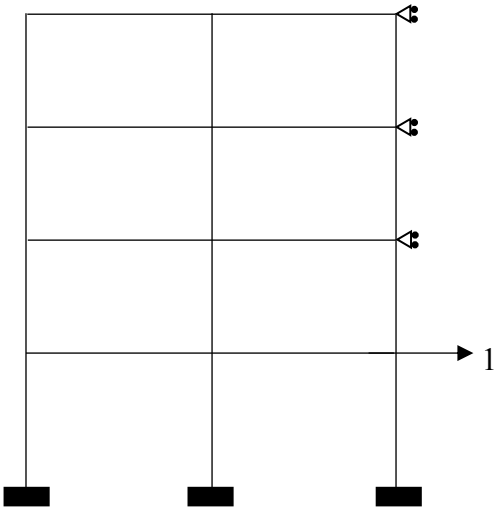

Figure 7.5: Simplified representation of left part of the RC frame

$$K_L = K_R = 3*\frac{12EI_{bc}}{L_{bc}^3} + 3*\frac{12EI_{tc}}{L_{tc}^3} + 2*\frac{12EI_b}{L_b^3} \quad (7.1)$$

where $I_{b,}$ $I_{tc\ and}$ I_{bc} are the second moment of area of the transverse beam, top column and bottom column section respectively.

The axial restraint stiffness from the elastic analysis of the frame without the missing column using GSA software is 88385KN/m while that obtained from the simplified expression in Equation (7.1) is 107511KN/m. It is seen that the axial stiffness from the simplified approach is about 18 percent more than the stiffness obtained from the elastic analysis of the entire frame. This difference may be due to assumption adopted in the simplified expression that is, ignoring the deformation in the upper columns. As can be observed in Figure 7.4, the upper joints are not completely rigid, hence the upper columns exhibit some swaying deformations and this reduces the axial stiffness. Nevertheless, the simplified approach can give an indication of the axial restraint for a given geometric properties of RC frame.

From Equation (7.1), it can be seen that axial stiffness depends on the size of the column and the larger the column, the higher the axial restraint stiffness. Since axial restraint is not the main focus of the present study, a reasonable axial restraint of value 3 x 10^5KN/m which is less than the axial stiffness of the beam (EA/L = 5 x 10^5KN/m) is selected for the investigative study.

With this simplification, the RC subassembly within the directly affected part may be considered as schematically shown in Figure 7.6.

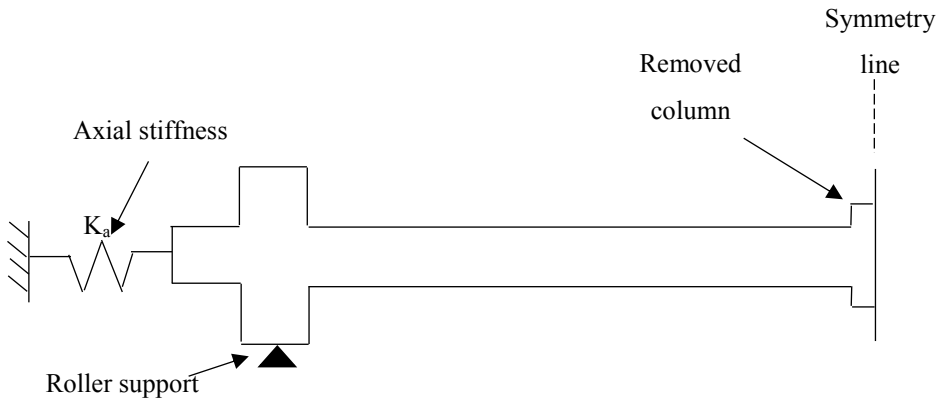

Figure 7.6: Directly affected subassembly of the building

7.4 Numerical modelling

7.4.1 Detail of the model

The FE modelling approach developed in Chapter 4 is used to model the quasi-static resistance and dynamic responses of the subassemblies. The subassemblies are modelled using a general-purpose finite element code (LS-DYNA). Concrete is modelled with KCC model while reinforcements in column and beam are modelled with PIECEWISE_LINEAR_PLASTICITY (mat_24). The mesh size of concrete and rebar is selected as 20mm. Due to symmetry, only one-half of the beam is modelled. The middle nodes of the bottom column are constrained in the vertical direction and the middle nodes of the end section are connected to elastic springs as schematically shown in Figure 7.6. This boundary condition allows moment to develop at end section due to the combined effect of axial constraint and roller pin. Thus, plastic hinges will develop at the middle and end sections. A group of elastic springs (nine here) are attached to the end face of the beam just to avoid force concentration to model the axial restraint with a total of axial stiffness being 3 x 10^5KN/m.

The compressive strength of concrete is taken as 30MPa and yield strength of transverse and longitudinal reinforcement are 400 and 500MPa, respectively. For simplicity, the longitudinal reinforcement is defined with trilinear elastic plastic

behaviour with an ultimate strength and rupture strain of 650MPa and 0.1 respectively as shown in Figure 7.7.

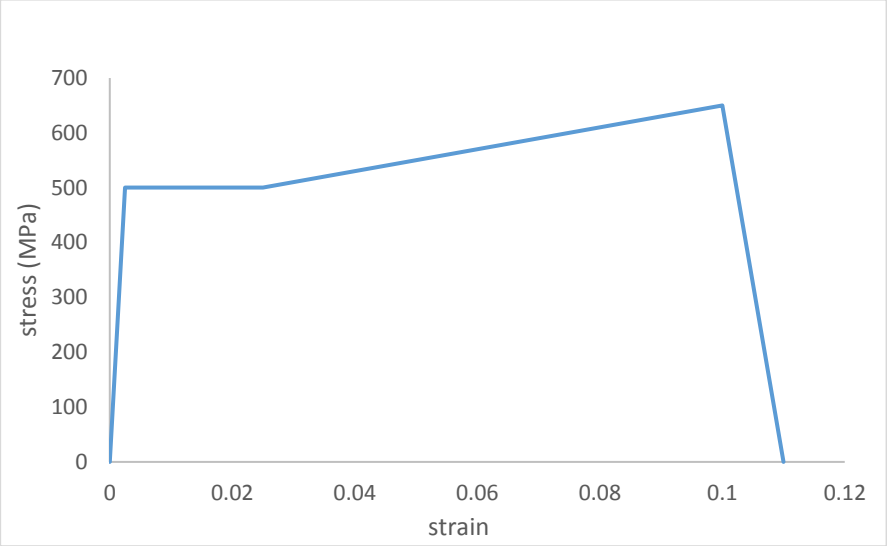

Figure 7.7: Stress strain curve for longitudinal reinforcement

To provide a good reference for comparison with the theoretical model prediction, the subassembly is first analysed under a quasi-static load acting at the middle column.

For the quasi static loading, displacement controlled loading approach is adopted to ensure the descending phase is captured properly.

7.4.2 Nonlinear dynamic analysis modelling approach

As stated in Chapter 3, the most direct method for assessing progressive collapse of building is the nonlinear dynamic analysis. Accordingly, nonlinear dynamic analysis is performed on the subassembly. The essence of the direct dynamic analysis herein is to compare with the assessment from the framework developed in this thesis.

In accordance with the procedure stipulated by GSA (2013), the nonlinear dynamic analysis consist of replacing the column from the structure with equivalent forces and at the same time applying the uniform gravity loads to the subassembly in a quasi-static manner, thus resembling the static equilibrium condition as in the original structure with the column in place. Following which the column reaction is then

removed within a stipulated time interval. In this study, the column removal time is made very small to represent a sudden column removal. The load combination for dynamic analysis is as per GSA (2013) and is given as:

$$G_{ND} = 1.2D + 0.5L \tag{7.2}$$

where D and L are the unfactored dead and live load respectively. From the RC building design presented in Section 7.2, the unfactored dead and live loads are 22.5 and 12.5KN/m respectively which result in gravity load of 33.3KN/m for the dynamic analysis. Consider one-half of the sub-assembly, the total load on the beam is 166.3KN and it is assumed that half of this load is carried by the middle column (removed column). Note that there will be another half of the beam load from the right side of the middle column, but by symmetry only the half load from the left beam is taken into account. Hence, the middle column is replaced by a reaction force of 83.3KN. The loading history used in applying the gravity load on the beam and the reaction force on the middle column is shown in Figure 7.8. Both loads are applied in a sufficiently long time duration t_0=5s such that the load are considered static and initial effects are minimized. The time of removal of the middle column reaction is 5ms, and this time duration is small enough to represents a sudden loss of column.

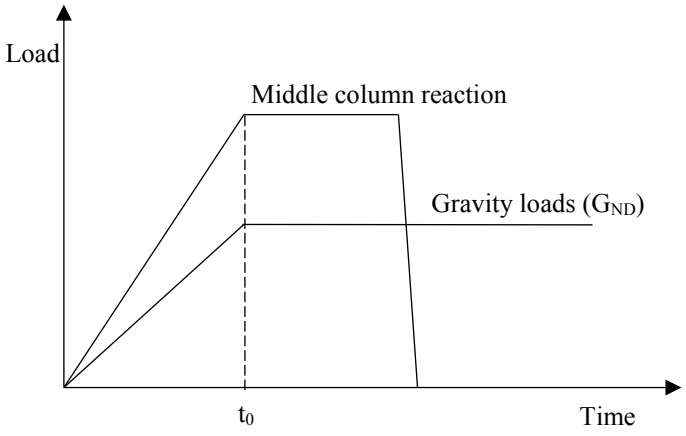

Figure 7.8: Loading history for simulating sudden column loss

7.4.3 Analysis of quasi static behaviour of the two subassemblies

The load displacement response of the two models are shown in Figure 7.9 together with their flexural load capacities. It can be seen that compressive arching action capacities are 1.46 and 2.3 times the flexural capacities for models A and B respectively. In terms of the axial compressive force, model B developed twice the axial compressive force than model A. This increases the moment capacity which in turn increased the maximum compressive arching action capacity of the subassembly in model B. However, in the catenary action stage, model A performs better because catenary action is a cable like behaviour which depends on the reinforcement and generally speaking the higher the reinforcement the higher the catenary action for the same axial stiffness (Yu & Tan 2013c; Su et al. 2009). Catenary action started at a displacement of about 430 and 620mm in models A and B respectively. The starting displacement for catenary action herein is slightly higher than the assumed starting displacement of one-beam depth (1.0d) in the catenary model developed in Chapter 6. However, as would be shown in subsequent section, the use of one-beam depth provides a reasonable conservative result.

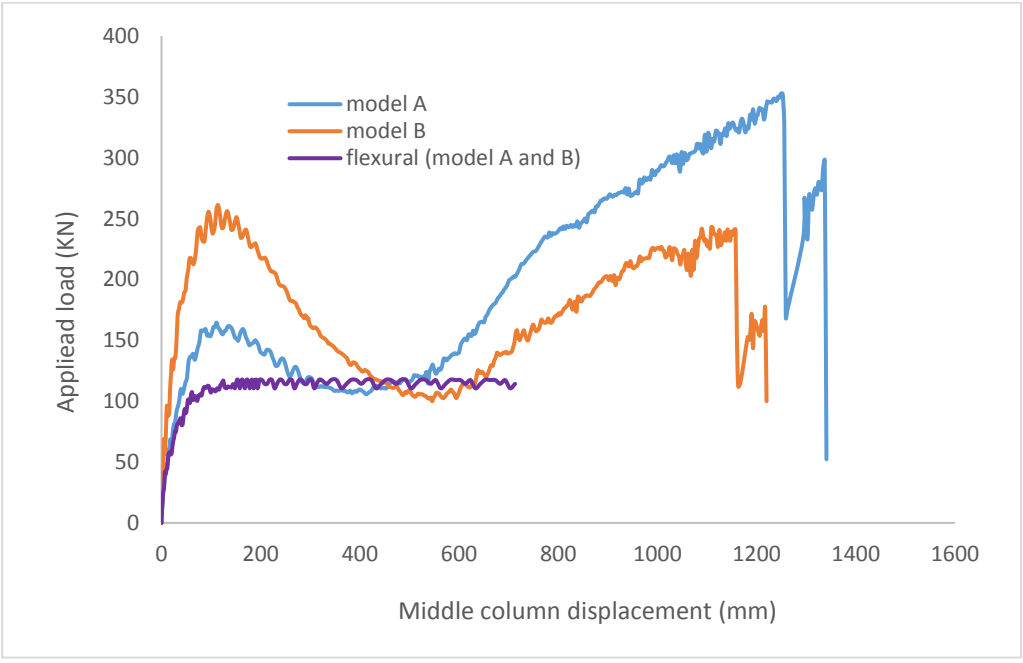

(a) Applied load-middle column displacement relationship

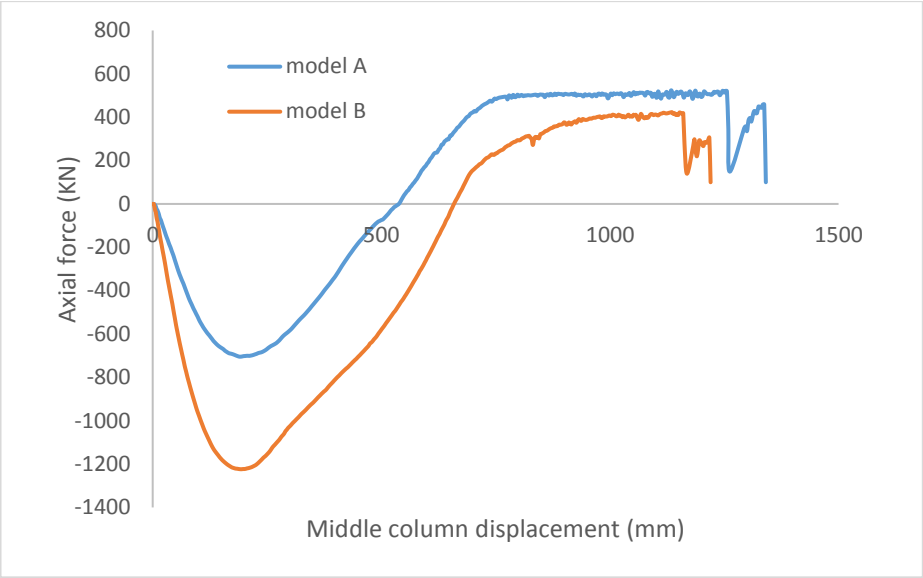

(b) Axial force-middle column displacement relationship

Figure 7.9: Applied load-middle column displacement and axial force-middle column displacement relationship of the subassemblies

In terms of damage, strain contour or plastic damage pattern may be further plotted. It should however be noted that in the large deformation regime, concrete plays little role in the strength of the beam, thus damage may well be represented by the strain contour distribution. Figure 7.10a and b shows the strain contour of the two models at a displacement of 1000mm prior to the rupture of bottom reinforcement.

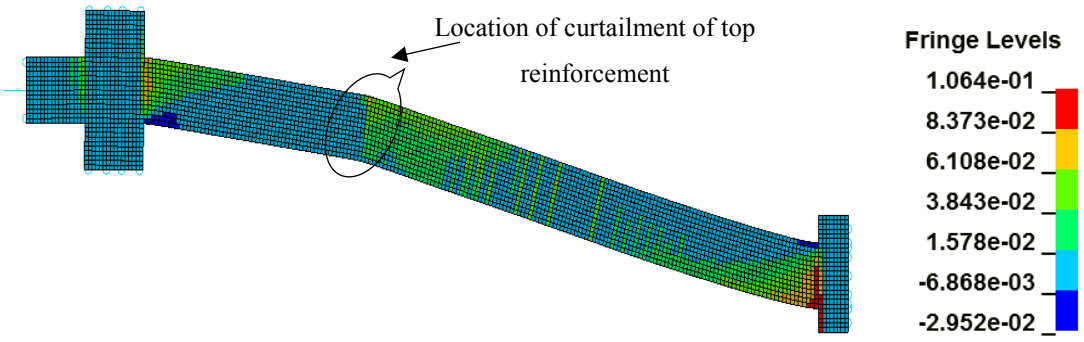

(a) Model A

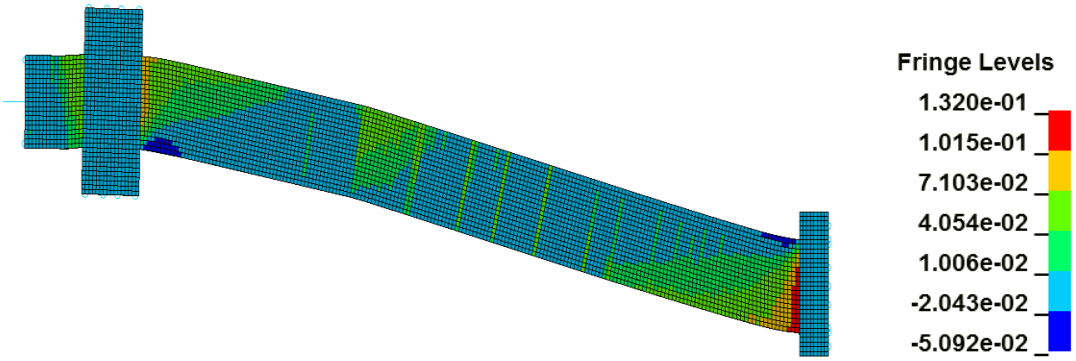

(b) Model B

Figure 7.10: Strain damage contour during the catenary action stage (middle column displacement of 1000mm)

The plastic strain in reinforcement is also plotted to have an understanding of its distribution during the large deformation regime. As shown in theoretical model in Chapter 6, the failure criteria for the rupture of reinforcement during catenary action stage was expressed in terms of the plastic zone length as shown in Equation (7.3).

$$\varepsilon_{cat} = \frac{0.5U_p}{L_{pc}} + \frac{\theta_p d}{2L_{pc}} \tag{7.3}$$

For RC beams subjected to bending, existing plastic hinge length expression in literature can be used. However, the behaviour of laterally restrained RC beam assemblies subjected to large deformation is different from that of bending. Thus, the equivalent plastic zone length should represent the damage at the catenary action stage which is tension dominated. Since no information for equivalent plastic zone length for RC beam assemblies under catenary action exist in the literature, herein the strain distribution in the top and bottom reinforcement for the two models at selected middle column displacement are plotted in Figure 2.10 to understand it variation during the catenary action stage. It could be seen that the plastic zone increases with increase in the middle column displacement. Although there is a slight difference in the plastic zone in models A and B, this difference is minimal. Since the displacement of 800mm is the midway between the start of catenary action and rupture of rebar, the equivalent plastic zone length can be determined using this displacement.Hence, using the strain

distribution at a displacement of 800mm an effective plastic zone length is determined such that the plastic strain lumped into the end and middle section . This is obtained by computing the area under the plastic strain curve and dividing it by the maximum strain. This gives a plastic zone length of 820mm. This can be expressed in terms of the span length as 0.18L where L is the length of one-half of the double span beam. The equivalent plastic zone length defined here is on the conservative side as the plastic zone length will further increase until the reinforcement ruptures.

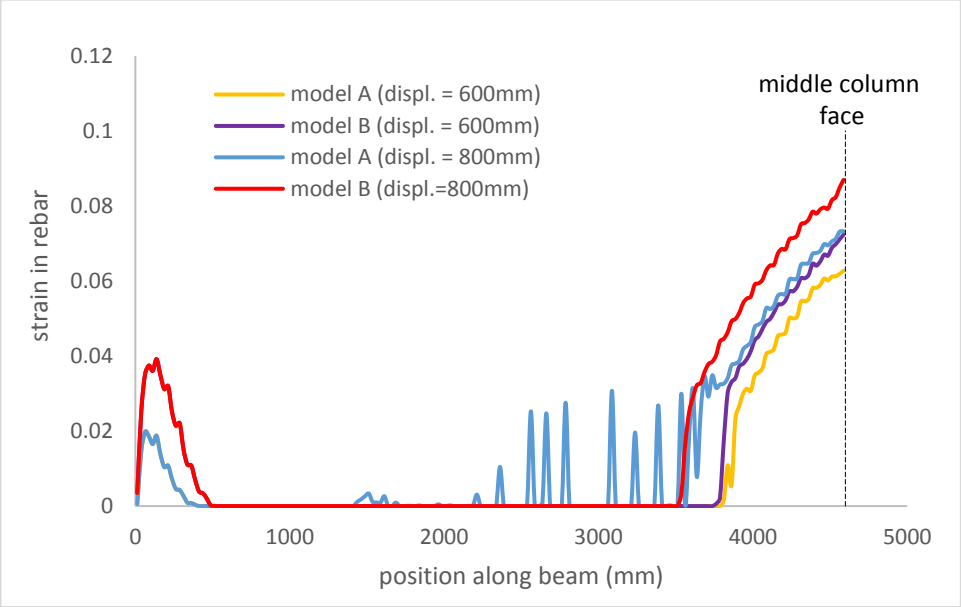

(a) Plastic strain distribution in bottom reinforcement

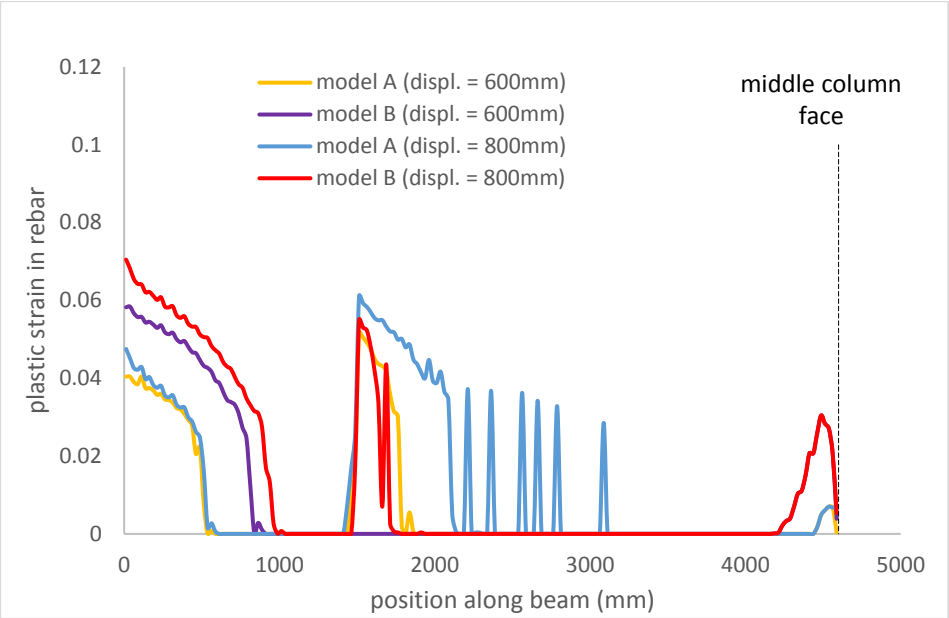

(b) Plastic strain distribution in top reinforcement

Figure 7.11: Reinforcement strain distribution in model A and B at selected displacement

7.5 Comparison of the predicted and FE modelling results

7.5.1 Determination of the yield function for the end and middle section of the plastic hinge

The theoretical model for catenary action developed in Chapter 6 is employed here to predict the load-displacement response. The axial force-moment interaction curve may be determined by performing sectional analysis on the section based on the geometric and reinforcement details at the support and mid-span sections. The interaction curve can be performed using the ultimate or yield strength of reinforcement. It should be noted that using the ultimate or yield strength will result in slightly different M-N curve. With ultimate strength, an upper bound curve will be obtained whereas using yield strength will result in lower bound result. Herein, the bending moment-axial force interaction curve is determined using the yield strength of reinforcement. The analysis is performed using a RC sectional analysis program RESPONSE-2000 (Benz

& Collins, 2001). The complete axial force-moment interaction for the two models is shown in Figure 7.12.

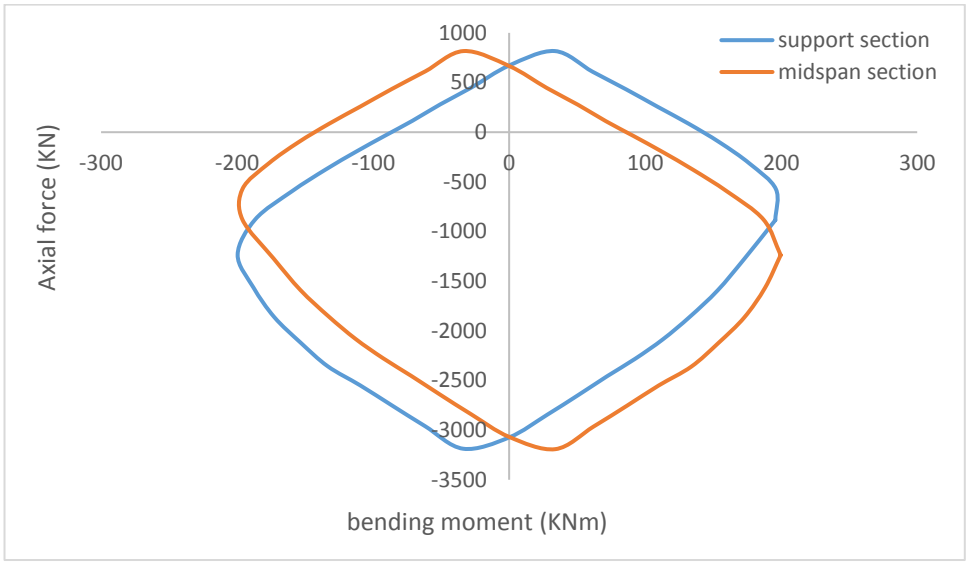

(a) Model A

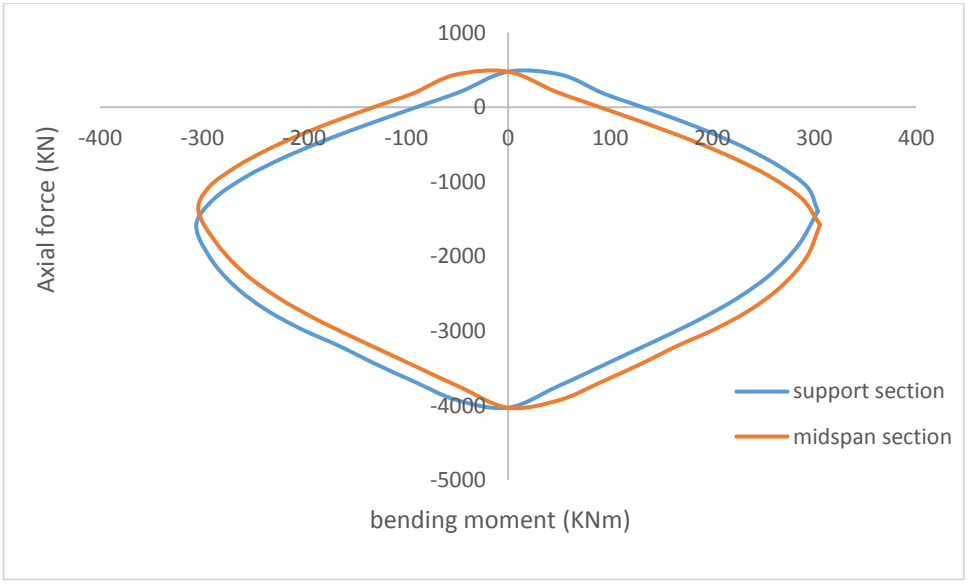

(b) Model B

Figure 7.12: Complete axial force-moment interaction curves for model A and B

During catenary action stage, the beam is in tension and thus the response is described by the axial force-bending interaction in the positive quadrant in Figure 7.12. As far as the interaction during catenary action stage is concerned, the interaction may be re-

plotted in terms of the normalised axial force-moment curves for the two models as shown in Figure 7.13 and the corresponding equations are:

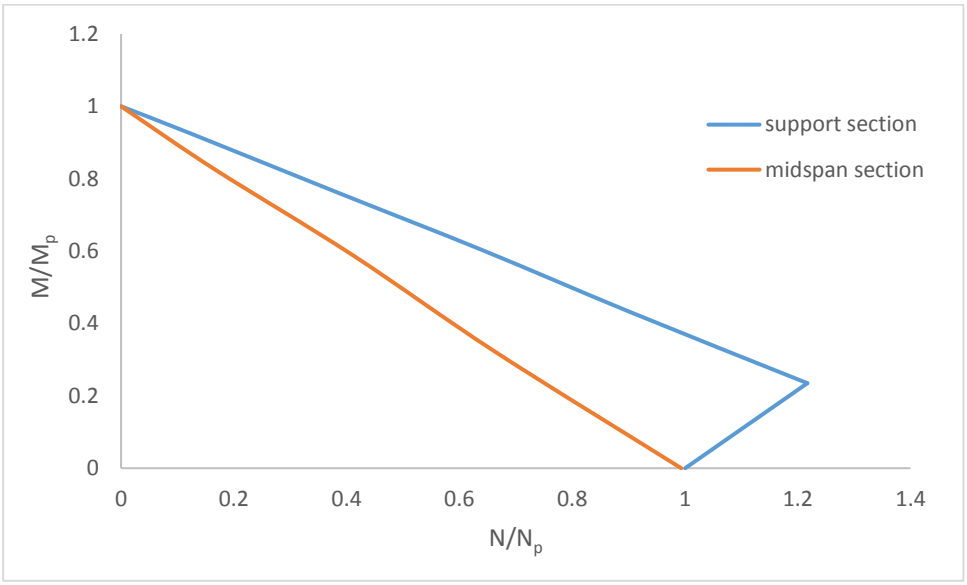

(a) Model A

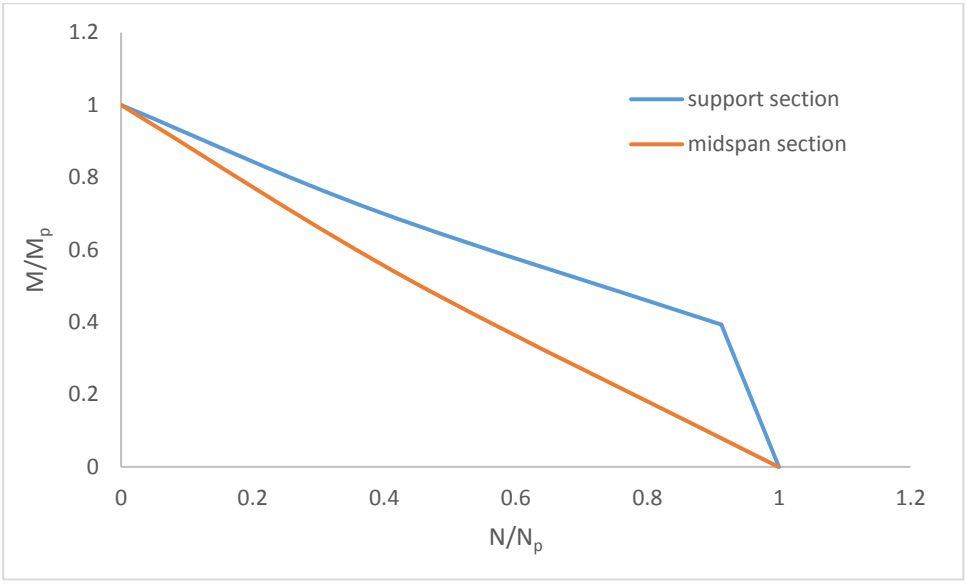

(b) Model B

Figure 7.13: Normalised axial force-bending moment interaction curves for the models

For model A support section:

$$\frac{M}{M_{pe}}+0.63\left(\frac{N}{N_p}\right)=1.0 \quad \text{for} \quad \frac{M}{M_{pe}}\geq 0.23 \tag{7.4}$$

$$\frac{M}{M_{pe}}-1.08\left(\frac{N}{N_p}\right)=-1.08 \quad \text{for} \quad \frac{M}{M_{pe}}< 0.23 \tag{7.5}$$

For model A mid-span section:

$$\frac{M}{M_{pm}}+\frac{N}{N_p}=1 \tag{7.6}$$

where M_{pm}, M_{pe} are the plastic moment capacities at the end and middle section which is equal to 85 and 145KNm respectively. N_p is the axial capacity of the beam section equal to 665KN.

For model B support section:

$$\frac{M}{M_{pe}}+0.66\left(\frac{N}{N_p}\right)=1 \quad \text{for} \quad \frac{M}{M_{pe}}\geq 0.39 \tag{7.7}$$

$$\frac{M}{M_{pe}}+4.5\left(\frac{N}{N_p}\right)=4.5 \quad \text{for} \quad \frac{M}{M_{pe}}< 0.39 \tag{7.8}$$

For model B mid-span section:

$$\frac{M}{M_{pm}}+\frac{N}{N_p}=1 \tag{7.9}$$

where M_{pm}, M_{pe} are the plastic moment capacities at the end and middle section which is equal to 95 and 136KNm respectively. N_p is the axial capacity of the beam section equal to 475KN.

7.5.2 Determination of equivalent axial stiffness of the end support

According to the theoretical model developed in Chapter 6, the equivalent axial stiffness can be expressed as:

$$K_e=\frac{1}{\frac{1}{K_a}+\frac{1}{K_s}+\frac{1}{K_a}} \tag{7.10}$$

where K_a is the axial stiffness of the end support and K_s is the axial stiffness of the beam (K_s=EA/L).

For RC beam assemblies, concrete is severely damage prior to the start of catenary action and this affect the axial stiffness of the beam that contribute effectively in the catenary action stage. As an illustration, Figure 7.14 shows the effect of axial stiffness of beam section on the response of RC beam during catenary action. Model A subassembly is used for the analysis and the axial stiffness of the end support (K_a) is taken as 3 x 10^5KN/m.

Three different cases are considered: first is RC beam with full uncracked axial stiffness (EA/L), second is half axial stiffness (0.5*EA/L) and one-quarter of axial stiffness (0.25*EA/L) of the beam. It can be observed that axial stiffness of the beam influences the state at which the plastic capacity of the beam section is reached. When the area of the full section is used, the beam enters its plastic state at a much smaller middle column displacement compared to when 25% of the section is used. Herein the axial stiffness of the beam is assumed to be 10% of the full section.

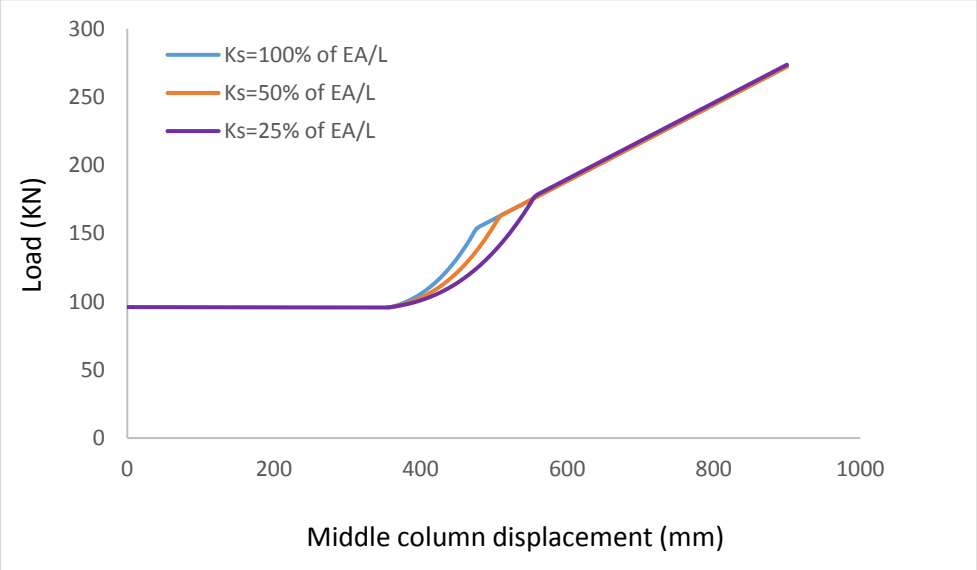

Figure 7.14: Effect of beam axial stiffness on the RC assembly behaviour during catenary action stage

7.5.3 Comparison and discussion of results

Figure 7.15 shows the comparison between the FE and theoretical predictions for the two models. It can be seen that the theoretical model predicts reasonably well the compressive arching catenary behaviour in the two RC beams. However, the model slightly under predict the compressive arching action capacity in model B. Also, the failure displacement predicted by the model is much smaller than that of FE predictions in both models. Aside these few differences, the predicted model captures well the behaviour of the two beam assemblies.

With the theoretical load-displacement response, the progressive collapse assessment can be evaluated as will be shown in the next section.

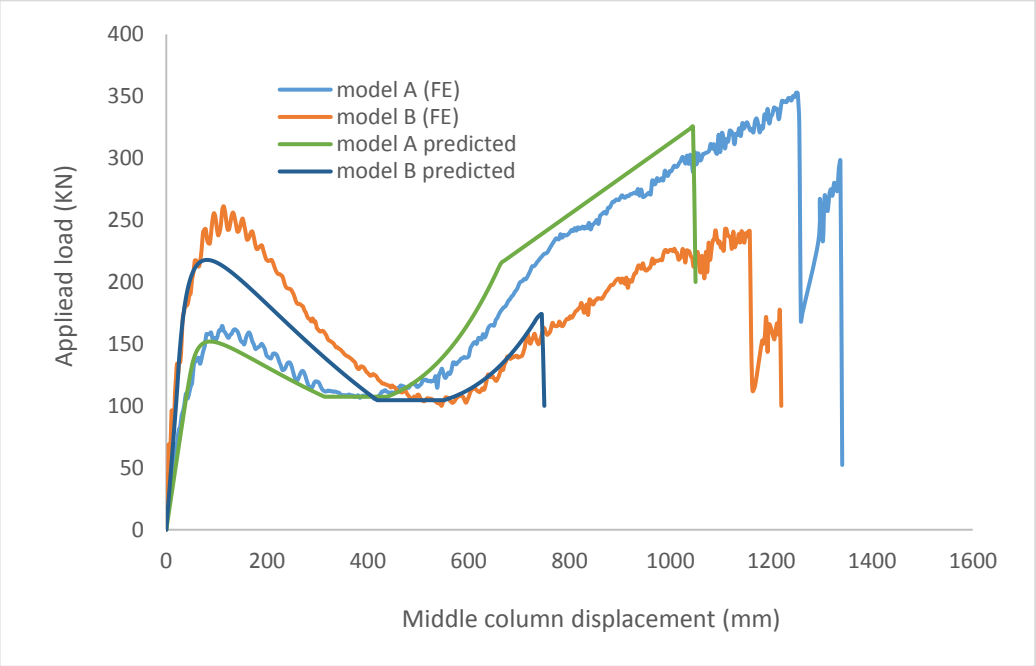

Figure 7.15: Load-middle column displacement response

7.6 Progressive collapse-resisting capacity curve

The nonlinear static curves in Section 7.5 can be converted to a pseudo static capacity curve for assessing progressive collapse based on the energy balance principle (Izzuddin et al. 2008). When a primary load carrying member in a building is lost, the

affected part of the building moves downward. The downward movement of the area creates potential and kinetic energies. The potential energy is caused by the falling structure whereas kinetic energy is due to the effective moving mass involved. In reaction to this strain energy is developed in the deformed components. At any given stage of the collapse process, comparison between the potential energy (external workdone) and strain energy (energy absorbed by the deformed components) is checked. According to energy equilibrium and assuming no loss of energy, the difference between potential and strain energy is equal to the kinetic energy. When this difference is positive, the building is still in downward motion and collapse is yet to be halted. If and when the difference becomes zero, the strain energy equals the potential energy and thus the structure comes to rest and collapse is prevented.

An example calculation for the conversion of nonlinear static curve to pseudo static curve for a simple bilinear nonlinear static resistance function is as schematically illustrated below and the result is shown in Figure 7.15.

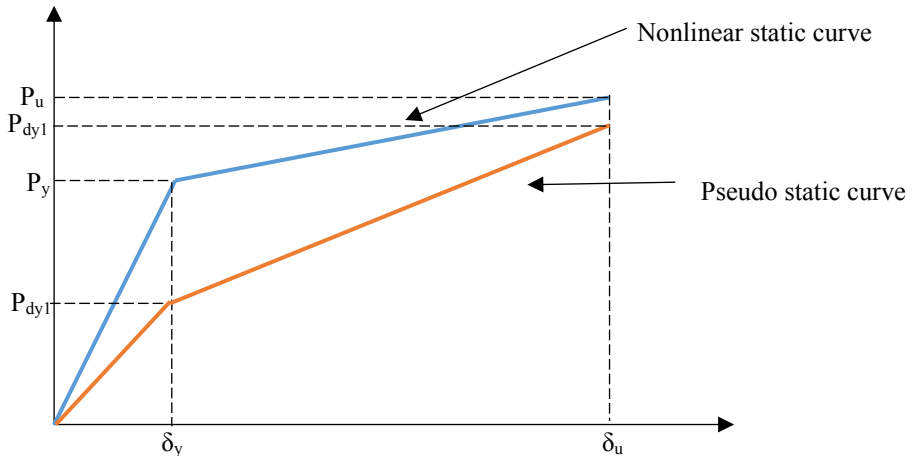

Figure 7.16: Illustration of the conversion of nonlinear static curve to pseudo static curve

From energy principle;

Internal work done = external work done

At a displacement δ_y;

$$P_{dy1}\delta_y = 0.5P_y\delta_y \quad \Rightarrow \quad P_{dy1} = 0.5P_y \tag{7.11}$$

At a displacement δ_u;

$$P_{dy2}\delta_u = 0.5P_y\delta_y + P_y(\delta_u - \delta_y) + 0.5(\delta_u - \delta_y)(P_u - P_y) \tag{7.12}$$

$$\Rightarrow P_{dy2} = \frac{0.5P_y\delta_y + P_y(\delta_u - \delta_y) + 0.5(\delta_u - \delta_y)(P_u - P_y)}{\delta_u} \tag{7.13}$$

Based on the above explanation, the nonlinear static curves for model A and B are converted to pseudo static curves. Also, the pseudo static curves are calculated from the flexural capacity of the models as shown in Figure 7.17.

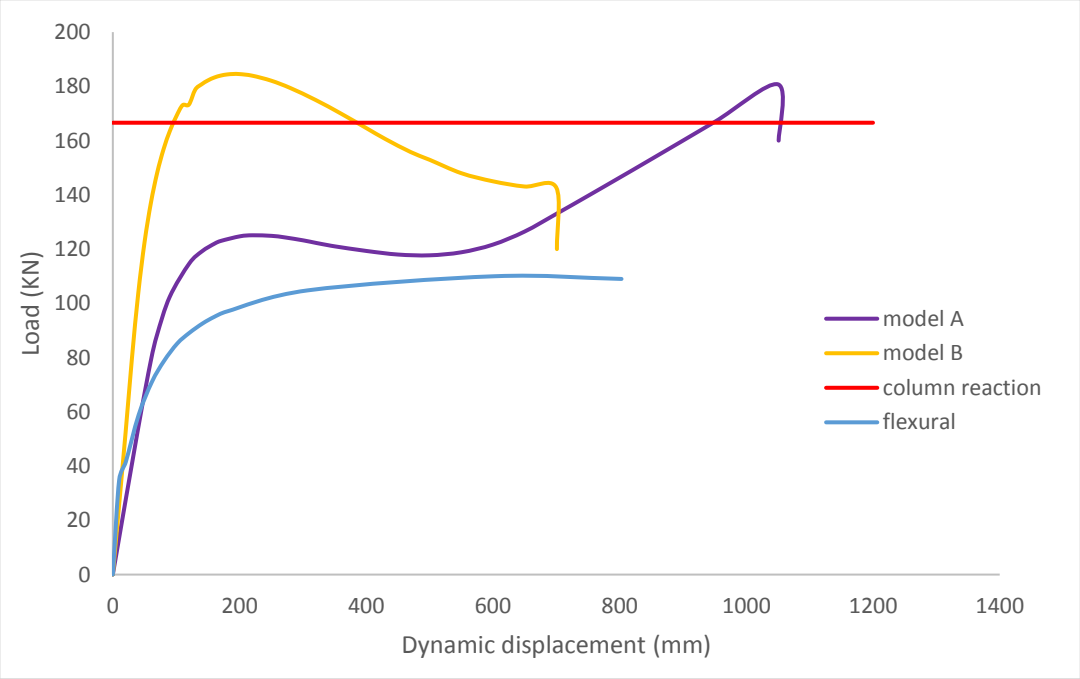

Figure 7.17: Pseudo static curves for the different RC subassemblies

It can be seen from Figure 7.17 that the load to be transferred through the bridging beam (i.e. the original reaction force in the lost column) crosses the pseudo static curves at different displacement in the different models. For model A, collapse is arrested at a displacement of about 950mm which is well into the catenary action stage. In model B, due to the markedly increased resistance capacity at bending-arching stage

as a result of compressive arching action, collapse is arrested at a considerably smaller displacement of 95mm. This again highlight the important of compressive arching action which is mostly ignored in the progressive analysis of RC buildings. It should be noted that there is also increased energy absorption capacity due to arching effect but that is not fully required to be mobilised in this case. In fact, a critical look at the figure further shows that model B can resist dynamic load of up 180KN and the structure will only displace downward by 200mm at that point. On the other hand, if the dynamic load of 180KN is applied to model A, the structure will displace to about 1150mm and such big displacement could practically be catastrophic to the structure. Considering only the flexural capacity of RC assemblies indicate that the structure will collapse as no balance could be reached between the internal energy and the external energy demand. The maximum resistance capacity of the structure based on pure flexural capacity is much less than the static reaction of the removed column, thus collapse cannot be prevented.

The result of the simplified dynamic approach shown above is further compared with the nonlinear dynamic result from FE. Figure 7.18 shows the time history plot of the two models and the baselines from the simplified approach. The maximum dynamic displacement from FE models are 985 and 78mm for model's A and B respectively. While the predicted dynamic displacement from the simplified approach is 950 and 95mm respectively.

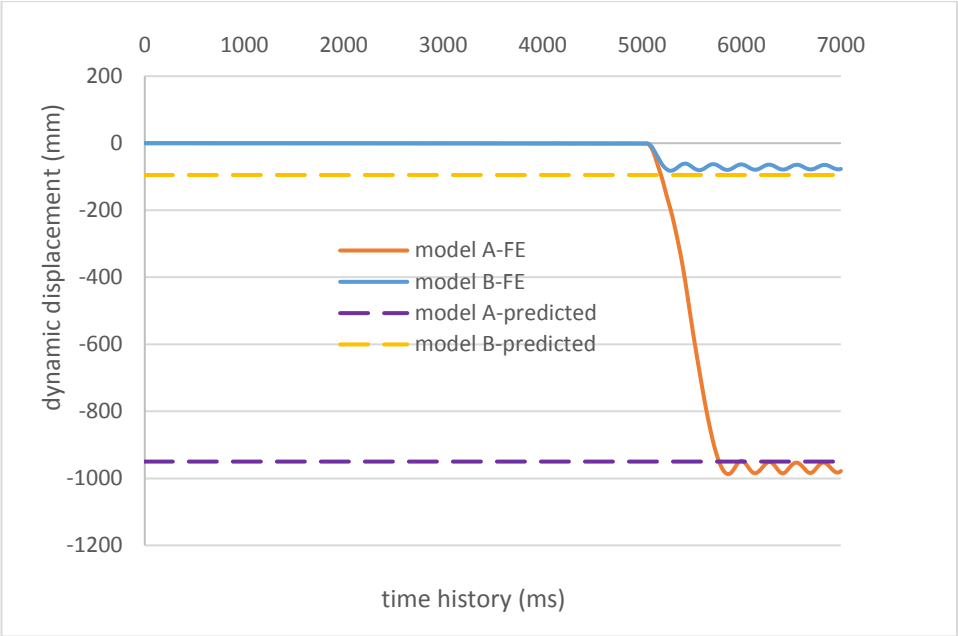

Figure 7.18: Pseudo static curves for the different RC subassemblies

7.7 Concluding remarks

This chapter investigated the progressive collapse behaviour of two different designs using the developed framework in the earlier chapters. The approaches on the determination of axial stiffness of the surrounding substructure and the moment interaction curves for the middle and support sections based on the material and geometric properties have beam succinctly presented. The illustration shows that the model framework in this thesis is able to predict the load-displacement response of the subassembly, including the compressive arching action and catenary action, and these can be employed to evaluate the amplitude dynamic response. With this simplified framework, the progressive collapse of RC assemblies can be easily assessed.

The illustrative example herein shows that the progressive collapse behaviour of two different designs having the same flexural capacity can be greatly different especially when the progressive collapse response is well beyond the flexural response stage. For RC beam assemblies with adequate axial restraint, compressive arching can provide additional energy absorption which may help avert collapse at a much lower

displacement. It is recommended based on this study, that in other to accurately assess progressive collapse potential of a structure, a realistic prediction of the compressive and catenary action should be carried out and incorporated into the design analysis. This can be achieved using the simplified framework developed in this thesis.

Chapter 8: Conclusions and recommendation for future work

To assess the progressive collapse potential of structures (RC or steel assemblies) in design applications, an engineering approach is preferred. Previous studies have shown that analysis using ALP method can provide a reliable means of assessment for progressive collapse. However, the use of this method requires that the resistance function of the assemblies be accurately predicted taking into consideration the possible failure modes; for steel assemblies, this may involve degradation of strength due to partial failure at connections and for RC assemblies this can be due to rupture of reinforcing bars. To take such factors into account in a sound mechanics-based manner, the thesis has focused on the different mechanisms that could develop in axially restrained RC frame structures following a column loss, and also on the quantification of such important mechanisms as the arching effect and the catenary action. Improved theoretical models for the compressive arching and catenary actions are developed to predict the complete load displacement behaviour taking into consideration the arching effect and the possibility of strength degradation due to failure of some connection component.

Although, beam-column fibre element can be used to model the response of progressive collapse in RC buildings, it still presents some challenges in modelling accurately the response under column removal. For instance, selection of suitable material model for the confine and unconfined concrete is necessary to better represent the compressive arching action. More so, the beam-to-column joint interface needs to be correctly modelled by specifying the properties of rotational springs between the beam and column which in turn must be calibrated. This present additional complexities to the modelling process. On the other hand, the simplified model presented in this study is easier to use and can produce accurate result with less effort.

8.1 Main conclusions

Based on the research in this study, the following main conclusions can be made:

1) Compressive arching action capacity is affected by the reinforcement ratio, concrete compressive strength, span-depth ratio and axial restraint. The effect of these parameters on arching compression can be predicted. Both axial restraint and span-depth ratio has a pronounced effect on both the relative increase in load due to arching and the normalised arching capacity whereas reinforcement ratio has pronounced effect only on the normalised increase in load but very minimal effect on the relative increase in between maximum arching and bending capacities. When evaluating the arching capacity, RC beam assemblies with axial stiffness coefficient (α_K) greater than 5 may be considered as rigid axial support to simplify the calculations.

2) By considering the compounding effect of bending and arching, a comprehensive theoretical model is proposed. With the developed model, the load-displacement behaviour (resistance function) in axially restrained RC beam assemblies can be accurately predicted. This model can be used along with the energy balance principle to determine the energy absorption that could be attributable to arching action.

3) Behaviour of RC and steel assemblies under progressive collapse will involve strength degradation due to failure of connection components. Accurate analysis should therefore consider the strength degradation that may develop. With the catenary model developed in this study, load-displacement behaviour and strength degradation can be correctly captured. Comparison with FE model and physical experiments confirms that the model's prediction is accurate. Damage in the beam and the criteria at which strength degradation will occur can be obtained by considering the axial elongation and rotation of the beam.

Depending on the type of structure, the damage may be based on only the rotation or both rotation and elongation of the plastic hinge zone.

4) Different RC assemblies having the same flexural capacities will behave differently when subjected to progressive collapse due to extreme loading. If adequate compressive arching action can develop in RC structure subjected to a column loss, progressive collapse may be resisted at a much smaller displacement compared to similar design having much higher reinforcement but with a reduced arching effect.

5) The load-displacement behaviour for RC beams located within the periphery frame in a column loss scenario can be predicted using the models developed in this study. The framework may be applied in practical design analysis for an engineering assessment of the progressive collapse potential of RC structures without the need for a more detailed (and hence computationally costly) FE modelling of the entire structure. This has been confirmed by the comparison of the analysis using a detailed nonlinear dynamic analysis and the result from the simplified framework developed in this study.

8.2 Recommendations for future work

This study presents improved analysis models for the evaluation of the resistance (load-displacement) function for beam assemblies taking into consideration of the degradation of strength, as well as the compressive arching action. Such resistance function can provide an engineering means for assessing progressive collapse potential of a structure using the energy method. However, the present study only focused on the assemblies located within the periphery of the structure and floor slab was not considered in the analytical study. Further research work is therefore recommended in the following related areas:

- Develop analytical model for the prediction of compressive arching action in RC assemblies incorporating the membrane effect in slab.

- In GSA (2013) guidelines, removal of interior column for progressive collapse assessment is also recommended. In such cases, the transverse beams may play an important role, hence analytical model should be able to capture the effect of beams in both directions. For this reason, analytical model for compressive arching action taking into consideration the transverse beams contribution in load resistance should be developed.

- The semi-empirical expressions for the prediction of arching effect developed in this study should be further validated with more experimental studies to ascertain its accuracy.

- It was shown in the development of the catenary model, that degradation of strength and actual failure limit is a necessary input for the prediction of complete load-displacement behaviour (resistance function). Accordingly, experimental and numerical studies on different connection details should be studied and a database of failure criteria for the different connections generated.

- As shown in the investigative studies, the final failure displacement for RC assemblies depends on the plastic zone length adopted. Further experimental studies should be conducted for different types of connections to determine the plastic length zone that can well capture the failure displacement in the models developed in this study.

References

Abbasnia, R. & Nav, F.M., 2016. A theoretical method for calculating the compressive arch capacity of RC beams against progressive collapse. *Structural Concrete*, 17(1), pp.21–31.

ADINA, 2006. *ADINA 8.3 Version User Manual, ADINA R&D, Inc., Watertown, Mass, USA, 1996.*,

Albrifkani, S. & Wang, Y.C., 2016. Explicit modelling of large deflection behaviour of restrained reinforced concrete beams in fire. *Engineering Structures*, 121, pp.97–119.

Alogla, K., Weekes, L. & Augusthus-Nelson, L., 2017. Theoretical assessment of progressive collapse capacity of reinforced concrete structures. *Magazine of Concrete Research*, 69(3), pp.145–162.

Ansari, F. & Li, Q., 1998. High-Strength Concrete Subjected to Triaxial Compression. *ACI Material Journal*, 95(6), pp.747–755.

ANSYS, 2009. *15317 AUTODYN User Manual Version 12.0 Canonsburg*,

Baker, A., 1956. *Ultimate Load Theory Applied to the Design of Reinforced and Prestressed Concrete Frames. Concrete Publications Ltd. London*,

Brannon, R.M. & Leelavanichkul, S., 2009. Survey of Four Damage Models for Concrete. , (August), pp.1–80.

Chen, W. & Han, D., 1988. *Plasticity for Structural Engineers*, Springer-Verlag, New York.

Choi, H. & Kim, J., 2011. Progressive collapse-resisting capacity of RC beam-column sub-assemblage. *Magazine of Concrete Research*, 63(4), pp.297–310.

Christiansen, K.P., 1963. The Effect of Membrane Stresses on the Ultimate Strength of the Interior Panel in a Reinforced Concrete Slab. *The Structural Engineer*,

41(8), pp.261–265.

Corley, G.W., 1966. Rotation Capacity of Reinforced Concrete Beams. *Journal of Structural Engineering, ASCE*, 92(10), pp.121–146.

Corley, W.G. et al., 1998. The Oklahoma City Bombing: Summary and Recommendations for Multihazard Mitigation. *Journal of Performance of Constructed Facilities*, 12(3), pp.100–112.

Crawford, J. et al., 2012. *Use and validation of the release III K&C concrete material model in LS-DYNA*,

Dafalias, Y.F. & Herrmann, L.R., 1986. Bounding surface plasticity. II: application to isotropic cohesive soils. *Journal of Engineering Mechanics*, 112(12), pp.1263–1291.

Dassault Systemes, 2007. Abaqus Analysis User's Manual. Simulia Corp. Providence, RI, USA.

Guo, L. et al., 2013. Experimental study and numerical analysis of progressive collapse resistance of composite frames. *Journal of Constructional Steel Research*, 89, pp.236–251.

Hinman, E.E. & Hammond, D.J., 1997. *Lessons from the Oklahoma City bombing, ASCE, New York.*,

Hognested, E., Hanson, N.W. & McHenry, D., 1955. Concrete Stress Distribution in Ultimate Strength Design. *American Concrete Institute Journal, Proceedings*, 52(4), pp.455–480.

Imran, I. & Pantazopoulou, S.J., 1996. Experimental Study of Plain Concrete under Triaxial Stress. *ACI Structural Journal*, 93(6), pp.589–601.

Izzuddin, B.A., 2005. A simplified model for axially restrained beams subject to extreme loading. *International Journal of Steel Structures*, 5(5), pp.421–429.

Izzuddin, B.A. et al., 2007. Assessment of Progressive Collapse in Multi-Storey Buildings. *Proceedings of the ICE - Structures and Buildings*, 160(4), pp.197–205.

Izzuddin, B.A. et al., 2008. Progressive collapse of multi-storey buildings due to sudden column loss - Part I: Simplified assessment framework. *Engineering Structures*, 30(5), pp.1308–1318.

Jirasek, M. & Bazant, Z.P., 2001. *Inelastic Analysis of Structures,* 1 edition., John Wiley & Sons.

Lew, H.S. et al., 2014. *An Experimental and Computational Study of Reinforced Concrete Assemblies under a Column Removal Scenario*,

Li, G. et al., 2008. Catenary action of restrained steel beam against progressive collapse of steel frameworks. *J. Cent. South Univ. Technol. (Engl. Ed.)*, 15(6), pp.830–834.

Li, L. et al., 2015. Effect of beam web bolt arrangement on catenary behaviour of moment connections. *Journal of Constructional Steel Research*, 104, pp.22–36.

Li, L. et al., 2013. Experimental investigation of beam-to-tubular column moment connections under column removal scenario. *Journal of Constructional Steel Research*, 88, pp.244–255.

Long, H. Van & Hung, N.D., 2008. Second-order plastic-hinge analysis of 3-D steel frames including strain hardening effects. *Engineering Structures*, 30(12), pp.3505–3512.

LSTC, 2012. *II LS-DYNA Keyword User's Manual. Livermore, California.*,

Maekawa, K., Pimanmas, A. & Okamura, H., 2003. *Nonlinear Mechanics of Reinforced Concrete*, Spoon Press Taylor & Francis Group.

Magallanes, J. et al., 2010. Recent improvements to release III of the K&C concrete model. *11th international LS- ...*, pp.37–48.

Magallanes, J.M., 2008. Importance of concrete material characterization and modelling to predicting the response of structures to shock and impact loading. *WIT Transactions on the Built Environment*, 98, pp.241–250.

Malvar, L.J. et al., 1997. A Plasticity Concrete Material Model for DYNA3D. *International Journal of Impact Engineering*, 19(97), pp.847–873.

Mattock, A.H., 1967. Discussion of Rotational Capacity of Reinforced Concrete Beams, by W. D. G. Corley. *Journal of Structural Division, ASCE*, 93(2), pp.519–522.

Mlakar, Sr., P.F. et al., 1998. The Oklahoma City Bombing: Analysis of Blast Damage to the Murrah Building. *Journal of Performance of Constructed Facilities*, 12(3), pp.113–119.

Mlakar, P.F. et al., 2003a. Description of Structural Damage Caused by the Terrorist Attack on the Pentagon. *Forensic Engineering, Proceedings of the Congress*, 19(August), pp.197–205.

Mlakar, P.F. et al., 2003b. Findings and recommendations from the Pentagon crash. *Forensic Engineering, Proceedings of the Congress*, 19(3), pp.220–221.

Mlakar, P.F. et al., 2005a. Response to Fire Exposure of the Pentagon Structural Elements. *Journal of Performance of Constructed Facilities*, 19(August), pp.212–219.

Mlakar, P.F. et al., 2005b. September 11, 2001, Airliner Crash into the Pentagon. *Journal of Performance of Constructed Facilities*, 19(January 1943), pp.189–196.

Moradi, Saber; Alam, S., 2013. Finite-Element Simulation of Posttensioned Steel Connections with Bolted Angles under Cyclic Loading. *Journal of Structural Engineering*, 1(2), pp.1–12.

Orton, S.L., 2007. *Development of a CFRP System to Provide Continuity in Existing*

Reinforced Concrete Buildings Vulnerable to Progressive Collapse.

Osteraas, J.D., 2006. Murrah Building Bombing Revisited: A Qualitative Assessment of Blast Damage and Collapse Patterns. *Journal of Performance of Constructed Facilities*, 20(4), pp.330–335.

Park, R., 1964. Ultimate Strength of Rectangular Concrete Slabs Under Short-Term Uniform Loading with Edges Restrained Against Lateral Movement. *Proceedings of the Institution of Civil Engineers*, 28, pp.125–150.

Pham, A.T., Tan, K.H. & Yu, J., 2016. Numerical investigations on static and dynamic responses of reinforced concrete sub-assemblages under progressive collapse. *Engineering Structures*.

Popovics, S., 1973. A Numerical Approach to the Complete Stress-Strain Curve of Concrete. *Cement and Concrete Research*, 3(4), pp.583–599.

Priestley, M.J.N. & Park, R., 1987. Strength and Ductility of Concrete Bridge Columns Under Seismic Loading. *ACI Structural Journal*, 84(1), pp.61–76.

Rankin, G.I.B. & Long, A.E., 1997a. Arching action strength enhancement in laterally-restrained. *Proceeding Institution of Civil Engineers Structs and Bldgs*, pp.461–467.

Rankin, G.I.B. & Long, A.E., 1997b. Arching Action Strength Enhancement in Laterally-Restrained Slab Strips. *Proceedings of the Institution of Civil Engineers - Structures and Buildings*, 122(4), pp.461–467.

Ruddle, M.E., Rankin, G.I.B. & Long, A.E., 2003. Arching Action—Flexural and Shear Strength Enhancements in Rectangular and Tee Beams. *Proceedings of the Institution of Civil Engineers - Structures and Buildings*, 156(1), pp.63–74.

Sadek, F. et al., 2011. Testing and analysis of steel and concrete beam-column assemblies under a column removal scenario. *Journal of Structural Engineering*, 137(9), pp.881–892.

Sasani, M. et al., 2011. Progressive collapse resistance of an actual 11-story structure subjected to severe initial damage. *Journal of Structural Engineering*, 137(9), pp.893–902.

Sasani, M. & Kropelnicki, J., 2008. Progressive Collapse Analysis of an RC Structure. *Structural Design of Tall and Special Buildings*, 17(4), pp.757–771.

Sawyer, H.A., 1964. Design of Concrete Frames for Two Failure States. In *Proceedings of the International Symposium on the Flexural Mechanics of Reinforced Concrete. ASCE-ACI*. pp. 405–431.

Seidalinov, G. & Taiebat, M., 2014. Bounding surface saniclay plasticity model for cyclic clay behavior. *International Journal for Numerical and Analytical Methods in Geomechanics*, (38), pp.702–724.

Sheikh, S.A. & Khoury, S.S., 1993. Confined Concrete Columns with Stubs. *ACI Structural Journal*, 90(4), pp.414–431.

Stinger, S.M. & Orton, S.L., 2013. Experimental evaluation of disproportionate collapse resistance in reinforced concrete frames. *ACI Structural Journal*, 110(3), pp.521–529.

Su, Y., Tian, Y. & Song, X., 2009. Progressive Collapse Resistance of Axially-Restrained Frame Beams. *ACI Structural Journal*, 106(5), pp.600–607.

Taylor, D.A., 1975. Progressive Collapse. *Canadian Journal of Civil Engineering*, 2(4), pp.517–529.

Vali, H. et al., 2015. Influence of Concrete Compressive Strength on the Arching Behaviour of Reinforced Concrete Beam Assemblages. , 18(8), pp.1199–1214.

Vesali, N.F. et al., 2013. Development of arching action in longitudinally-restrained reinforced concrete beams. *Construction and Building Materials*, 47, pp.7–19.

Vlassis, A.G. et al., 2009. Progressive collapse of multi-storey buildings due to failed floor impact. *Engineering Structures*, 31(7), pp.1522–1534.

Wood, R.H., 1961. *Plastic andd Elastic Design of Slabs and Plates*, London, Thames and Hudson.

Xu, J. & Lu, Y., 2016. Numerical modelling for reinforced concrete response to blast load : understanding the demands on material models. *American Concrete Institute - Special Publication*, 306, p.3.1-3.22.

Yang, B. & Tan, K.H., 2014. Behavior of composite beam-column joints in a middle-column-removal scenario: experimental tests. *Journal of Structural Engineering*, 140(2), p.4013045.

Yang, B. & Tan, K.H., 2013a. Experimental tests of different types of bolted steel beam-column joints under a central-column-removal scenario. *Engineering Structures*, 54, pp.112–130.

Yang, B. & Tan, K.H., 2013b. Robustness of bolted-angle connections against progressive Collapse: experimental tests of beam-column joints and development of component-based models. *Journal of Structural Engineering*, 139(9), pp.1498–1514.

Yi, W. et al., 2008. Experimental Study on Progressive Collapse-Resistant Behavior of Reinforced Concrete Frame Structures. *ACI Structural Journal*, (105), pp.433–439.

Yin, Y.Z. & Wang, Y.C., 2005. Analysis of catenary action in steel beams using a simplified hand calculation method, Part 1: theory and validation for uniform temperature distribution. *Journal of Constructional Steel Research*, 61(2), pp.183–211.

Yu, J., 2012. *Structural Behavior of Reinforced Concrete Frames Subjected to Progressive Collapse*. Nanyang Technological University.

Yu, J. & Tan, K.H., 2014. Analytical model for the capacity of compressive arch action of reinforced concrete sub-assemblages. *Magazine of Concrete Research*, 66(3), pp.109–126.

Yu, J. & Tan, K.H., 2013a. Experimental and numerical investigation on progressive collapse resistance of reinforced concrete beam column sub-assemblages. *Engineering Structures*, 55, pp.90–106.

Yu, J. & Tan, K.H., 2013b. Structural Behavior of RC Beam-Column Subassemblages under a Middle Column Removal Scenario. *Journal of Structural Engineering*, 139(2), pp.233–250.

Zolghadr Jahromi, H. et al., 2012. Robustness assessment of building structures under explosion. *Buildings*, 2(4), pp.497–518.